UNIVERSITY OF LIVERPOOL

Mucoadhesive Emulsions for the Delivery of Therapeutic Agents

Stephanie Ellen Edwards

Thesis submitted in accordance with the requirements of the University of Liverpool for the degree of Doctor in Philosophy

September 2018

Abstract

Mucus lines the moist cavities in the body and acts as a barrier for these surfaces, protecting the underlying cells against the external environment but also unfortunately hindering the permeation of drugs and delivery systems. As the rate of diffusion across this barrier is low, the development of drug delivery systems that can increase retention time at the mucosal interface would be beneficial. Mucus is highly rich in cysteine groups, which have been targeted recently for a new generation of mucoadhesive thiol-functional polymers, able to form disulphide bonds with cysteine rich areas. The aim of this study was to synthesise thiol-functional branched copolymers to stabilise oil-in-water emulsions and test their potential as mucoadhesive therapeutic drug delivery systems.

Atom-transfer radical polymerisation was used to synthesise amphiphilic linear and branched copolymers of oligo (ethylene glycol) monomethyl ether methacrylate, with a hydrophobic initiator, dodecyl α-bromoisobutyryl bromide, for testing as polymeric surfactants for oil-in-water macroemulsions and nanoemulsions. Branched polymer architecture was determined to be critical for the formation of successful and stable emulsions. The number of hydrophobic chain ends which can be substituted with hydrophilic functionality, while retaining emulsion stabilisation was evaluated by co-initiating branched copolymerisations with a poly(ethylene glycol)-derived initiator. Systematic reduction of hydrophobic chain ends showed that a minimum of 25 mole percent were necessary to retain emulsion stability.

Mucoadhesive functionality was incorporated into the branched copolymers *via* a xanthate based initiator which contains a masked thiol group. The polymers were then deprotected post-polymerisation to reveal thiol groups at varying concentrations, and used as surfactants to successfully generate functional macroemulsions and nanoemulsions. Mucoadhesive properties of the thiol functionalised emulsions were tested using a novel flow through model which determined that an increase in mole percentage of thiol chain ends did lead to an increase in nanoemulsion adherence to biosimilar mucus. *Ex vivo* multiple particle tracking, using porcine intestinal mucus confirmed that an increase in thiol chain ends was critical to the mucoadhesive behaviour, where 42 % of particles tracked from a non-thiol functional nanoemulsion were highly diffusive and an increase to 90 mole percent thiol chain ends drastically reduced the amount of diffusive particles to 6 %.

The potential of using the mucoadhesive emulsions for ophthalmic treatments utilising mucus content within the tear film was investigated. Cytotoxicity of nanoemulsions was evaluated against mucus secreting human conjunctival epithelial cells and human corneal epithelial cells, and determined to be non-toxic below 9.1 v/v % concentration of emulsion diluted in culture media. Nanoemulsions were also successfully loaded with two common drugs for ophthalmic treatments, amphotericin B and cyclosporin A at doses matching commercial topically dosed products. Overall the potential for thiol-functional macroemulsions and nanoemulsions to have mucoadhesive characteristics has been demonstrated, and the number of thiol chain ends critical to the level of adhesion determined.

Acknowledgements

I would like to thank my Mum and Dad for their unwavering support and love through this entire journey. I cannot begin to express how thankful I am for everything you have done for me in life, every achievement has felt monumental and every low manageable thanks to you two. I will always admire not only your positive outlook on life but also the strength and resilience you both possess. I love you both very much.

To Fraser, thank you for being the greatest big brother a sister could wish for, you've always been my biggest supporter but I will always look up to you. To Ronnie, thank you for not only all your support during my PhD but for also being the sister I always wanted. To Sophie, Evie, Joshua and Molly, you all bring me so much unconditional joy and Auntie Steph hopes you enjoy this bedtime story!!

Thank you to my supervisor Steve for giving me the opportunity to undertake a PhD in his group and for helping me to grow in confidence in my own ability as well as fully supporting my research independence. I am so grateful for all the places I was able to visit during my PhD and the people I have met, the last four years have been wonderful.

Thank you to Muthanna and Mark at Cardiff University for allowing me to come and work with you. Those trips to Cardiff are some of my fondest memories from my PhD. Thank you as well to Rachel, Andy and Kyle in the Department of Eye and Vision Science for allowing a materials chemist to learn cell culture!

Helen, I value you so much for all the advice you have given me throughout my PhD, you've always been there for me no matter what and your friendship has been invaluable. Sean, over the last eight years you have been the greatest of friends. Thank you for every coffee break, every piece of advice you've given me and most importantly – every pro/con list. Thank you for also suggesting that I applied for this PhD. Jay, Alison and Sam – the dream team; thank you for all the laughter, cups of tea and glasses of red wine. You five have been the greatest support system I could have asked for. To all of the Rannard group past and present, it has been a real pleasure working in the group with you all!

To Emma, Dani, Cat and Jade, I'm so thankful that doing a degree in chemistry allowed me to meet you all. I couldn't ask for a better group of friends. Fay and Philly you make me laugh every day and I'll always be grateful for that! To Sue, Tony, Hannah and Eve, thank you for welcoming me into your family so openly and being so wonderful to me over the last three years.

Rogue, everything has been better since I met you. Thank you for your belief in me and constant words of encouragement. I am beyond grateful to have you by my side.

I would like to dedicate this thesis to my brother Robert, whose zest for life was infectious and who taught me that everything in life is better with a big smile, much laughter and a whole lot of good music. I will carry you in my heart always.

List of Abbreviations

μCi	Microcurie(s)
AA	Amino Acid Subunits
Amp B	Amphotericin B
ANOVA	Analysis of Variance
ATRP	Atom Transfer Radial Polymerisation
Bpy	Bipyridyl
BSA	Bovine Serum Albumin
$CDCl_3$	Deuterated Chloroform
CMC	Critical Micelle Concentration
CRP	Controlled Radical Polymerisations
CsA	Cyclosporin A
DBiB	Dodecyl α-bromoisobutyrate
DLS	Dynamic Light Scattering
DMEM	Dulbecco's Modified Eagles Medium
DMSO	Dimethyl Sulphoxide
DP_n	Degree of Polymerisation
EGDMA	Ethylene Glycol Dimethacrylate
EtOAc	Ethyl Acetate
GI	Gastrointestinal Tract
GPC	Gel Permeation Chromatography
HLB	Hydrophilic-Lipophilic Balance
$MgCl_2$	Magnesium Chloride
M_n	Number Average Molecular Weight
MPT	Multiple Particle Tracking
M_w	Weight Average Molecular Weight
MW	Molecular Weight
NaOH	Sodium Hydroxide
NMR	Nuclear Magnetic Resonance
O/W	Oil in Water
OEGMA	Oligo (Ethylene Glycol) Methyl Ether Methacrylate
PBS	Phosphate Buffered Saline
PBiB	Poly(Ethylene Glycol) α-bromoisobutyrate

PdI	Poly Dispersity Index
PEG	Polyethylene Glycol
RALS	Right Angle Light Scattering
RI	Refractive Index
STP	Serine, Threonine and Proline
THF	Tetrahydrofuran
W/O	Water in Oil

CONTENTS

CHAPTER 1

General Introduction

1.1. MUCUS AND MUCOSAL MEMBRANES

Mucus is defined as a viscoelastic, gel-like substance which lines many of the cavities within the body, including the oral, gastrointestinal, genital and ocular regions. Its main function is to act as a barrier for these surfaces, protecting the underlying cells against the external environment. Mucus is secreted by goblet cells which are found scattered within the epithelium lining of organs, for example in the gastrointestinal (GI) tract mucus is secreted along the epithelial surfaces which lines the stomach to the colon, Figure 1.1.[1] The structure of epithelia can either be a single layer of cells as in the GI tract, or the cells are stratified and are next to specialised glands, such as in the cornea; in both models the goblet cells are vital to mucus production.[2]

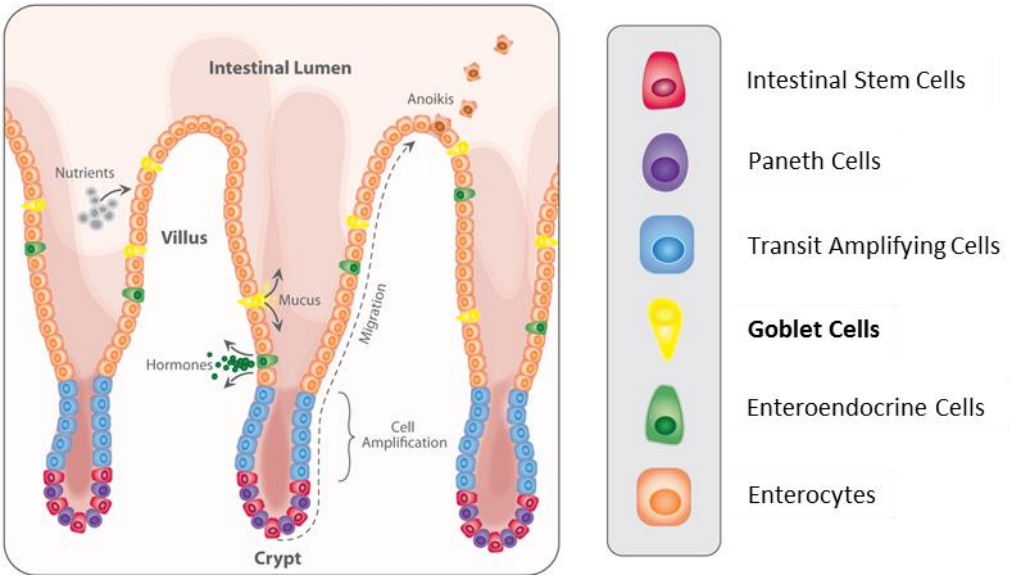

Figure 1.1 Intestinal epithelium containing a number of cells including the goblet cells which secret mucus to produce a layer of mobile and stationary mucus. Adapted from J.H Rothchild *et al.*[3]

Mucus linings are composed of a mobile layer which is removed quickly and a stationary gel–like layer,[4] which is secreted sporadically through the villi and adheres to the surface of the goblet cells,[5] Figure 1.2. The life-cycle of the stationary mucosal layer varies depending on the part of the body, but it is usually short lived as it is continuously being reformed.[6] The ocular and respiratory tract mucosal life-time is short at 5-8 and 10-20 minutes respectively, whereas the mucus in the gastrointestinal tract of a rat has a longer life-time of 4-6 hours, similar values likely to be found in humans.[7]

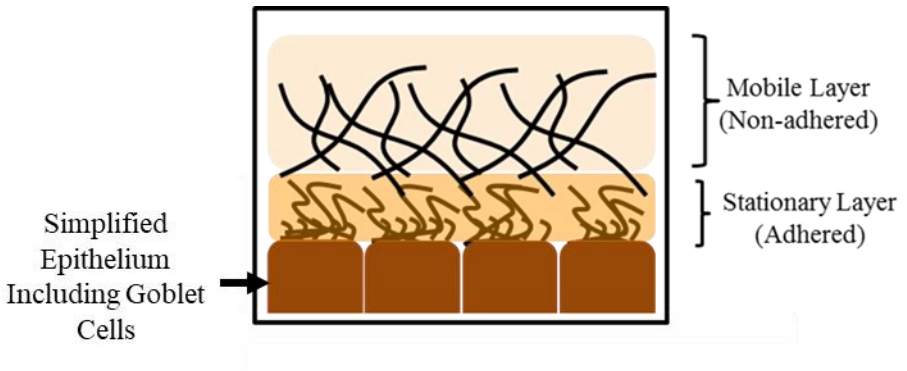

Figure 1.2 An illustration of the layers of adherent and non-adherent mucus, where rapid clearance of particles occurs in the mobile layer. Adapted from L. M. Ensign *et al.*[8,7]

The thickness of mucus layers also varies depending on the physical location within the body, for example the average thickness of the mucus layer in the eye is 0.035 μm,[9] but the mucin containing tear film has been reported to vary from 5 - 40 μm.[9-11] Reports of human mucus thickness in the GI tract are rare, however, the adherent GI mucus layer in humans has been reported to have a thickness of up to 200 μm.[7] Studies have highlighted person to person variability of the thickness of the mucus layers; a multiple patient investigation sampled the antrum mucus which is located near the bottom of the stomach, next to the pyloric sphincter and found to range between 112 – 180 μm.[12] More commonly the thickness of GI mucus has been studied in animals such as pigs, rats and rabbits and despite inter-species differences it was generally found that the thickness of the mucus lining was stomach>large intestine>small intestine.[1,7,12] The values shown in Table 1.1 detail the thickness of the mucus layer lining of the GI tract of a rat, and exhibits the increasing thickness of both the adherent and non-adherent layer of mucus from the stomach through to the colon. An alternate *in vivo* study was conducted on rat GI mucus and showed contradictory values between 30 – 60 μm, therefore, showing the inherent study-to-study variability when measuring mucus thickness.[12] The thickness of porcine antrum mucus was also studied and found to be most representative of human mucus, at 222 μm compared to 112 – 180 μm.[12]

Table 1.1 Mucus thickness of mobile and adhered layers from an *in vivo* study of rat GI mucus including the antrum (near the bottom of the stomach), duodenum (first section of the small intestine close to the stomach), jejunum (middle section of the small intestine), ileum (final section of the small intestine close to the colon) and colon (also known as the large intestine). Mucus thickness presented as mean values (μm) with ± standard error.[13]

Mean Mucus Thickness (μm)	Antrum	Duodenum	Jejunum	Ileum	Colon
Total	274±41	170±38	123±4	480±47	830±110
Adhered	154±16	16±3	15±2	29±8	116±51
Mobile	120±38	154±39	108±5	447±47	714±109

In vivo studies of the rat GI mucus gel layer have also shown that the mobile layer is loosely adhered and could be removed with gentle suction, while the stationary layer was fully adhered to the surface and could not be removed. It was observed that the loosely adhered mucus layer was continuous; however upon removal of the firmly adhered layer the contours of the villi were found. Alternatively the adhered mucus layer of the stomach and colon was continuous but had sporadic distribution in the small intestine.[13,8]

1.1.1 Mucins

Mucins are high molecular weight, heavily glycosylated proteins and are the main components of mucus. Mucins can vary considerably in length with some composed of >500 amino acid subunits (AA), whilst others are composed of thousands of repeat units, therefore can be classed as one of the largest proteins in the body.[14] There are various mucins found around the body, within the GI tract the following membrane bound mucins are expressed: MUC1, MUC3, MUC4, MUC12, MUC13, MUC16 and

MUC17,[15,16] as well as the mobile mucins: MUC2, MUC5AC, MUC5B, MUC6 and MUC7. These mobile mucins are typical gel-forming mucins which are produced by the goblet cells.[17,18] The MUC2 mucin is the main mucin secreted in the small intestine of rats,[19] mice[20] and humans[21] with the mucin monomer being formed of 5100 AA.[22,23] In comparison to another gel-forming mucin, MUC5AC which in humans has been determined to only have 8 AA in its tandem repeat unit.[24] Each mucin ranges in size from 200 kDa to 200 MDa and is formed of a linear peptide backbone, which consist of carbohydrate side chains which are O- and N-linked.[25],[19]

A common feature of mucins is that they are mainly composed of carbohydrates at approximately 80 % mass, the remainder is composed of the protein core.[26] Mucin polypeptide chains repeat serine, threonine and proline (STP) AA,[27] which form O-glycosidic linkages with oligosaccharides between hydroxyl groups of the rich AA domains. This results in a 'bottle-brush' like structure with cysteine-rich subdomains flanking the repeat units, shown in Figure 1.3.[28,29] The repeat units of mucins can vary in terms of sequence and amount of amino acids, but in all cases the high concentration of serine and threonine results in a high potential of O-glycosylation.[30] Cysteine regions flank both the amino and carboxyl terminals as cysteine knots and are dispersed through the STP repeat units.[31] The cysteine sections of the glycoproteins form disulphide bonds to form mucin oligomers from the monomers present, which give rise to the gel-like network of the mucus structure.[17] Studies show that alongside the cysteine knot that is necessary for forming dimers, the *N*-linked oligosaccharides also functions in the disulphide linkage between monomers.[32,33] These repeat sequences differ between mucins and vary in length and number.[30]

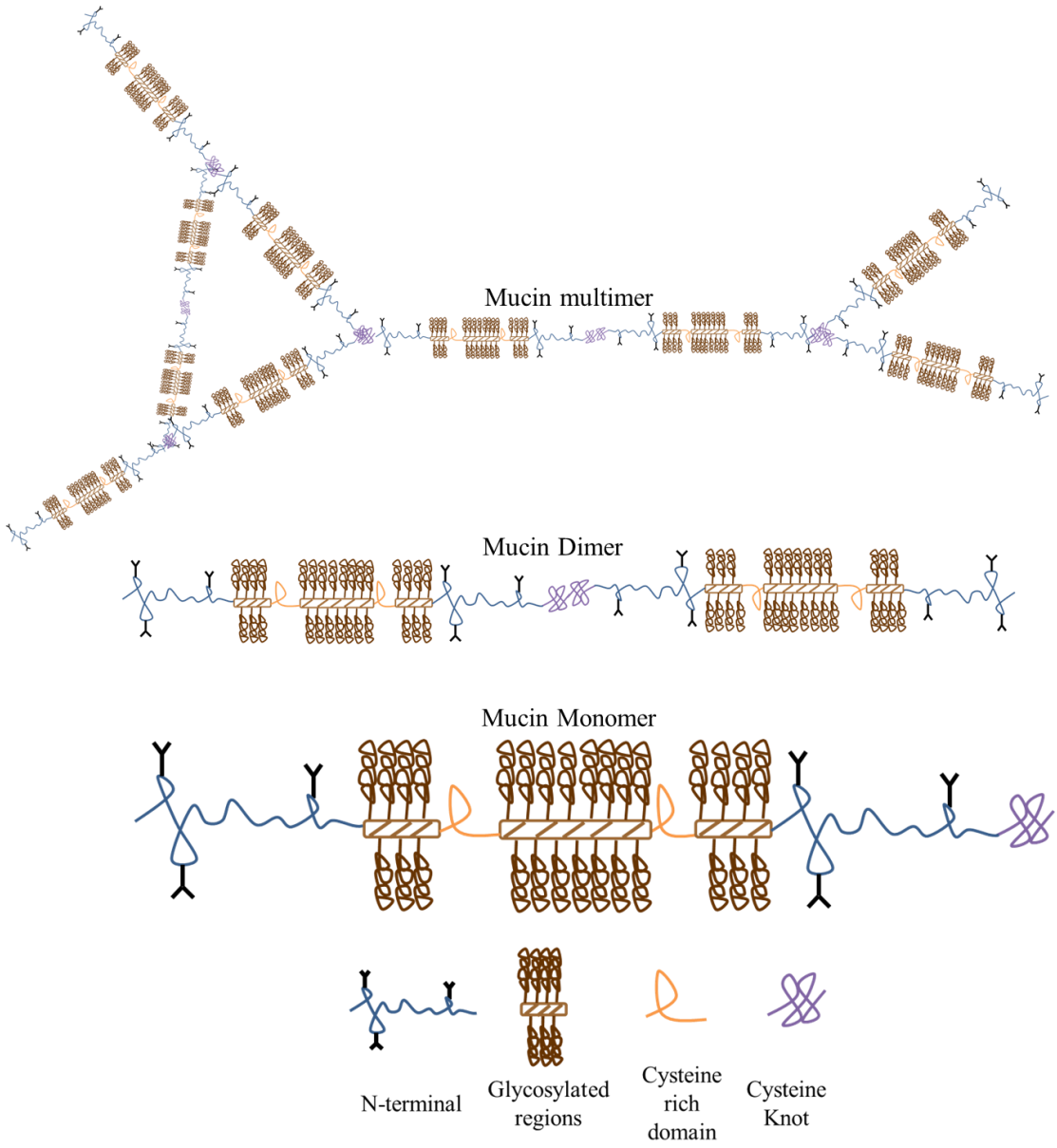

Figure 1.3 Cartoon representations of the glycosylated regions, N-terminal with N-linked oligosaccharide, cysteine rich domains present in a mucin as well as disulphide bond formation through cysteine knot leading to dimers and multimers. Adapted from R. Bansil *et al*. and M. T. Cook *et al.*[34,35]

1.1.2 Mucus Mesh Spacing

Individual mucins aggregate together to form a highly crosslinked network of mucin fibres and a dense porous structure also known as mucus mesh. The mesh pore size (10 - 200 nm)[36] between these fibres has been shown to have size filtering properties, with smaller nanoparticles being able to diffuse through and avoid steric obstruction

to reach the underlying cells, Figure 1.4.[37] Larger particles however, can become entangled in the mobile mucus layer which forms adhesive interactions *via* hydrophobic and electrostatic interactions and hydrogen bonding, these larger particles are therefore cleared more rapidly due to mucus turnover.[25,38]

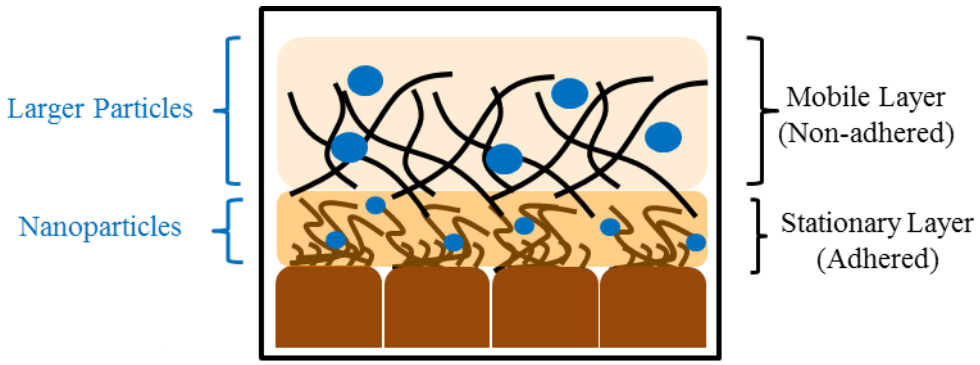

Figure 1.4 An illustration of the effect of particle size on the ability to permeate through the mobile and stationary mucosal layers. Adapted from O. Lieleg *et al.*[37]

Ex vivo studies of porcine intestinal mucus have shown that both adhered and mobile mucus layers were present and the pore sizes were determined to be heterogeneous, with a 7-fold range in pore size (60 - 400 nm). The distribution consisted of 50 % pores sizes of less than 200 nm, whilst 33 % of the population was between 300 - 400 nm.[39] Pore sizes of 211 ± 7 nm have been successfully stained from a porcine small intestine MUC2 layer, and shown a continuous layer of mucus throughout the small intestine which covered the villi.[40] Alternatively atomic force microscopy has been utilised to image porcine jejunum including trimers of MUC2 which had assembled into a mesh structure with pore sizes between 20 – 200 nm.[41] Overall the discrepancy between pore size determination from methodology used to visual the mucus structure studies has been highlighted.

1.1.3 Drug Delivery through Mucosal Membranes

Mucus acts as a barrier for the epithelial surfaces it lines and protects underlying cells against the external environment inhibiting many infectious diseases.[42] Unfortunately the mucosal membrane also hinders the permeation of drugs and delivery systems, and therefore has become a high priority for healthcare research programmes.[43, 44, 45] The rate of drug diffusion across this barrier is low and impedes drug efficacy, therefore

the development of drug delivery systems that can increase retention time at the mucosal interface and increase permeation would be beneficial.[23]

The mucus mesh network does not usually sterically hinder the permeation of drugs as they are commonly smaller than the pore size, however, interactions with drugs can occur due to the overall hydrophilicity of mucus and the negative charge of mucus glycoproteins. Studies have shown that poorly soluble drugs will interact with mucus glycoproteins.[44] Unfortunately as many drugs are poorly water soluble they are reformulated to improve dosing, however this does lead to the production of bigger particles which can be removed by the mobile phase of the mucus.

As mentioned the mesh network can form adhesive interactions with particles, therefore particle surface properties can exert a major influence on the diffusion of particles through mucus. For example, particles which exhibit strong interactions with the mucus matrix may become firmly entangled and remain in the mobile mucus layer and are rapidly cleared. Stealthy particles however, may only demonstrate weak interactions with the mucus and be able to diffuse through to the underlying cells. Multiple particle tracking (MPT) was used to probe the diffusion depth of polystyrene particles over the size range 20 - 500 nm coated simultaneously with carboxylate and polyethylene glycol (PEG) functionality.[46] It was shown that the carboxylate coated particles had increased permeation ability with decreasing particle size, and PEGylated particles led to a large increase on particle diffusion. Further studies have shown that regardless of mucus pore size, particles of 500 nm or greater can permeate through the mucin network if coated in a suitable mucus penetrating functionality.[36,47] Variation in number average molecular weight (M_n) PEG has been studied and shown that a greater M_n achieved particles which exhibited more adhesive properties than their lower M_n counterparts, i.e. entrapment of larger particles in the mobile mucus layer, Figure 1.4.[6] In an *ex vivo* study of human cervicovaginal mucus it was shown that PEG (10-40 kDa) densely grafted onto the surface of nanoparticles enhanced diffusion through the mucus. These particles have also exhibited the ability to line the colorectal mucus and vaginal epithelium *in vivo.*[48]

A balance between stealth properties of the particles and ability to adhere to the mucosal layer, factoring in molecular weight of grafted polymers, particle size and chemical interaction with the mucosal layer are all necessary for producing a mucus

penetrating system. Alternatively a system which retains drug particles at the site of action within the mucus *via* adhesion may be advantageous to drug efficacy.

Mucoadhesive systems have the potential to be used as prophylaxis treatments, where prevention is one of the most effective actions against diseases that can be spread through sexual contact. For example, microbicides have been assessed for their ability of prevention;[49] human immunodeficiency virus (HIV) could have increased prevention rates if a drug was able to be administered to the cervicovaginal mucus. The development of these microbicides can lead to better protection than current prevention strategies as they offer bidirectional protection to both partners.[50]

1.2. MUCOADHESION

1.2.1 Theory of Mucoadhesion

Adhesion is defined as the 'the sticking together of particles of different substances'[51], while the terminology referring to the biologically relevant mechanism is known as bioadhesion.[52] Mucoadhesion can be further classified when one of the two substances being referred to is a mucosal surface.

Mucoadhesion occurs through various physical and chemical mechanisms, and is dependent on the properties of the polymer or material tested. For adhesion to occur bonds must be formed: ionic, covalent, hydrogen, Van-der-Waals or hydrophobic bonds. There are six general theories of adhesion which can be adapted to investigate mucoadhesion including: wetting (the contact stage for liquid systems), adsorption, diffusion, consolidation (establishment of interactions), electronic and fracture processes.

1.2.1.1 Adhesive Theory of Liquid Systems

The wetting theory of mucoadhesion applies mainly to liquid adhesive systems and incorporates surface and interfacial energies. It suggests observed adhesive properties results from the successful flow of liquid into the cavities of the substrate with subsequent hardening,[53] Figure 1.5. The contact angle of the interaction is therefore highly important as it indicates the wettability of the surface by the contact liquid. The contact angle between the liquid system and mucosal surface must be near zero to

form a site in which systems can adhere.[54] The surface tension subsequently restricts the movement of the substance along the substrate site, and can therefore be used to predict the spreading.

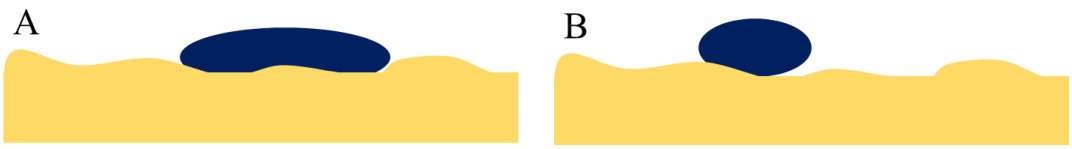

Figure 1.5 Wetting theory of mucoadhesion mechanism in a liquid system; A) Successful wetting of a mucosal surface, with spreading into surface irregularities and contact angle near zero. B) Poor wetting of a mucosal surface, low affinity of the liquid to the surface and large contact angle. Adapted from J.D. Smart *et al.*[55]

1.2.1.2 Adhesive Theories of Polymers and Solid Dosing Systems

The electronic theory of mucoadhesion is based on the occurrence of electron transfer upon contact of adhering surfaces with differing electronic structure, for example between mucoadhesive polymer and mucous glycoproteins. Adhesion is then caused through the formation of an electronic double layer.[56]

An alternative theory is the diffusion theory which states that the interdiffusion and entanglement of both the polymer and mucins chains are required for adhesion, where the more structurally similar the mucoadhesive is to the mucosa the greater the extent of mucoadhesion, Figure 1.6. This process is driven by a concentration gradient, the chain length and the flexibility of the polymer chain.[57]

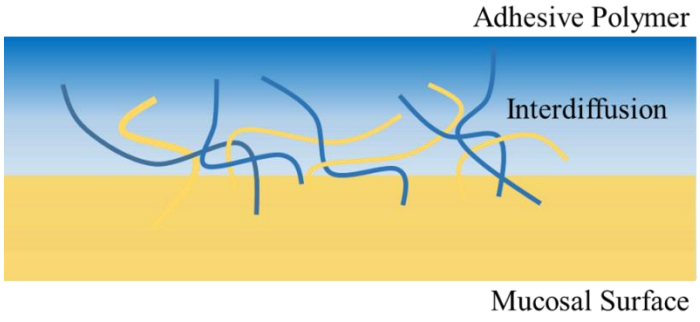

Figure 1.6 Diffusion theory of adhesive polymer and mucus; interdiffusion and entanglement between polymer and mucin chains across an adhesive interface.

The basis for adsorption theory in mucoadhesion is centred on chemical interactions and bonding; the adhesion between the substrate and the adhesive is due to primary

and secondary bonding. The primary bonding results from permanent bonding (ionic or covalent bonding), whereas the secondary bonding is due to weaker interactions such as Van-der-Waals forces, hydrophobic interactions or hydrogen bonding.[58]

Fracture theory differs from the previous theories as it is based on the force required for the detachment of the two substrates after adhesion. This theory is typically used to determine mucoadhesion of solid substrates, usually polymers, gels or tablets. The maximum tensile strength produced during detachment can be determined, i.e. the force required to separate two surfaces after adhesion which assumes failure of the adhesive bond occurs at interface. The fracture however normally occurs at the weakest component, where cohesive failure can cause a break in adhesive substrate or in the mucosal surface.

1.2.2 Mucoadhesive Polymers

Mucoadhesive polymers can be categorised as either water-soluble or water-insoluble polymers which are usually as a swellable network formed by covalent or ionic bonds *via* a cross-linking agent. These are separated by the water-soluble polymers' retention on the surface of the mucosal tissue controlled by the dissolution of the polymer, where it is removed from the surface as it dissolves. Whereas the water insoluble polymer has a surface retention time based on the mucosal life cycle.[59] Common factors controlling mucoadhesion have become apparent across the various materials; the bioadhesive must be able to spread across the substrate, be able to interdiffuse into the mucus to give a greater contact area and exhibit dominant attractive forces such as Van der Waals or hydrogen bonding.[59]

The 'first-generation' mucoadhesive polymers were hydrophilic macromolecules which contained hydroxyl and amine groups capable of forming hydrogen bonds with the mucosal membrane,[60,61] Figure 1.7. These mucoadhesives are termed 'wet' adhesives as they are activated upon moistening when in contact with the mucosal surface.[62] These hydrated adhesives however, were shown to have stronger interactions with dry surfaces over mucosal ones, where if they are left to dry, strong adhesive bonds are formed.[60]

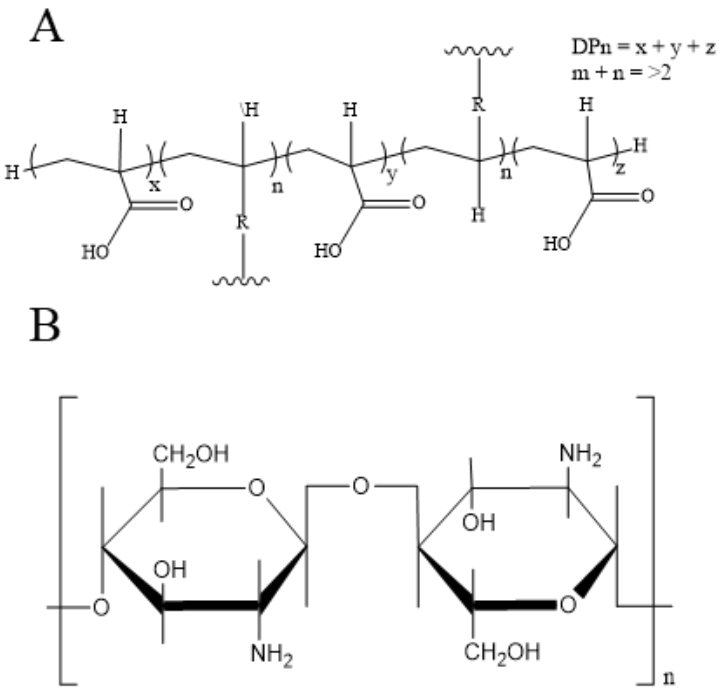

Figure 1.7 Structure of the common 'first-generation' mucoadhesive polymers; A) Poly(acrylic acid) R= allyl sucrose or allyl pentaerythritol (carbopols) or divinyl glycol (polycarbophil), B) Chitosan. Adapted from J.D Smart *et al.*[55]

1.2.3 Thiolated Polymers

A recent advancement in mucoadhesive polymers by Bernkop-Schnürch *et al.* produced novel thiolated polymers deemed 'thiomers',[63] which contain multiple thiol groups to form strong covalent disulphide bonds to the mucus glycoproteins. Examples of thiomers include hydrophilic polymers with side chains containing thiol groups,[64] such as poly(acrylates)[65] and chitosans.[66] Thiomer structures can include cationic and anionic polymers for mucoadhesion. Cationic thiomers are typically based on chitosans, where the primary amino group can covalently attach to sulfhydryl groups.[67] One example, is a cysteine modified chitosan polymer as shown in Figure 1.8, where the carboxyl acid group has reacted with a number of primary amine groups pendant to the main carbohydrate chain to generate amine and thiol functionality.[68] To avoid oxidation of the thiol groups during synthesis, the reaction was performed under inert conditions as well as keeping the reaction conditions at a pH <5 to reduce the presence of reactive thiolate-anions.[67] Anionic thiomers have also been synthesised,

where the sulfhydryl can be attached to the polymer by formation of amide bonds mediated by carbodiimides.[69]

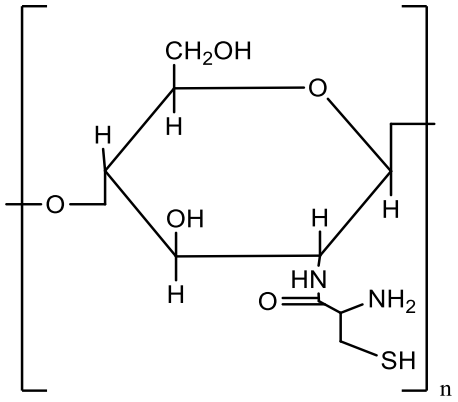

Figure 1.8 Thiolated polymer structure; Chitosan-Cysteine. Adapted from A. Bernkop-Schnürk *et al.*[67]

Mucoadhesive thiomers improve the retention time of polymers at their intended therapeutic sites due to the formation of intrachain and interchain disulphide bonds, this provides adhesion through covalent bonding as shown in Figure 1.9.[64]

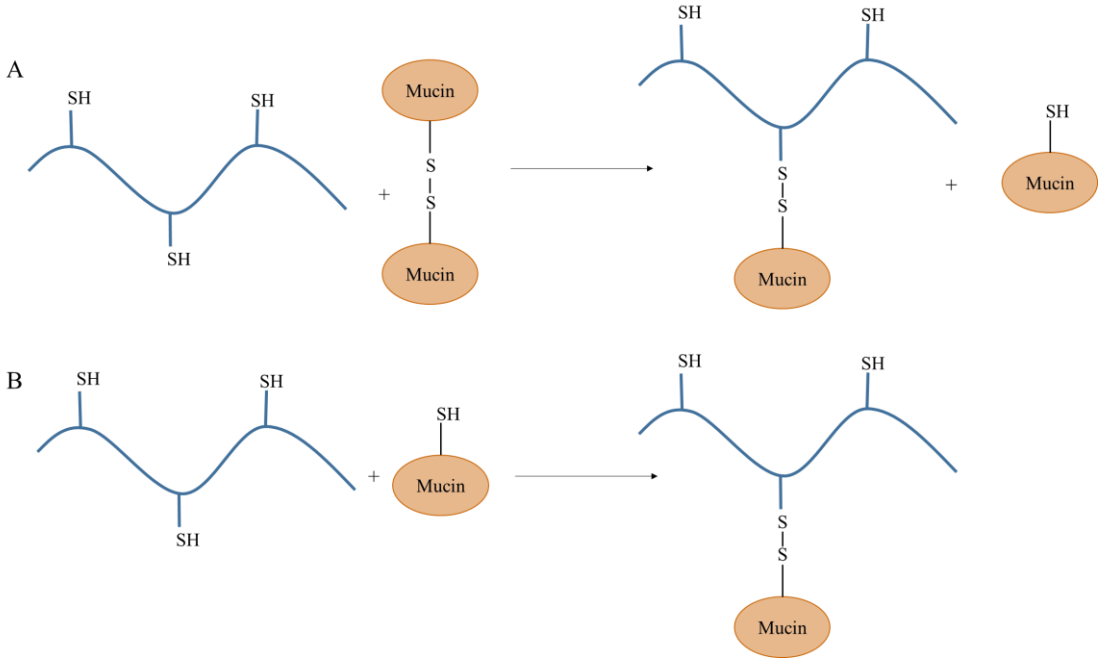

Figure 1.9 Covalent bond formation between thiolated polymers and sulphide linked mucin glycoproteins *via*; A) Thiol/disulphide exchange reaction and B) Oxidation of the free thiol group. Adapted from V. M. Leitner *et al.*[64]

One proposed mechanism for the interaction of thiol groups with mucus is based on disulphide exchange reactions,[70] cleavage of the intramolecular disulphide bridges in

the mucus causes a breakdown of the mucus. The other is an oxidation reaction between the reactive thiol groups on the mucoadhesive polymer and the cysteine rich subdomains of the mucin monomer.[28] Thiomers are also thought to improve mucoadhesion by in situ cross-linking *via* the free thiol chain ends during the interpenetration of the polymer chains into the mucus, therefore anchoring the polymer into the mucosal layer, Figure 1.10.

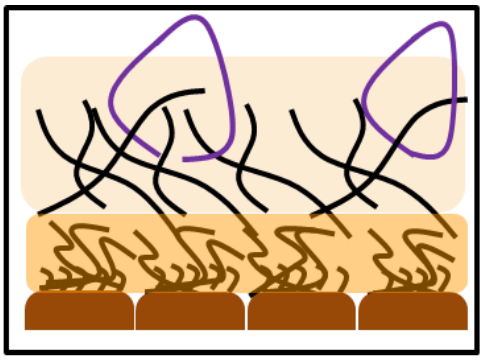

Figure 1.10 Representation of the interpenetration of polymer chain (purple) into the mucus layers, with in situ cross-linking of free thiol chain ends. Adapted from A. Bernkop-Schnürk *et al.* and J. O. Morales *et al.*[67,71]

1.3. EMULSIONS

An emulsion is comprised of two immiscible phases;[72] one phase is dispersed within the other and typically stabilised by a surface active agent, commonly known as a surfactant. Emulsions are typically described as either oil-in-water (o/w) or water-in-oil (w/o), which defines the dispersed and continuous phases within each example. Figure 1.11 shows the formation of an o/w emulsion.

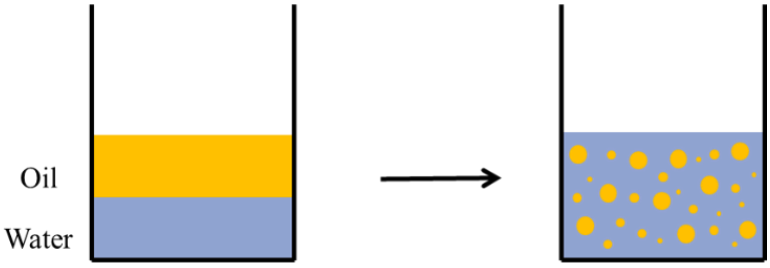

Figure 1.11 Schematic representation of the dispersion of oil (yellow) in water (blue) to form an oil-in-water emulsion.

Emulsions typically have a cloudy white appearance due to the scattering of light through the dispersed phase, and can be subdivided into macroemulsions, miniemulsions, microemulsions and nanoemulsions, due to the droplet sizes. The IUPAC definition of the subclasses of emulsions state that macroemulsions have diameters ranging from 1 to 100 μm, while miniemulsions have diameters from 50 nm to 1 μm and microemulsions have diameters varying between 1 to 100 nm but mainly in the 10 to 50 nm range.[73] Nano- and microemulsions have a translucent appearance as droplets are less than 100 nm, which is less than the range of the wavelengths of visible light (400 – 700 nm).[74] Macroemulsions have droplets with larger diameters, therefore have an opaque appearance as they readily interact with visible light.[75]

Whereas there is currently no IUPAC definition for nanoemulsions, the two terms miniemulsion and nanoemulsions are used interchangeably. Microemulsions and nanoemulsions can be separated by their thermodynamic stabilities; nanoemulsions are thermodynamically unstable while microemulsions are thermodynamically stable. Microemulsions have a lower free energy state (ΔG) than the separated phases but nanoemulsions have a higher free energy state.[76] This is because as the droplet radius is decreased below 1000 nm, there is an increase in free energy once droplet size decreases to a minimum. However, the free energy increases again when droplet surface is further reduced. Nanoemulsions can be preferable due to their much lower surfactant content (3-10 wt %) compared to microemulsions (20 wt%).[77] Typically nanoemulsion is the preferred terminology over microemulsions as it leads to less confusion as droplet diameters are quoted on the nanoscale.[78]

1.3.1 Emulsion Instability

Emulsions can be formed spontaneously if immiscible liquids are in non-equilibrium and the different chemical potential between phases triggers emulsification.[79,80] More commonly however the formation of an emulsion is a non-spontaneous process with the need for a sufficient amount of energy to be put into the system for the dispersion of one phase into the other. This is thermodynamically unfavourable, with the two phases constantly trying to reduce their interfacial free energy by forming two separate layers.

The free energy change associated with the formation of dispersed droplets can be modelled by the Gibbs surface free energy term (ΔG_I) and the entropy of configuration

(ΔS_{config}). At constant temperature (T) and pressure, Equation 1.1 is equal to Equation 1.2, where there is a change in surface area (ΔA) and interfacial tension (γ).

$$\Delta G_{formation} = \Delta G_I - T\Delta S_{config} \qquad (1.1)$$

$$\Delta G_I = \gamma \Delta A \qquad (1.2)$$

Equation 1.3 is taken from the second law of thermodynamics, where $\gamma\Delta A >> -T\Delta S$, meaning that as ΔG is positive, emulsion formation is nonspontaneous and thermodynamically unstable without the presence of a surfactant.[81]

$$\Delta G_{formation} = \gamma \Delta A - T\Delta S_{config} \qquad (1.3)$$

The Laplace pressure is the difference in pressure between the inside and outside of a droplet, where the pressure difference is caused by the interfacial tension (γ).

The Young-Laplace Equation (Equation 1.4), gives the ratio of the difference between the pressure inside (P_{in}) and outside (P_{out}) of the droplet, where the internal pressure is inversely proportional to the droplet radius (r). This is a driving force for emulsion instability which leads to an increase in droplet size.

$$P_{in} = P_{out} + 2\gamma/r \qquad (1.4)$$

If a high amount of energy is inputted into the system a deforming force occurs which breaks the droplets into smaller ones if the Laplace pressure is overcome.[82]

As the two phases of an emulsion drive to separate to their lowest energy state, there are various ways in which the emulsion can return to a two layer state. As shown in Figure 1.12, an emulsion can become unstable *via* the phenomena of creaming, sedimentation, flocculation and coalescence.

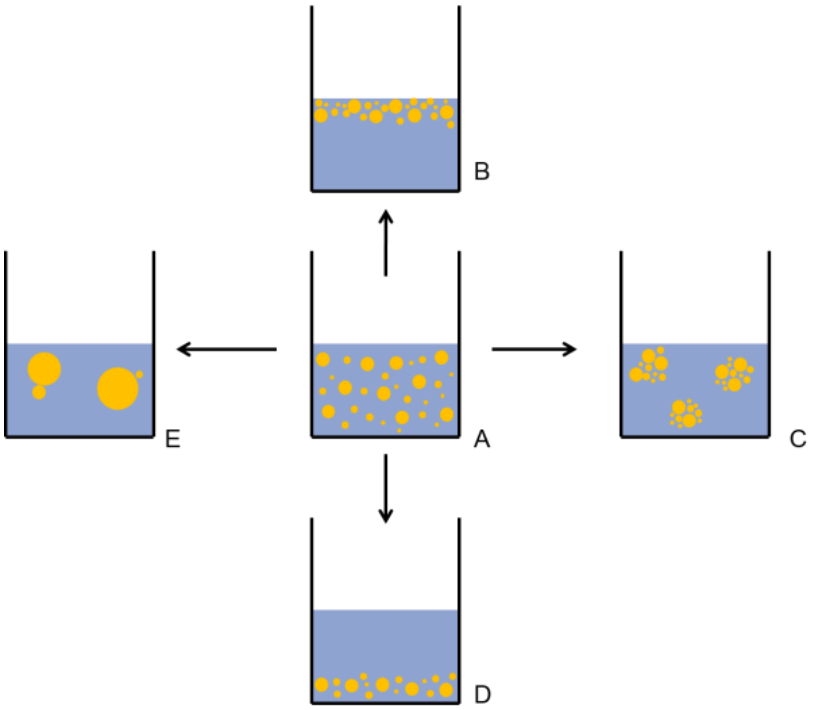

Figure 1.12 A schematic representation of the various breakdown mechanisms of an oil-in-water emulsion; A) Stable oil-in-water emulsion, B) Creaming, C) Flocculation, D) Sedimentation, E) Coalescence.[83]

Creaming occurs as the dispersed phase droplets rise to the surface of the emulsion due to their lower density in comparison to the continuous phase.[84] Creaming leads to an increased likelihood of droplet collision and coalescence and therefore the formation of larger droplets. Flocculation occurs when the droplets join together to form 'bunch-like' aggregates[85] and sediment as the droplets sink to the bottom of the sample due to the density difference. Coalescence is the most common form of instability and occurs *via* the merging of two or more individual droplets to form a larger, single droplet.[86] Coalesence occurs when droplets collide and the attractive forces between the droplets is greater than repulsive forces, leading to rupture of the stabilising film. This leads to the total energy of the emulsion favourably decreasing as the size of the dispersed phase increases and overall interfacial area decreases.[87] Ostwald ripening occurs due to the increased pressure inside smaller droplets, to relieve this pressure the droplets dissolve through the continuous phase until they can collide.[88,89]

1.4 SURFACTANTS

Surfactants or emulsifiers can be classified as: polymeric, anionic, cationic, zwitterionic and are typically amphiphilic molecules.[90] Surfactants act at the interface, lowering interfacial tension between the two phases and allowing for successful dispersion.[91] Surfactants form a thin layer over the dispersed droplets causing other droplets to repel by steric or electrostatic repulsion and decrease coalescence. They can also work by increasing the viscosity of the continuous phase which maintains the droplet suspension.[92] Figure 1.13 shows the variety in surfactant structure that can be used to stabilise emulsions, including; Pickering emulsifiers, linear block copolymers, complex polymeric surfactants, polymeric nanoparticles, small molecule surfactants and branched polymeric surfactants.

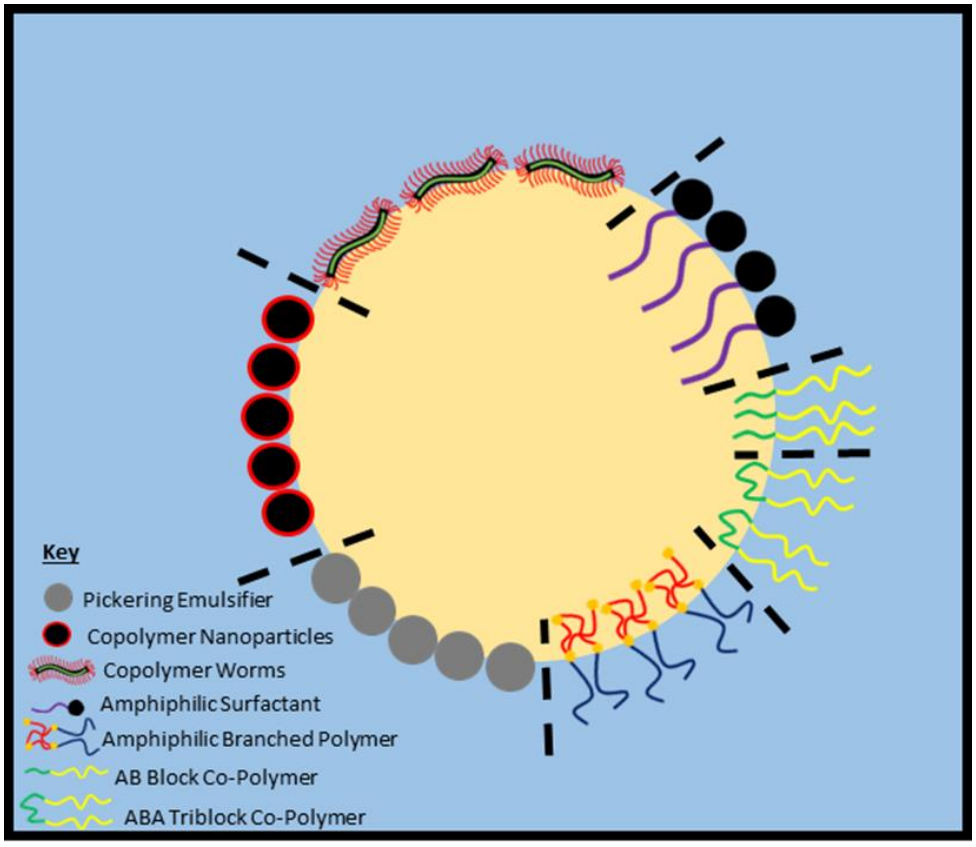

Figure 1.13 Oil-in-water emulsion droplet stabilised by various surfactants: Pickering emulsifiers, linear block copolymers, complex polymeric surfactants, polymeric nanoparticles, small molecule surfactants and branched polymeric surfactants.[93–95]

1.4.1 Hydrophilic-Lipophilic Balance

The HLB is used to describe the ratio between hydrophobic and lipophilic components of a surfactant. It was first described by Griffin in 1949 to detail non-ionic surfactants as shown in Equation 1.5, where the molecular weight of the hydrophilic portion, M_h, is analysed as a percentage of the molecular weight of the entire molecule, M.[96] This gives the HLB result on an arbitrary scale of 0 - 20, where a result of 0 corresponds to a completely hydrophobic surfactant, while the other end of the scale 20, results in a completely hydrophilic surfactant. Therefore if an o/w emulsion is targeted then a surfactant or surfactant blend should be chosen with a high HLB value and conversely a w/o emulsion would require a value low on the scale, <10 for greater emulsification. Griffin discovered that when two non-ionic surfactants, one hydrophilic and the other lipophilic were mixed together in varying ratios, the blend efficiency for a particular surfactant went through a maximum. This corresponded to same weight percent of hydrophilic surfactant in the mixture, where the HLB value is a function of the molecular weight of the hydrophilic portion in relation to the whole molecule. Griffin's method, is shown in Equation 1.5, for HLB value of a non-ionic surfactant. Mh = molecular weight of hydrophilic of the surfactant, M = molecular weight of whole surfactant.

$$HLB = \frac{1}{5} * \left(\frac{Mh}{M} * 100\right) \qquad (1.5)$$

1.4.2 Small Molecule Surfactants

Small molecule surfactants incorporate amphiphilic characteristics, typically as a hydrophobic tail group and a hydrophilic head group, which lowers the interfacial tensions between the two phases.[97] These surfactants can be classified as either non-ionic, ionic (anionic or cationic) or zwitterionic. One of the most commonly used commercially available ionic surfactants is sodium dodecyl sulphate, shown in Figure 1.14, frequently used in detergents, and composed of a hydrophobic alkyl chain and an ionic hydrophilic head group.

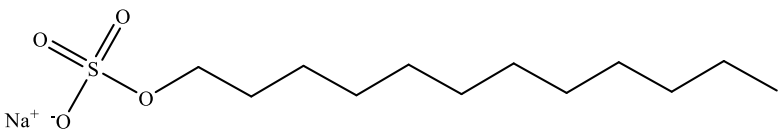

Figure 1.14 Structure of sodium dodecyl sulphate.

1.4.3 Linear Polymeric Surfactants

Linear polymers with amphiphilic character have also been shown to successfully stabilise emulsions. These polymers have clear defined hydrophobic and hydrophilic sections, shown in Figure 1.15. An advantage of these block copolymers is that there is a variety of monomers that can be used to design a purpose fit surfactant. However, the majority of linear polymers studied have been limited to poly(ethylene oxide) as the hydrophilic block and poly(propylene oxide) as the hydrophobic block.[98]

Figure 1.15 Schematic representations of linear polymeric surfactants with hydrophilic (yellow) and hydrophobic (green) regions; A) AB copolymer and B) ABA block copolymer.

1.4.4 Pickering Emulsifiers

Pickering emulsions[99] are stabilised by solid particles instead of surfactants, with one common stabiliser being silica.[100] They act to reduce the interfacial tension by accumulating at the oil/water interface, Figure 1.16. An advantage of using a Pickering emulsifier is that they are highly resistant to coalescence, with the particles absorbing at the oil/water interface creating a steric barrier between neighbouring droplets. The most widely accepted theory for this behaviour is that the particles are able to irreversibly absorb at the interface which leads to a more efficient stabilising effect compare to typical surfactants.[101]

Figure 1.16 Schematic representation of Pickering emulsion stabilised by solid particles (grey).

For a solid particle to stabilise an emulsion it has to be partially wetted by each of the liquid phases. The wettability of Pickering emulsifiers is determined by their contact

angle (as measured through the water phase); if the contact angle is < 90 ^{o} particles are termed hydrophilic and are oil-in-water stabilisers, while a contact angle of > 90 ^{o} particles are more hydrophobic and act as water-in-oil stabilisers.[102] In a study by Binks and Lumsdon it was determined that the contact angle had to be near 90 ^{o} to be an efficient Pickering emulsifier,[103] otherwise the particles tended to remain dispersed in either the water or oil phase if the contact angle is too high or too low.

1.4.5 Complex Polymeric Surfactants

Due to their relatively simple structure, block copolymers are usually studied as surfactants, but the use of more complex polymer structures can vary the interaction at the oil/water interface over a linear copolymer. Diblock copolymers have been shown to form polymeric nanoparticles which absorb onto the interface in a similar manner as Pickering emulsifiers, leading to semi-stable emulsions, Figure 1.17 A.[93] These diblock copolymers were composed of hydrophilic poly(glycerol monomethacrylate) (PGMA) and hydrophobic poly(2,2,2-trifluoroethyl methacrylate) (PTFEMA) and nanoparticles produced by polymerisation-induced self-assembly (PISA). The block copolymer nanoparticles (7 % w/w) were able to stabilise *n*-dodecane based macroemulsions (22 – 46 μm) by mechanical homogenisation, with further processing using a high pressure microfluidiser to refine the coarse macroemulsion reducing droplet size to sub 200 nm. Similarly, ABC triblocks of PGMA, poly(2-hydroxypropyl methacrylate) (PHPMA)-poly(benzyl methacrylate) (PB_zMA) synthesised *via* PISA, formed worms, Figure 1.17 B.[94] These again were used to form dodecane based macroemulsions, however using only low-shear homogenisation (hand shaking), which produced macroemulsions (1 % w/w surfactant concentration) with droplet diameters of 115 μm.

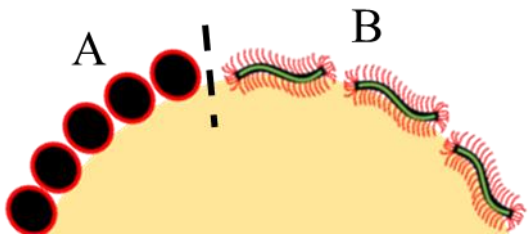

Figure 1.17 Schematic representation of A) diblock copolymer nanoparticles of PGMA (red), PTFEMA (black) and B) ABC triblock worms of PGMA (red), PHPMA (black) and PB_zMA (green) as oil-in-water emulsion stabilisers.

Recently amphiphilic brush copolymers have been utilised as w/o emulsion stabilisers, which were described as a fusion of diblock copolymers. The polymer was composed of hydrophilic poly(ethylene oxide) (PEO) and hydrophobic poly(n-butyl acrylate) (PBA) side chains, allowing for arrangement at the oil/water interface due to their difference in solubility. It was shown that having a higher number of PEO side chains improved emulsification due to increased affinity for the aqueous phase, and was able to stabilise the emulsion at low surfactant content, 0.005 wt %.[104]

1.4.6 Branched Polymeric Surfactants

Branched polymeric surfactants have been shown to be more successful as stabilising groups over linear equivalents due to the increased steric bulk offered. Due to the branched architecture, polymers have multiple linear primary chains joined together, which under specific polymerisation conditions can lead to multiple anchoring points being available for interaction with the emulsion droplet. The interaction between branched polymers at the oil/water interface will be unfavourable due to the thicker polymer 'film' leading to repulsive interactions. Branched polymers also allow for functionality to be incorporated into their architecture due to variation of the monomer, chain end, or divinyl component leading to responsive emulsions. This has allowed for formulation of emulsions which can be effected be stimuli responsive.[95]

Weaver *et al.*, synthesised branched copolymers using poly(ethylene glycol) methacrylate (PEGMA) with a pH responsive 2-(dimethylamino) ethyl methacrylate (DEA) component, with ethylene glycol dimethacrylate (EGDMA) used as the branching unit. The polymer chain end composition was varied between hydrophobic 1-dodecanethiol (DDT), non-ionic hydrophilic 1-thioglycerol (TG) and ionic hydrophilic mercaptopronanoic acid (MPA). In a previous study, nanoparticles composed of branched copolymers of PEGMA with DEA blocks were fully protonated in aqueous media at pH 2, with a subsequent increase to pH 10 leading to DEA becoming fully deprotonated, creating compact amphiphilic nanoparticles with diameters of 24 nm.[105] The branched analogues of these copolymers were used to stabilise *n*-dodecane macroemulsions at pH 10 at a polymeric surfactant concentration of 0.05 w/v %. The rate of demulsification was studied over a 12 hour period after the addition of acid; it was shown polymers containing hydrophobic chain ends were not subject to any demulsification, whereas polymers with TG and MPA chain ends were

subject to 30 and 50 % demulsification. It was suggested that the high emulsion droplet stability was due to branched copolymer surfactant stabilising the emulsion by the multiple hydrophobic chain ends anchoring into the oil droplet surface.[106] To further probe these properties the branching unit was changed for hydrophilic poly(ethylene glycol)dimethacrylate (PEGDMA). Unsurprisingly, the branched copolymers containing hydrophilic chain ends were subject to complete demulsification after 12 hours, while the branched copolymer with a hydrophobic chain end remained stable. This further confirmed the importance of hydrophobic chain ends in the branched polymer architecture for emulsion stability.

Most recently oligo ethylene glycol(methyl ether) methacrylate (OEGMA) was polymerised with a hydrophobic initiating group, dodecyl α-bromoisobutyrate bromide (DBiB) with divinyl monomer ethylene glycol dimethacrylate (EGDMA) to produce a highly branched, high molecular weight amphiphilic polymer, with a targeted degree of polymerisation (DP_n) of 90. This branched copolymeric surfactant was shown to stabilise a castor oil o/w nanoemulsion with droplet diameters of less than 250 nm, at a concentration of 5 wt % (with respect to the aqueous phase).[107] These nanoemulsions were also highly stable against dilution, with a 4096-fold dilution in distilled water achievable without any loss in droplet stability. These nanoemulsions also had neutral charge as expected for a highly branched OEGMA containing polymer.

1.5 RESEARCH HYPOTHESIS

As mentioned a branched homopolymer of hydrophilic OEGMA has been synthesised using DBiB, a hydrophobic ATRP initiator, to achieve a polymeric structure with amphiphilic characteristics.[107] The resultant amphiphilic branched polymer structure had the ability to stabilise an o/w emulsion while remaining water soluble. This investigation confirmed that solitary OEGMA was required to give the polymer the hydrophilicity required to produce a successful polymeric surfactant. A question arises whether all of the chain ends are required to be hydrophobic to successfully stabilise nanoemulsions; it is hypothesised that some of the hydrophobic chain ends can be removed whilst still maintaining their stabilising properties. Utilising a co-initiation technique shown previously in literature with dendritic initiators,[108,109] mixed chain

end functionality could be incorporated and a range of polymers with varying chain end composition could be synthesised, see Figure 1.18.

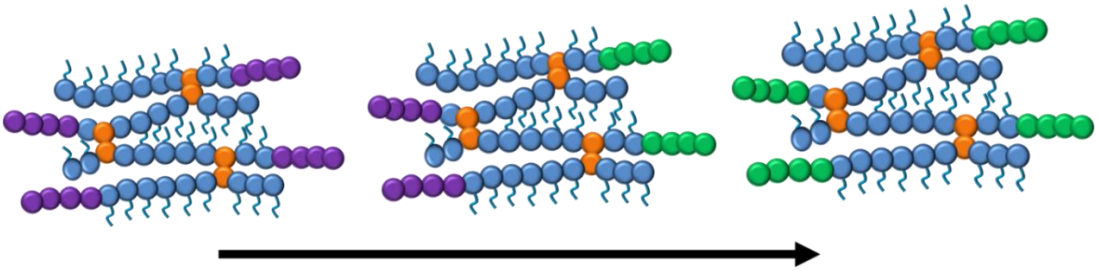

Figure 1.18 Reduction of hydrophobic chain ends following manipulation of starting materials for polymer synthesis using the co-initiation technique.

The surfactant properties of the linear and branched homopolymers will be assessed by their ability to produce stable emulsions. The reduction of hydrophobic chain ends of the branched polymers will be investigated to determine if the oil/water interface can be successfully stabilised in comparison to a more classic branched polymeric surfactant, as shown in Figure 1.19.

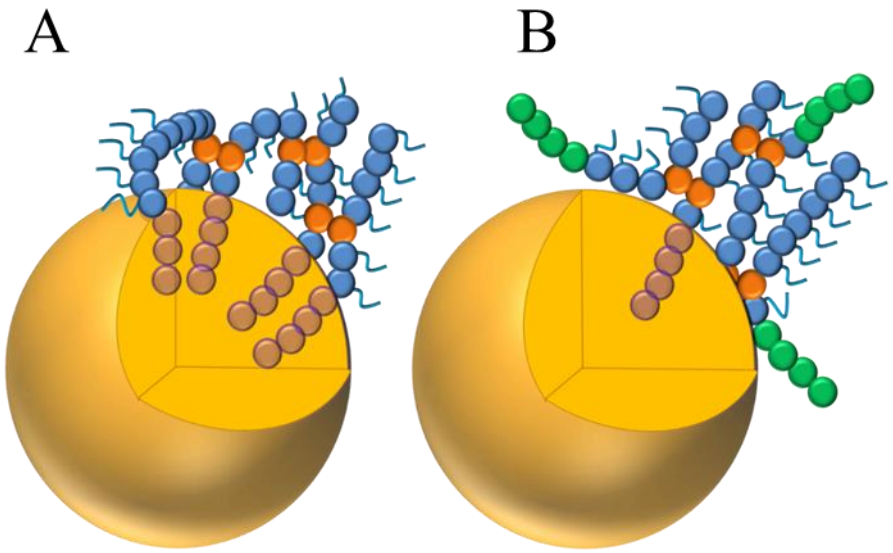

Figure 1.19 Arrangement of branched polymeric surfactants at the interface of the oil droplets with differing chain end functionality; A) All hydrophobic chain ends and B) Inclusion of both hydrophobic and hydrophilic chain ends.

Synthetic aims include co-initiation of OEGMA *via* ATRP inclusive of both a hydrophilic PEG initiator and a long alkyl chain hydrophobic initiator of varying

molar ratios. If polymerisations and subsequent emulsifications are successful, the hydrophilic chain ends will be substituted for functional groups where o/w macroemulsions and nanoemulsions are consistent with emulsions previously reported. This would allow for introduction of thiol groups into the polymeric architecture *via* the discussed co-initiation strategy, creating a new thiomer based surfactant and functional emulsion. Through the incorporation of thiol groups there is potential for the emulsions to have mucoadhesive properties.

1.6 RESEARCH AIMS

This project will begin by investigating the role of hydrophobic chain ends in stabilising o/w macroemulsions and nanoemulsions, with systematic removal of hydrophobic stabilising groups. Firstly initiators will be synthesised to incorporate the functionality required and ATRP conducted to produce branched polymers, see Figure 1.20. Co-initiation of ATRP allows the ratio of hydrophobic to hydrophilic chain ends can be systematically varied by altering the molar ratios of each initiator.

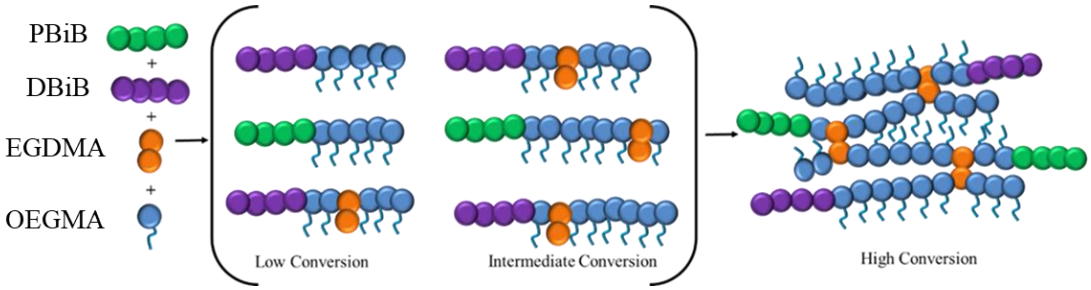

Figure 1.20 Co-initiation of an ATRP reaction using hydrophilic (green) and hydrophobic (purple) initiator molecules to synthesise an amphiphilic branched polymeric surfactant of OEGMA (blue) with EGDMA (orange), with mixed chain end functionality.

If the removal of some of the hydrophobic chain ends is successful, the stability of emulsions will be studied to determine the minima of hydrophobic chain ends required without sacrificing emulsion stability. A proof-of-concept PEG based, hydrophilic initiator will initially be used, followed by replacement with a functional thiol based initiator group. Thiol functionality will allow potential mucoadhesive character to be incorporated into the polymers and therefore emulsions. Mucoadhesive emulsions could be tailored by varying the ratio of functional initiator to hydrophobic initiator group in the same way as for the hydrophilic initiator molecule. Therefore, it is

anticipated that functional mucoadhesive particles could be formulated to exhibit greater adhesive effect with increased thiol content, as well as greater mucus penetrating character when the amount of thiol groups are vastly reduced. If material characterisation and functionalisation is successful, biological evaluation of these materials will be undertaken, including *in vitro, ex vivo* and *in vivo* testing.

CHAPTER 2

Amphiphilic Branched Copolymers and Linear Homopolymers for use as Surfactants

2.1 INTRODUCTION

The aim of this investigation was to synthesise a polymeric surfactant *via* atom-transfer radical polymerisation (ATRP) for use in an oil-in-water (o/w) emulsion.[110] A surfactant is used to lower the surface tension between two liquids; in o/w emulsions this is the interface between the small volume of oil and the continuous phase of water. Therefore the polymer synthesised to be used as a surfactant must be amphiphilic i.e. have both hydrophilic and hydrophobic components to be able to stabilise the interface. For an o/w emulsion the surfactant must have a large portion of hydrophilic properties and in comparison a small amount of hydrophobic. ATRP allows functionality/hydrophilicity/hydrophobicity to be incorporated into polymeric structures at various points by integration of different components: initiator (chain end), monomer (chain) and branching unit, see Figure 2.1. In this study a novel branched polymeric surfactant was synthesised which exhibited amphiphilic properties; a hydrophobic initiator group and a hydrophilic monomer was used.

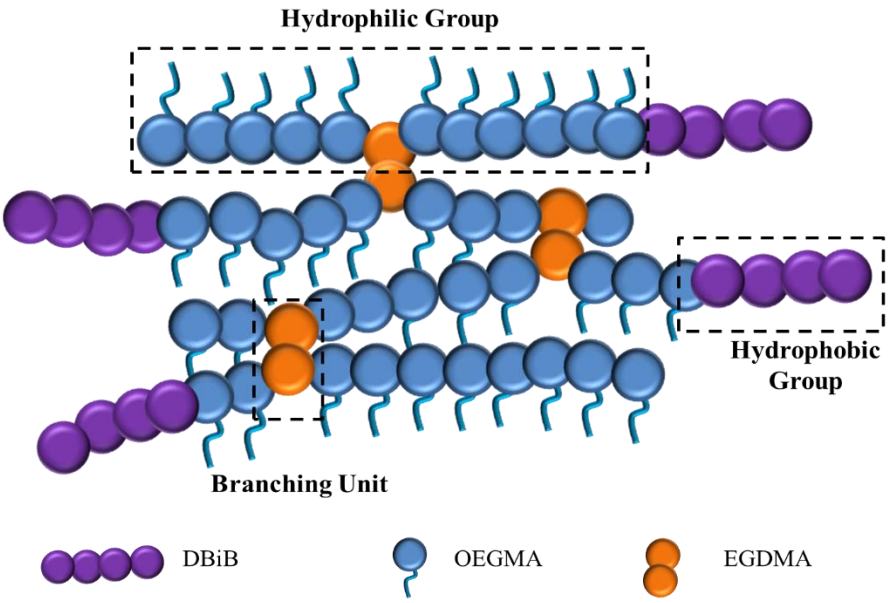

Figure 2.1 Representation of an amphiphilic branched copolymer with hydrophobic chain end (purple), hydrophilic polymer monomer, oligo (ethylene glycol) methacrylate (OEGMA) (blue) and branching unit, ethylene glycol dimethacrylate (EGDMA) (orange).

By incorporating a hydrophobic initiator, and a hydrophilic monomer each growing polymer chain had amphiphilic characteristics. Through the addition of a divinyl monomer, the polymeric surfactant is given a novel branched structure, with a high molecular weight. This branching element allows for multiple amphiphilic polymer chains to be joined together, giving the surfactant multiple anchoring points *via* the hydrophobic initiator groups into the oil droplets. It is hypothesised that the novel branched architecture does not require a co-surfactant to stabilise o/w emulsions, which can be typical for successful emulsion generation, due to the high molecular weight polymers and multiple anchoring points being able to cover to the droplet surface.

2.1.1 Synthesis of Branched Copolymers by ATRP

ATRP is a controlled radical polymerisation (CRP), where the atom transfer stage is key for the controlled nature of the polymerisation. It is a controlled polymerisation due to a low concentration of active species which guarantees the rate of polymerisation being maintained, this is done by establishing equilibrium with the dormant state. In ATRP the active species ($R^{\cdot}$) is generated by a reversible redox reaction which is catalysed by a transition metal complex (Mt^n-Y/Ligand).[110] The transition metal complex undergoes a one electron oxidation process by abstraction of a halogen atom from the dormant species (R-X). One successful route to controlled ATRP polymers and copolymers is the use of the catalytic system: copper (Cu(I)Br, Cu(I)Cl)) and bypyridyl (bpy) which complexes together. An initiator which is usually an alkyl halide (R-X)[111] is used, but the synthesis of these can be designed for inclusion of specific functionality into the polymer. The reversible redox reaction occurs with an activation rate constant (K_{act}) and a deactivation constant of (K_{deact}) with the general mechanism for ATRP shown in Scheme 2.1.

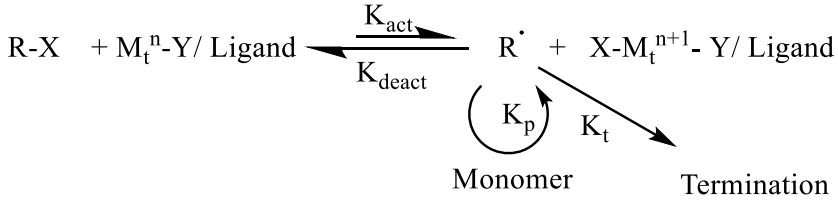

Scheme 2.1 General ATRP mechanism where an alkyl halide (R-X) is under equilibrium with the active species ($R^{\cdot}$) which can undergo propagation with the monomer at a rate of k_p or termination at a rate of k_t.

The rate of activation (k_{act}) is kept low in comparison to rate of deactivation (k_{deact}), pushing the equilibrium to the left to keep the concentration of radicals low thereby reducing the probability of unfavourable termination reactions occurring. Due to this low number of propagating radical species, there is a high concentration of dormant chains present. Kinetic studies of the polymerisation allows monitoring of ATRP reactions and determination of rate; when monomer conversion is plotted against time on a semi-logarithmic scale and a linear increase in molecular weight with conversion is observed it indicates that the polymerisation obeys first order kinetics.[112,113] This means the active species undergoes monomer addition with the propagation rate constant (k_p) but also terminated with rate constant (k_t). Termination reactions are unfavourable, but they are controlled due to the low concentration of the active species during polymerisation.

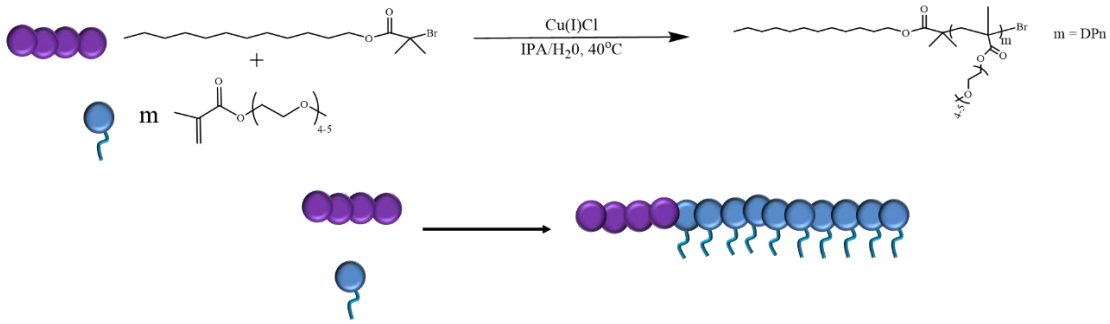

Figure 2.2 Synthesis of linear polymer, where the concentration of monomer:initiator is varied to control the degree of polymerisation (DP_n), in this example $DP_n = 10$.

The formation of branched copolymers *via* ATRP occurs by the addition of a divinyl monomer which is statistically added to growing polymer chains.[114] In a branched polymerisation, Figure 2.3, there is a statistical incorporation of divinyl and vinyl monomers in a ratio to give each growing primary chain less than one potential branching point through the pendant vinyl chain per chain.[115] This ratio avoids gelation of the polymer at high molecular weight through *in situ* cross-linking which occurs if there is 1 or more branching points per chain. At low conversion during polymerisation, monomer concentration is relatively high in comparison to the pendant vinyl groups, so branching is limited. During this stage, the evolution of M_n is identical to linear polymerisations where there is a linear increase in M_n with monomer conversion. At intermediate conversion the number of branching points per chain is increased. At high conversion, the polymerisation is dominated by

intermolecular coupling of the primary polymer chains by reaction of the pendant vinyl groups. This is more likely to occur at high conversion as there is an increased likelihood for reaction between pendant vinyl groups due to the low concentration of monomer. It is at high conversion that the large increase in M_w and M_n is observed due to chain growth being dominated by the intermolecular coupling.

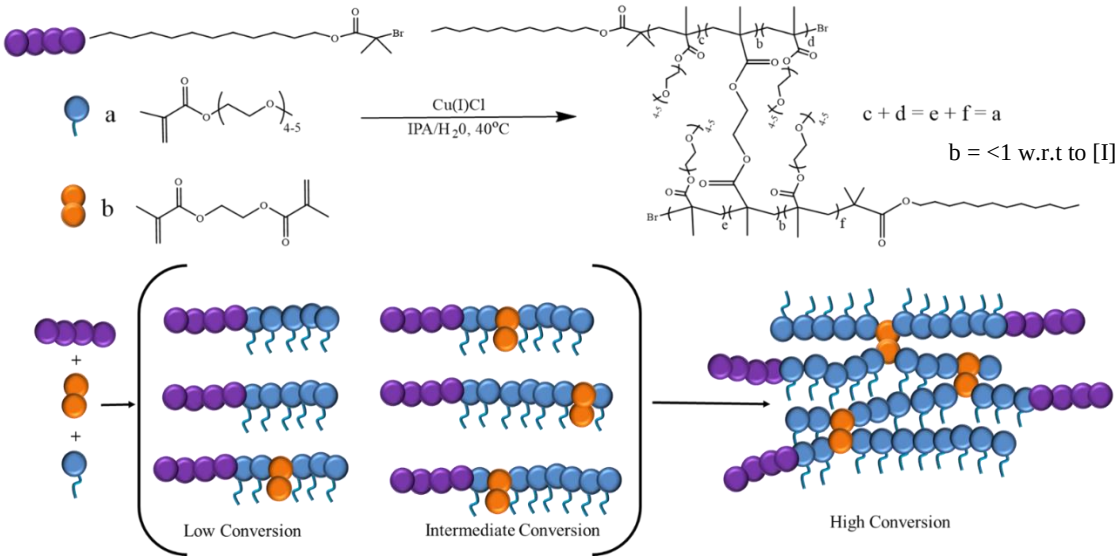

Figure 2.3 Synthesis of branched copolymers by ATRP,[115] primary chain growth is initiated and at low conversion propagation more likely to occur with vinyl monomers. At intermediate conversion statistical incorporation of divinyl monomer occurs and at high conversion intermolecular branching of chains occurs.

2.2 AMPHIPHILIC COPOLYMER SYNTHESIS

2.2.1 ATRP Initiator Synthesis

As discussed in Section 2.1 hydrophobic initiators were required to give the surfactant amphiphilic properties. To introduce hydrophobic chain ends into the branched copolymer structure, the long alkyl chain ATRP initiator, dodecyl α-bromoisobutyrate (DBiB), was synthesised (Scheme 2.2). The trimethylamine catalysed esterification reaction was conducted using 1-dodecanol and α-bromoisobutyryl bromide; the $Et_3NH^+Br^-$ salt that formed immediately on addition of α-bromoisobutyryl bromide was filtered after the reaction had been left to stir for 24 hours. The purified product was analysed by ^1H, ^{13}C nuclear magnetic resonance spectroscopy (NMR), electrospray mass spectroscopy and elemental analysis.

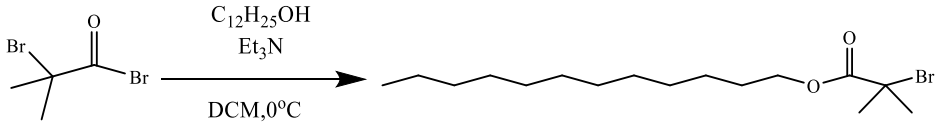

Scheme 2.2 Schematic of dodecyl α-bromoisobutyrate (DBiB) synthesis.

The ^{1}H NMR spectrum of purified DBiB is presented in Figure 2.4A. The reaction is shown to be completed *via* a well resolved singlet peak at 1.8 ppm attributed to $C\underline{H}_3C\underline{H}_3$ (labelled e). If any unreacted starting material (α-bromoisobutyryl bromide) is present in the material, a secondary singlet is seen up field of this peak, therefore the product would require further purification. The ^{13}C NMR spectrum confirmed the lack of impurities present in the sample.

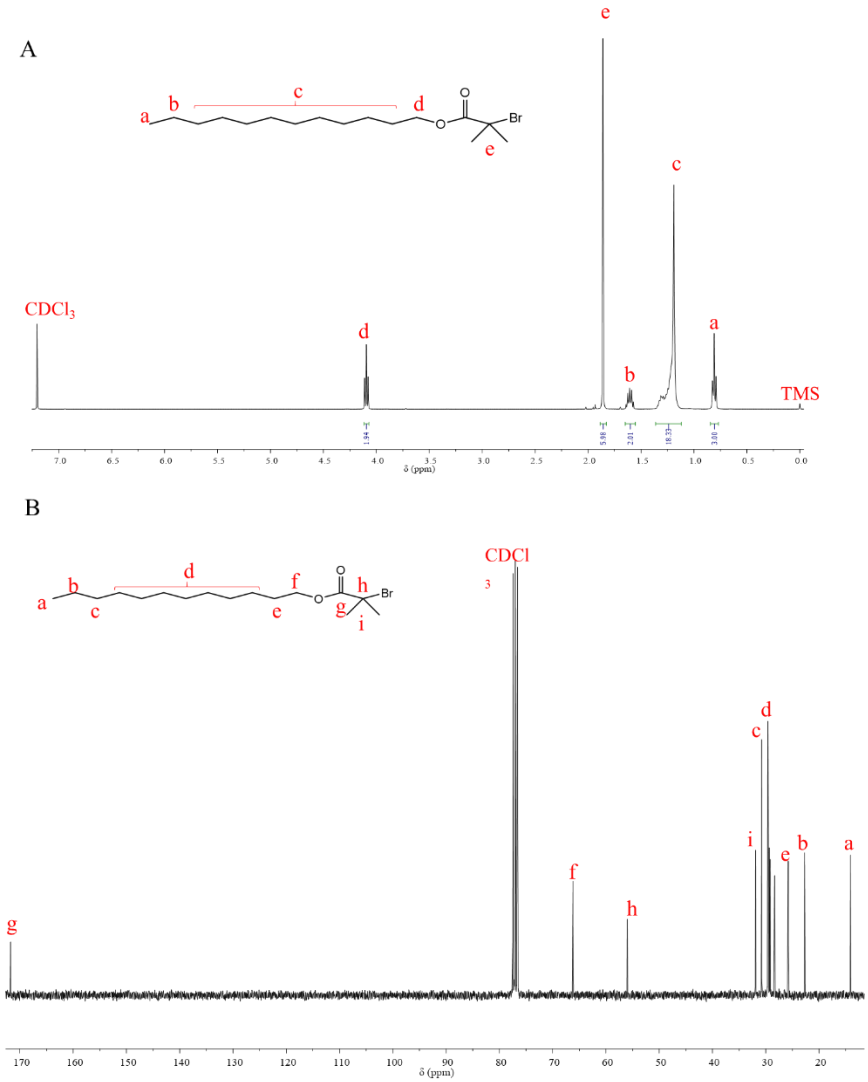

Figure 2.4 Nuclear magnetic resonance spectra of dodecyl α-bromoisobutyrate (DBiB) A) ^{1}H NMR spectra ($CDCl_3$, 400 MHz) and B) ^{13}C NMR spectra ($CDCl_3$, 100 MHz).

2.2.2 Synthesis of Linear Homopolymers and Branched Copolymers

ATRP was used to synthesise both branched and linear amphiphilic polymers. The monomer polymerised was hydrophilic OEGMA, number average degree of polymerisation (DP_n) = 4-5 ethylene glycol units, M_n = 300 g/mol). Initial studies to establish the polymerisation conditions targeted a linear polymeric chain as it is more simplistic than the branched analogue as there are fewer components. The subsequent branched polymerisations were only varied by the inclusion of a divinyl monomer, EGDMA, therefore any changes observed in molecular weight were attributed to the presence of a branching unit.

The polymerisation of OEGMA under aqueous conditions has been previously reported,[107,116,117] with the presence of water accelerating the polymerisation of OEGMA. In this study the catalytic system for ATRP was CuCl:bpy and the solvent mixture was isopropyl alcohol/water (IPA:H_2O, 92.5:7.5 v/v) at 55 % w/v (monomer:solvent). The reaction was conducted at 40 ^oC, the schematic is shown in Scheme 2.3. A DP_n of 50 monomer units (DP_{50}), was targeted for the ATRP of OEGMA, this followed previous research from within the Rannard research group where DP_{90} was targeted.[107] Reducing the DP_n increased the weight fraction of hydrophobic chain end per polymer primary chain which was required for the polymer to be used successfully as a surfactant of o/w emulsions.

Polymerisation reactions were monitored *via* ^1H NMR, and the conversion determined *via* inclusion of an internal standard, anisole, to which the vinyl monomer peaks could be referred against. All reactions were left to reach high conversion (target > 99 %), this was especially important when conducting ATRP targeting branched polymeric architectures. Removal of the copper-based catalytic system was performed by using a neutral alumina column; the polymers and copolymers were purified by precipitation into petroleum ether (40/60).

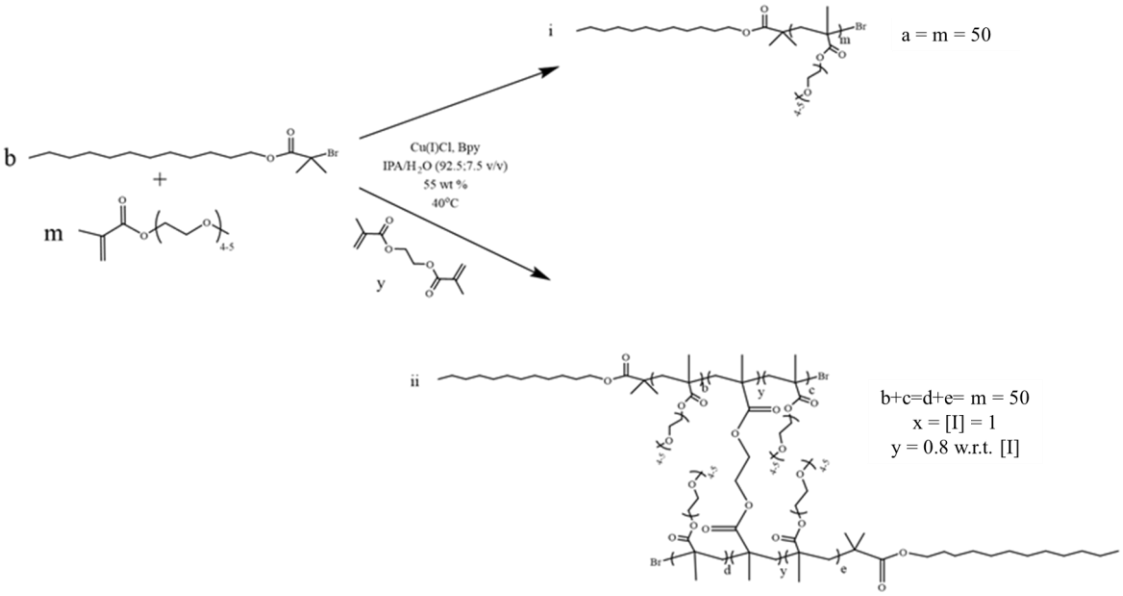

Scheme 2.3 ATRP of i) DBiB-*p*(OEGMA$_{50}$) and the branched analogue ii) DBiB-*p*(OEGMA$_{50}$-*co*-EGDMA$_{0.8}$).

Branched copolymers with synthesised *via* ATRP under the same conditions as described for the linear homopolymers but with the addition of a branching unit, ethylene glycol dimethacrylate (EGDMA). EGDMA was incorporated at an initiator ratio of 0.80:1.00 ($[EGDMA]_0 / [I]_0 = 0.80$) and yielded branched copolymers after 24 hours, shown in Scheme 2.3 ii. Linear and branched polymers take the compositions DBiB-*p*(OEGMA$_{50}$) and DBiB*p*(OEGMA$_{50}$-*co*-EGDMA$_{0.8}$) respectively.

2.3 POLYMER CHARACTERISATION

All polymers were characterised by gel permeation chromatography (GPC) and ^{1}H NMR, GPC data is shown below in Table 2.1. Reaction conversion was determined *via* ^{1}H NMR; a crude sample of the reaction mixture was taken and the disappearance of vinyl monomer peaks against an internal standard, anisole, was measured to calculate conversion of monomer to polymer. Branched polymerisations were left to reach > 99 % conversion to allow for maximum branching between chains through the incorporation of divinyl monomer.

Table 2.1 GPC data for linear and branched *p*(OEGMA).

Target Polymer Composition	^{1}H NMR[b] Conversion (%)	Theoretical M_n	GPC[a] M_w (g/mol)	GPC[a] M_n (g/mol)	GPC[a] Đ (M_w/M_n)	DP $_n$
DBiB-*p*(OEGMA$_{50}$)	99	15 353	39 760	30 750	1.2	101
DBiB-*p*(OEGMA$_{50}$-*co*-EGDMA$_{0.8}$)	>99%	-	235 700	57 600	4.09	-

[a]Determined using GPC (DMF/0.01 M LiBr Eluent 60°C) [b]Determined using ^{1}H NMR ($CDCl_3$,400 MHz)

Figure 2.5 A and B compares the refractive index (RI) chromatograms of the linear and branched *p*(OEGMA$_{50}$), and the increase in molecular weight from the addition of branching unit EGDMA is shown. Branched polymers have a higher weight average molecular weight (M_w), and elute at a much lower retention volume in comparison to the linear polymer. Branched polymers have a broad distribution of polymer due to the statistical incorporation of EGDMA and subsequent branching between growing polymer chains through the pendant vinyl group on the branching unit. A broad distribution is therefore observed as the primary chains joined together. The right angle light scattering (RALS) detector responds to a polymer chain (or grouped chains) particularly those with a high molecular weight which scatter light based on the r^6 dependence, therefore a small number of large molecules will dominate the scattering from any broad distribution polymer solution. In contrast the RI response is dependent on the concentration of the individual separated fractions of the polymer sample. The RALS chromatographs, Figure 2.6 B confirm the presence of high M_w branched material, with an intense scattering signal seen at low elution volumes that correspond to the low concentrations of high molecular weight material seen in the RI analysis. This is in contrast to the linear polymer RALS trace, which is scattering at a higher retention volume due to the lack of high M_w species.

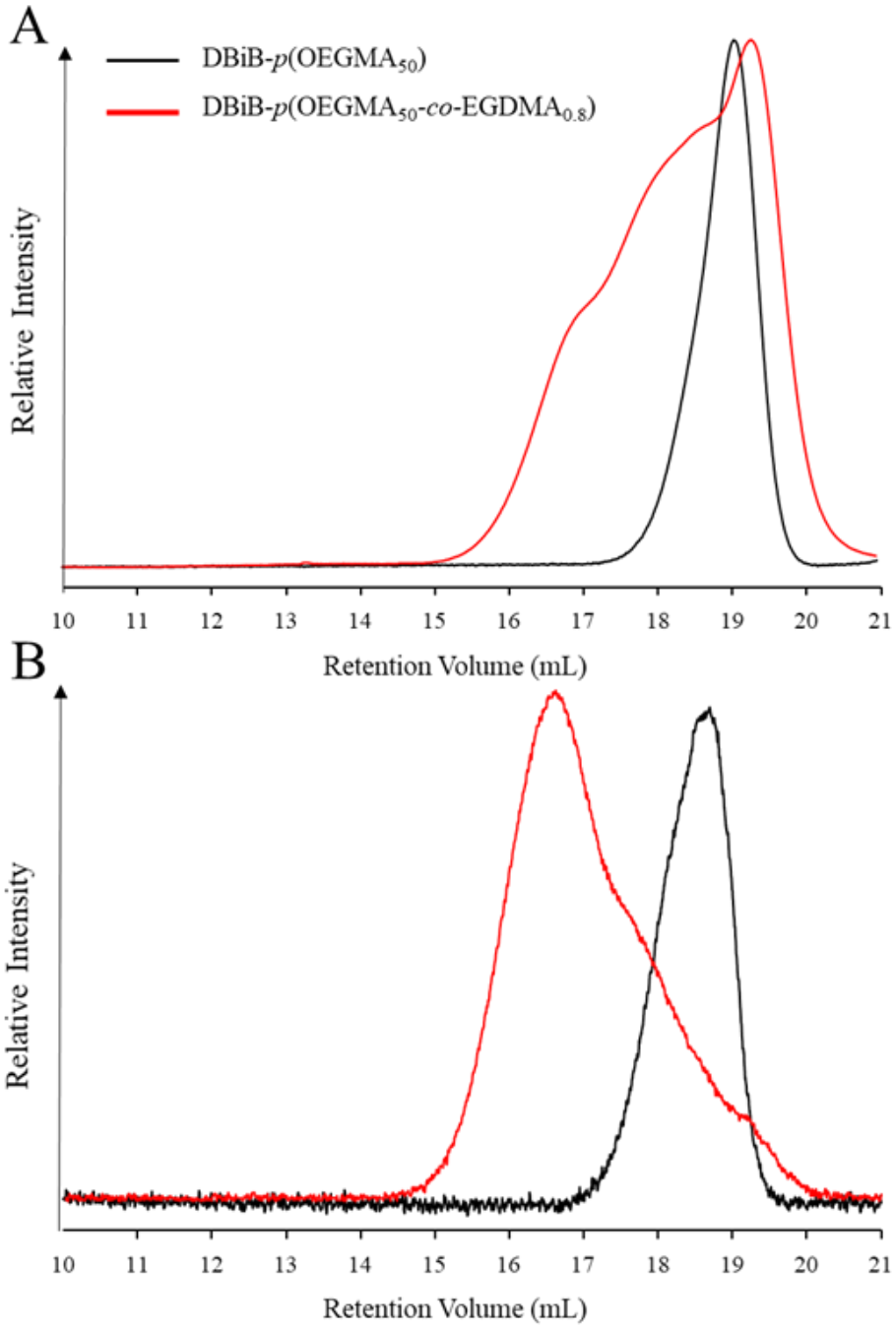

Figure 2.5 GPC chromatograms of DBiB-*p*(OEGMA$_{50}$) (black) and DBiB-*p*(OEGMA$_{50}$-*co*-EGDMA$_{0.8}$) (red) A) RI and B) RALS.

The RI trace of the DBiB-*p*(OEGMA$_{50}$) is typical of a linear polymerisation, eluting at a higher retention volume due to the presence of low molecular weight species, however there is a slight shoulder to the higher M_w side of the trace. This could be due to coupling of the chain ends at high conversion, which correlates with the M_w data for the linear polymer being higher than theoretically expected.

2.3.1 Linear Polymer Kinetics

To investigate whether a polymerisation is controlled, an experiment to investigate the kinetics of the reaction was conducted to determine the rate of reaction. Samples were taken at defined time points throughout the polymerisation and analysed *via* ^{1}H NMR to determine whether the polymerisation follows first order kinetics with respect to monomer concentration.

As discussed in Section 2.1.1, the rate of polymerisation is dependent on the concentration of active species throughout the reaction, this is controlled by the equilibrium constant ($K_{eq} = k_{act} / k_{deact}$) of the redox reaction which generates the active species.[118] If K_{eq} is small then the active species concentration will be low and the rate of polymerisation slow,[119] conversely if K_{eq} is high the concentration of the active species will be high which will result in a faster rate of polymerisation. However, an increase in active species concentration also increases the probability of unfavourable reactions occurring such as chain termination, which will impact the dispersity of the polymer chains.

The synthesis of a linear *p*(OEGMA$_{50}$) initiated by DBiB was monitored to determine whether the polymerisation was controlled and followed first order kinetics with respect to the monomer concentration. The conversion of OEGMA was monitored by ^{1}H NMR spectroscopy; the vinyl peaks at 6.13 and 5.58 ppm decreased throughout the reaction indicating that the monomer was being consumed, Figure 2.7. The polymerisation was sampled every hour for 7 hours and the ratio between OEGMA vinyl peaks and O-C$\underline{H}_3$ *p*(OEGMA) pendant chain at 3.4 ppm used to determine conversion, as shown in Figure 2.6.

The kinetic plot of DBiB-*p*(OEGMA$_{50}$) is shown in Figure 2.7, and this analysis confirms high conversion was reached between 4–7 hours and that the linear polymerisation followed first order kinetics as shown by semi-logarithmic plot obtained. This provides confidence for the copolymerisation of OEGMA to form a branched copolymer with divinyl monomer EGDMA.

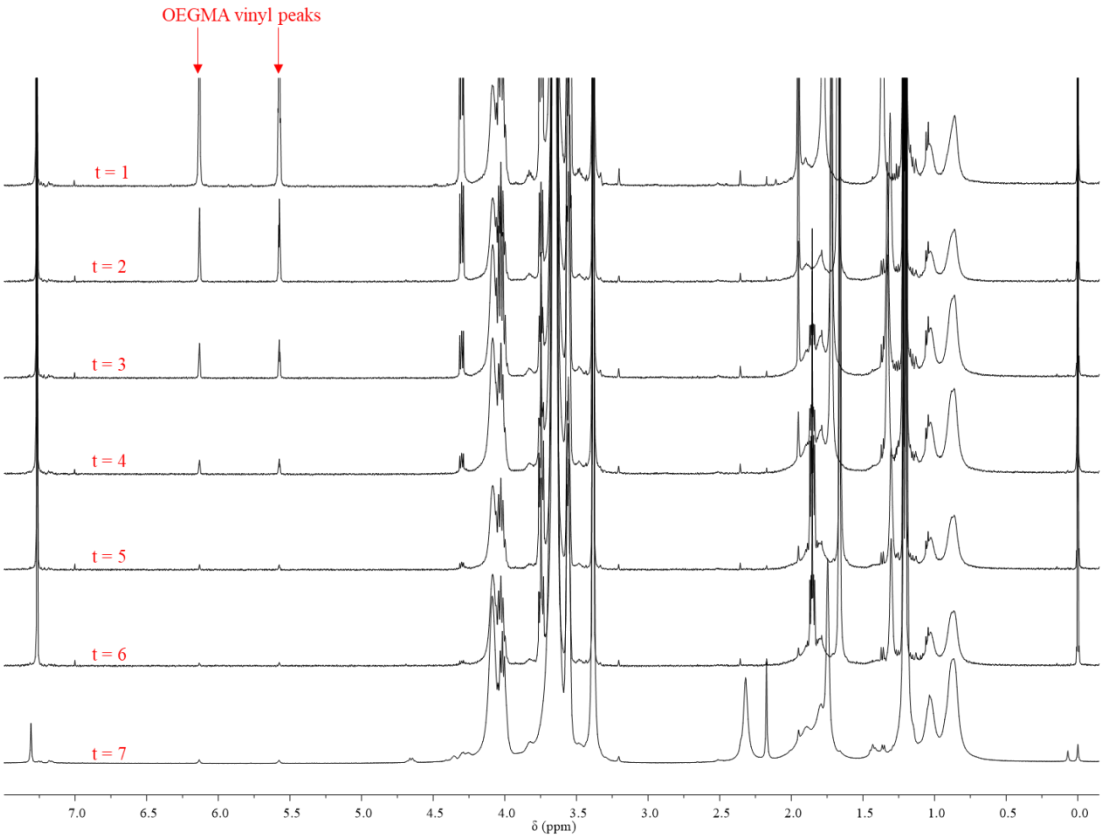

Figure 2.6 ^{1}H NMR spectra ($CDCl_3$, 400 MHz) for DBiB-*p*($OEGMA_{50}$) sampled over 7 hours, monitoring decrease of monomer OEGMA vinyl peaks at 6.13 and 5.58 ppm.

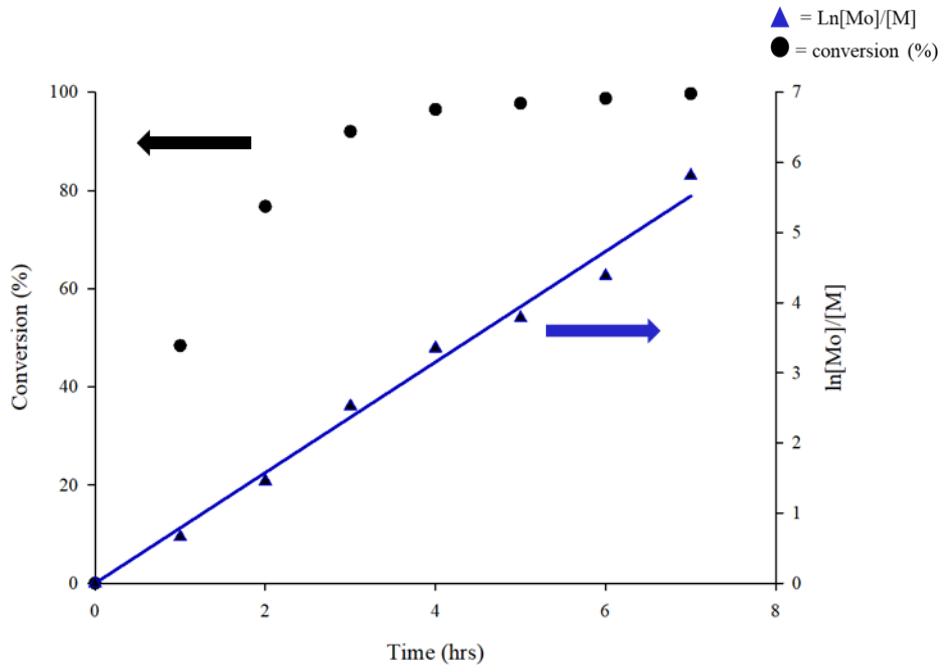

Figure 2.7 Kinetic plot of A) DBiB-*p*($OEGMA_{50}$) determined by ^{1}H NMR, sampled every hour for t = 7.

2.4 EMULSION FORMATION AND CHARACTERISATION

Following successful synthesis of linear and branched copolymers, these polymers were tested for their ability to successfully stabilise emulsions as surfactant molecules. Macroemulsions were generated *via* mechanical shearing, using an overhead shear homogeniser (Ultra-Turrax 25, IKA). Dodecane was chosen as the oil phase due to its high compatibility with the chosen hydrophobic chain end functionality (DBiB). Aqueous polymer solutions were prepared at concentrations of 5 mg/mL and were homogenised with dodecane in a 1:1 ratio for 2 minutes at 24,000 rpm as per the previously reported method and left overnight to equilibrate.[107] Quantitative analysis was performed by laser diffraction spectroscopy using distilled water as dispersant and measurements taken at 20 ^{o}C.

2.4.1 Visual Characterisation of Macroemulsions

Successfully stabilised macroemulsions were characteristically white opaque solutions. Due to the lower oil density of dodecane compared to water, creaming of the oil-in-water emulsion was observed however no oil separation was apparent after 40 days storage at ambient temperature, as shown in Figure 2.8. Linear polymers showed no ability to stabilise o/w emulsions, with demulsification occurring after 3 days, as shown in Figure 2.8 D presumably due to the rapid desorption of linear polymer chains from the oil/water interface, inducing coalescence of neighbouring droplets. This is in agreement with previously published research within the group, for branched DBiB initiated OEGMA copolymers and linear polymers with a higher target DP_n = 90.[107]

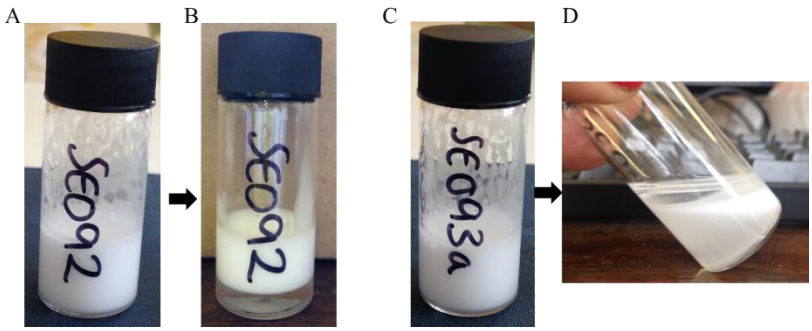

Figure 2.8 Visual characterisation of branched DBiB-*p*(OEGMA$_{50}$-*co*-EGDMA$_{0.8}$) (5 mg/mL) stabilised macroemulsion with dodecane as oil phase stored at ambient temperature for A) 24 hrs and B) 40 days, and DBiB-*p*(OEGMA$_{50}$) (5 mg/mL) stabilised macroemulsions after C) 24 hrs and D) 3 days.

2.4.2 Laser Diffraction

Analysis of o/w macroemulsions was performed using laser diffraction using Mastersizer 2000 (Malvern), quoting the $D_{[4,3]}$ (De Brouckere Mean Diameter) value, Equation 2.1. $D_{[4,3]}$ is the volume average mean of droplets present in emulsion, which does not rely on knowing the number of droplets present. The $D_{[4,3]}$ is widely quoted as it reflects the size of the particles that make up the bulk of the sample volume, and is more appropriate then the surface area moment mean ($D_{[3,2]}$) in this study, which is more sensitive to the fine particles present.[120] The laser diffraction technique averages the various droplet dimensions, to produce a size distribution. The particle size measurement includes percentiles, where D50 is the median, therefore the diameter where half the population lies below this value. Whereas D10 represents the value at which 10 % of the population lie below and D90 represents the diameter at which 90 % of the population fall below.

$$D_{[4,3]} = \Sigma d^4 / \Sigma d^3 \qquad (2.1)$$

Dodecane based macroemulsion stabilised with DBiB-*p*(OEGMA$_{50}$-*co*-EGDMA$_{0.8}$) a branched copolymer surfactant was measured *via* laser diffraction, with water as the dispersant. Figure 2.9 shows a typical graphical size distribution of the DBiB-*p*(OEGMA$_{50}$-*co*-EGDMA$_{0.8}$) stabilised dodecane macroemulsion, plotting volume percent against particle diameter ($D_{[4,3]}$). The $D_{[4,3]}$ analysis determined the average droplet diameter to be 11.9 µm.

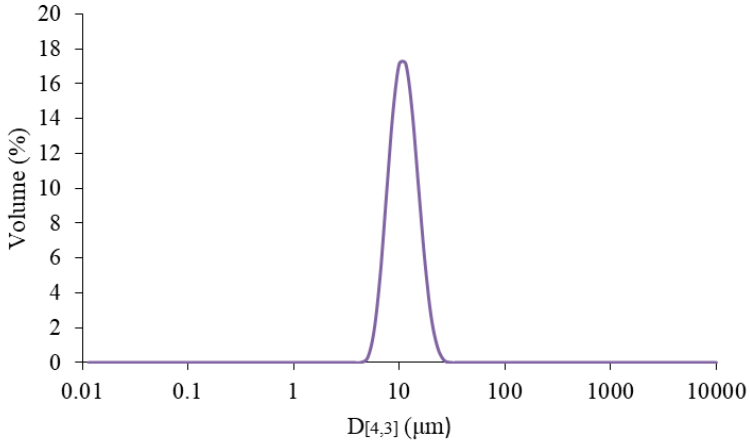

Figure 2.9 Particle size distribution curve of dodecane macroemulsion stabilised with DBiB-*p*(OEGMA$_{50}$-*co*-EGDMA$_{0.8}$) as polymeric surfactant after 24 hrs of storage at ambient temperature.

The impact of polymer concentration in the aqueous phase of the emulsion was studied to assess the ability of the branched copolymer surfactant, DBiB-*p*(OEGMA$_{50}$-*co*-EGDMA$_{0.8}$), used to stabilise a dodecane based o/w emulsion. Aqueous polymer solutions of DBiB-*p*(OEGMA$_{50}$-*co*-EGDMA$_{0.8}$) at 1, 3 and 5 mg/mL were generated for use within the emulsions. After homogenisation, emulsions were stored at ambient temperature, and samples taken at regular intervals over a 40 day time period for laser diffraction analysis.

As shown in Figure 2.10, emulsions with the lowest surfactant concentration of 1 mg/mL produced oil droplets which had increased in size from 13.8 µm at 1 day to 23 µm at 5 days. Whereas when higher concentrations of 3 and 5 mg/mL branched copolymer surfactant had been used there was relatively little variation in droplet sizes over the 30 day time period with $D_{[4,3]}$ values of 12.7 – 14.2 µm and 11.9 – 13.4 µm respectively. After 40 days however, the final droplet diameters of the 3 mg/mL branched copolymer surfactant concentration rose to 34 µm whilst 5 mg/mL still showed consistent $D_{[4,3]}$ values of 13.5 µm. The sharp rise in droplet diameter in the emulsion produced using a surfactant concentration of 3 mg/mL could be indicative of droplet coalescence within the emulsion layer, therefore a lower polymer concentration could potentially not provide a great enough stabilising film at the oil/water interface.

It was concluded from this study that emulsions stabilised by a branched copolymer surfactant concentration of 5 mg/mL, yielded the smallest droplet diameter with prolonged levels of stability and least variation in droplet size, therefore all further emulsions in this work were generated using a 5 mg/mL polymeric surfactant concentration in the aqueous phase.

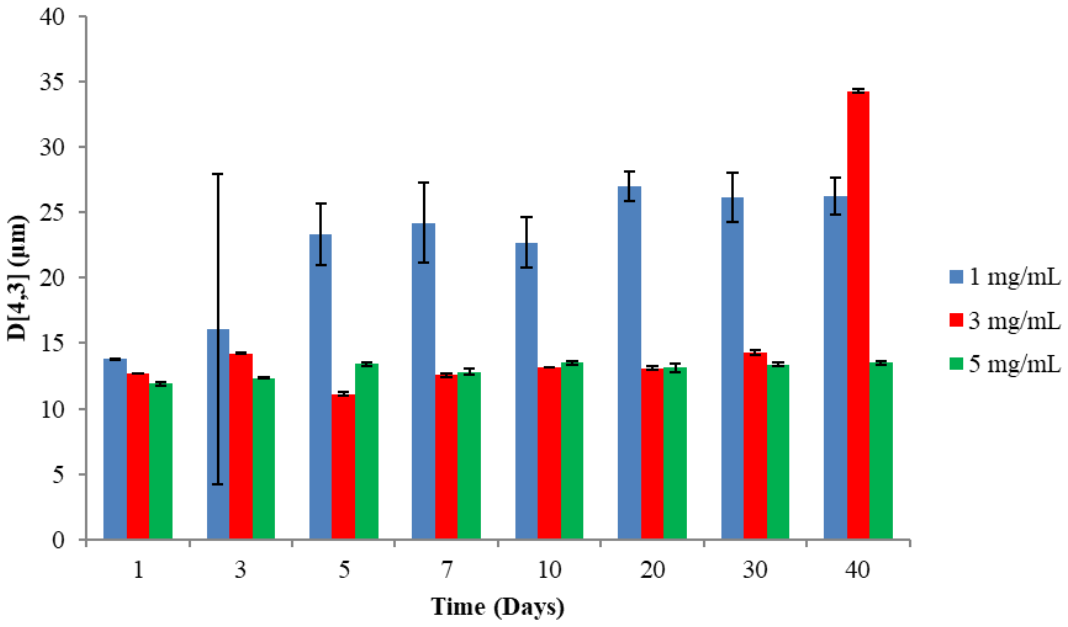

Figure 2.10 Concentration study of polymeric surfactant DBiB-*p*(OEGMA$_{50}$-*co*-EGDMA$_{0.8}$) used to stabilise dodecane macroemulsions. Concentrations of 1, 3 and 5 mg/mL DBiB-*p*(OEGMA$_{50}$-*co*-EGDMA$_{0.8}$) with respect to aqueous phase were generated and analysed by laser diffraction analysis over 40 days. Error bars = standard deviation, n= 3.

2.4.3 Optical Microscopy Analysis

An additional analytical technique of optical microscopy (Leica, DM4 B) was used to visually assess the droplet shape as well as to study the diameter, $D_{[1,0]}$. Optical microscopy imaging is a good secondary analytical technique as it allows for visualisation of the oil droplet geometry as well as calculating the diameter of a vast amount of droplet diameters in a sample of the emulsion. Macroemulsions were imaged after 1 day and 11 months of storage at ambient temperature. Laser diffraction measurements were also taken at the same time points for comparison of analytical techniques.

O/w macroemulsions were formulated in a 1:1 ratio of dodecane:aqueous polymer solution (5 mg/mL) and homogenised for 2 minutes at 24,000 rpm as described in Section 2.4. Concentrated emulsion was placed on a glass slide and viewed at 20x zoom magnification and imaged using a Leica DM4, Figure 2.12.

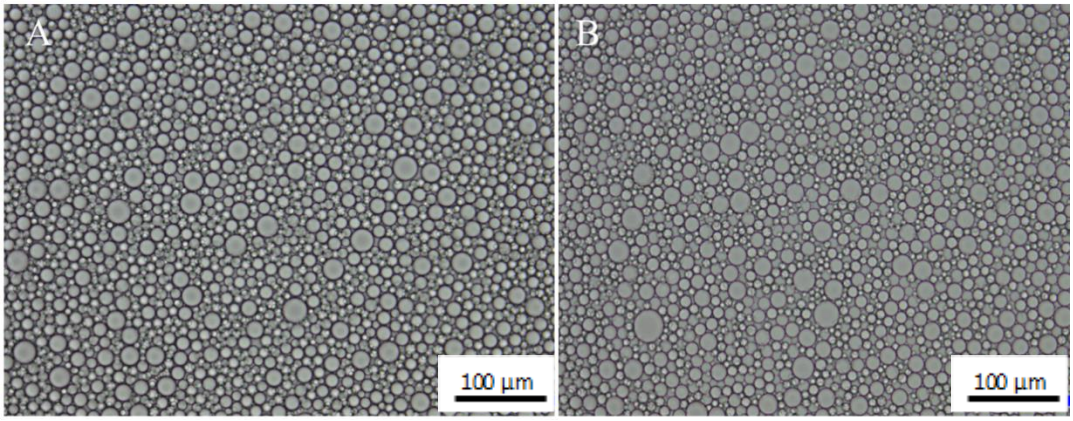

Figure 2.11 Optical microscopy image of a dodecane emulsion stabilised by DBiB-*p*(OEGMA$_{50}$-*co*-EGDMA$_{0.8}$) after A) 1 day and B) 11 months of storage at ambient temperature. 20x zoom magnification, scale bar = 100 µm.

A macroemulsion stabilised by DBiB-*p*(OEGMA$_{50}$-*co*-EGDMA$_{0.8}$) was comprised of spherical droplets, with clearly defined boundaries. Figure 2.11 shows that the macroemulsion is densely packed with individual well-defined oil droplets, with an intact stabilising film at the interface between droplets. From optical microscopy imaging, a processing software (FIJI V 1.51n) was used to highlight individual droplet boundaries and calculate a circumference value based on the scaling. The diameters of individual droplets were then able to be calculated from the circumference, where the frequency of droplet diameters was determined in a range of 1 – 20 µm. A histogram frequency distribution was plotted as it allows for an accurate representation of the distribution of the droplet diameters, assessing the frequency distribution as well as the cumulative frequency (%). A histogram of the 2-dimensional droplet diameters was able to be produced, as shown in Figure 2.12.

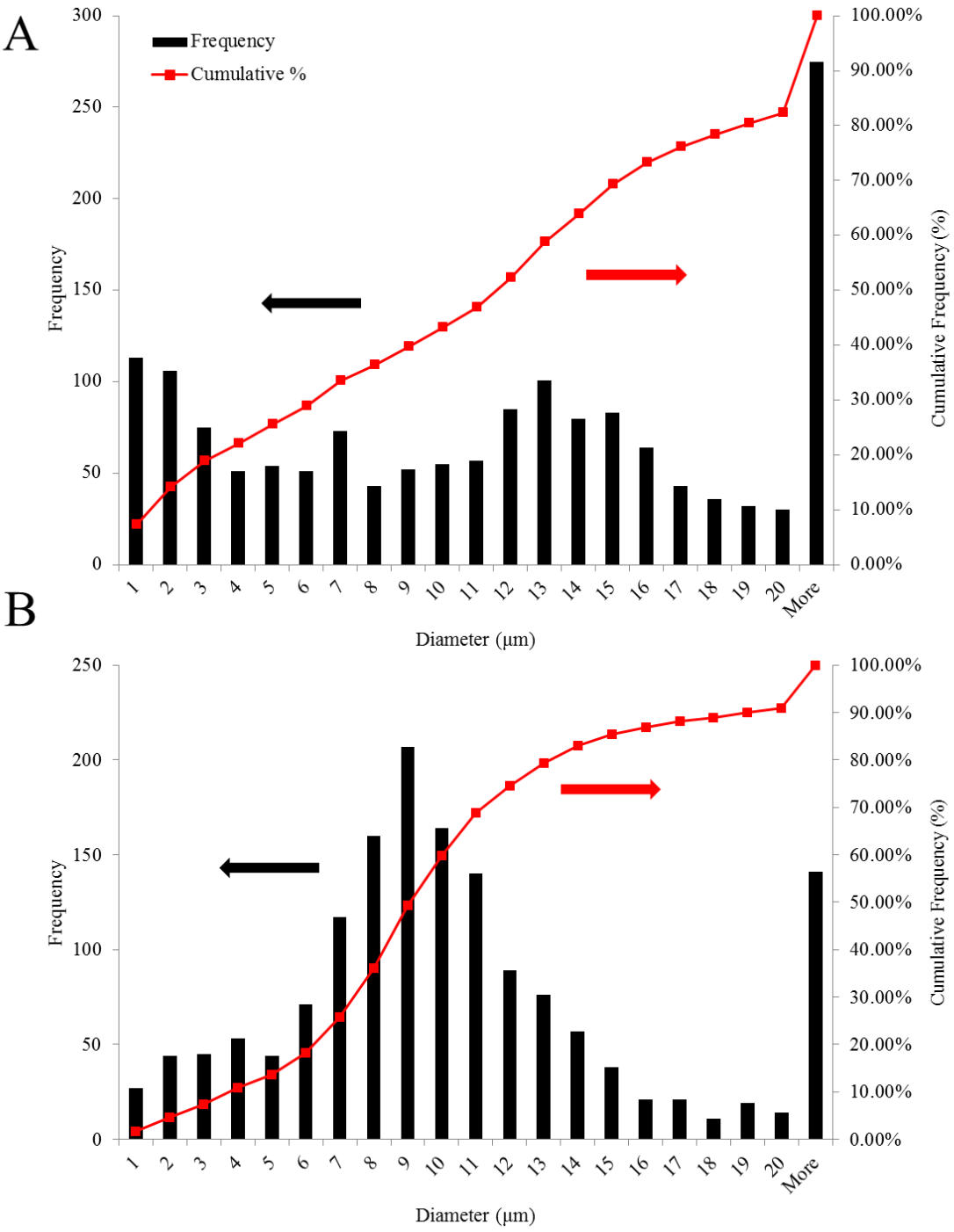

Figure 2.12 Histogram of dodecane macroemulsion stabilised with polymeric surfactant DBiB-*p*(OEGMA$_{50}$-*co*-EGDMA$_{0.8}$) at 5 mg/mL comparing size (diameter) after A) 1 day and B) 11 months storage at ambient temperature.

From this analysis of DBiB-*p*(OEGMA$_{50}$-*co*-EGDMA$_{0.8}$) stabilised dodecane macroemulsion droplets after 24 hours of equilibration, Figure 2.12 A, it was determined that the greatest droplet frequency was for droplet diameters over 20 µm, with over 275 droplets, 17 % analysed in this range. However, over 80 % of the droplets analysed were under 20 µm, so for this sample, droplet diameters measured by microscopy would appear to be much more polydisperse than indicated by the $D_{[4,3]}$. The histogram of the sample stored for 11 months, Figure 2.12 B, showed that the frequency of oil droplets was greatest at 9 µm with 273 droplets in this range, which equates to 52 % of the total population. Although 90 % of particles present were under 15 µm in comparison to the $D_{[4.3]}$ results after 40 days (13 µm) . Therefore the results after 11 months of storage of emulsion at ambient temperature correlate with that of $D_{[4,3]}$ measured *via* laser diffraction, this shows that it is representative of the droplet volume which make up the bulk of the emulsion.

2.4.4 Macroemulsion Dilution Studies

Conventional surfactant-stabilised emulsions are subject to demulsification if they are diluted below the critical micelle concentration (CMC); the concentration above which micelles form and if additional surfactants are added also form micelles. However Pickering emulsions as discussed in Chapter 1 Section 1.6.3. are dilution stable due to the near-irreversible adsorption of particles to the droplet surface. It was hypothesised that the branched copolymer surfactants act somewhere in between a traditional surfactant and a Pickering emulsion due to the multiple chain ends which anchor one polymer to the surface of the droplet. The droplet stability of the branched copolymer stabilised emulsions was studied by diluting concentrated macroemulsions over a dilution range in distilled water. The diameter of these droplets was measured *via* optical microscopy so that the droplet geometry could easily be visualised, Figure 2.13 A-D.

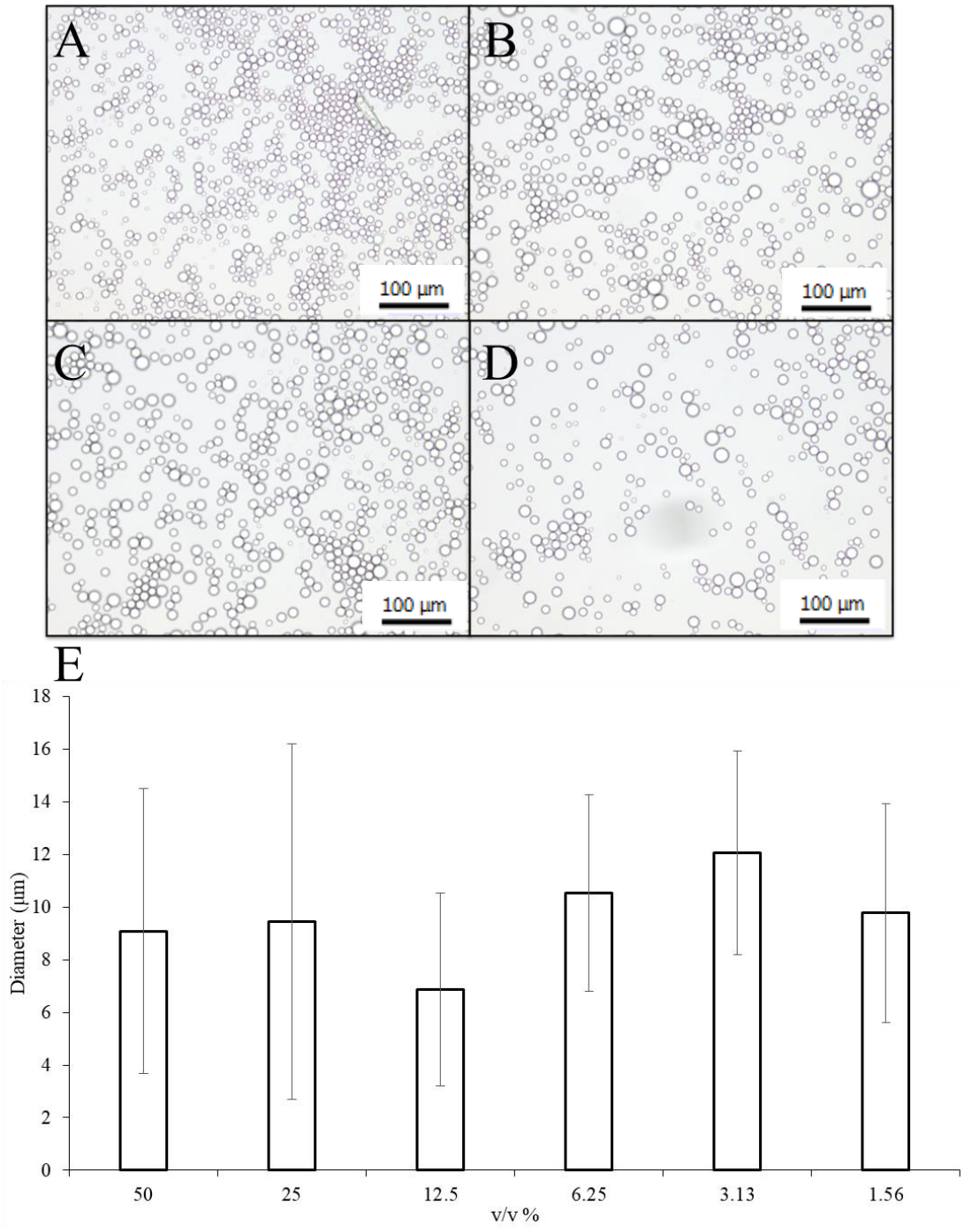

Figure 2.13 Optical microscopy images of DBiB*p*(OEGMA$_{50}$-*co*-EGDMA$_{0.8}$) stabilised dodecane macroemulsion, over serial dilutions in distilled water; A) 50 v/v %, B) 25 v/v %, C) 12.5 v/v % and D) 6.25 v/v %, 20 x magnification, scale bar = 100 µm. E) droplet diameters determined by FIJI (V 1.51n) over dilution range of 50 – 1.56 v/v % in distilled water, error bars = standard deviations.

As shown *via* optical microscopy imaging, through serial dilution of a concentrated sample, emulsions remain stable to the increased volume of the continuous phase retaining their spherical geometry with good definition of individual stabilised droplets. The average diameter is shown in Figure 2.13 E, with macroemulsions maintaining a consistent average droplet diameter over a dilution range of 50 - 1.56 v/v %.

2.5 AMPHIPHILIC BRANCHED COPOLYMER STABILISED NANOEMULSIONS

Following on from previously published work, nanoemulsions were generated utilising a solvent evaporation method, shown in Figure 2.14, homogenisation was conducted using an over-head shear homogeniser.[107] Nanoemulsions were generated in a 1:1 ratio of oil:aqueous polymer solution, where the oil phase was a mixture of volatile and non-volatile oils, ethyl acetate and castor oil. Varying the ratio of the two oils altered the final nanoemulsion droplet diameter due to the removal of the volatile oil phase i.e. the higher the proportion of volatile oil the smaller the resulting emulsion droplet.

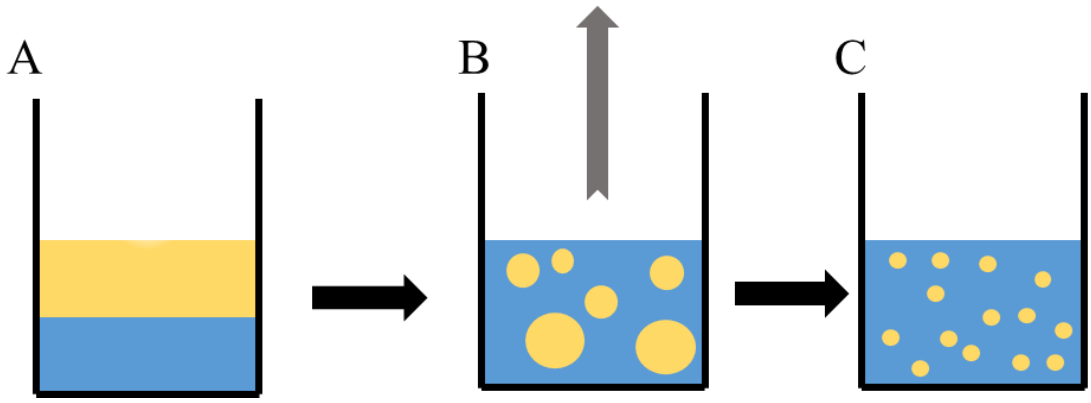

Figure 2.14 General representation of nanoemulsion generation using solvent evaporation method; A – B) 1:1 Aqueous polymer solution (5 wt %) and oil phase composed of volatile and non-volatile oil is homogenised, B-C) emulsion is left overnight for full evaporation of the volatile oil, enabling the droplets to reduce to the nanoscale.

In this study, the ability to tailor the size of nanoemulsions was investigated by varying the concentration of volatile co-solvent to non-volatile oil in ratios of: 50:50, 60:40, 70:30, 80:20, 90:10 and 99:1. The branched copolymer concentration was maintained

at 5 wt % throughout. Castor oil, Figure 2.15 A, was selected as the non-volatile oil phase for nanoemulsion generation due to it being a naturally derived oil and highly biocompatible.

Castor oil is a vegetable oil derivative which is obtained from the seeds of the plant *Ricinus communis.*[121] It is a triglyceride in which approximately 90 % of fatty acid chains are ricinoleic acid, shown in Figure 2.15 B and the other 10 % consists of: oleic acid (~ 4 %), linoleic acid (~3 %), α-linoleic acid (~ 0.75 %), stearic acid (~ 0.75 %), palmitic acid (~ 0.75 %), dihydrooxystearic acid (~ 0.4 %) and others (~ 0.35 %). The medical value of castor oil can be traced back to ancient years, where it was commonly used as a laxative.[122,123] In previously published work, castor oil was shown to be the oil of choice for the loading of anti-retroviral drugs as well as being a constituent of a non-toxic nanoemulsion formulation which was dosed *in vitro* to Caco-2 cells.[107]

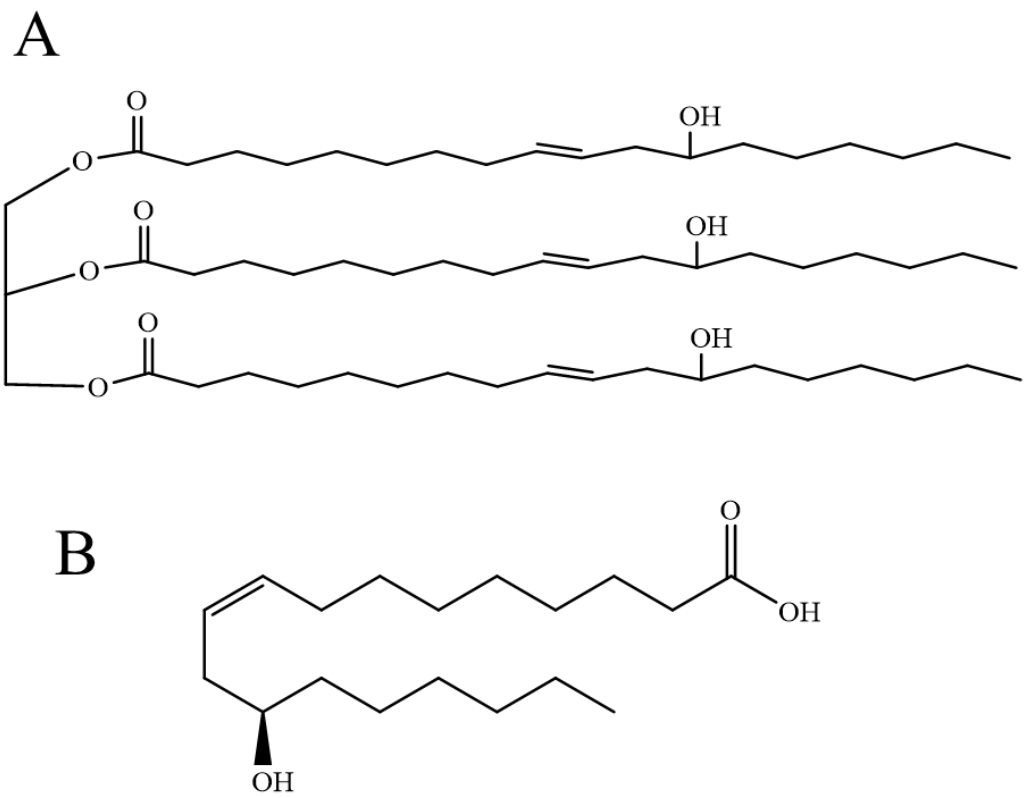

Figure 2.15 Structure of A) castor oil and B) ricinoleic acid the main constituent of castor oil.

2.5.1 Dynamic Light Scattering

Following generation of the nanoemulsions *via* the homogenisation and solvent evaporation method dynamic light scattering (DLS) was used to characterise nanoemulsions. DLS has an accuracy of up to 1 µm, while the laser diffraction Mastersizer values can be deemed accurate from 1 µm upwards. DLS calculates particle size by using the correlation between Brownian motion of particle and its hydrodynamic diameter. The software uses an autocorrelation function to correlate scattering over time which can be used to calculate particle size. The correlation will be high over a short period of time due to small movement of the particle, while over a long period of time correlation will be low due to the Brownian movement of the particle. This method of cumulants analysis is then used to calculate the z-average diameter (D_z). The D_z is calculated from the translational diffusion coefficient by using the Stokes-Einstein equation, Equation 2.2) where D_t is the intensity weighted average translation diffusion calculated by the method of cumulants analysis, k is Boltzmann's constant, T is the absolute temperature, η is viscosity.

$$D_z = kT/ 3\pi\eta D_t \qquad (2.2)$$

The polydispersity index (PdI) of the sample measures the size of distribution and is also calculated using the method of cumulants. DLS measurements were performed at a 1 % concentration of nanoemulsion in water, as consistent with published analysis.

2.5.2 Tailoring of Nanoemulsion Droplet Diameter

Aqueous polymer solutions were prepared at a 5 wt% concentration and solubilised in water overnight. O/w nanoemulsions were generated by over-head shear homogenisation of a 1:1 ratio of oil:aqueous polymer solution, where the oil phase was a mixture of volatile solvent to non-volatile oil. The oil phase was a mixture of ethyl acetate and castor oil, and ratios of volatile to non-volatile oil were varied between: 50:50, 60:40, 70:30, 80:20, 90:10 and 99:1. Emulsions were left at ambient temperature overnight following homogenisation, allowing for full removal of volatile co-solvent by evaporation which was monitored gravimetrically. The ratio of oil to co-solvent was varied which allowed for systematic variation of the nanoemulsion droplet size, yielding a droplet range from 1044 – 203 nm, shown in Table 2.2.

Table 2.2 DLS characterisation of DBiB*p*(OEGMA$_{50}$-*co*-EGDMA$_{0.8}$) stabilised nanoemulsion with varied ratios of ethyl acetate:castor oil as volatile:non-volatile oil phase.

Polymer	Ethyl acetate:castor oil Ratio	D_z (nm)	D_n (nm)	PdI
DBiB*p*(OEGMA$_{50}$-*co*-EGDMA$_{0.8}$)	50:50	1055	614	0.37
	60:40	689	544	0.21
	70:30	520	427	0.19
	80:20	470	395	0.15
	90:10	351	305	0.18
	99:1	203	177	0.06

Increased volume of volatile oil (ethyl acetate) in the nanoemulsion preparation not only results in the droplet diameter being systematically reduced, but also the nanoemulsions becoming more monodisperse which is indicated by reduced value of PdI from 0.37 – 0.06, Figure 2.16.

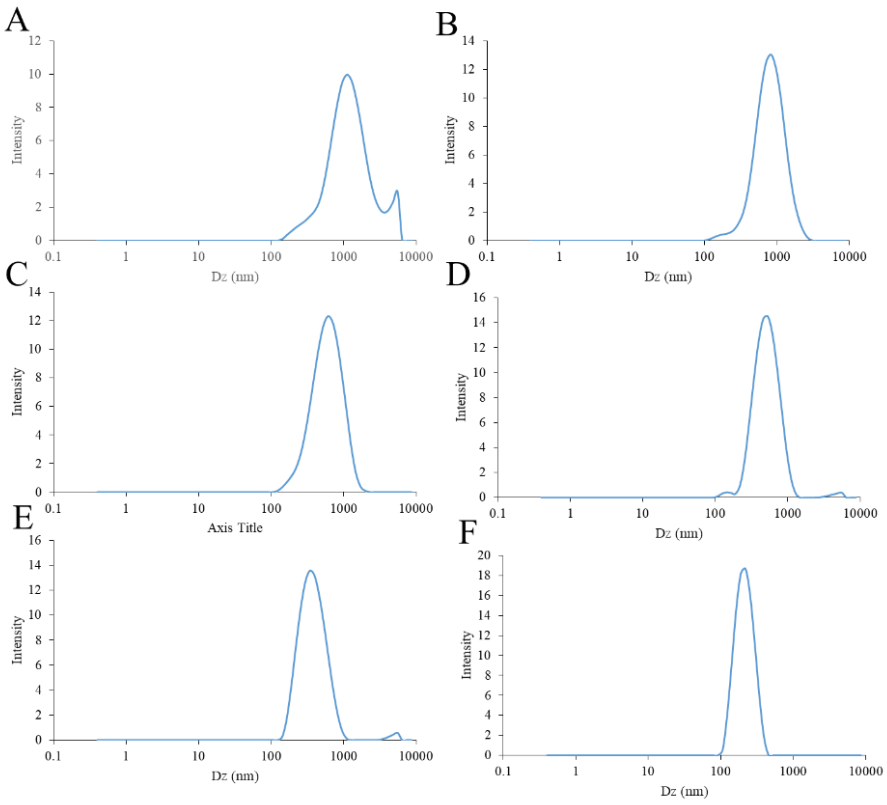

Figure 2.16 DLS analysis of DBiB-*p*(OEGMA$_{50}$-*co*-EGDMA$_{0.8}$) stabilised nanoemulsions generated with ratios of ethyl acetate:castor oil at: A) 50:50, B) 60:40, C) 70:30, D) 80:20, E) 90:10 and F) 99:1.

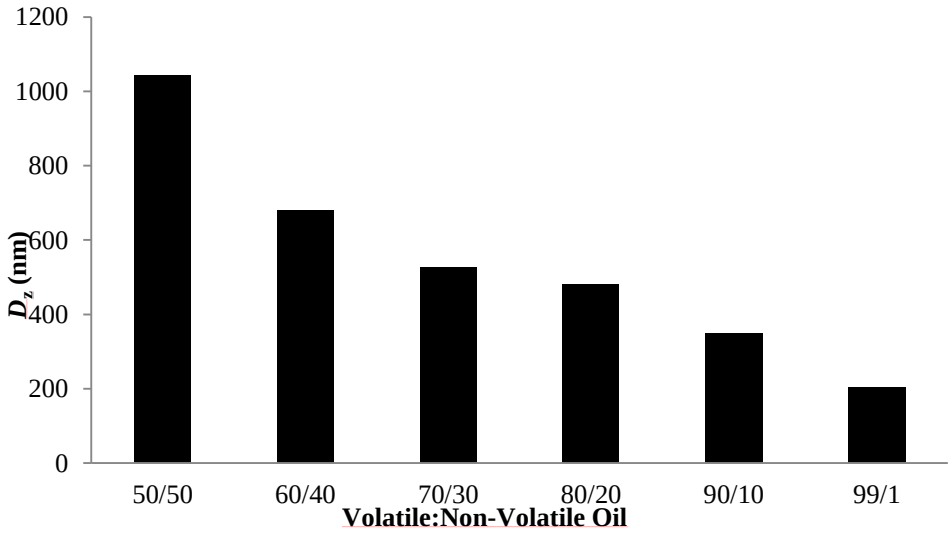

Figure 2.17 D_z (nm) of tailored nanoemulsions stabilised with DBiB-*p*(OEGMA$_{50}$-*co*-EGDMA$_{0.8}$), showing the decrease in droplet size with increased volume of co-solvent. Voltaile oil:non-volatile oil ratios of ethyl acetate:castor oil at 50:50 – 99:1 were used.

2.6 CONCLUSIONS

This study aimed to replicate previously published work using the surfactant DBiB-*p*(OEGMA$_{50}$-*co*-EGDMA$_{0.8}$) compared to DBiB-*p*(OEGMA$_{90}$-*co*-EGDMA$_{0.95}$)[107] Protocols and procedures were established for a successful and controlled polymer synthesis where an understanding of how polymer synthesis could be manipulated to vary the polymeric architecture was vital to understanding how surfactant functionality could be varied.

A hydrophobic ATRP initiator, DBiB, was synthesised *via* a successful trimethylamine catalysed esterification reaction and used in polymerisations of the hydrophilic OEGMA monomer which generated amphiphilic polymers. Linear and branched polymers, DBiB-*p*(OEGMA$_{50}$) and DBiB-*p*(OEGMA$_{50}$-*co*-EGDMA$_{0.8}$) were successfully polymerised using ATRP and well defined using NMR and GPC analytical techniques. The linear polymer was unable to successfully stabilise either a macroemulsions or nanoemulsion whilst the branched polymeric architecture was able to act as a single emulsifier and produce highly stable emulsions over sustained time periods. The high molecular weight branched copolymer contained multiple hydrophobic chain ends which act as stabilisers as they anchor into the oil and hold the extending hydrophilic polymer at the interface at the droplet surface. Which resulted in the branched copolymer surfactant having characteristics which lie somewhere between the characteristic behaviour of a classical amphiphilic surfactant and a Pickering emulsifier.

The impact of polymer concentration in the aqueous phase of the emulsion was studied to assess the ability of the branched copolymer surfactant, DBiB-*p*(OEGMA$_{50}$-*co*-EGDMA$_{0.8}$). A dodecane based o/w emulsion was generated at 1, 3 and 5 mg/mL surfactant concentration in the aqueous phase and studied over a 40 day time period. It was concluded that emulsions stabilised by 5 mg/mL polymeric surfactant yielded the smallest droplet diameter with prolonged levels of stability and least variation in droplet size, therefore all further emulsions throughout this work will be generated using a 5 mg/mL polymeric surfactant concentration in the aqueous phase.

Droplet stability was tested through serial dilution of a dodecane based, DBiB-*p*(OEGMA$_{50}$-*co*-EGDMA$_{0.8}$) stabilised macroemulsion. The diameters of the emulsion droplets, PdI and optical microscopy to investigate droplet structure were

used to determine emulsion stability over a dilution range in water of 50 – 1.56 v/v %. It was found that the diameters of the emulsion droplets remain stable to the increased volume of the continuous phase and retained their spherical geometry with good definition of individual stabilised droplets throughout the entire dilution range.

Finally the tailoring of size nanoemulsion droplet was studied by varying the concentration of volatile co-solvent to non-volatile oil in ratios of: 50:50, 60:40, 70:30, 80:20, 90:10 and 99:1. Increased volume of volatile oil (ethyl acetate) in the nanoemulsion preparation resulted in the droplet diameter being systematically reduced and the nanoemulsions becoming more monodisperse. This ability to control the size of the emulsion droplet will allow further studies to be conducted at specific droplet sizes and to determine if size of the droplet contributes to any affects observed.

CHAPTER 3

Use of Co-Initiated Branched Copolymers as Surfactants

3.1. INTRODUCTION

The aim of this investigation was to include a hydrophilic co-initiator into the synthesis of amphiphilic branched copolymers and systematically reduce the number of hydrophobic chain ends by varying the molar ratio of two initiators DBiB and poly(ethylene glycol) 2-bromoisobutyrate (PBiB). It is unclear how many hydrophobic chain ends are required for efficient surfactant behaviour, therefore identification of the mole percent of hydrophobic chain ends required to form stable macroemulsions and nanoemulsions will be determined. This will also provide mechanistic information and options for further copolymer design modifications. Co-initiation is a unique option available to branched copolymerisations and allows chain end functionality within the resulting branched copolymers to be controlled by varying the molar ratio of initiating groups, see Figure 3.1. This synthetic method for highly branched polymers was chosen as previous work in the research group has shown co-initiation leading to branched copolymers with multi-functional chain ends, for example when mixing dendritic and non-dendritic initiator groups.[124,125]

In Chapter 2, highly branched amphiphilic polymers were used to successfully stabilise both macroemulsions and nanoemulsions as a single emulsifier; all chain ends were hydrophobic and the polymer core was hydrophilic. It was hypothesised the number of hydrophobic chain ends could be significantly reduced without impacting the ability of the branched copolymer to act as a successful single surfactant producing droplet diameters similar to those previously seen when using DBiB-*p*(OEGMA$_{50}$-*co*-EGDMA$_{0.8}$) as the surfactant. In this study PBiB (~750 g/mol) will be used to act as the hydrophilic initiator for model studies; replacing the dodecyl-derived initiator systematically to allow for detailed study.

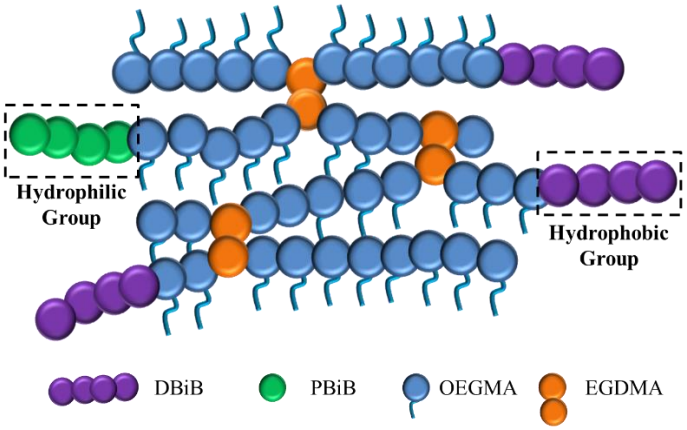

Figure 3.1 Schematic representation of a branched copolymeric surfactant, co-initiated with hydrophilic (green) and hydrophobic (purple) initiator molecules to vary the amphiphilic nature of the copolymer.

Systematic variation of the molar ratio of PBiB:DBiB within the reaction from 0 to 1, leads to a theoretical decrease in the number of hydrophobic dodecyl chain ends present in the branched material, Figure 3.2. Studies of the resulting copolymers' ability to act as surfactants will be conducted using detailed laser diffraction (Mastersizer) for macroemulsions and dynamic light scattering (zetasizer) nanoemulsions. Larger emulsions will also be studied using optical microscopy analysis to investigate the impact of reducing the number of hydrophobic chain ends on the structure of the droplet. It is hypothesised that a critical number of chain ends can be determined, at which polymeric surfactants do not forfeit emulsion stability at both the macroscale and nanoscale but allow the potential placement of functionality.

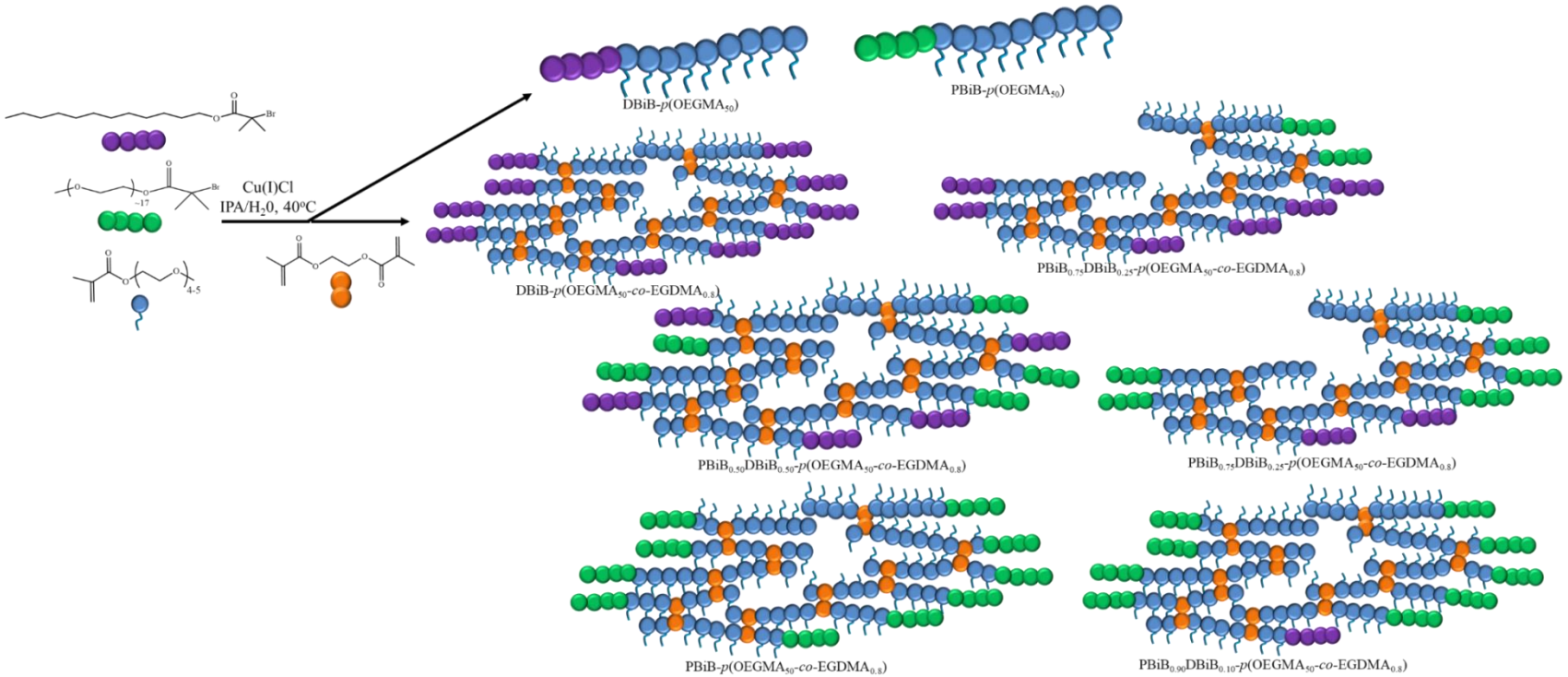

Figure 3.2 Synthesis of linear polymers and branched copolymers using a co-initiation strategy: OEGMA (blue) based polymers is co-initiated by initiators derived from DBiB (purple) and PBiB (green) groups and branched when copolymerised with EGDMA (orange) to generate copolymers with mixed chain end functionalities.

3.2 SYNTHESIS OF OEGMA BASED POLYMERIC SURFACTANTS USING CO-INTIATORS

3.2.1 Synthesis of Poly(ethylene glycol) methyl ether 2-bromoisobutyrate

A hydrophilic ATRP macroinitiator, PBiB, was synthesised as shown in Scheme 3.1, *via* a trimethylamine catalysed esterification of poly(ethylene glycol) with commercially available α-bromoisobutyryl bromide; $Et_3NH^+Br^-$ salt formed immediately on addition of α-bromoisobutyryl bromide. The reaction was left for 24 hours and the precipitate was removed by filtration, followed by solvent removal *in vacuo* and precipitation of the resulting crude product twice from acetone into petroleum ether (30 – 40 ^oC) to give the purified product. A yellow oil was isolated and the purified product was fully characterised by NMR (^1H and ^{13}C), shown in Figure 3.3 and elemental analysis, see Experimental 7.4.2, all of which were in agreement with the desired product.

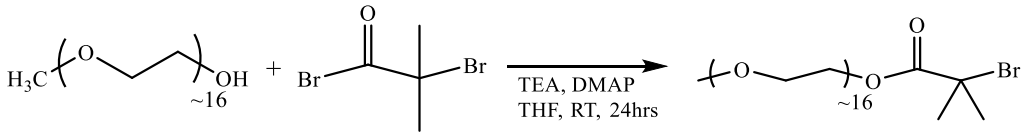

Scheme 3.1 Synthesis of poly(ethylene glycol) methyl ether 2-bromoisobutyrate initiator (PBiB).

The chain-length of the PEG initiator after purification was confirmed by ^1H NMR *via* integration of the multiplet peak at 3.6 ppm assigned to (-O-C$\underline{H}_2$C$\underline{H}_2$-), and the singlet at approximately 3.3 ppm corresponding to the monomethoxy chain end; as shown in the structure assignment, Figure 3.3 A, the number of repeat units in the purified initiator was able to be determined as n = 15. Confirmation of this determination is also possible through analysis of the protons g (Figure 3.3A) which also leads to a calculation of 15 repeat units within the final macroinitiator. The ^{13}C NMR confirmed the structure and the lack of impurities within the sample (Figure 3.3B).

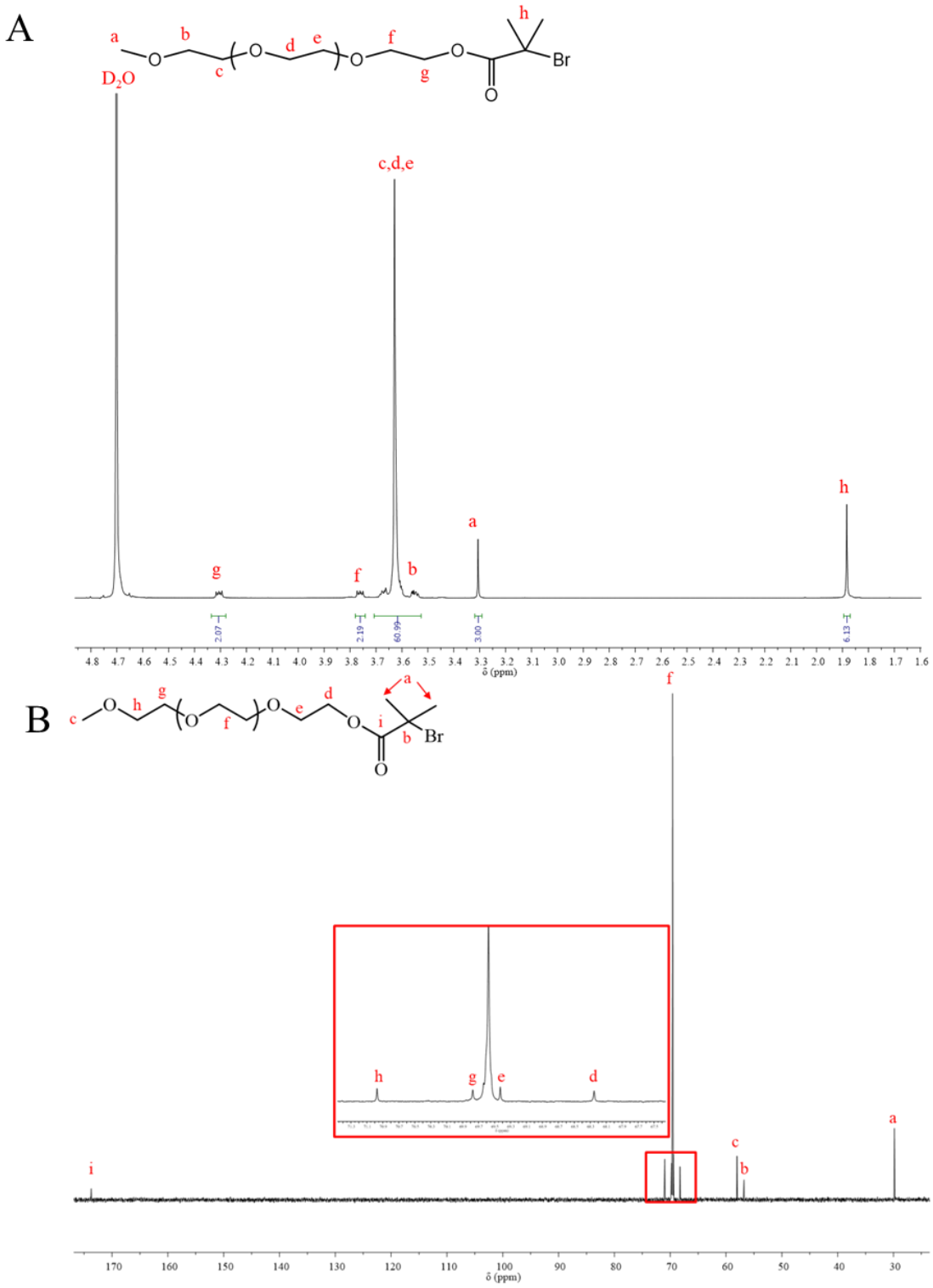

Figure 3.3 NMR spectra of purified PBiB A) ^{1}H NMR spectrum (D_2O, 400 MHz) and B) ^{13}C NMR spectrum (D_2O, 100 MHz).

3.2.2 Synthesis and Characterisation of Linear and Branched Copolymers

3.2.2.1 Kinetic Evaluation of PBiB Initiated and Co-Initiated ATRP of OEGMA-derived linear polymers

The synthesis of linear polymers initiated by PBiB or a mixture of DBiB:PBiB in a 1:1 ratio was investigated to determine whether the polymerisations followed first order kinetics with respect to the monomer concentration and whether significant differences in initiator efficiency would potentially prevent accurate incorporation into the targeted co-initiated branched copolymers.

ATRP was used to synthesise linear polymers of the commercially available hydrophilic monomer, OEGMA, (DP_n = 4-5 ethylene glycol units, M_n = 300 g/mol) using a 1:2 ratio of CuCl:bpy (with respect to [I]) catalytic system and targeting DP_n = 50; a mixed IPA/water (92.5/7.5 v/v) solvent was used and polymerisations were conducted at 55 % w/v (monomer:solvent) and 40 °C. The development of M_n compared to monomer conversion was evaluated by triple-detection GPC and OEGMA conversion was monitored by ^{1}H NMR spectroscopy; the decreasing vinyl peaks at 6.13 and 5.58 ppm were compared to the C$\underline{H}_3$-O- chain end of the OEGMA pendant chain at 3.4 ppm to determine conversion, as shown in Figure 3.4A. Linear polymerisations were sampled every hour for 7 hours for polymerisations either initiated by PBiB (forming PBiB-*p*($OEGMA_{50}$)) or co-initiated using a 50:50 DBiB:PBiB molar ratio (forming a 1:1 mixture of DBiB-*p*($OEGMA_{50}$) and PBiB-*p*($OEGMA_{50}$)) in the reaction. As observed by ^{1}H NMR, Figure 3.4 A, the OEGMA monomer was completely consumed within 6 hrs for the formation of PBiB-*p*($OEGMA_{50}$) and within 5 hours for the simultaneous formation of DBiB-p($OEGMA_{50}$) and PBiB-*p*($OEGMA_{50}$)), Figure 3.4 B. The slightly faster reaction suggests a small difference in initiation rate for the two initiators but full conversion of monomer suggests that this may not present a significant problem in the formation of branched copolymers by co-initiation which will combine the resulting polymers into mixed copolymer structures.

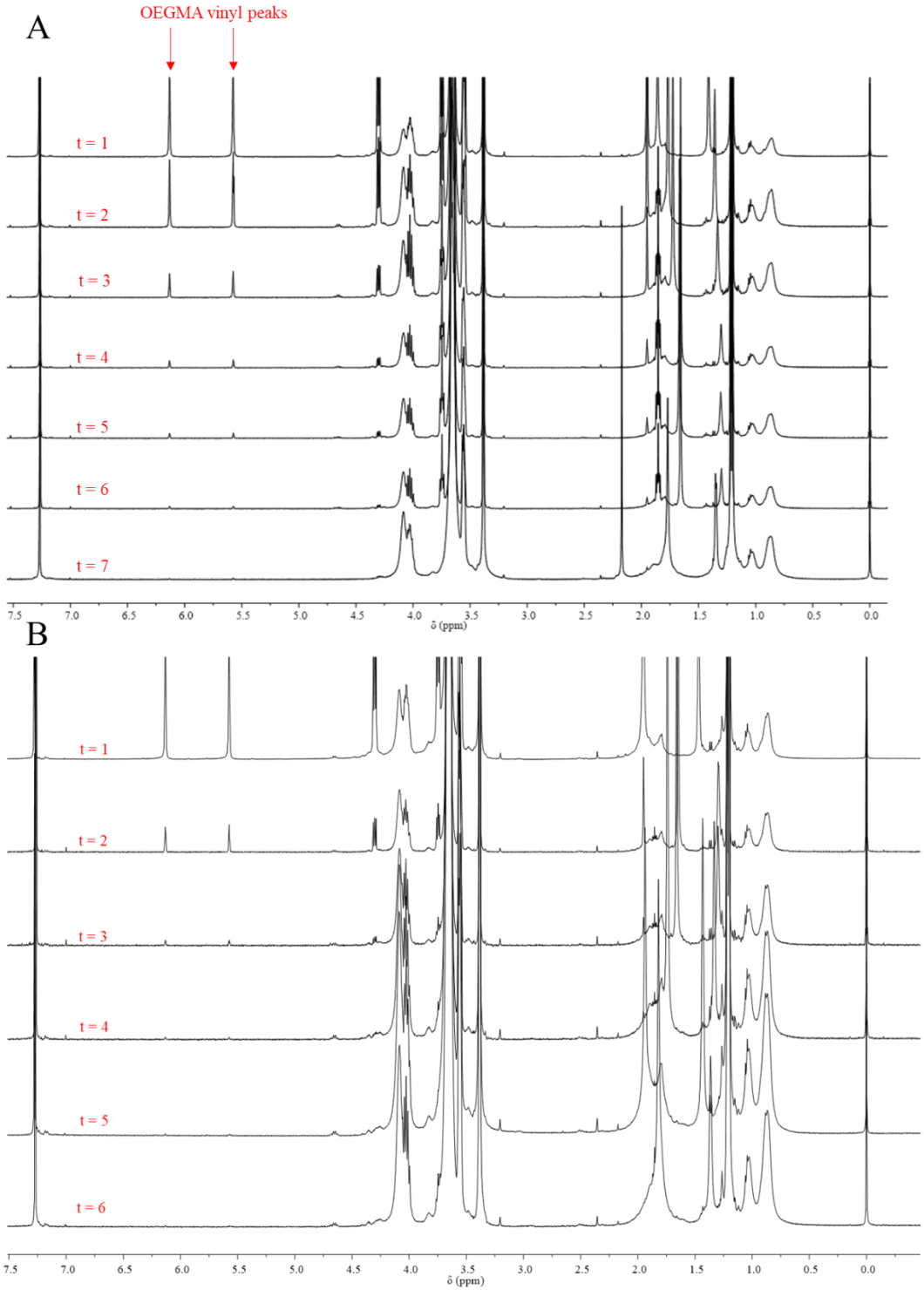

Figure 3.4 ^{1}H NMR spectra ($CDCl_3$, 400 MHz) for the ATRP synthesis of A) PBiB-*p*(OEGMA$_{50}$) and B) DBiB-*p*(OEGMA$_{50}$) and PBiB-*p*(OEGMA$_{50}$) using a co-initiated simultaneous polymerisation using a 50:50 DBiB:PBiB molar ratio. The loss of monomer OEGMA vinyl peaks at 6.13 and 5.58 ppm was monitored for 6-7 hours and reactions conducted in an IPA/water (92.5/7.5 v/v) mixed solvent at 55 % w/v (monomer:solvent) and 40 °C

The kinetics of the different polymerisations was studied to confirm the similarities of the two polymerisations, Figure 3.5. This analysis confirms high conversion was reached between 4 – 7 hours within each reaction and that the linear polymerisations followed first order kinetics as shown by semi-logarithmic plot obtained, whether using one or a mixture of two initiators; this provides confidence for the co-initiated copolymerisation of OEGMA to form the branched copolymers with varying chain end compositions described in Figure 3.2.

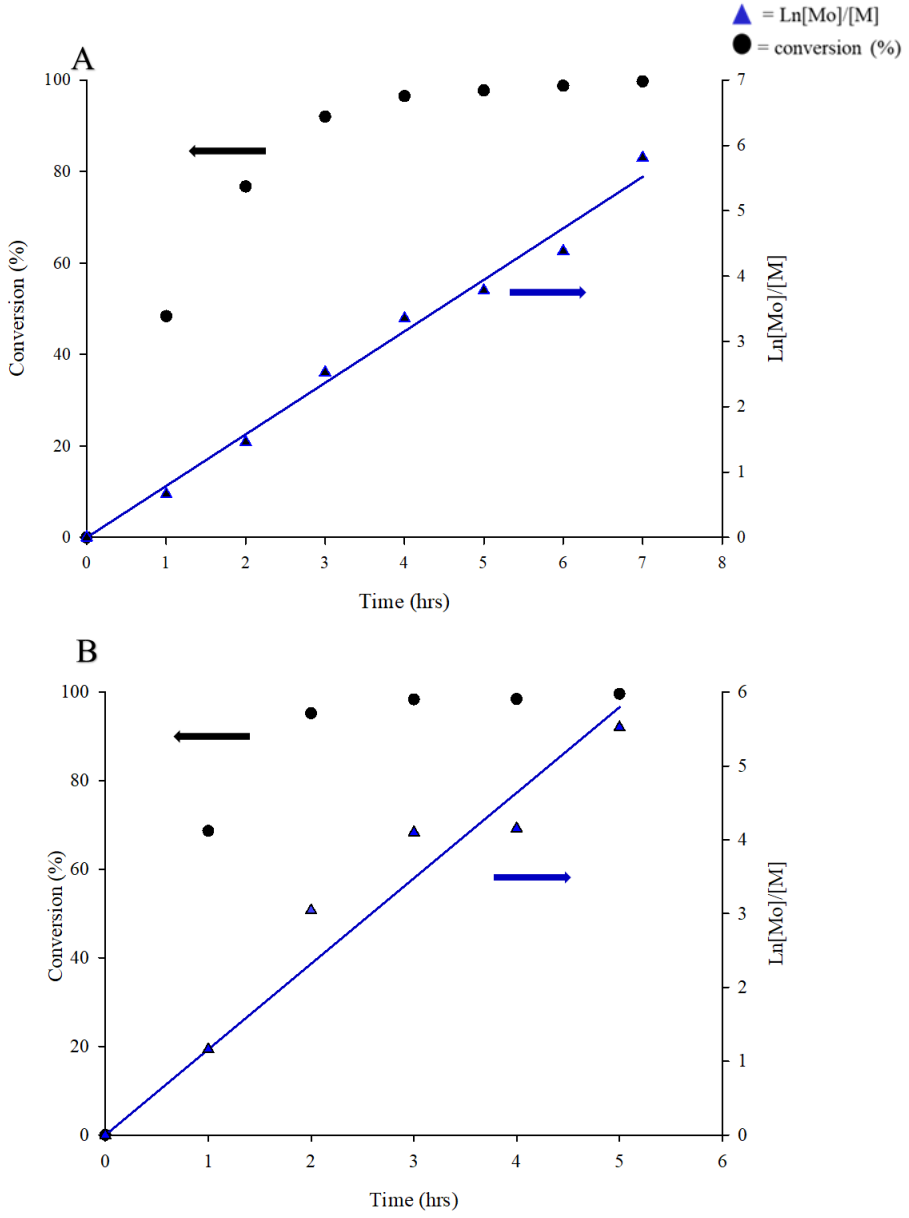

Figure 3.5 Kinetic studies for the linear polymerisation of A) PBiB-*p*(OEGMA$_{50}$) and B) simultaneous formation of DBiB-*p*(OEGMA$_{50}$) and PBiB-*p*(OEGMA$_{50}$) determined by ^{1}H NMR, sampled every hour for 6 - 7 hours.

3.2.2.2 Branched Copolymer Synthesis

As shown in Chapter 2, Section 2.2.2, addition of the divinyl monomer EGDMA to a linear ATRP forms branched copolymers; an $[EGDMA]_0/ [I]_0$ ratio of 0.8:1 was therefore incorporated into the polymerisations described in Section 3.2.2.1 to yield branched copolymers after an extended reaction time of 24 hrs, see Scheme 3.2. All polymerisations were monitored using ^{1}H NMR spectroscopy (Appendix A5) to allow analysis of vinyl functionality conversion relative to an internal standard, anisole, and all reactions achieved > 99 % conversion. Removal of copper was performed *via* a neutral alumina column and all polymers were purified by precipitation into cold petroleum ether (40/60).

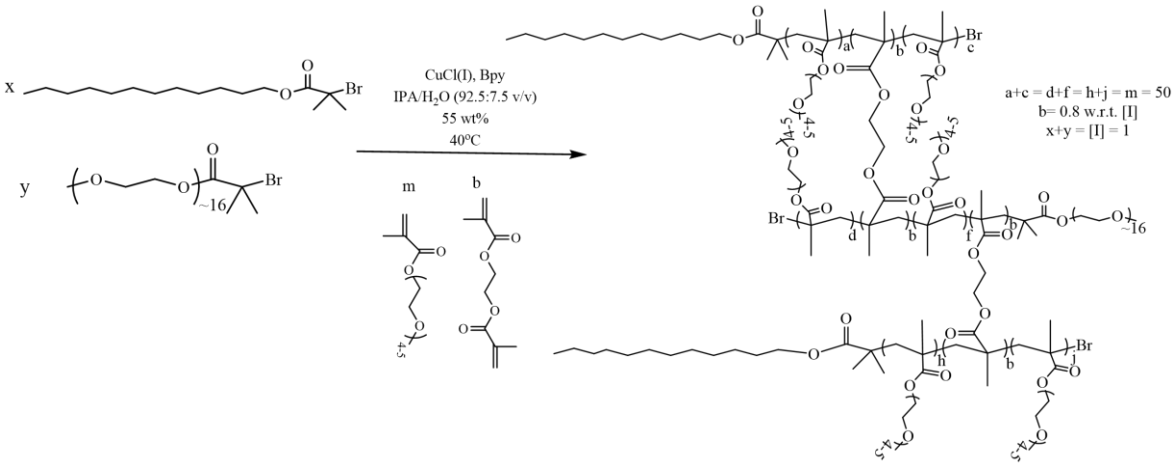

Scheme 3.2 Co-initiated branched polymerisation of OEGMA and EGDMA with varying ratios of DBiB(x):PBiB(y). The idealised structure of the branched copolymer shows three conjoined chains, however larger numbers of chains are incorporated in the disperse copolymer sample.

In this series of co-initiated copolymerisations, the DBiB:PBiB molar ratio was varied systematically from 1:0 through to 0:1, so the final polymer composition can be generally described as $DBiB_xPBiB_y$-*p(*$OEGMA_{50}$-*co*-$EGDMA_{0.8}$) where x + y = 1, see Figure 3.6.

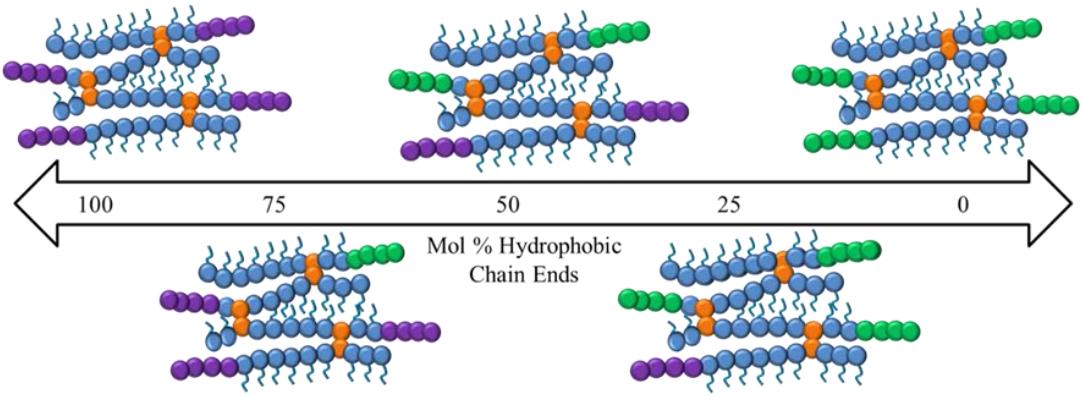

Figure 3.6 Cartoon representation (showing 4 conjoined chains) of the systematic change of DBiB:PBiB chain ends derived from varying initiator mole ratios leading to varied hydrophobic/hydrophilic chain end compositions.

The hydrophilic monomer OEGMA was polymerised with DBiB:PBiB in ratios of 0.9:0.1, 0.75:0.25, 0.5:0.5, 0.25:0.75 and 0.1:0.9, to give a wide range of chain end functionality within this library of copolymers. The branched and linear homopolymers of OEGMA using the single initiators DBiB or PBiB were also synthesised as comparators.

3.2.2.3 Linear Polymer and Branched Copolymer Characterisation

All polymers and copolymers were characterised by GPC and ^{1}H NMR; the data are presented below in Table 3.1 with data from Chapter 2 of DBiB-*p(*OEGMA$_{50}$) and DBiB-*p(*OEGMA$_{50}$-*co*-EGDMA$_{0.8}$) included for ease of comparison with copolymers synthesised using mixed initiation.

Table 3.1 ^{1}H NMR and GPC data for linear and branched *p(*OEGMA).

Target Polymer Composition	^{1}H NMR[b]		GPC[a]		
	Conversion (%)	Theoretical M_n	M_w (g/mol)	M_n (g/mol)	Đ (M_w/M_n)
DBiB-*p(*$OEGMA_{50}$)	99	15 353	39 760	30 750	1.20
PBiB-*p(*$OEGMA_{50}$)	98	15 750	70 350	38 000	1.85
DBiB-*p(*$OEGMA_{50}$-*co*-$EGDMA_{0.8}$)	>99	-	235 700	57 600	4.09
$DBiB_{0.90}PBiB_{0.10}$-*p(*$OEGMA_{50}$-*co*-$EGDMA_{0.8}$)	99	-	136 100	22 300	3.60
$DBiB_{0.75}PBiB_{0.25}$-*p(*$OEGMA_{50}$-*co*-$EGDMA_{0.8}$)	99	-	257 700	62 500	4.12
$DBiB_{0.50}PBiB_{0.50}$-*p(*$OEGMA_{50}$-*co*-$EGDMA_{0.8}$)	99	-	163 700	54 500	3.00
$DBiB_{0.25}PBiB_{0.75}$-*p(*$OEGMA_{50}$-*co*-$EGDMA_{0.8}$)	99	-	410 600	76 400	5.37
$DBiB_{0.10}PBiB_{0.90}$-*p(*$OEGMA_{50}$-*co*-$EGDMA_{0.8}$)	99	-	303 800	40 050	6.74
PBiB-*p(*$OEGMA_{50}$-*co*-$EGDMA_{0.8}$)	99	-	169 800	63 600	2.66

[a]Determined using GPC (DMF/0.01 M LiBr Eluent 60°C) [b]Determined using ^{1}H NMR ($CDCl_3$,400 MHz)

The addition of a 0.8 molar equivalent of EGDMA with respect to initiator groups, led to a dramatic increase in M_w and dispersities of all copolymers as characterised by double detection GPC (DMF). All polymers synthesised with a mixture of DBiB and PBiB initiators reached ≥ 99 % conversion, as determined by the loss of OEGMA vinyl peaks at 6.13 and 5.58 ppm in ^{1}H NMR spectrum, Appendix A5, which is known to be important to achieve intermolecular branching. As shown in Table 3.1, M_w values for co-initiated branched copolymers reached values up to 410,600 g/mol, representing a significant increase from the values obtained for DBiB-*p(*$OEGMA_{50}$) and PBiB-*p(*$OEGMA_{50}$) linear polymerisations. The variation in the M_w achieved across the different co polymers may reflect the slight variations in initiation, with the lowest

value obtained as 136,100 g/mol. GPC chromatograms for co-initiated polymers are shown in Figure 3.7, where all polymers show significant branching and presence of high M_w materials, as further confirmed by right angle light scattering (RALS) detection.

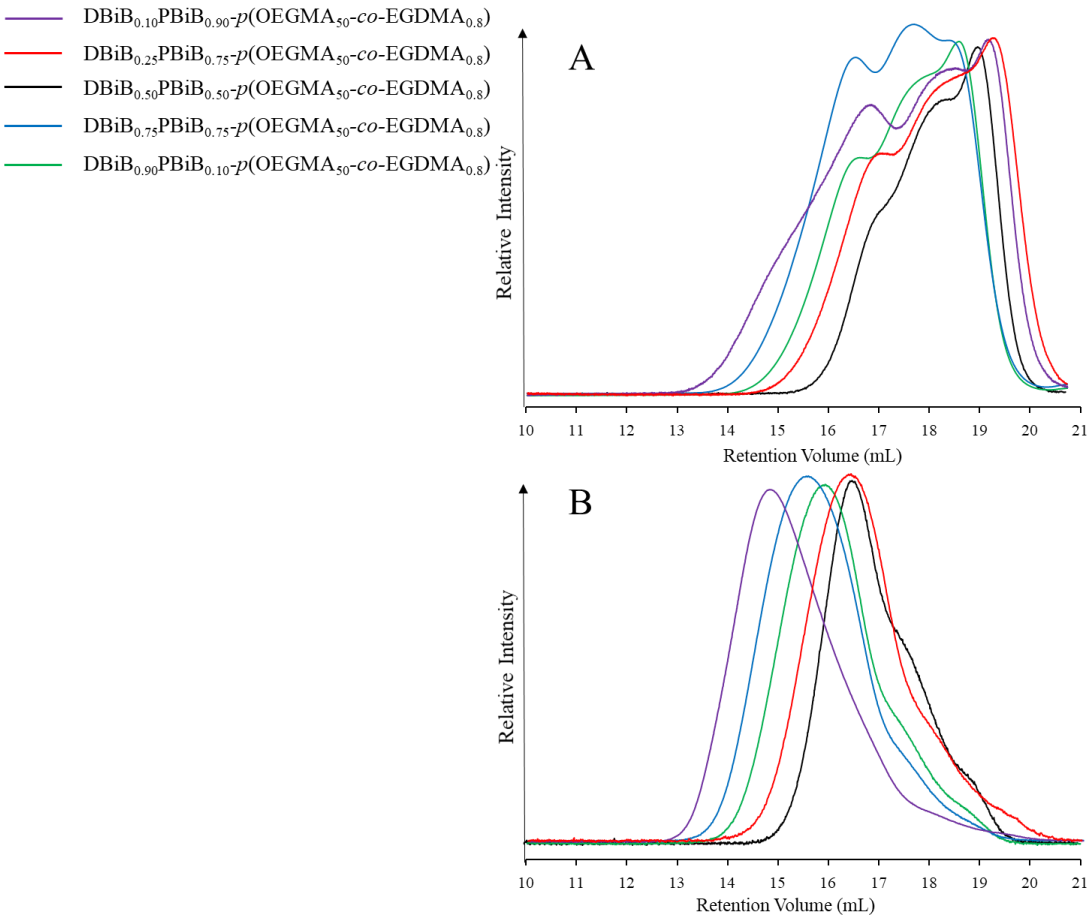

Figure 3.7 GPC (DMF/0.01 M LiBr Eluent 60 °C) chromatogram overlays of A) RI and B) RALS signals for *p*(OEGMA$_{50}$-*co*-EGDMA$_{0.8}$) with varying ratios of DBiB:PBiB chain ends; DBiB$_{0.10}$PBiB$_{0.90}$ (purple) DBiB$_{0.25}$PBiB$_{0.75}$ (red), DBiB$_{0.50}$PBiB$_{0.50}$ (black), DBiB$_{0.75}$PBiB$_{0.25}$ (blue) or DBiB$_{0.90}$PBiB$_{0.10}$ (green).

Comparison of GPC analysis of linear analogue polymers (using single initiation) with branched materials synthesised in the presence of EGDMA also clearly shows the formation of a broader molecular weight distribution, which is typical for branched copolymers, Figure 3.8. The statistical nature of the branching process means there are both linear chains and branched copolymers of varying composition within the final product, with the RALS trace clearly indicating the presence of higher M_w

material in the branched copolymer. The RI analysis of the linear polymer PBiB-*p*(OEGMA$_{50}$), Figure 3.8 A, shows the presence of a shoulder at higher molecular weight for this linear polymer. This is assigned as products from termination by dissociation; a known issue with methacrylate polymers. Such a termination process will form reactive macromonomers that may be incorporated into other, non-terminated chains when reactions are left at high conversion for extended periods. This also results in a higher dispersity value of 1.85, in comparison to DBiB-*p*(OEGMA$_{50}$) of 1.2. This is further confirmed by an observed M_n obtained *via* GPC analysis of 38,000 g/mol which is approximately double the theoretical targeted value, Table 3.1.

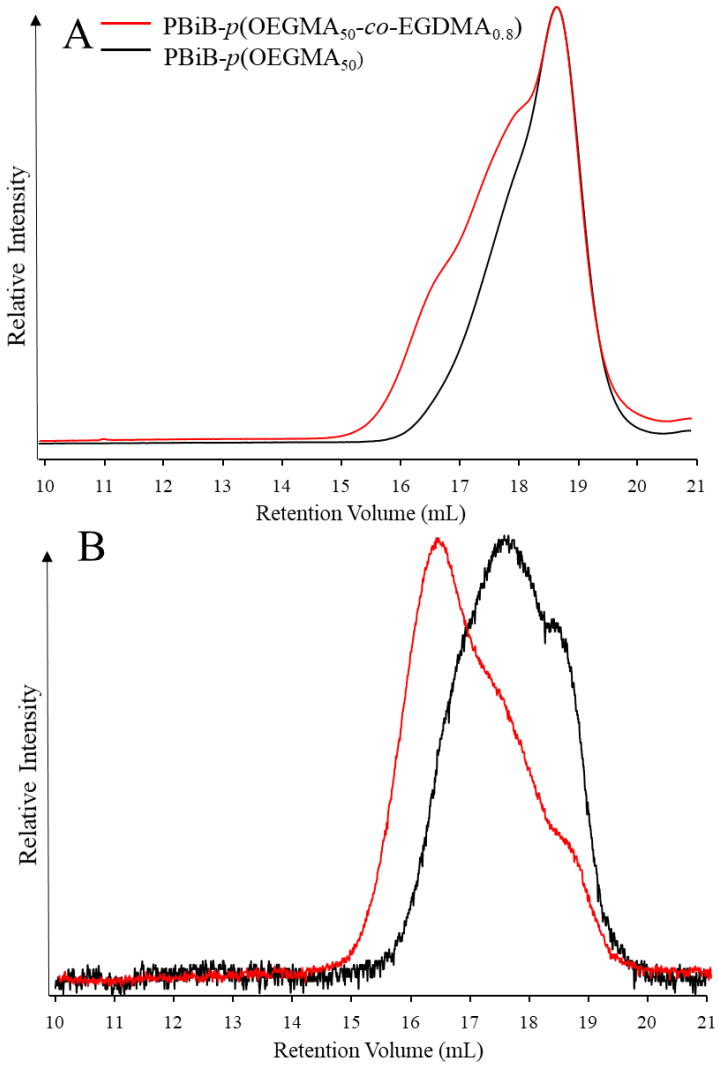

Figure 3.8 GPC (DMF/0.01 M LiBr Eluent 60 °C) chromatogram overlays of A) RI and B) RALS signals for linear PBiB-*p*(OEGMA$_{50}$) (black) and branched equivalent PBiB-*p*(OEGMA$_{50}$-*co*-EGDMA$_{0.8}$) (red).

As mentioned earlier, the co-initiated branched copolymers have considerable variation in architecture, composition and molecular weight. This is derived from the statistical branching between polymer chains that are simultaneously synthesised using DBiB and PBiB initiators in varying ratios. The final branched copolymers will possess statistical variation in molecular weight within the primary chains, number of conjoined chains, ratio of hydrophilic and hydrophobic chain ends and branching density. To investigate the implications of the wide diversity of materials produced, the GPC data was analysed to determine the cumulative weight fraction *vs* molecular weight relationship to provide an indication of what weight fraction of each sample contained highly branched structures, Figure 3.9.

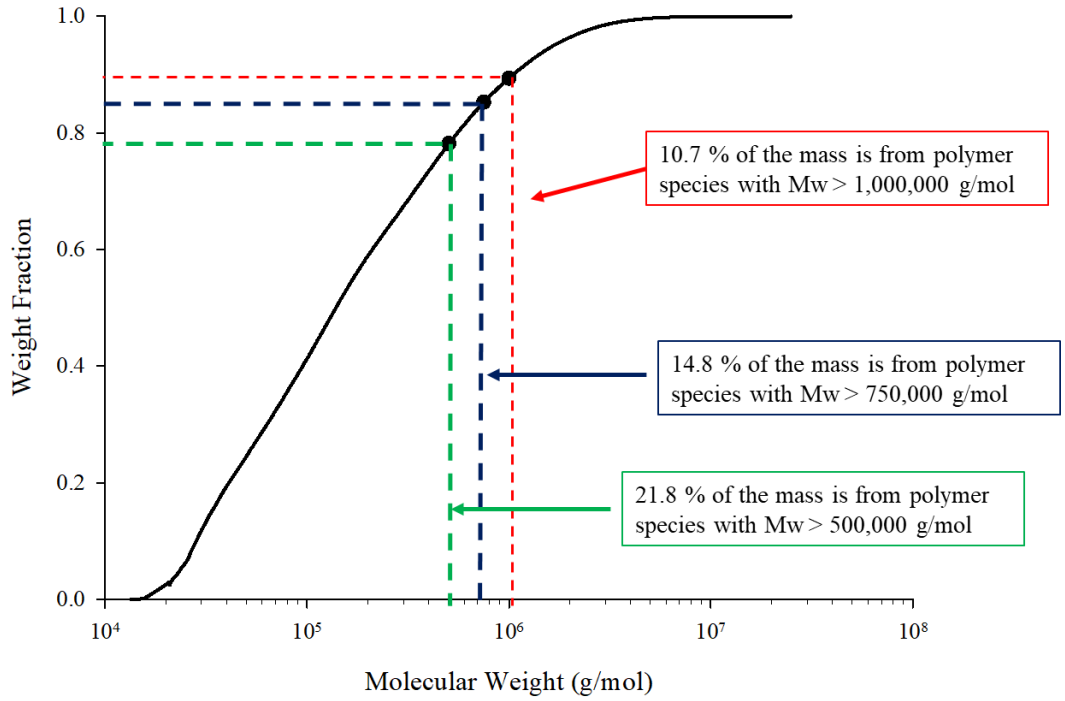

Figure 3.9 Cumulative weight fraction analysis of branched copolymer $DBiB_{0.25}PBiB_{0.75}$-*p*($OEGMA_{50}$-*co*-$EGDMA_{0.8}$) highlighting the percentage of the mass from polymer species with M_w > 500,000 (green), 750,000 (blue) and 1,000,000 (red) g/mol derived from GPC analysis (DMF/0.01 M LiBr Eluent 60 °C).

Three arbitrary molecular weights 500,000, 750,000 and 1,000,000 g/mol were chosen to establish the physical mass of each polymer sample that is present with molecular weights above these values, see Table 3.2. In principle, these molecular weight values represent structures that have approximately 15, 22 and 29 conjoined primary chains

respectively, assuming an average M_n of the primary chains is 34,375 g/mol which is the average of the linear polymer M_n values for the $p(OEGMA)_{50}$ linear polymer samples created by single initiation using DBiB or PBiB (Table 3.1). The presence of branched copolymers containing large numbers of chain ends is key to the sample exhibiting the surface active behaviour observed and discussed in Chapter 2, Section 2.4 and 2.5.

Table 3.2 Weight fraction of $DBiB_xPBiB_y$-*p(*$OEGMA_{50}$-*co*-$EGDMA_{0.8}$) branched copolymers with molecular weights greater than 500,000, 750,000 and 1,000,000 g/mol.

Polymer Composition	Wt% >500,000 g/mol	Wt% >750,000 g/mol	Wt% >1,000,000 g/mol
DBiB-*p(*$OEGMA_{50}$-*co*-$EGDMA_{0.8}$)	11.2	2.47	2.8
$DBiB_{0.90}PBiB_{0.10}$-*p(*$OEGMA_{50}$-*co*-$EGDMA_{0.8}$)	14.2	8.5	5.4
$DBiB_{0.75}PBiB_{0.25}$-*p(*$OEGMA_{50}$-*co*-$EGDMA_{0.8}$)	15.6	9.1	5.9
$DBiB_{0.50}PBiB_{0.50}$-*p(*$OEGMA_{50}$-*co*-$EGDMA_{0.8}$)	5.9	2.19	0.9
$DBiB_{0.25}PBiB_{0.75}$-*p(*$OEGMA_{50}$-*co*-$EGDMA_{0.8}$)	21.8	14.8	10.7
$DBiB_{0.10}PBiB_{0.90}$-*p(*$OEGMA_{50}$-*co*-$EGDMA_{0.8}$)	33.7	27.19	2.3
PBiB-*p(*$OEGMA_{50}$-*co*-$EGDMA_{0.8}$)	6.4	2.9	1.4

As a general trend, an increasing PBiB:DBiB ratio (up to 0.9:0.1) within the co-initiated polymerisations appears to lead to an increasing weight fraction of higher molecular weight structures (> 500,000 g/mol; 15 conjoined chains) within the samples, Figure 3.10. Interestingly $DBiB_{0.25}PBiB_{0.75}$-*p(*$OEGMA_{50}$-*co*-$EGDMA_{0.8}$) has the highest weight fraction of branched copolymers with a weight fraction of species with a molecular weight >1,000,000 g/mol (>29 primary chains) at nearly 11 wt %.

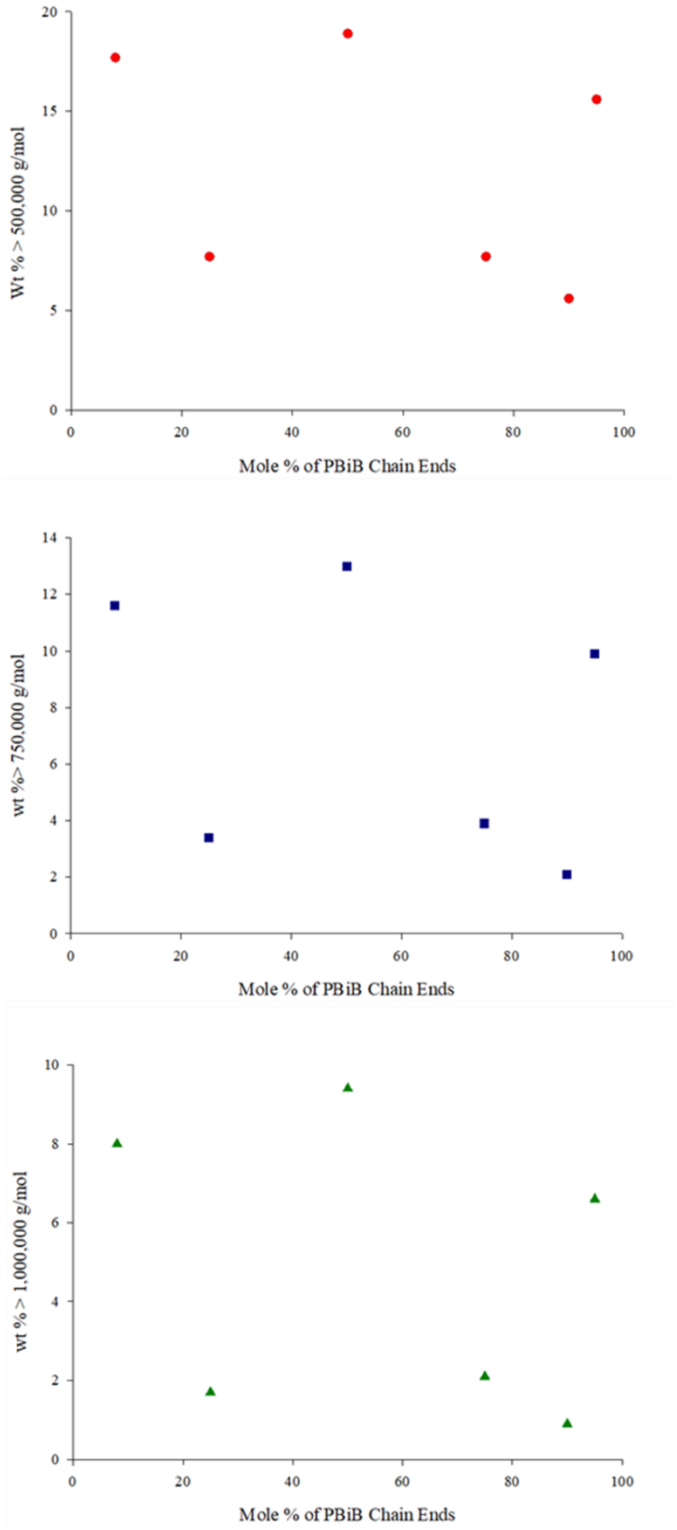

Figure 3.10 Weight fraction of co-initiated $DBiB_xPBiB_y$-*p*($OEGMA_{50}$-*co*-$EGDMA_{0.8}$) branched copolymers with molecular weights greater than A) 500,000, B) 750,000 and C) 1,000,000 g/mol, plotted against molar percent of PBiB initiator used in the co-initiated copolymerisation.

Overall, all branched copolymers produced contain species comprising significant weight fractions of branched copolymers with molecular weights >500,000 g/mol (>15 primary chains) within the complex distribution of structures formed, therefore even at co-initiation ratios of 0.9:0.1, a mixture of both chain ends would be expected in these high molecular weight structures.

3.2.2.4 Cloud Point Studies

Polymers that contain significant amounts of ethylene oxide repeat units are known to have lower critical solution behaviour which manifests itself as a temperature limit (the LCST) where uniform, single-phase molecular solutions can be maintained.[126,127] LCST behaviour is understood as being entropically driven, with the considerable release of bound water molecules solvating the polymer chains leading to a large increase in global entropy, outweighing the loss of entropy during collapse of the solvated polymer chains; in many reports, the solvated polymer chains are described as "becoming hydrophobic" at the LCST. Due to the use of OEGMA as monomer and PEG as a co-initiator, both of which contain ethylene oxide repeat units, cloud point studies were undertaken to assess the behaviour of aqueous branched copolymer solutions. Aqueous copolymer solutions were prepared at a 1 wt % concentration and heated through three cycles using an oil bath until the cloud point was determined, i.e. when the transparent solution turned opaque, indicating precipitation of the dissolved macromolecules. The change in polymer composition showed little impact on aqueous solubility as all branched copolymers were readily water-soluble. However, a meaningful decrease in lower critical solution temperatures (LCST) of 6 °C between the linear polymers PBiB-*p(*OEGMA) and DBiB-*p(*$OEGMA_{50}$) was observed as may be expected from increasing hydrophobicity in the polymer architecture derived from the chain end, Figure 3.11.

The inclusion of the divinyl monomer EGDMA to yield branched copolymers led to a decrease in LCST by 3.6 °C even from PBiB-*p(*OEGMA) to PBiB-*p(*$OEGMA_{50}$-*co*-$EGDMA_{0.8}$); further decreases were observed after the inclusion of hydrophobic chain ends from the co-initiation and formation of $DBiB_{0.25}PBiB_{0.75}$-*p(*$OEGMA_{50}$-*co*-$EGDMA_{0.8}$) (decrease of 2.0 °C compared to PBiB-*p(*$OEGMA_{50}$-*co*-$EGDMA_{0.8}$).

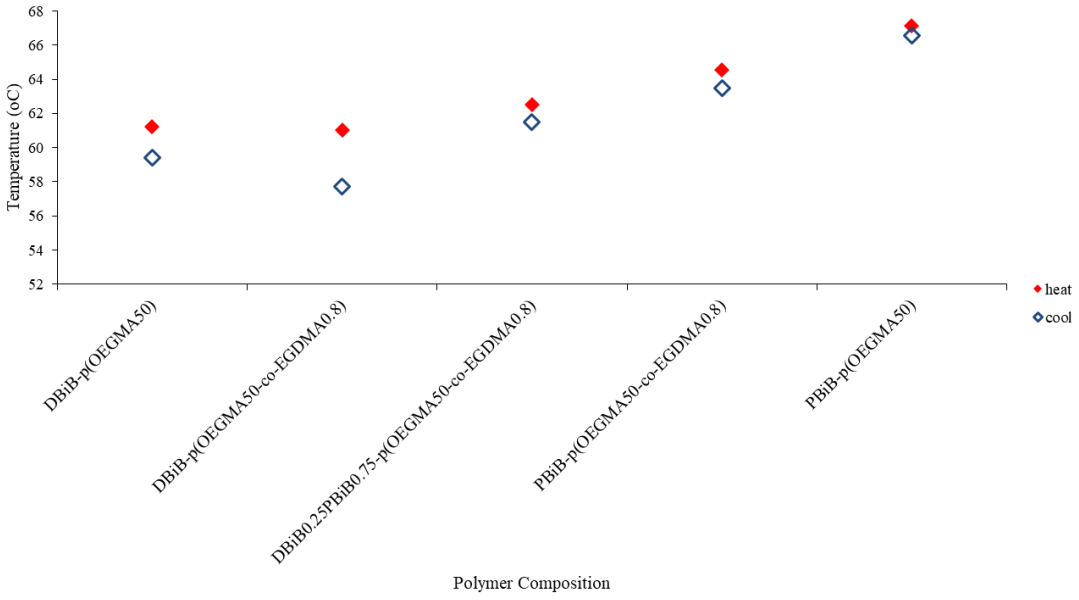

Figure 3.11 Cloud point studies of DBiB-*p*(OEGMA$_{50}$), DBiB-*p*(OEGMA$_{50}$ -*co*-EGDMA$_{0.8}$), DBiB$_{0.25}$PBiB$_{0.75}$-*p*(OEGMA$_{50}$-*co*-EGDMA$_{0.8}$), PBiB-*p*(OEGMA$_{50}$-*co*-EGDMA$_{0.8}$) and PBiB-*p*(OEGMA$_{50}$).

3.2.3 Contact Angle of Liquid on Hydrophobic Surface Determined by Young's Equation

The water contact angle is the angle measured at the point where the liquid-vapour interface of a water droplet meets a solid surface. This allows for application of Young's equation,[128] Equation 3.1, which quantifies the wettability of a solid surface by a liquid, where the contact angle is derived from the thermodynamic equilibrium between the three phases. Young's equation takes into consideration the tension between the liquid-vapour (γ_{LV}), solid-vapour (γ_{SV}) and solid-liquid (γ_{SL}) interfaces, Figure 3.12.

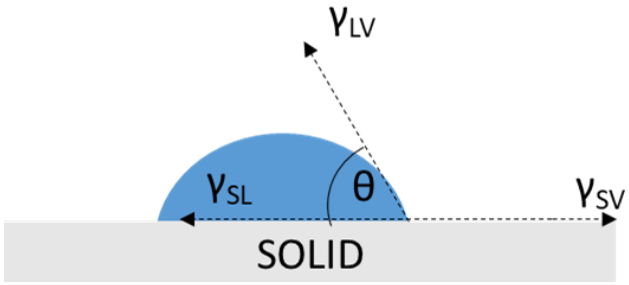

Figure 3.12 Contact angle (Θ), of a droplet on a solid surface with interfacial tensions of solid-vapour = γ_{SV}, solid-liquid = γ_{SG} and liquid-gas = γ_{LV}.[129]

If the contact angle is above 90 º then the surface is deemed hydrophobic, with contact angles above 150 º corresponding to a super hydrophobic surface, while an angle of less than 90 º characterises the surface as hydrophilic, Figure 3.12.[129] If a surfactant is added to the aqueous liquid and progressively increased, the contact angle should decrease due to a lessening of surface tension at the liquid-solid interface.

$$\gamma_{lg}cos\theta = \gamma_{sv} - \gamma_{sl} \qquad (3.1)$$

The contact angle determines how well liquids interact with a solid surface, and the wettability of a surface can therefore be studied. If the contact angle is > 90 ° there is low wettability of the surface, and a contact angle of < 90 ° indicates good surface wetting. As shown in Figure 3.13, when a liquid comes into contact with a solid surface the lower contact angle means the fluid can spread over a large surface area. If the contact angle is high, and interaction is unfavourable the liquid will bead on the surface to minimise its contact with the surface.

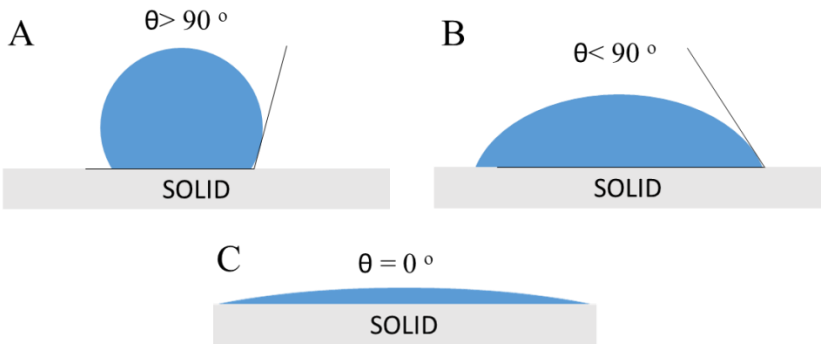

Figure 3.13 Varying contact angle of liquids on a hydrophobic surface, A) bad wetting, θ > 90 °, B) good wetting, θ < 90 ° and C) complete wetting θ = 0 °.

3.2.3.1 Contact Angle Measurement of Linear Polymers and Branched Copolymers

Throughout the aqueous contact angle studies employed here, a consistent hydrophobic solid surface (PTFE) was used and the aqueous droplet added to the surface varied in the dissolved branched copolymer, or linear polymer, that was solubilised into distilled water. The impact of the varying end-group composition of the branched copolymers was expected to be observed as a systematic change in measured aqueous contact angles through alterations of droplet-surface tension. Hypothetically, the *p(*OEGMA) chains that comprise the majority of the polymer and copolymer structures will be dissolved into the water and any hydrophobic areas, such

as the DBiB chain ends will be displayed at the air-water interface, enabling interactions with the hydrophobic surface and an increase in observed wetting (i.e. a decrease in contact angle). Variation in chain end composition with increasing DBiB or PBiB groups would lead to systematic changes in contact angles observed; a decrease indicating the presence of hydrophobic chains at the interface and an increase suggesting increasing hydrophilicity.

In all cases, aqueous polymer solutions of 5 wt % were used and droplets were analysed using a drop shape analyser (DSA), using a static sessile drop method. The sessile drop method is the standard method of contact angle measurement using drop shape analysis and static the angle is measured on a solid surface instead of a dynamic sessile drop, where the droplet size is either increased or decreased to measure the advancing and receding angle. The high aqueous polymer concentration of 5 wt % was selected as packing at the air/water interface, by the branched copolymer emulsifier, can be assumed. A hydrophobic polytetrafluoroethylene (PFTE) substrate in tape form was applied to a glass slide, and 5 µL droplets of polymer solution were applied and the contact angle measured (n = 10). Distilled water was applied to the PTFE substrate, which has been previously shown to have a contact angle between 108 – 110 °.[130–132] However, in a subsequent study it was shown that increasing the axial extension ratio of the tape, based on initial width and extended width of the tape, the contact angle of water can increase from 118 - 165 °.[133] The application and stretching of PTFE tape on the glass slide explained the measured contact angle for water of 125 ° ± 3.6 °.

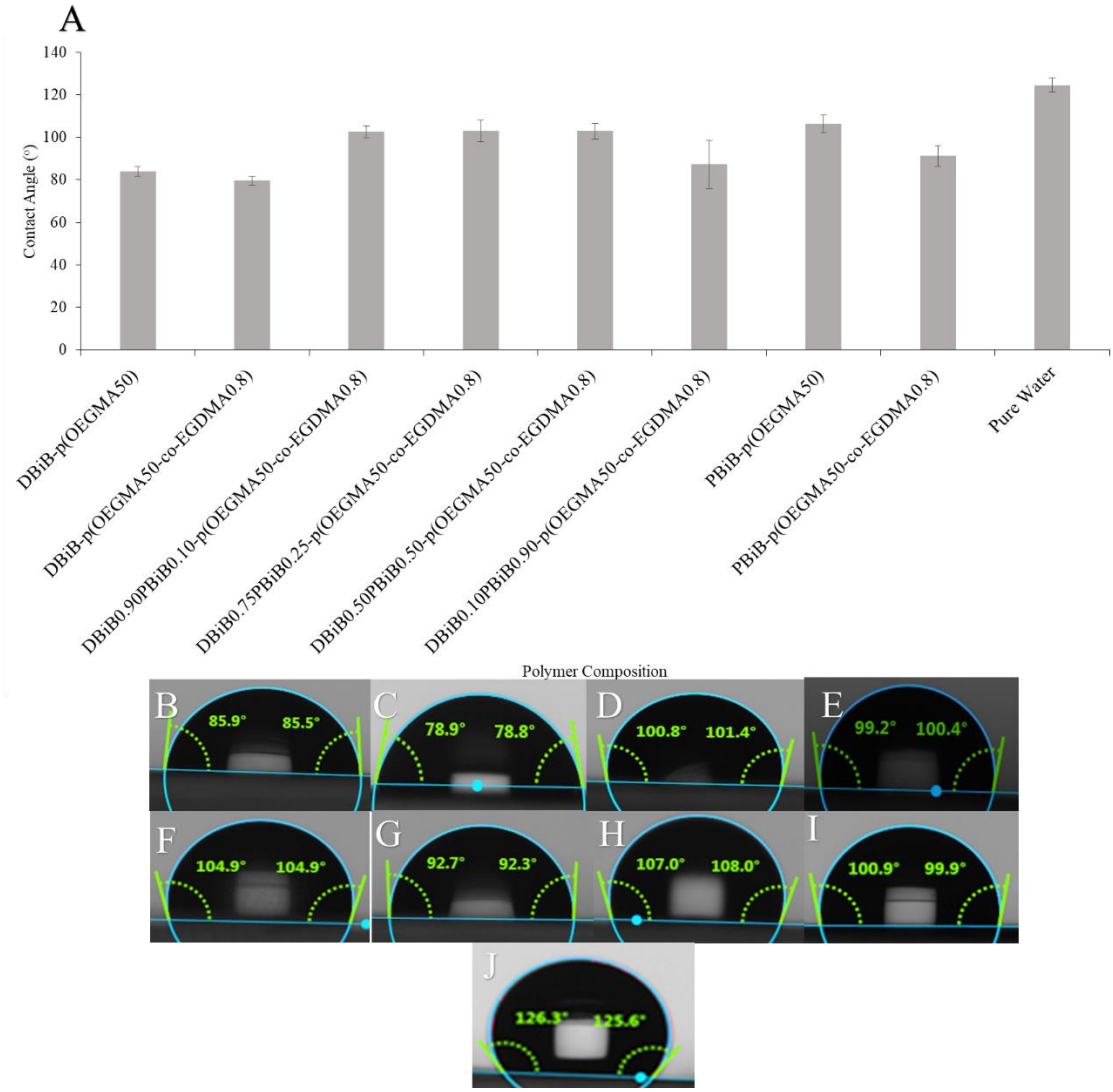

Figure 3.14 A) Contact angle measurements of aqueous polymer and branched copolymer solutions at 5 wt %, n = 10, error bars = standard deviation on a PTFE tape substrate. Microscopy images of droplet shapes; B) DBiB-*p(*$OEGMA_{50}$), C) DBiB-*p(*$OEGMA_{50}$-*co*-$EGDMA_{0.8}$), D) $DBiB_{0.90}PBiB_{0.10}$-*p(*$OEGMA_{50}$-*co*-$EGDMA_{0.8}$), E) $DBiB_{0.75}PBiB_{0.25}$-*p(*$OEGMA_{50}$-*co*-$EGDMA_{0.8}$), F) $DBiB_{0.50}PBiB_{0.50}$-*p(*$OEGMA_{50}$-*co*-$EGDMA_{0.8}$), G) $DBiB_{0.10}PBiB_{0.90}$-*p(*$OEGMA_{50}$-*co*-$EGDMA_{0.8}$), H) PBiB-*p(*$OEGMA_{50}$), I)PBiB-*p(*$OEGMA_{50}$-*co*-$EGDMA_{0.8}$) and J) pure water.

Contact angle measurements (with respect to pure water values of 125 ° ± 3.6 °), Figure 3.14 A, indicate that the inclusion of PBiB-*p(*$OEGMA_{50}$) lowered the contact angle to 106 ° ± 4.0 °. As this polymer structure contains no hydrophobic chain ends, this may suggest that the hydrophobic methacrylate backbone may align preferentially at the

air/water interface to minimise the interfacial tension and thereby result in a small decrease in the observed contact angle through slight spreading of the droplet on the PTFE surface. As this linear polymer is chemically near-identical to the branched copolymer PBiB-*p(*$OEGMA_{50}$-*co*-$EGDMA_{0.8}$) it is interesting to observe that the measured contact angles are similar (91 ° ± 4.9 °), although the presence of EGDMA in the structure and/or restriction of conformational rotation may also offer the potential for hydrophobic segments to align at the interface, resulting in the lower values than those seen using the linear PBiB-*p(*$OEGMA_{50}$).

Addition of the linear DBiB-*p(*$OEGMA_{50}$) polymer to the aqueous solution leads to a considerable decrease in the observed contact angle to values < 90 ° (84 ° ± 2.3 °) which is considered as good wetting; this suggests that the arrangement of the DBiB chain ends at the droplet surface does in fact lead to a considerable change in droplet surface tension. As seen previously for branched and linear structures derived from PBiB initiation, the formation of the chemically near-identical DBiB-*p(*$OEGMA_{50}$-*co*-$EGDMA_{0.8}$) led to similar measured contact angles although the branched copolymer again showed lower values of 80 ° ± 2.2 º. Inclusion of DBiB-*p(*$OEGMA_{50}$-*co*-$EGDMA_{0.8}$) into the aqueous solution displayed the lowest contact angles observed, suggesting that this branched copolymer is the most surface active of the library synthesised here, including the linear DBiB-*p(*$OEGMA_{50}$) and potentially explaining the high stability of the emulsions described in Chapter 2, Section 2.4.2.

Across the series of $DBiB_xPBiB_y$-*p(*$OEGMA_{50}$-*co*-$EGDMA_{0.8}$) branched copolymers of varying chain end composition, all branched copolymer solutions displayed a higher contact angle than DBiB-*p(*$OEGMA_{50}$-*co*-$EGDMA_{0.8}$), indicating a decrease in hydrophobicity (or an increase in surface tension); the branched copolymers from $DBiB_{0.90}PBiB_{0.10}$-*p(*$OEGMA_{50}$-*co*-$EGDMA_{0.8}$) through to $DBiB_{0.50}PBiB_{0.50}$-*p(*$OEGMA_{50}$-*co*-$EGDMA_{0.8}$) all exhibited a contact angle of 102 ° suggesting a reduced number of hydrophobic chain ends at the air-water interface compared to DBiB-*p(*$OEGMA_{50}$-*co*-$EGDMA_{0.8}$). Assuming packing of polymer structures at the interface at this copolymer concentration, it may also suggest that the interface may not be tightly packed with hydrophobic chain ends. Interestingly, the inclusion of the branched copolymer $DBiB_{0.10}PBiB_{0.90}$-*p(*$OEGMA_{50}$-*co*-$EGDMA_{0.8}$) into the aqueous solution resulted in a measured contact angle of 87 ° ± 11.4 ° which is (within error)

very similar to the value of the PBiB-*p(*$OEGMA_{50}$-*co*-$EGDMA_{0.8}$) (91 ° ± 4.9 °), and indicating that the low concentration of available DBiB chain ends are still able to modify the air-water interface tension over and above the presence of the EGDMA or hydrophobic methacrylate backbone – the large error in the measurements for this branched copolymer may also indicate the considerable diversity of chain end composition.

3.2.4 Theory and Determination of the Critical Micelle Concentration

The critical micelle concentration (CMC) is the concentration of surfactant in solution above which additional surfactant or co-surfactants will from micelles.[134] The CMC is a defining point in emulsion formation, as the interfacial tension changes rapidly up to this point with the addition of further surfactants. After the CMC is reached, interfacial tension between the two phases remains relatively stable with additional surfactant only increasing the concentration of micelles or oil droplets rather than further reducing the overall interfacial tension. Below the CMC, interfacial tension is linearly dependent on the surfactant concentration and above the CMC the interfacial tension is completely independent of the surfactant concentration.

As shown in Figure 3.15, upon addition of surfactant to water leads to alignment at the oil-water interface and a linear decline of surface tension until the interface becomes fully saturated. At this point addition of further surfactants does not affect the surface tension, but surfactants will self-assemble in the continuous phase to shield the hydrophobic chains. Following the CMC point, there is no correlation between surface tension and surfactant concentration, as the addition of further surfactants no longer has any effect on surface tension but instead increases the concentration of micelles. It is at this sharp break point of surface tension plotted against a logarithm of surfactant concentration, that CMC value can be determined.[135]

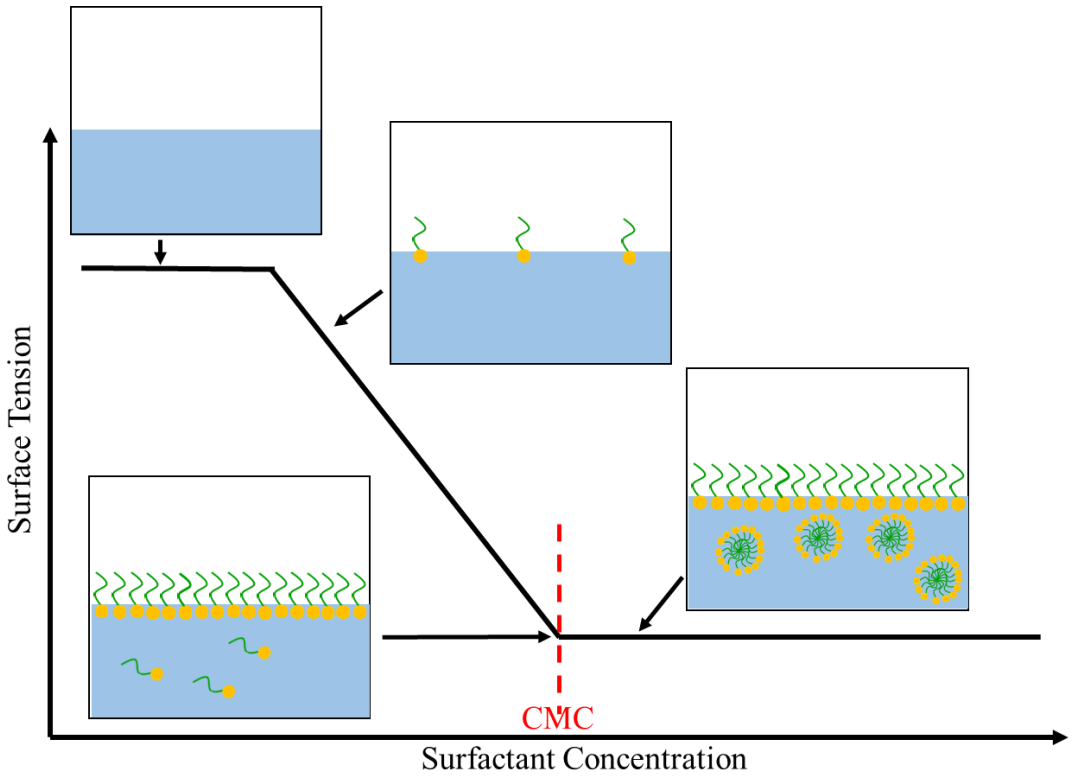

Figure 3.15 Schematic of an idealised CMC measurement representing the change in surface tension as surfactant concentration is increased, including micelle formation above the CMC and plateau at very low concentrations relating to the surface tension of water.

To increase the stability of an emulsion a co-surfactant can be included to further lower surface tension by aligning at the interface between the initial surfactant molecules, therefore resulting in a mixed surfactant monolayer.[136]

3.2.4.1 CMC Measurement of Branched Copolymers and Linear Polymers

Surface tension measurements were conducted on the range of polymers and branched copolymers synthesised here, using a Kibron Delta-8 surface tensiometer at 20°C, over a serial dilution series. Aqueous polymer solutions were initially prepared at 30 wt % and subsequent dilutions gave 30 different concentrations down to 6.9 x 10^{-9} wt %. Use of a 96 well-plate allowed for high throughput analysis of samples; 50 µL of each polymeric surfactant (n=8) was used per well and measured against pure water as a control. Following measurement, surface tension was plotted against a log concentration of surfactant. The CMC value was obtained by calculating the lines of best fit for the linear decrease in surface tension (slope) and the lower plateau area, and utilising the resulting y=mx+c equation of each section with rearrangement to

determine the intercept (x), Figure 3.16. To calculate graphical percentage error for CMC measurements, the minimum and maximum gradient was determined by plotting the minimum and maximum lines of best fit.

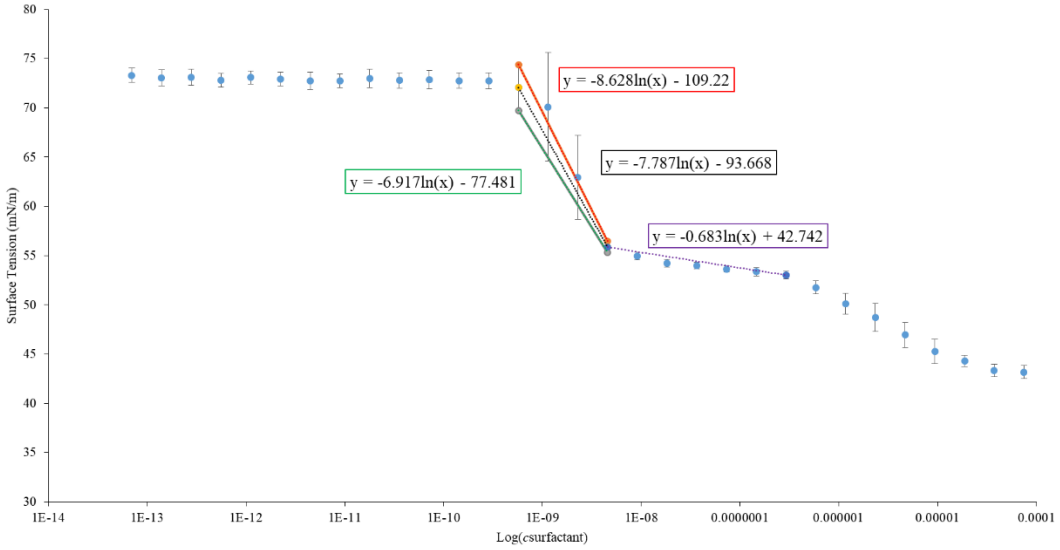

Figure 3.16 Example of CMC calculations by plotting the line of best fit for slope and lower plateau region with equations of the line shown for; best fit (black), maximum slope (red), minimum slope (green) and lower plateau (purple).

Surface tension measurements for branched copolymers and linear polymers are shown in Figure 3.17 and Figure 3.18. All surface tensiometer measurements observed the typical high plateau characteristic for very low concentrations of polymeric surfactant, with measurements of pure water at 73 mN/m. However, the traditional decrease in surface tension to the CMC did not lead to a steady plateau region as expected with a second decrease in surface tension observed in many cases. This suggests a complex surface tension behaviour with these materials that is most prevalent for branched copolymers with varied chain end composition, Figure 3.17, but is also seen to a lesser extent in the measurements of linear and branched copolymers containing single chain end chemistry, Figure 3.18.

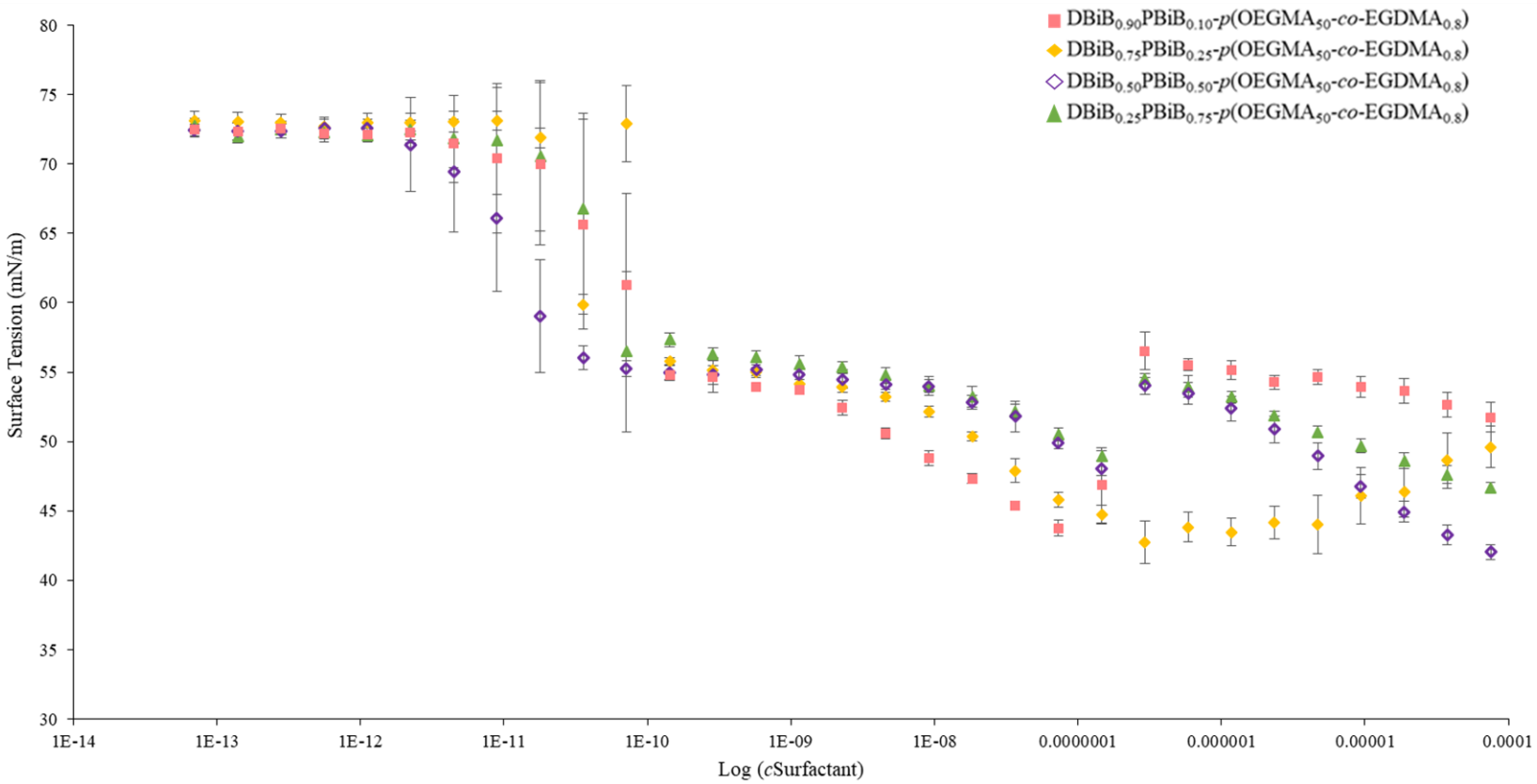

Figure 3.17 CMC data for aqueous branched copolymer solutions over a concentration gradient; $DBiB_{0.90}PBiB_{0.10}$-*p*($OEGMA_{50}$-*co*-$EGDMA_{0.8}$) (■),$DBiB_{0.75}PBiB_{0.25}$-*p*($OEGMA_{50}$-*co*-$EGDMA_{0.8}$) (◆),$DBiB_{0.50}PBiB_{0..50}$-*p*($OEGMA_{50}$-*co*-$EGDMA_{0.8}$) (◇), and $DBiB_{0.25}PBiB_{0.75}$-*p*($OEGMA_{50}$-*co*-$EGDMA_{0.8}$) (▲). n=8, error bars = standard deviation.

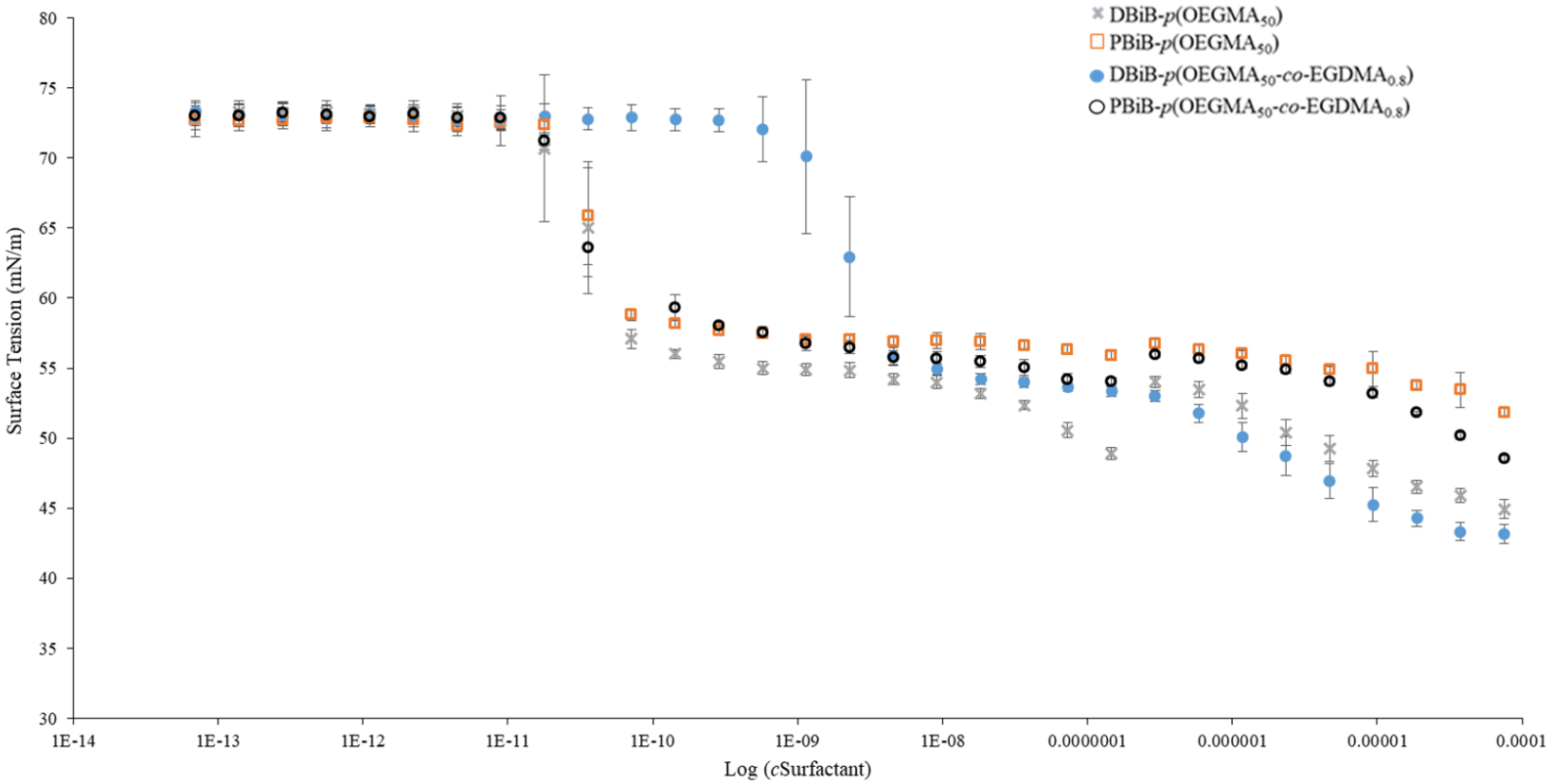

Figure 3.18 CMC data for aqueous linear polymers and branched copolymer solutions; DBiB-*p*(OEGMA$_{50}$) (✖), PBiB-*p*(OEGMA$_{50}$) (□), DBiB-*p*(OEGMA$_{50}$-*co*-EGDMA$_{0.8}$) (●), and PBiB-*p*(OEGMA$_{50}$-*co*-EGDMA$_{0.8}$) (○), over a concentration gradient. n=8, error bars = standard deviation.

This complex behaviour is analogous to mixed non-ionic surfactant solutions where two time-dependent events occur, causing a dynamic surface tension curve that describes assembly at the interface of one surfactant followed by disruption of the interface and closer packing as co-assembly of the second surfactant occurs, leading to a further decrease in surface tension. Within the branched copolymers, the presence of linear, lightly branched structures and highly branched structures is analogous to a complex multi-surfactant mixture; where chain end composition also varies, a further complexity to the mixture is introduced. Presumably, the linear amphiphilic fraction of the distributions are able to pack most efficiently at the interface (as seen for linear DBiB-*p(*$OEGMA_{50}$) in Figure 3.18) and subsequent rearrangement with the more highly branched structures creates the optimised lower surface tension values. In these measurements, the first plateau will be described as the initial CMC value as it is not representative of the lowest surface tension measurement, while this minimum measured value will be described as ST_{min}, Table 3.3.

Table 3.3 CMC and ST_{min} values determined for polymers and branched copolymers using a Kibron Delta-8 at 20 ^{o}C. Values are expressed as mg/L and errors are expressed as a graphical percentage error.

Polymer	Initial CMC (mg/L)	ST_{min} (mg/L)
DBiB-*p(*$OEGMA_{50}$)	4.72×10^{-8} (± 8 %)	9.30×10^{-3}
PBiB-*p(*$OEGMA_{50}$)	7.4×10^{-8} (± 2 %)	9.30×10^{-3}
DBiB-*p(*$OEGMA_{50}$-*co*-$EGDMA_{0.8}$)	2.36×10^{-6} (±10 %)	7.5×10^{-2}
$DBiB_{0.90}PBiB_{0.10}$-*p(*$OEGMA_{50}$-*co*-$EGDMA_{0.8}$)	2.79×10^{-8} (± 7 %)	7.30×10^{-5}
$DBiB_{0.75}PBiB_{0.25}$-*p(*$OEGMA_{50}$-*co*-$EGDMA_{0.8}$)	4.74×10^{-8} (± 2 %)	2.92×10^{-4}
$DBiB_{0.50}PBiB_{0.50}$-*p(*$OEGMA_{50}$-*co*-$EGDMA_{0.8}$)	1.08×10^{-8} (±16 %)	9.30×10^{-3}
$DBiB_{0.25}PBiB_{0.75}$-*p(*$OEGMA_{50}$-*co*-$EGDMA_{0.8}$)	2.35×10^{-8} (± 17 %)	1.46×10^{-4}
PBiB-*p(*$OEGMA_{50}$-*co*-$EGDMA_{0.8}$)	7.25×10^{-8} (± 0.7 %)	7.5×10^{-2}

CMC profiles of co-initiated polymeric surfactants were similar, Figure 3.17, and branched copolymers which contained a PBiB-derived chain ends appear to have

lower CMC values. Overall, it is unclear whether any definitive trends can be reported for the CMC or ST_{min} values of the branched copolymers, possibly due to the complex heterogeneity of structures within the samples. As a comparison, Sodium dodecyl sulphate is a common ionic surfactant and has an experimental CMC 2.6 $x10^{-4}$ M (approximately 57 mg/L) that is nearly identical to Triton X-100, a non-ionic surfactant based on the alkyl phenylether of PEG, with a reported CMC of 2.0 $x10^{-4}$ M (approximately 129 mg/L)[74]; the copolymers presented here appear to be considerably more mass efficient than these commonly used commercial surfactants.

3.3 CO-INITATED POLYMERIC SURFACTANT STABILISED MACROEMULSIONS

3.3.1 Macroemulsion Characterisation

Macroemulsions were generated *via* mechanical shear, using an overhead shear homogeniser (Ultra-Turrax 25, IKA) and dodecane as the oil phase due to its high compatibility with the hydrophobic chain end functionality of the DBiB-derived macromolecules. Aqueous polymer solutions (5 mg/mL) were homogenised with dodecane in a 1:1 ratio for 2 minutes at 24,000 rpm and left overnight to equilibrate before quantitative analysis by laser diffraction spectroscopy. For example, a typical macroemulsion was prepared to a final volume of 6 mL using dodecane (3 mL) as the oil (dispersed) phase and aqueous polymer solution (3 mL) for the continuous phase.

In all emulsions stabilised by branched copolymer surfactants containing DBiB chain ends, creaming of the stable emulsion was observed due to the dispersed dodecane oil phase having a lower density (0.75 g/mL at 25 °C) than the continuous aqueous phase; however, the emulsions were considered stable if no separation of free oil was observed and the emulsions appeared characteristically white and opaque. Emulsion stability was initially assessed visually due to ease of measurement; Figure 3.19 shows an example of the visible breakdown of macroemulsions, characterised by the clear separation of oil from the emulsion layer. Unstable oil droplets are subject to breakdown during creaming as they are forced together into an oil-rich region of the sample and insufficient interfacial stabilisation will not prevent the oil droplets from subsequently coalescing.

Figure 3.19 Breakdown of dodecane macroemulsion characterised by creaming of oil layer and phase separation between emulsion and aqueous polymer solution. Pictured is a macroemulsion with PBiB-*p(*OEGMA$_{50}$-*co*-EGDMA$_{0.8}$) as branched copolymer surfactant.

Emulsion instability and release of oil was apparent in emulsions prepared when linear DBiB-*p(*OEGMA$_{50}$) and PBiB-*p(*OEGMA$_{50}$) were used as surfactants. These polymers were unable to stabilise macroemulsions and rapid demulsification occurred after homogenisation. Although a defined oil layer was visible, a small sample of the creamed emulsion layer was able to be sampled and the linear polymer stabilised macroemulsions were characterised *via* laser diffraction. The emulsions that were studied contained bimodal droplet distributions Figure 3.20 and all linear polymeric surfactant-stabilised emulsions underwent full demulsification after 3 days of storage at ambient temperature.

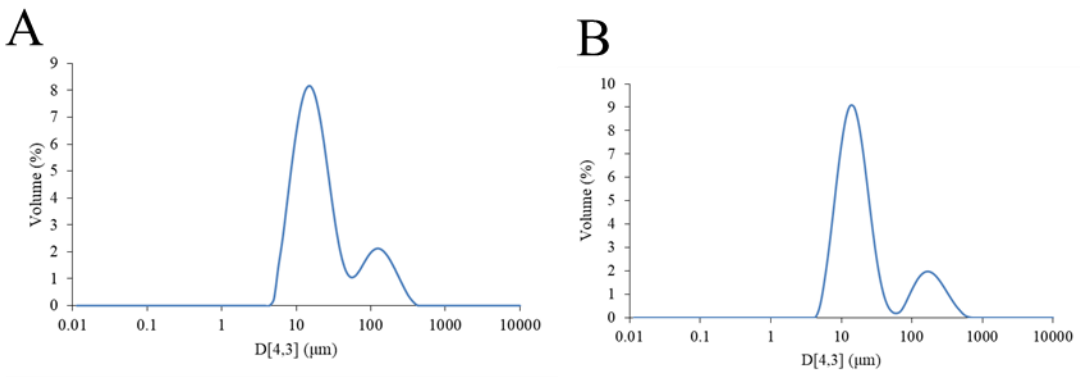

Figure 3.20 Laser diffractograms of linear polymer stabilised dodecane macroemulsions A) DBiB-*p*(OEGMA$_{50}$) and B) PBiB-*p*(OEGMA$_{50}$).

Macroemulsions were also prepared using PBiB-*p(*OEGMA$_{50}$-*co*-EGDMA$_{0.8}$) as the branched copolymer surfactant; immediately after homogenisation emulsions were formed but after 24 hours storage at ambient temperature, separation of the oil phase was apparent and a droplet diameter of 16.9 μm was measured from the remaining emulsion layer, Figure 3.21 A and B. Three days later, full separation of the oil and water phases had occurred.

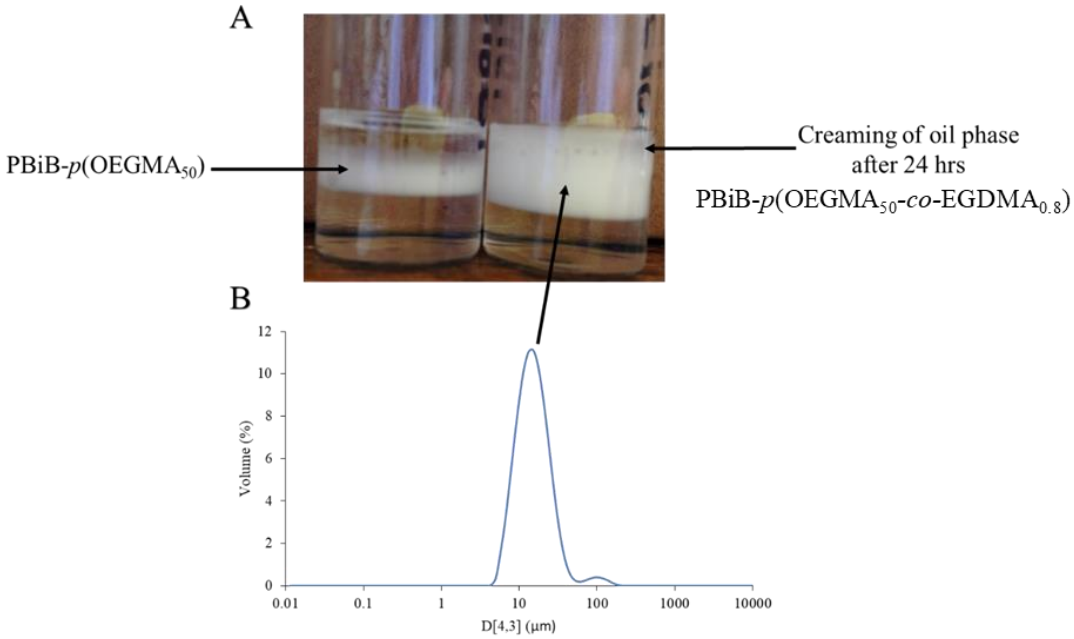

Figure 3.21 Studies of emulsion stability: A) Digital images of demulsified PBiB-*p(*OEGMA$_{50}$) and PBiB-*p(*OEGMA$_{50}$-*co*-EGDMA$_{0.8}$) stabilised dodecane macroemulsions with separation of oil layer. B) Average D$_{[4,3]}$ of PBiB-*p(*OEGMA$_{50}$-*co*-EGDMA$_{0.8}$) stabilised dodecane macroemulison after 24 hrs storage at ambient temperature.

The poor performance of PBiB-*p(*OEGMA$_{50}$) is comparable to that of its branched analogue, PBiB-*p(*OEGMA$_{50}$-*co*-EGDMA$_{0.8}$), and can be expected due to the limited hydrophobicity of the polymer. Surprisingly when DBiB-*p(*OEGMA$_{50}$) was tested as a polymeric surfactant, where all polymer chain ends are the hydrophobic dodecyl initiator the macroemulsion is also unstable. This low emulsion stability is likely due to the dynamic nature of emulsifiers where reversible desorption of the linear chains leads to equilibrium of bound and solution polymer chains, Figure 3.22. As a result linear polymers appear to potentially reside more in the aqueous continuous phase, rather than bound at the oil-water interface and are not able, therefore, to prevent

neighbouring oil droplets from coalescing; the equilibrium appears to lie in favour of dissolved unimeric polymer chains.

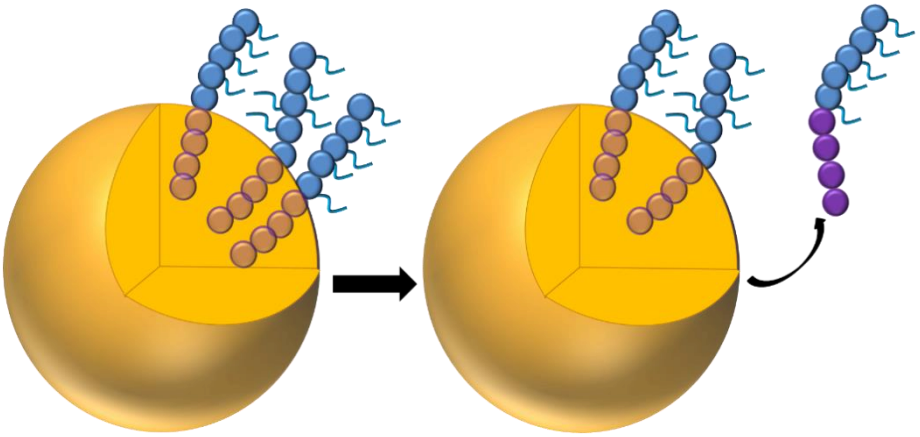

Figure 3.22 Hypothetical model of desorption of linear polymer chains from the oil/water interface, leading to emulsion instability *via* interaction of neighbouring oil droplets.

Macroemulsions stabilised using the range of branched copolymers with varying chain end compositions, i.e. DBiB-*p*(OEGMA$_{50}$-*co*-EGDMA$_{0.80}$), DBIB$_{0.75}$PBiB$_{0.25}$-*p*(OEGMA$_{50}$-*co*-EGDMA$_{0.80}$), DBiB$_{0.50}$PBiB$_{0.50}$-*p*(OEGMA$_{50}$-*co*-EGDMA$_{0.80}$) and DBiB$_{0.25}$PBiB$_{0.75}$-*p*(OEGMA$_{50}$-*co*-EGDMA$_{0.80}$), showed $D_{[4,3]}$ values of 11.9, 13.0, 14.5 and 15.3 µm after 24 hours respectively and unimodal size distributions as measured by laser diffraction, Figure 3.23. A general increase in droplet diameters is observed as the percentage of hydrophobic chain ends is reduced. This is somewhat expected due to the decreasing concentration of surface active chain ends, however it is surprising that a greater difference is not observed due to the overall four-fold decrease in dodecyl chain ends. The laser diffraction of macroemulsions stabilsised by PBiB-*p*(OEGMA$_{50}$-*co*-EGDMA$_{0.8}$) showed a broadening of the distribution and a secondary peak at ~ 100 µm was observed, attributed to initial coalescence of the droplets and eventual creaming of the dispersed phase was observed after 3 days, Figure 3.23 E.

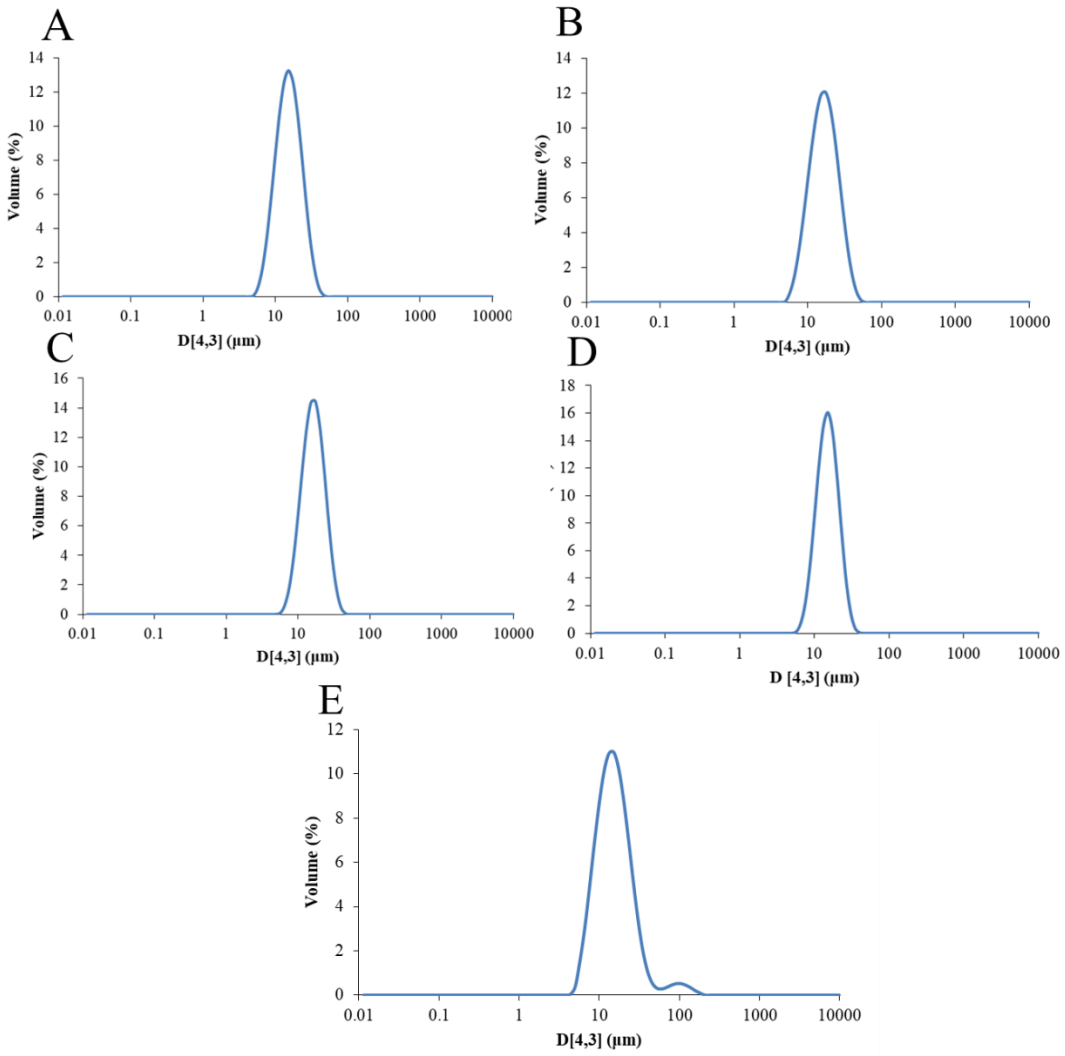

Figure 3.23 Laser diffractograms of dodecane macroemulsions stabilised with; A) DBiB-*p(*OEGMA$_{50}$-*co*-EGDMA$_{0.8}$), B) DBiB$_{0.50}$PBiB$_{0.50}$-*p(*OEGMA$_{50}$-*co*-EGDMA$_{0.8}$), C) DBiB$_{0.75}$PBiB$_{0.25}$-*p(*OEGMA$_{50}$-*co*-EGDMA$_{0.8}$), D) DBiB$_{0.25}$PBiB$_{0.75}$-*p(*OEGMA$_{50}$-*co*-EGDMA$_{0.8}$) and E) PBiB-*p(*OEGMA$_{50}$-*co*-EGDMA$_{0.8}$).

To assess the long term stability of the macroemulsions, a study was undertaken to assess the impact of storage at ambient temperature on the droplet diameter. After 40 days of storage under these conditions, the macroemulsions had $D_{[4,3]}$ values of 13.5, 15.6, 13.8 and 15.1 µm for samples stabilised with DBiB-*p(*OEGMA$_{50}$-*co*-EGDMA$_{0.80}$), DBiB$_{0.75}$PBiB$_{0.25}$-*p(*OEGMA$_{50}$-*co*-EGDMA$_{0.80}$),DBiB$_{0.50}$PBiB$_{0.50}$-*p(*OEGMA$_{50}$-*co*-EGDMA$_{0.80}$) and DBiB$_{0.25}$PBiB$_{0.75}$-*p(*OEGMA$_{50}$-*co*-EGDMA$_{0.80}$) respectively i.e. a negligible change in emulsion droplet diameter was seen, Figure 3.24. Overall, the macroemulsions remained stable over this time period, with samples

stabilised by DBiB-*p(*OEGMA$_{50}$-*co*-EGDMA$_{0.8}$) and DBiB$_{0.75}$PBiB$_{0.25}$-*p(*OEGMA$_{50}$-*co*-EGDMA$_{0.8}$) showing the greatest change in $D_{[4,3]}$ with an increase in diameter of ~ 2 μm. The emulsions stabilised with DBiB$_{0.50}$PBiB$_{0.50}$-*p(*OEGMA$_{50}$-*co*-EGDMA$_{0.8}$) and DBiB$_{0.25}$PBiB$_{0.75}$-*p(*OEGMA$_{50}$-*co*-EGDMA$_{0.8}$) showed negligible differences over the 40 day storage. A general trend of reduction in hydrophobic chain end concentration leading to slight increase in droplet size was observed; for example, branched copolymers containing 75 mol % hydrophilic chain ends yielded emulsions with droplet diameters ~2 μm larger than DBiB-*p(*OEGMA$_{50}$-*co*-EGDMA$_{0.8}$). As the macroemulsions were stored under ambient conditions, the small differences in droplet diameter may be due to variation in temperature and sampling but no meaningful difference between samples was observed over the full timescale of the study.

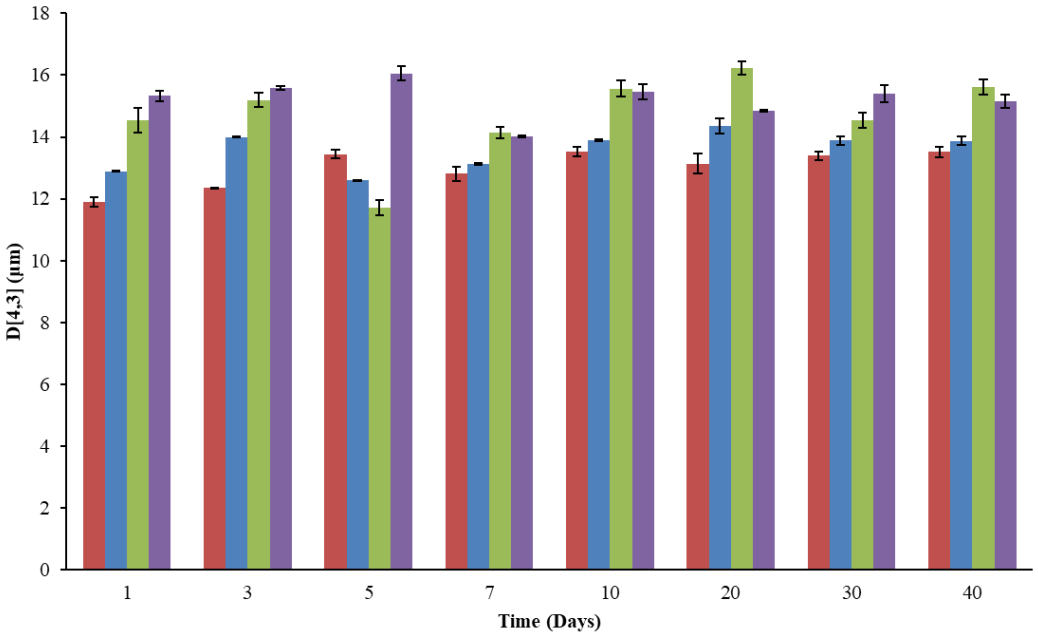

Figure 3.24 Storage stability of macroemulsions: $D_{[4,3]}$ values of dodecane macroemulsions stabilised by; DBiB-*p(*OEGMA$_{50}$-*co*-EGDMA$_{0.8}$) (red), DBiB$_{0.75}$PBiB$_{0.25}$-*p(*OEGMA$_{50}$-*co*-EGDMA$_{0.8}$) (blue), DBiB$_{0.50}$PBiB$_{0.50}$-*p(*OEGMA$_{50}$-*co*-EGDMA$_{0.8}$) (green), DBiB$_{0.25}$PBiB$_{0.75}$-*p(*OEGMA$_{50}$-*co*-EGDMA$_{0.8}$) (purple).

A series of macroemulsions were also stored under uncontrolled ambient conditions for 3 years, to assess very long term storage stability, Figure 3.25. Macroemulsions stabilised with mixed chain end functionality showed no visual creaming or coalescence of the oil phase during this time. This remarkable stability is in stark

contrast to PBiB-*p(*OEGMA$_{50}$-*co*-EGDMA$_{0.8}$) stabilised macroemulsions which separated into two well defined phases, with no emulsion layer present.

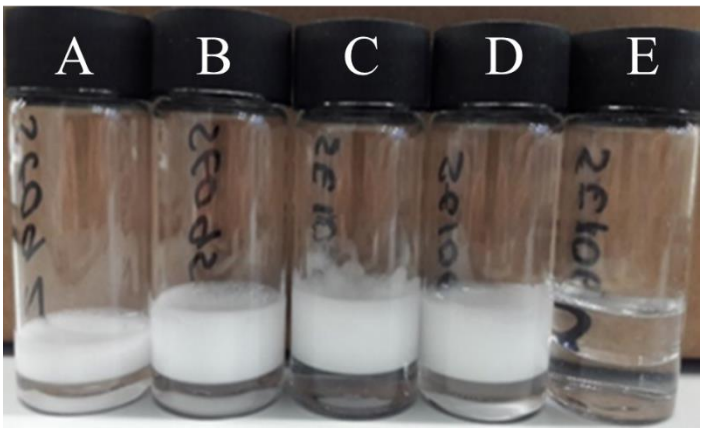

Figure 3.25 Dodecane macroemulsions stored at ambient temperature for 3 years stabilised with; A) DBiB-*p(*OEGMA$_{50}$-*co*-EGDMA$_{0.8}$), B) DBiB$_{0.25}$PBiB$_{0.75}$-*p(*OEGMA$_{50}$-*co*-EGDMA$_{0.8}$), C) DBiB$_{0.50}$PBiB$_{0.50}$-*p(*OEGMA$_{50}$-*co*-EGDMA$_{0.8}$), D) DBiB$_{0.75}$PBiB$_{0.25}$-*p(*OEGMA$_{50}$-*co*-EGDMA$_{0.8}$), E) PBiB-*p(*OEGMA$_{50}$-*co*-EGDMA$_{0.8}$).

It is important to fully establish that the beneficial effects of the branched copolymer stabilisers is due to the novel branched architectures and not merely a synergistic effect of the mixed polymers within the samples; therefore, a control experiment which blended aqueous solutions of the linear polymers DBiB-*p(*OEGMA$_{50}$) and PBiB-*p(*OEGMA$_{50}$) was performed. The aqueous linear polymer solutions were prepared at 5 mg/mL and blended to obtain ratios comparable to the molar percentage of PEG and dodecyl chain ends within the various branched copolymer structures. The resulting macroemulsions prepared with linear polymer blends were not stable; multiple peaks were observed in the laser diffraction traces of the emulsion layers which represented a large distribution of droplet diameter throughout each sample, Figure 3.26. The distribution was progressively more disperse and bimodal with decreasing DBiB-*p(*OEGMA$_{50}$) content, which was in a marked contrast to the branched copolymer-stabilised emulsions with similar ratios of the different chain ends, Figure 3.21. Full separation of linear polymer blend stabilised macroemulsions was observed after approximately 3 days of storage at ambient temperature.

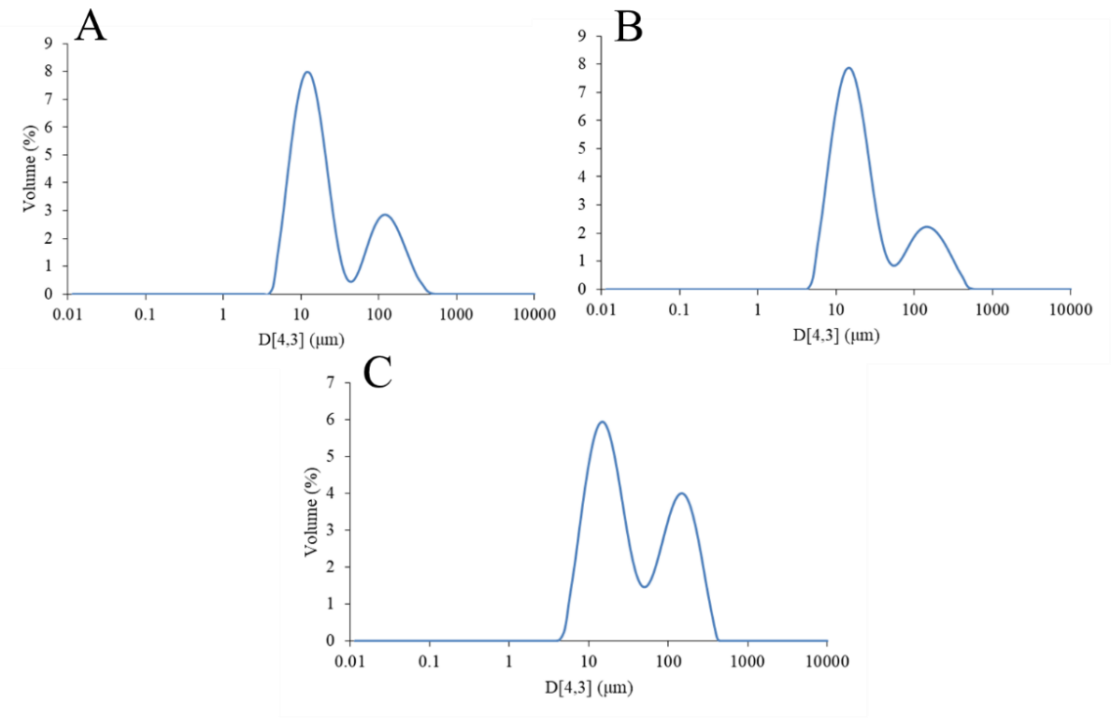

Figure 3.26 Laser diffractograms of dodecane macroemulsions stabilised with linear blends of polymeric surfactants prepared at 5 mg/mL with ratios of; A) DBiB-*p*(OEGMA$_{50}$)/PBiB-*p*(OEGMA$_{50}$) 0.75/0.25, B) DBiB-*p*(OEGMA$_{50}$)/PBiB-*p*(OEGMA$_{50}$) 0.50/0.50 and C) DBiB-*p*(OEGMA$_{50}$)/PBiB-*p*(OEGMA$_{50}$) 0.25/0.75.

The behaviour of the blended linear polymer solutions clearly demonstrated the crucial role that polymeric architectures play within the co-initiated branched copolymer emulsifiers. The arrangement of combinations of PEG and dodecyl initiator-derived chain ends at the oil droplet surface would not be possible without the branching by EGDMA that connects the varying primary chains into the complex branched copolymer architectures. Hydrophobic chain ends allow anchoring of polymers at the oil/water interface thus reducing high interfacial tensions between the immiscible phases and providing emulsion stability *via* steric stabilisation from the branched *p*(OEGMA) chains. It is also now possible to produce emulsions of comparable size and long term stability containing as low as 25 % hydrophobic chain end composition. This can be considered the current critical hydrophobic chain end composition at which stable o/w macroemulsions can be formed.

3.3.2 Optical Microscopy of Branched Copolymer Stabilised Macroemulsions

Optical microscopy was used to further analyse the macroemulsion droplets and visualise the dispersity of the samples. Following microscopy, image analysis was

conducted using FIJI (V 1.51n) software to determine the diameter of individual droplets measured per image. After 11 months storage at ambient temperature, a concentrated sample was studied and oil droplets retained their near-monodisperse distribution with well-defined circular geometry with no sign of coalescence between droplets, Figure 3.27.

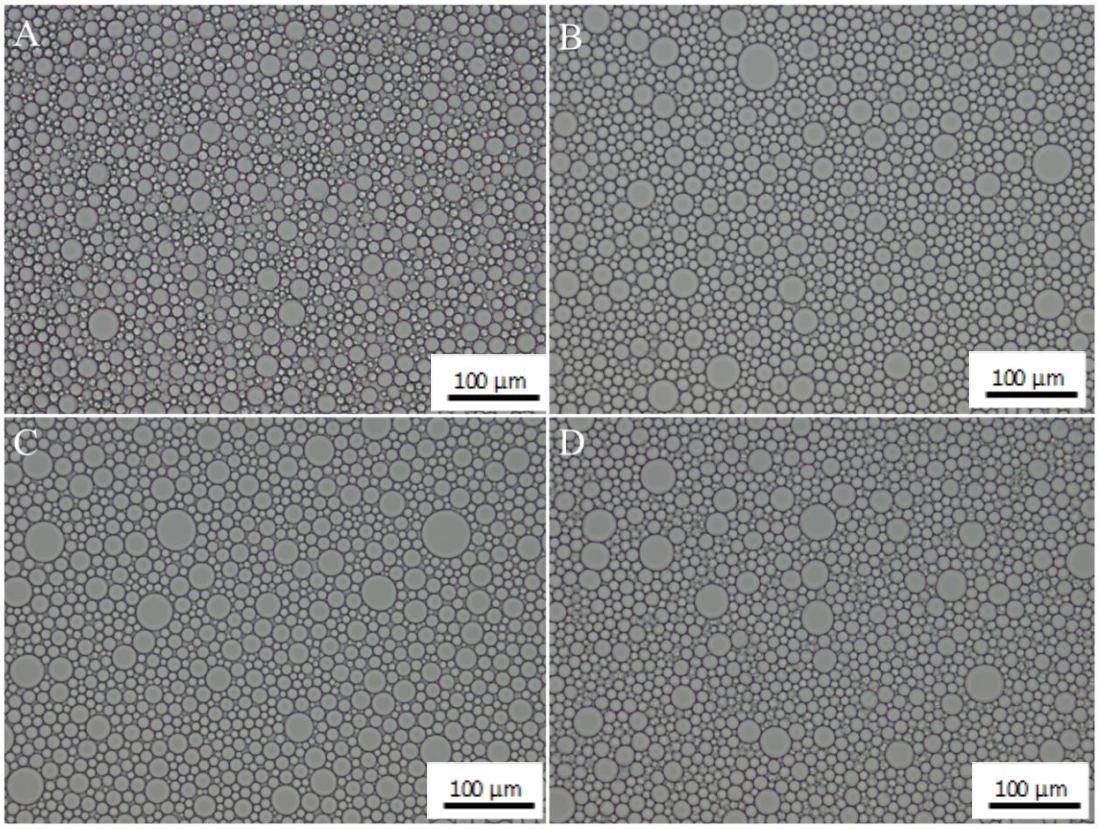

Figure 3.27 Optical microscopy images of concentrated dodecane macroemulsion after 11 months storage at ambient temperature; A) DBiB-*p(*$OEGMA_{50}$-*co*-$EGDMA_{0.8}$), B) $DBiB_{0.75}PBiB_{0.25}$-*p(*$OEGMA_{50}$-*co*-$EGDMA_{0.8}$), C) $DBiB_{0.50}PBiB_{0.50}$-*p(*$OEGMA_{50}$-*co*-$EGDMA_{0.8}$), D) $DBiB_{0.25}PBiB_{0.7\text{-}5}$*p(*$OEGMA_{50}$-*co*-$EGDMA_{0.8}$), 20x magnification, scale bar = 100 µm.

Size distribution data from the optical microscopy images showed 11 month old emulsions stored at ambient temperature stabilised with $DBiB_{0.50}PBiB_{0.50}$-*p(*$OEGMA_{50}$-*co*-$EGDMA_{0.8}$) had an average droplet diameter of 9 µm, with 90 % of droplets present being under 15 µm, whereas the $D_{[4,3]}$ measured by laser diffraction after 40 days was 13.8 µm. This highlights the differences of the different analytical

techniques; $D_{[4,3]}$ analysis is a volume average mean and a two dimensional diameter (number mean) is generated by optical microscopy.

$DBiB_{0.25}PBiB_{0.75}$-*p(*$OEGMA_{50}$-*co*-$EGDMA_{0.8}$) stabilised macroemulsions had an average droplet diameter of 9.4 μm determined *via* optical microscopy with 90 % of the droplet population under 17 μm, Figure 3.28 A. This was in comparison to droplet diameters determined by laser diffraction where the $D_{[4,3]}$ was 15.6 μm after 40 days. $DBiB_{0.75}PBiB_{0.25}$-*p(*$OEGMA_{50}$-*co*-$EGDMA_{0.8}$) stabilised macroemulsions had a lower average diameter at 8.3 μm determined by optical microscopy in comparison to Mastersizer analysis, with 90 % of the population size under 14 μm, Figure 3.28 B. Overall this showed that the reduction of hydrophobic chain ends caused a minimal increase in droplet diameter.

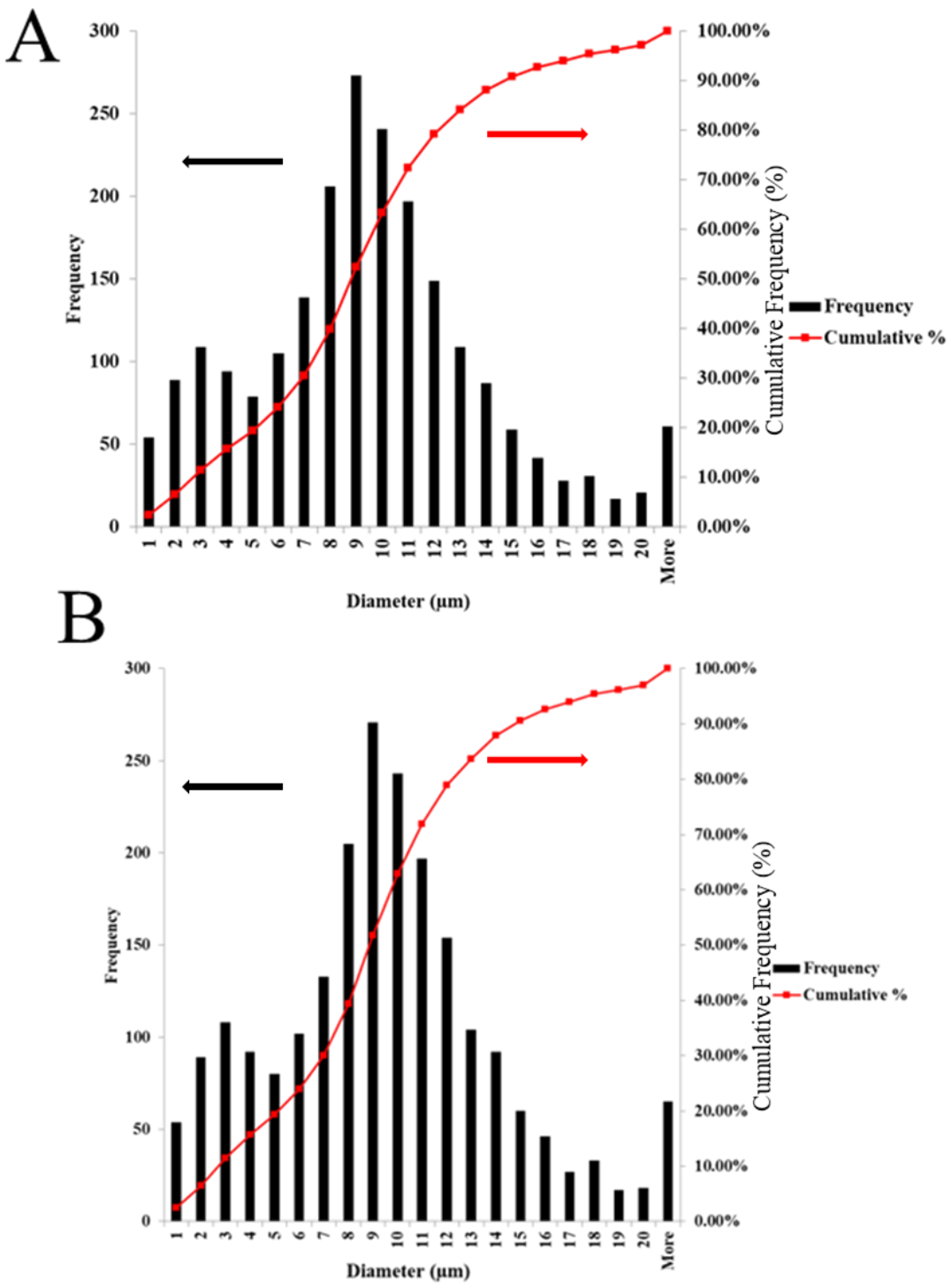

Figure 3.28 Example of histogram data of $D_{[1,0]}$ of emulsions with varying hydrophobic chain end composition, with cumulative %; A) DBiB$_{0.50}$PBiB$_{0.50}$-*p*(OEGMA$_{50}$-*co*-EGDMA$_{0.8}$) and B) DBiB$_{0.25}$PBiB$_{0.75}$-*p*(OEGMA$_{50}$-*co*-EGDMA$_{0.8}$).

3.4 CO-INITIATED POLYMERIC SURFACTANT STABILISED NANOEMULSIONS

As described in Section 2.5, branched copolymer surfactants have been utilised to generate nanoemulsions *via* the removal of a volatile co-solvent from the internal dispersed phase. The use of the co-initiated branched copolymers was also studied to establish whether the variation in hydrophobic and hydrophilic chain end chemistry would impact nanoemulsion formation. Aqueous branched copolymer solutions were prepared at a 5 wt % concentration and dissolved overnight. These solutions were used as the aqueous phase for a range of nanoemulsions, using overhead shear homogenisation followed by solvent evaporation as detailed in Section 2.5. In a typical nanoemulsion preparation, a final emulsion volume of approximately 3 mL was targeted after evaporation of the co-solvent from an original total emulsion volume of 6 mL; 3 mL of aqueous polymer solution and 3 mL of the mixed dispersed oil-phase with varying ratios of ethyl acetate and castor oil were used across all samples. For example, for nanoemulsions prepared using a 99:1 ratio of ethyl acetate:castor oil, the oil phase contained a mixture of 2.97 mL ethyl acetate and 0.03 mL castor oil.

As expected from previous observations, combinations of linear polymers did not form stable nanoemulsions, and rapid demulsification occurred during solvent evaporation. PBiB-*p(*$OEGMA_{50}$-*co*-$EGDMA_{0.8}$) was also unsuccessful as a stabiliser for nanoemulsion formation, with no stable emulsion being formed after solvent evaporation. In contrast, all branched copolymers containing DBiB-derived chain ends successfully stabilised nanoemulsions that were analogous to samples generated using DBiB-*p(*$OEGMA_{50}$-*co*-$EGDMA_{0.8}$) that were described in Chapter 2, Table 3.4.

Table 3.4 DLS data for nanoemulsions[a] with aqueous branched copolymer solutions (5 wt %) with varying chain end composition.

Polymer	D_z (nm)	D_n (nm)	PdI
DBiB-*p(*$OEGMA_{50}$-*co*-$EGDMA_{0.8}$)	203	176	0.063
$DBiB_{0.90}PBiB_{0.10}$-*p(*$OEGMA_{50}$-*co*-$EGDMA_{0.8}$)	237	217	0.039
$DBiB_{0.75}PBiB_{0.25}$-*p(*$OEGMA_{50}$-*co*-$EGDMA_{0.8}$)	252	236	0.126
$DBiB_{0.50}PBiB_{0.50}$-*p(*$OEGMA_{50}$-*co*-$EGDMA_{0.8}$)	253	206	0.147
$DBiB_{0.25}PBiB_{0.75}$-*p(*$OEGMA_{50}$-*co*-$EGDMA_{0.8}$)	271	248	0.104
$DBiB_{0.10}PBiB_{0.90}$-*p(*$OEGMA_{50}$-*co*-$EGDMA_{0.8}$)	646	423	0.314

[a]Nanoemulsions were generated with an oil phase composed of EtOAc:castor oil in a 99:1 ratio.

The hydrodynamic diameter (D_z) of the droplets present in the nanoemulsions were comparable across the majority of the range of polymeric surfactants with a noticeable, but small, trend to increasing diameters with decreasing hydrophobic chain end content. The sizes were maintained below 300 nm across these samples, even when the amount of hydrophobic chain ends present was considerably reduced to only 25 mol %; PdI values remained remarkably low. The exception to this overall trend was the stabiliser with the lowest hydrophobic chain end content, $DBiB_{0.10}PBiB_{0.90}$-*p(*$OEGMA_{50}$-*co*-$EGDMA_{0.8}$), which had an large D_z = 667 nm, higher PdI = 0.30 and higher number average diameter (D_n) value. Figure 3.29 shows the DLS particle diameter distributions for the nanoemulsions also described in Table 3.4. The monomodal and narrow nature of the distributions shown is lost when dodecyl chain ends present within the branched copolymer emulsifier are significantly decreased; nanoemulsions formed using $DBiB_{0.10}PBiB_{0.90}$-*p(*$OEGMA_{50}$-*co*-$EGDMA_{0.8}$) exhibit a broad and multimodal distribution.

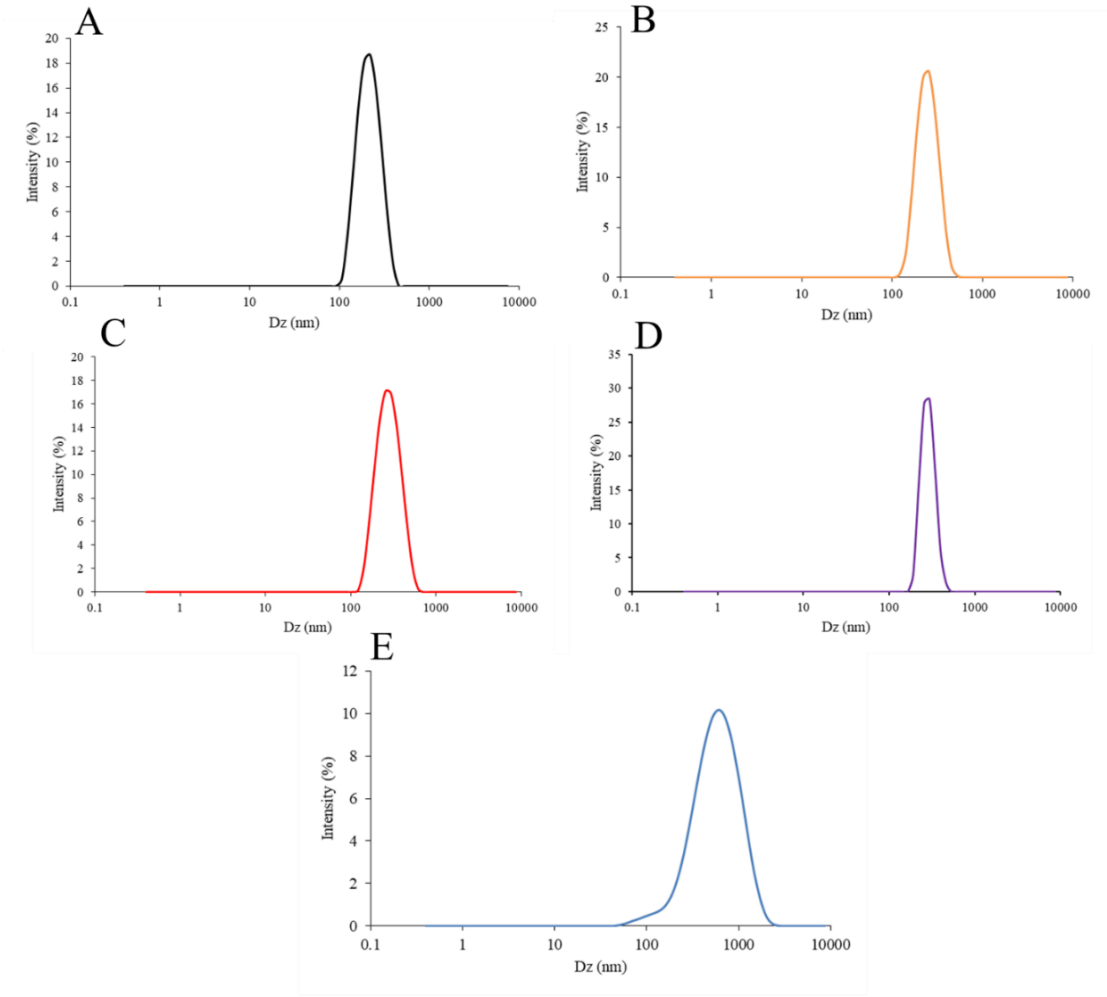

Figure 3.29 DLS size distributions for nanoemulsions generated at a 99:1 ratio of ethyl acetate:castor oil stabilised with branched copolymers as surfactants; A) DBiB-*p(*OEGMA$_{50}$-*co*-EGDMA$_{0.8}$) (black), B) DBiB$_{0.90}$PBiB$_{0.10}$-*p(*OEGMA$_{50}$-*co*-EGDMA$_{0.8}$) (orange), C) DBiB$_{0.75}$PBiB$_{0.25}$-*p(*OEGMA$_{50}$-*co*-EGDMA$_{0.8}$) (red), D) DBiB$_{0.50}$PBiB$_{0.50}$-*p(*OEGMA$_{50}$-*co*-EGDMA$_{0.8}$) (purple) and E) DBiB$_{0.25}$PBiB$_{0.75}$-*p(*OEGMA$_{50}$-*co*-EGDMA$_{0.8}$) (blue).

3.4.1 Tailoring of Nanoemulsion Droplet Diameter Stabilised by Co-initiated Branched Copolymer

As discussed in the previous chapter, Section 2.5.2, variation of the volatile to non-volatile oil ratio should allow control of the nanoemulsion droplet size. For this study, DBiB$_{0.25}$PBiB$_{0.75}$-*p(*OEGMA$_{50}$-*co*-EGDMA$_{0.8}$) was selected as the branched copolymer surfactant, castor oil was again used as the non-volatile oil and ethyl acetate as the co-solvent; the volatile:non-volatile oil phase ratios varying from 50:50, 60:50, 70:30, 80:20, 90:10 to 99:1, Figure 3.28. The ability to reduce the number of dodecyl

chains within the branched copolymer surfactant whilst maintaining the ability to stabilise nanoemulsions from 2500 nm down to 270 nm was confirmed, Figure 3.30.

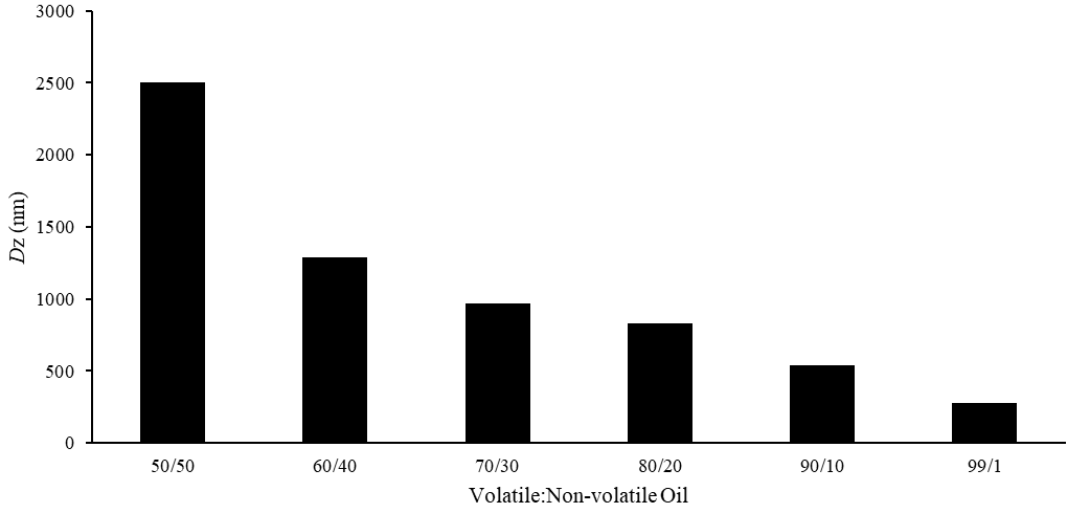

Figure 3.30 Nanoemulsion size tailored *via* solvent evaporation method with $DBiB_{0.25}PBiB_{0.75}$-*p(*$OEGMA_{50}$-*co*-$EGDMA_{0.8}$) as polymeric surfactant at a 5 wt% concentration. Volatile:non-volatile oil phase was composed of ethyl acetate:castor oil.

Interestingly, the use of DBiB-*p(*OEGMA-*co*-$EGDMA_{0.8}$) at a ratio of volatile to non-volatile oil ratio of 50:50 formed emulsion droplets with diameters less than 1 μm and the reduction in hydrophobic chain ends to 25 mole % led to a larger emulsion droplet size; this has not been studied in any further detail; however it is plausible that the reduction in surface tension modification, as seen in Section 3.2.2.1, results in a higher concentration of surfactant required to reduce the surface tension and stabilise a higher surface area that would be expected from smaller droplets at the same physical mass of oil. Within the series of nanoemulsions shown in Figure 3.29, the PdI values decreased from 0.258 for the largest nanoemulsion down to 0.07 for the smallest diameter, Table 3.5.

Table 3.5 DLS data of tailored nanoemulsions with $DBiB_{0.25}PBiB_{0.75}$-*p(*$OEGMA_{50}$-*co*-$EGDMA_{0.8}$) as the polymeric surfactant. Oil ratio refers to the ratio of volatile:non-volatile oil blend of Ethyl acetate:castor oil.

Oil Ratio	D_z (nm)	PdI
50:50	2500	0.258
60:40	1290	0.242
70:30	960	0.244
80:20	820	0.194
90:10	540	0.119
99:1	270	0.07

DLS analysis of the nanoemulsion size distributions reflect the decreased droplet diameter and the lowered polydispersity, Table 3.5. As the amount of ethyl acetate is increased, nanoemulsion distributions are consistently monodisperse in concordance with the PdI values determined, Figure 3.31.

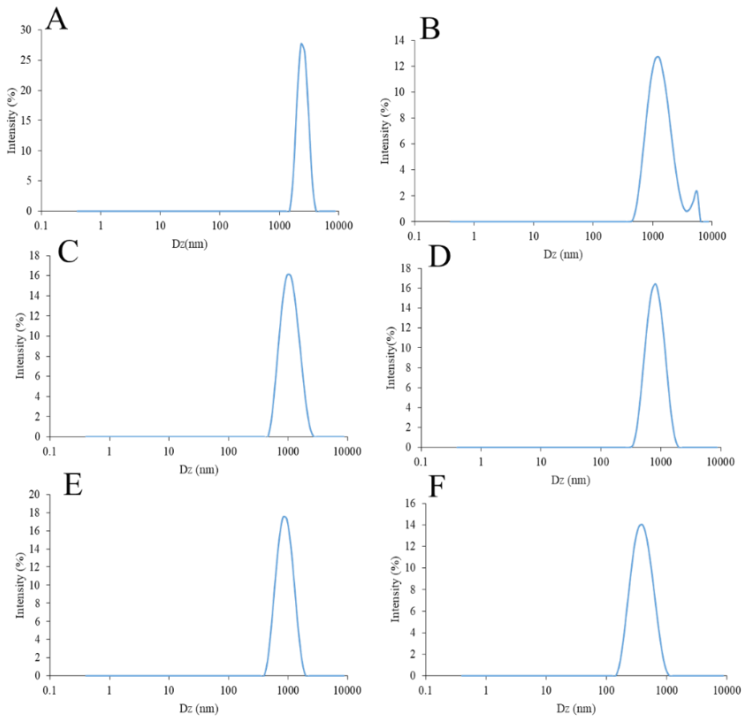

Figure 3.31 DLS measurements of tailored nanoemulsion droplet size with $DBiB_{0.25}PBiB_{0.25}$-*p(*$OEGMA_{50}$-*co*-$EGDMA_{0.8}$) as the polymeric surfactant. Oil phase ratios of ethyl acetate:castor oil; A) 50:50, B) 60:40, C) 70:30, D) 80:20, E) 90:10 and F) 99:1.

3.5 CONCLUSIONS

The hypothesis tested within this Chapter attempted to extend the value of the branched copolymer surfactants described in Chapter 2 by taking advantage of the joining of chains during the branching process. In principle, it was believed that a branched polymerisation containing mixed initiators would controllably and systematically allow control of the overall chain end composition of the surfactants. To test this hypothesis, a PEG-derived macroinitiator was substituted into the branching ATRP polymerisation of OEGMA at varying levels and in combination with a dodecyl-derived initiator and the variation of behaviour of the amphiphilic branched copolymers was studied. All studies, showed variations of behaviour that could be attributed to the varying chain end composition of the complex macromolecular samples.

The ability of the branched amphiphilic copolymers, and the failure of all linear polymers and mixtures of linear polymers, to stabilise emulsions is hypothesised to be due to manipulation of a fine balance of the solution equilibrium of adsorbed and desorbed molecules at macro and nanoemulsion interfaces. The branched copolymer PBiB-*p(*$OEGMA_{50}$-*co*-$EGDMA_{0.8}$) was also unsuccessful in forming stable emulsions, presumably due to the lack of hydrophobic chain ends as hypothesised when designing this study. The removal of up to 75 mole % of hydrophobic chain ends, whilst still providing excellent emulsifier behaviour, is remarkable; comparative droplet sizes to DBiB-*p(*$OEGMA_{50}$-*co*-$EGDMA_{0.8}$) studied in Chapter 2, at both the macro- and nanoscale were observed.

The results discussed in this chapter highlight the impact of the branched architecture on the copolymers' ability to act as an efficient surfactant. The branched architecture appears to provide multiple hydrophobic chain ends per macromolecule thus creating a multiple anchoring effect at the oil/water interface and promoting rapid re-adsorption of hydrophobic chain ends following individual desorption, Figure 3.32; the desorbed primary chain ends are held in close proximity to the oil droplet surface and prevented from releasing into solution. In essence, to desorb the entire surfactant molecule would require the concerted and simultaneous desorption of multiple chain ends which is highly unlikely. It is important to recognise the slight changes that are seen between emulsions stabilised with branched copolymers of relatively low hydrophobic chain

end content. The D_z and D_n values are subtly higher for nanoemulsions formed under identical conditions and the packing of hydrophobic chains at interfaces may be less dense than materials with higher contents of hydrophobic chain ends; this may be of interest when considering the behaviour of materials in later Chapters.

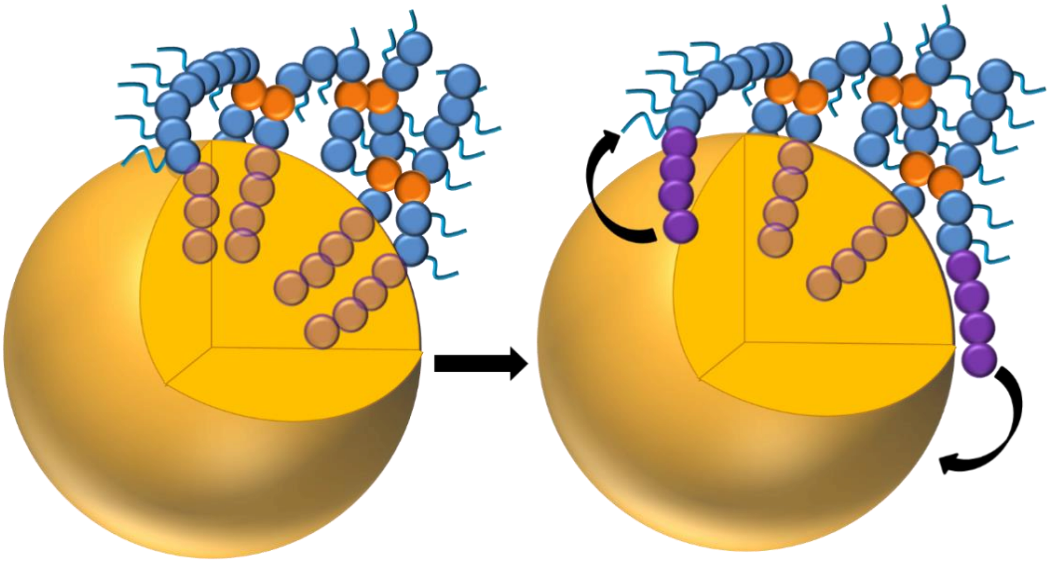

Figure 3.32 Effect of branched architecture on anchoring polymer chains near to the oil/water interface for ready readsorption.

The anchoring of branched polymer emulsifiers to the oil/water interface is a key factor influencing the long term stability of the o/w emulsions. This was further shown by blending of linear polymers in statistical ratios to match the branched polymer counterparts. Blending of linear polymers led to multimodal laser diffraction traces, with multiple droplets being present in the emulsions spanning 1 – 20 μm and low levels of stability.

The branched copolymer surfactants draw comparisons to Pickering emulsifiers which are stabilised by solid particles, as discussed in Section 1.6.3., due to the high molecular weights as well as their ability to stabilise macroemulsions and nanoemulsions over long periods of time. Pickering emulsifiers act by adsorbing onto the interface and preventing coalescence by the solid particles forming a rigid mechanical barrier.[137] It is thought that the branched copolymers discussed in this investigation are preventing coalescence in a similar manner, where the highly branched structure with multiple hydrophobic anchoring points creates a dense coating as the polymer arranges itself at the interface. This provides a strong barrier further

reducing the chance of neighbouring droplets coalescing and cause emulsion phase separation.

As it has been determined that a safe minimum of 25 mol % of the chain ends are required to be hydrophobic, the incorporation of a functional initiator group instead of PBiB can be explored and will be the subject of Chapter 4. This allows for tailoring of not only the emulsion droplet diameters but also the amount of functionality that is present at the surface of the oil droplet.

CHAPTER 4

Effect of Thiol-functionalised Copolymer Surfactants within Mucoadhesive Emulsions

4.1 INTRODUCTION

In Chapter 3, branched copolymers with a reduced number of hydrophobic chain ends were successfully used as surfactants to form o/w stabilised emulsions at both the macro- and nano-scale. It was shown that a) branched copolymers with as few as 10 mole percent hydrophobic chain ends were able to produce stable macroemulsions, and b) branched macromolecules with just 25 mole percent of their chain ends bearing hydrophobic dodecyl groups were able to stabilise nanoemulsions with comparative droplet sizes to systems stabilised with DBiB-*p*(OEGMA$_{50}$-*co*-EGDMA$_{0.8}$); containing 100 % of its chain ends as hydrophobic alkyl groups. Further reduction to just 10 mole percent of the chain ends bearing dodecyl groups also formed potentially biologically-relevant nanoemulsions below 700 nm. Here, we hypothesise that the non-stabilising hydrophilic chain ends of these branched copolymers, derived in Chapter 3 from PEG-based macroinitiators, can be replaced with functional groups such as thiols, Figure 4.1, which may provide useful interaction with mucus-lined surfaces and resultant mucoadhesion.

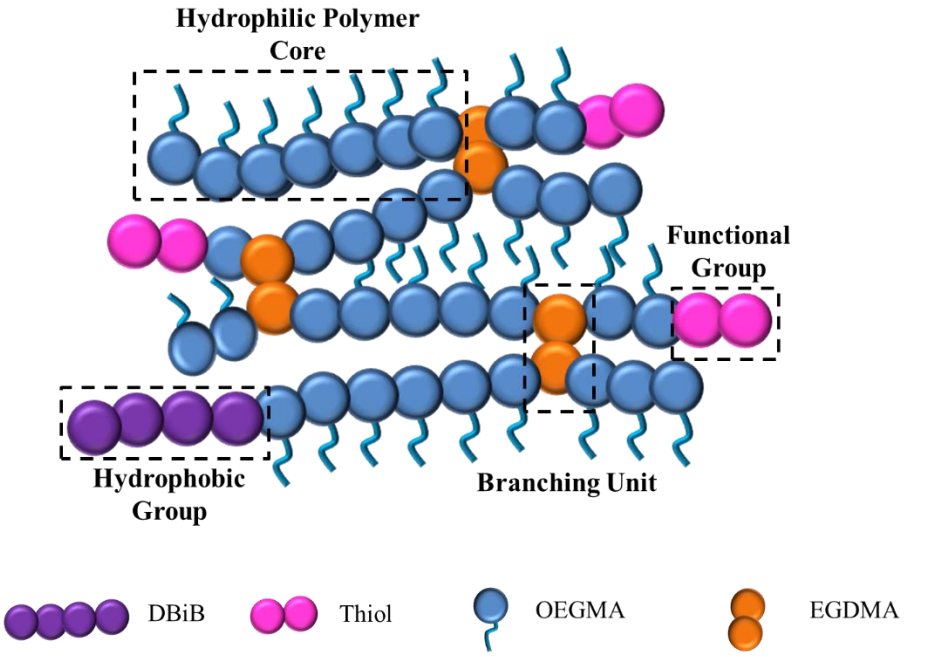

Figure 4.1 Inclusion of thiol functionality at the chain ends of branched copolymer surfactants. General polymer composition; SH$_x$DBiB$_y$-*p*(OEGMA$_{50}$-*co*-EGDMA$_{0.8}$).

4.1.1 Development of Masked-Thiol Functionalised ATRP Initiators

Previously published work, from within the group, has shown masked thiol groups can be incorporated into a range of polymers by the use of xanthate-based initiators, including dendritic initiators, with the control expected from an ATRP reaction and the formation of linear and branched copolymers with high M_w at high monomer conversion, Figure 4.2.[108] The dendritic initiator molecules have also been shown to successfully co-initiate an ATRP reaction in combination with a relatively short macroinitiators derived from PEG.[109,125] Xanthate groups have been shown to be relatively easily de-protected to expose the masked thiol functionality post-polymerisation; this approach avoids complications such as the laboratory use of thiols and oxidation or disulphide formation during storage.

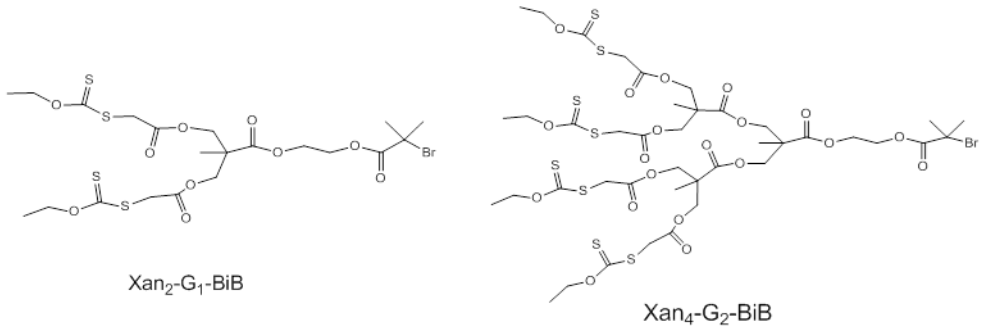

Figure 4.2 Dendritic initiator groups as previously used, with thiol groups masked by xanthate protecting groups. [1,2]

For the functional-emulsions targeted here, a small molecule ATRP initiator XanBiB, Figure 4.3, previously referred to as a generation zero dendritic initiator in literature reports,[108] will be used in conjunction with DBiB to form a range of branched copolymer stabilisers containing varying thiol functionality after deprotection. This will subsequently target one thiol group per polymer chain end and the molar ratio of XanBiB:DBiB will be varied using the co-initiated polymerisation method described in Chapter 3.

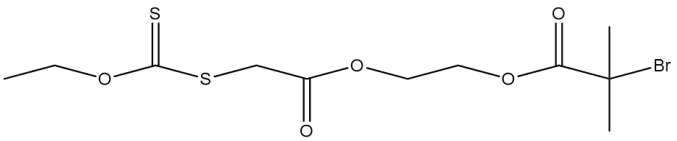

Figure 4.3 First generation xanthate initiator, Xan-G_0-BiB, referred to as XanBiB in this study.

The scope of the target polymers is highlighted in Figure 4.4. As shown a large range of functionality may be achieved and varied within the polymer architecture. Emulsion characterisation using laser diffraction, optical microscopy and DLS will allow direct comparison of functional emulsions formed through this strategy and macroemulsions/nanoemulsions formed using the non-functional and mixed hydrophilic/hydrophobic branched copolymer emulsifiers described in Chapters 2 and 3. The aim of this study was to determine whether thiolated chain end functionalised branched copolymers were able to stabilise macro- and nanoemulsions, whether such systems would be stable and, if so, whether variation of thiol content within the polymeric surfactant would direct the subsequent behaviour of the samples. This methodology could thereby potentially provide a route to tailor the properties and behaviour of macro- and nanoemulsions and offer benefits for future applications.

As mentioned earlier, modified mucus-penetration and mucoadhesion is the main goal of the research, therefore, both quantitative and qualitative approaches to determine mucus interactions of these novel emulsions will be required. Taking a lead from literature reports, flow-through and static models of liquids will be evaluated, including the use of biosimilar (synthetic representations) and *ex vivo* mucus samples to assess emulsion behaviour with varying functionality.

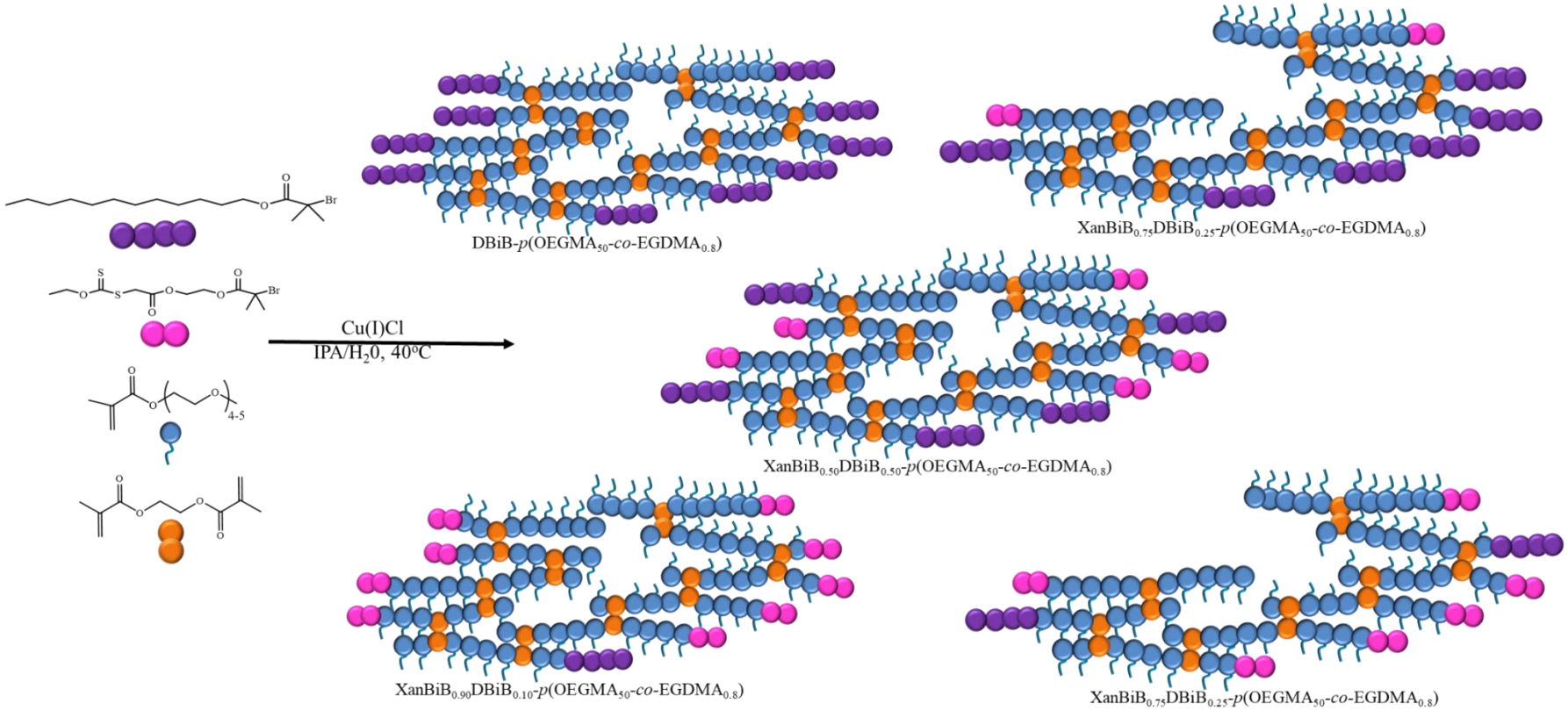

Figure 4.4 Schematic representation of masked-thiol functional branched copolymer emulsifiers targeted within this Chapter; OEGMA derived primary chains (blue), with branching derived from copolymerisation of EGDMA (orange) and co-initiation to include mucoadhesive character at different ratios by varying the molar ratios of XanBiB (pink) and DBiB (purple) initiators.

4.1.2 Quantification of Mucoadhesion

The variety of methods used to assess mucoadhesion has led to wide diversity in the quantification and reporting of adhesion properties for different materials. For example, solid adhesives, tablets or hydrogels, can be assessed by the force required to detach them from an *ex vivo* mucosal surface.[139] Force-detachment curves can subsequently be produced to determine adhesion; however, for liquid-based dosage systems such as emulsions, a more appropriate model is required. In the previous reports, methods such as rheology[140], flow-through model combined with HPLC[141] or fluorescently labelling of mucoadhesives have been utilised.[142,143]

A 'gutter' flow-through model has been reported widely and a "typical" example is shown in Figure 4.5. Sections of *ex vivo* mucosal tissue are placed within the gutter and a liquid/semi-solid mucoadhesive is dosed to the tissue; flow of simulated biological fluid is then pumped to the top of a gradient and allowed to flow over the surface. If the mucoadhesive sample is drug-loaded, the amount of drug removed by the simulated biological fluid can be quantified *via* HPLC. Alternatively, the mucosal surface can be imaged post-flow, to visually assess the remaining sample and asses adhesion to the tissue substrate.[35]

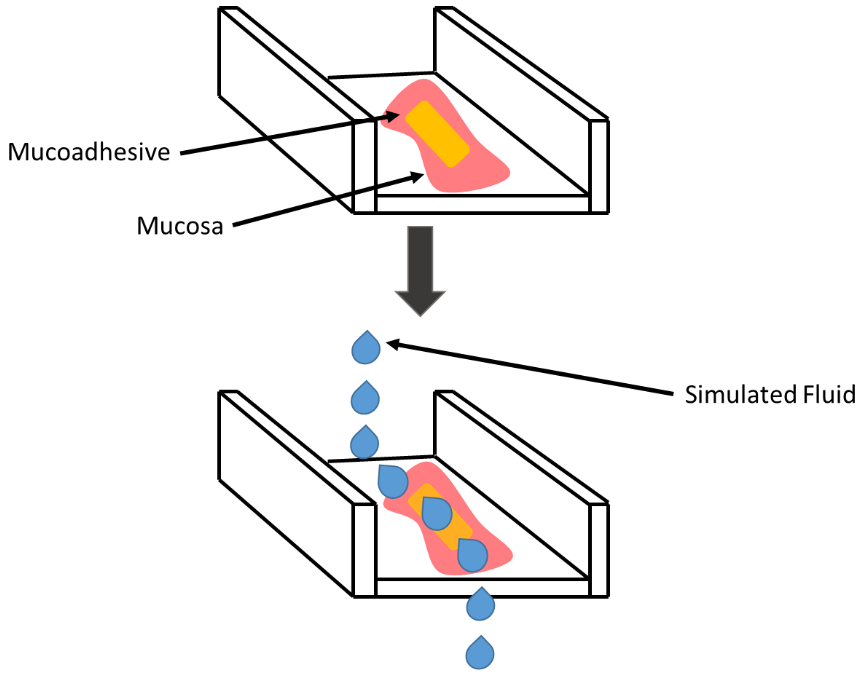

Figure 4.5 Schematic of a typical 'gutter' model for studies of mucoadhesives in liquid form; *ex vivo* mucosal tissue is often used for testing. Adapted from: M. T. Cook and V. V. Khutoryanskiy.[35]

An issue with many of the currently reported mucoadhesion studies is that they require the use of *ex vivo* tissue, where animals have been sacrificed specifically for their mucosal tissue. However, recently there has been a greater use of biosimilar mucosal mimics, which avoid the use of animal tissue as well as providing a readily accessible and reproducible method for adhesion studies within non-biological laboratories.

4.2 SYNTHESIS OF CO-INTIATED THIOLATED POLYMERS FOR USE AS SURFACTANTS

To synthesise the functional ATRP initiator XanBiB, two precursors 2-((ethoxycarbonothioyl)thio) acetic acid, XanCOOH, and 2-hydroxyethyl bromoisobutyrate, HBiB, were required, Scheme 4.1.

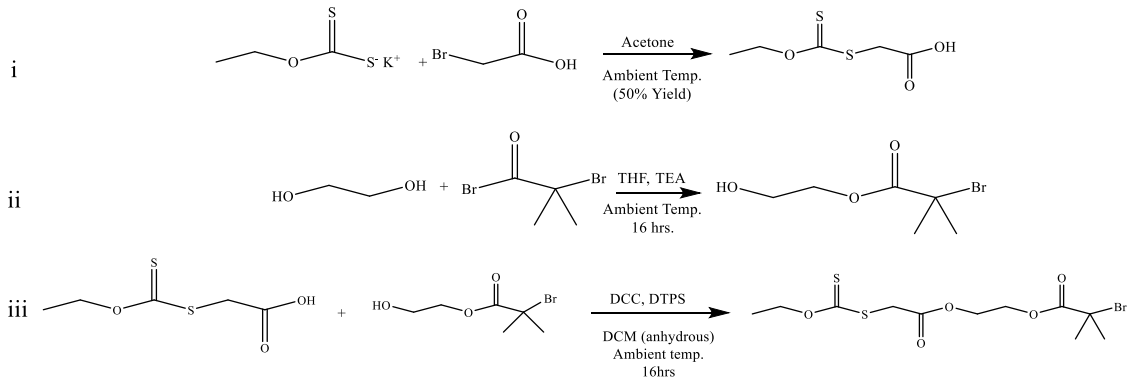

Scheme 4.1 Synthesis of i) 2-((ethoxycarbonothioyl)thio) acetic acid (XanCOOH), ii) 2-hydroxyethyl bromoisobutyrate (HBiB) and iii) first generation xanthate bromoisobutyrate (XanBiB).

XanCOOH was synthesised following reported methods, by reacting potassium ethyl xanthogenate with 2-bromoacetic acid for 16 hours, Scheme 4.1i, followed by isolatation by filtration and purification using liquid-liquid extraction to yield a white solid. The purified product was fully characterised by NMR (^{1}H and ^{13}C), Figure 4.6, and mass spectrometry (Appendix A7). HBiB synthesis also followed previous reports and required a TEA-catalysed mono-esterification of ethylene glycol with α-bromoisobutyryl bromide, Scheme 4.1ii. The reaction was also left for 16 hrs, and the purified product was isolated by a simple liquid-liquid extraction to yield a yellow oil; full characterisation was achieved by NMR (^{1}H and ^{13}C), Figure 4.7, and mass spectrometry (Appendix A8).

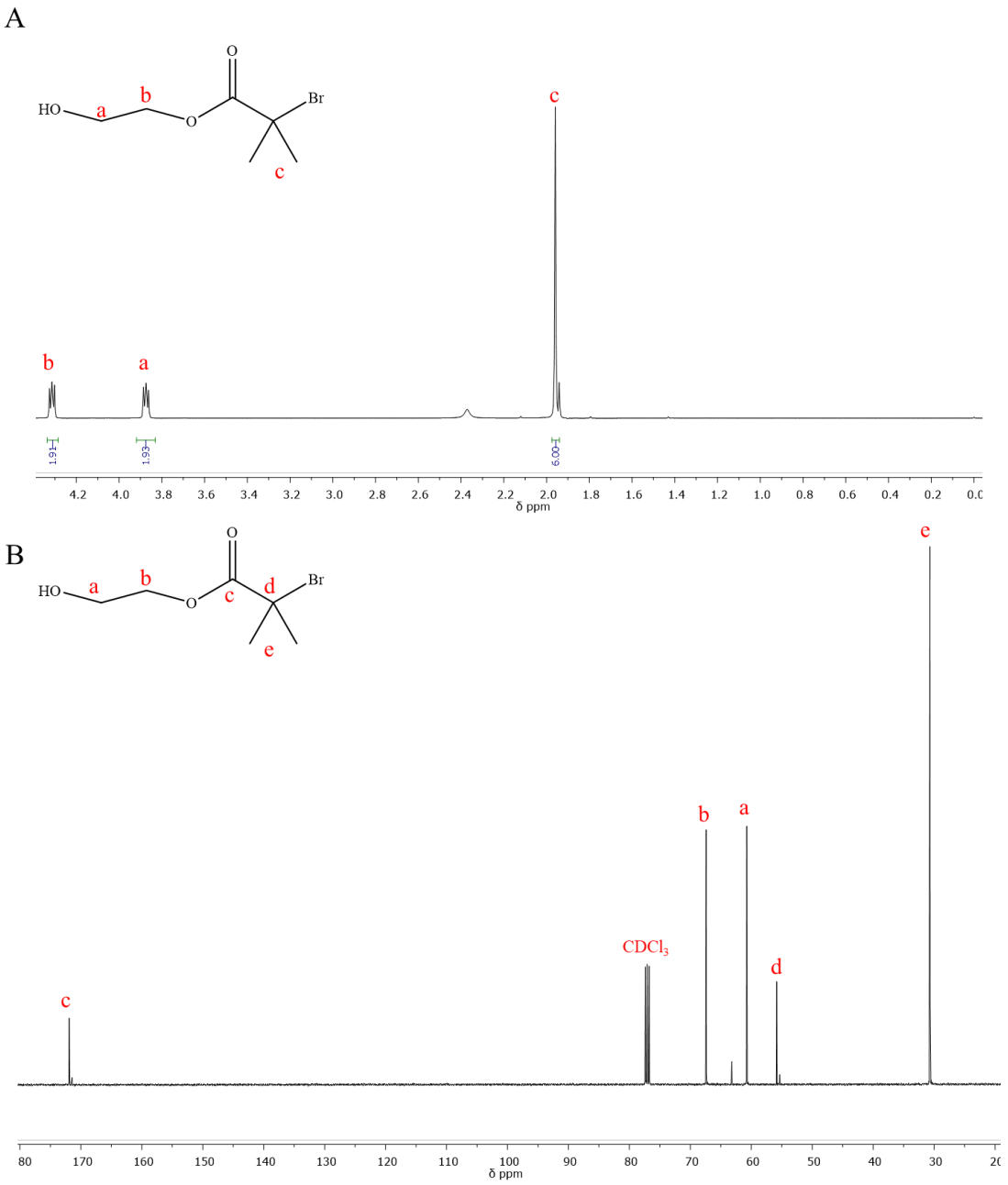

Figure 4.6 A) ^{1}H NMR ($CDCl_3$, 400 MHz) and B) ^{13}C NMR ($CDCl_3$, 100 MHz) of HBiB.

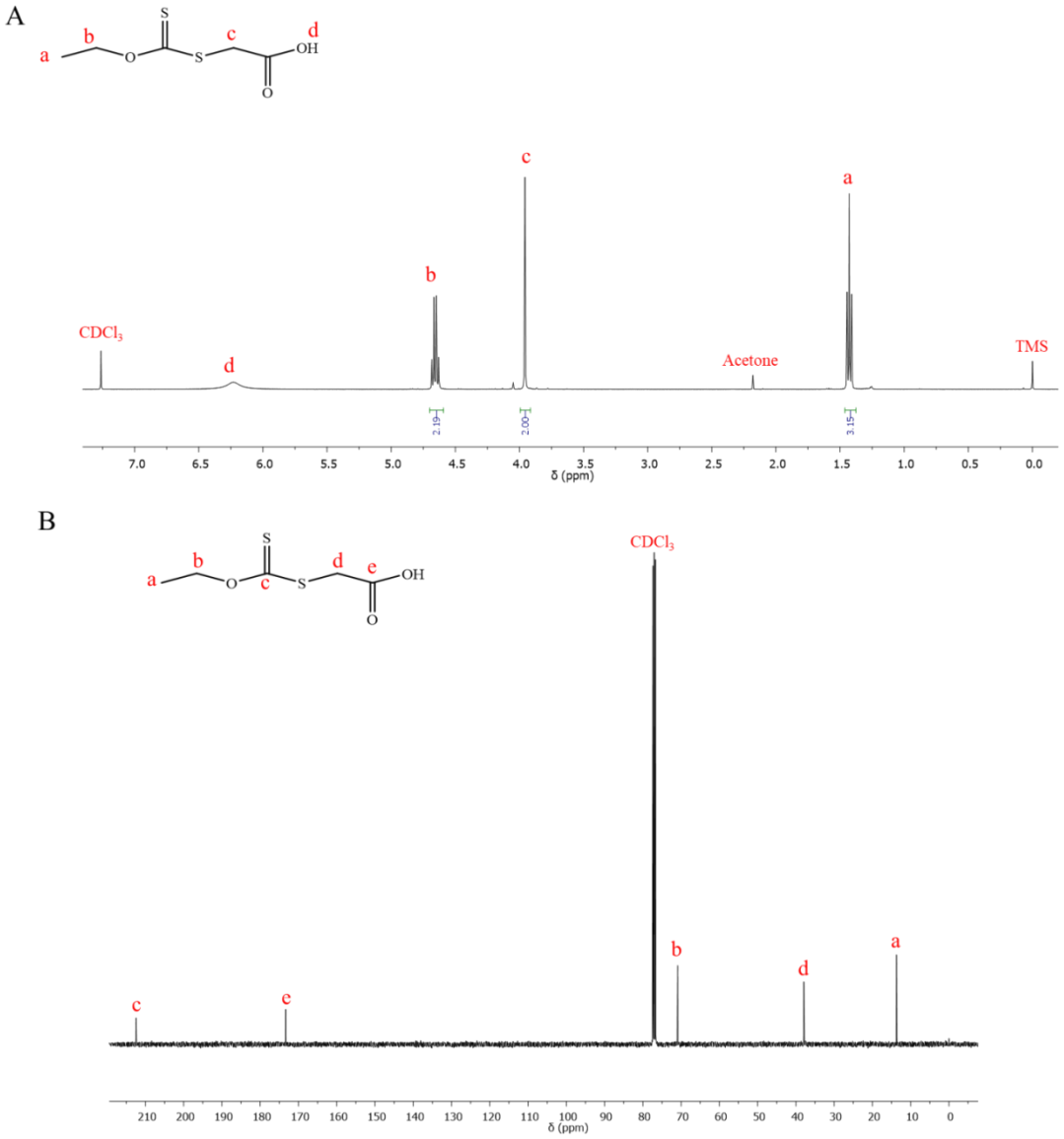

Figure 4.7 A) ^{1}H NMR ($CDCl_3$, 400 MHz) and B) ^{13}C NMR ($CDCl_3$, 100 MHz) of XanCOOH.

The formation of the XanBiB ATRP initiator was accomplished by an esterification between these molecules (HBiB and XanCOOH), Scheme 4.1iii, using N,N'-dicyclohexylcarbodiimide/4-(dimethylamino)pyridinium *p*-toluenesulfonate (DCC/DPTS) coupling. Removal of the *N,N'*-dicyclohexylurea by-product by filtration was followed by liquid-liquid extraction. The crude product was further purified by column chromatography, eluting ethyl acetate:hexane (30:70). A yellow oil was recovered and fully characterised by NMR (^{1}H and ^{13}C), Figure 4.8 A-B and mass spectrometry, Figure 4.9.

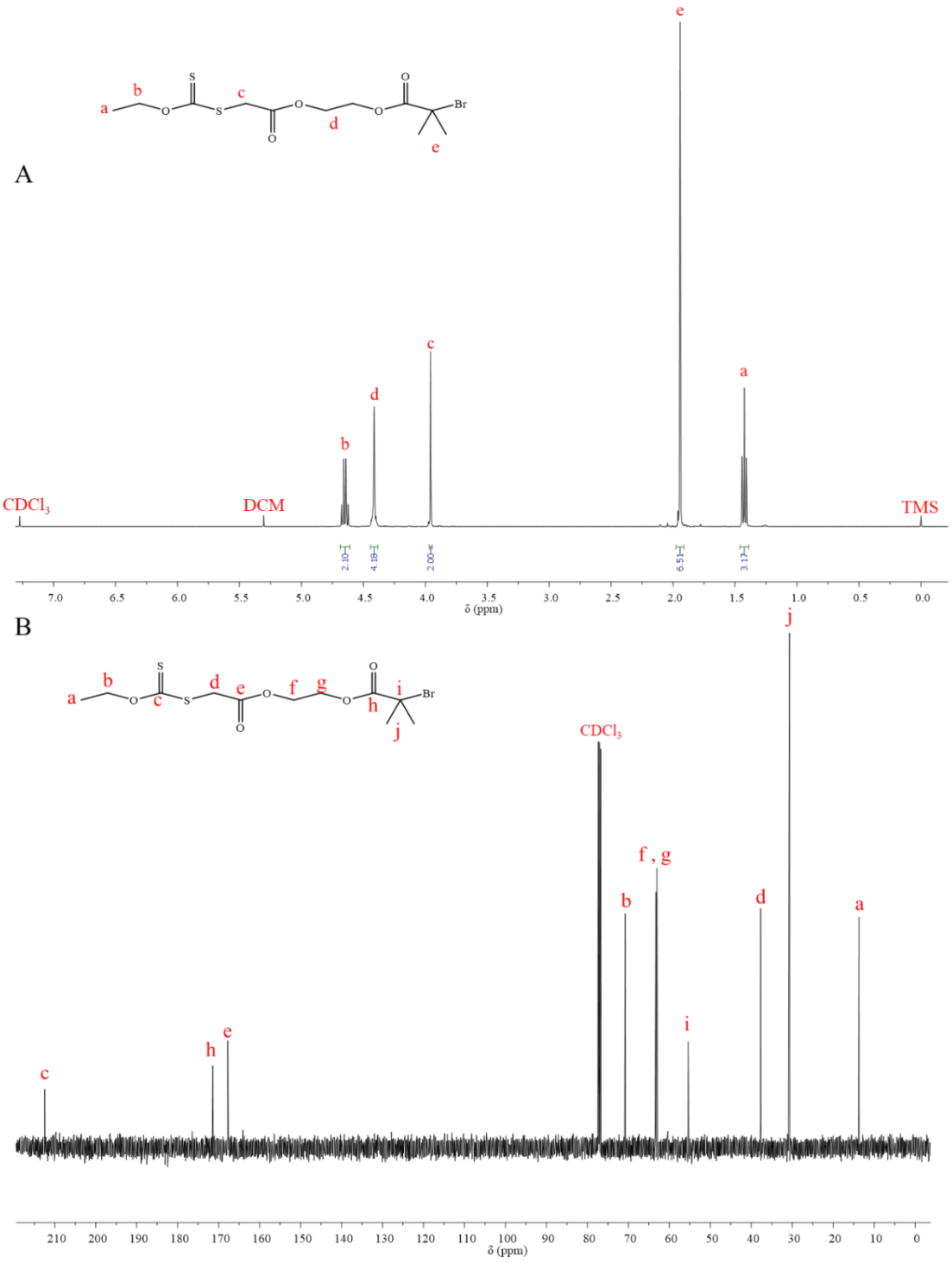

Figure 4.8 A) ^{1}H NMR ($CDCl_3$, 400 MHz) and B) ^{13}C NMR ($CDCl_3$, 100 MHz) of XanBiB.

The ^{1}H NMR spectrum of a purified XanBiB is presented in Figure 4.8A, with the presence of some residual DCM which was later removed *in vacuo*. Reaction of HBiB with XanCOOH is shown to be completed *via* the appearance of a multiplet peak at

4.41 ppm attributed to C<u>H</u>$_2$C<u>H</u>$_2$ (labelled d). This peak is the merging of two well resolved triplets from HBiB attributed to HO-C<u>H</u>$_2$ and C<u>H</u>$_2$OC=O at 3.87 and 4.31 ppm respectively, Figure 4.6A. The loss of a broad singlet at 6.4 ppm –O<u>H</u>, Figure 4.7A, from XanCOOH is also observed. Electrospray (ES) mass spectrometry was in agreement with the desired product, where XanBiB exact mass = 372 and the ES mass spectrometry experimentally determined $[M+Na]^+$ m/z = 395.

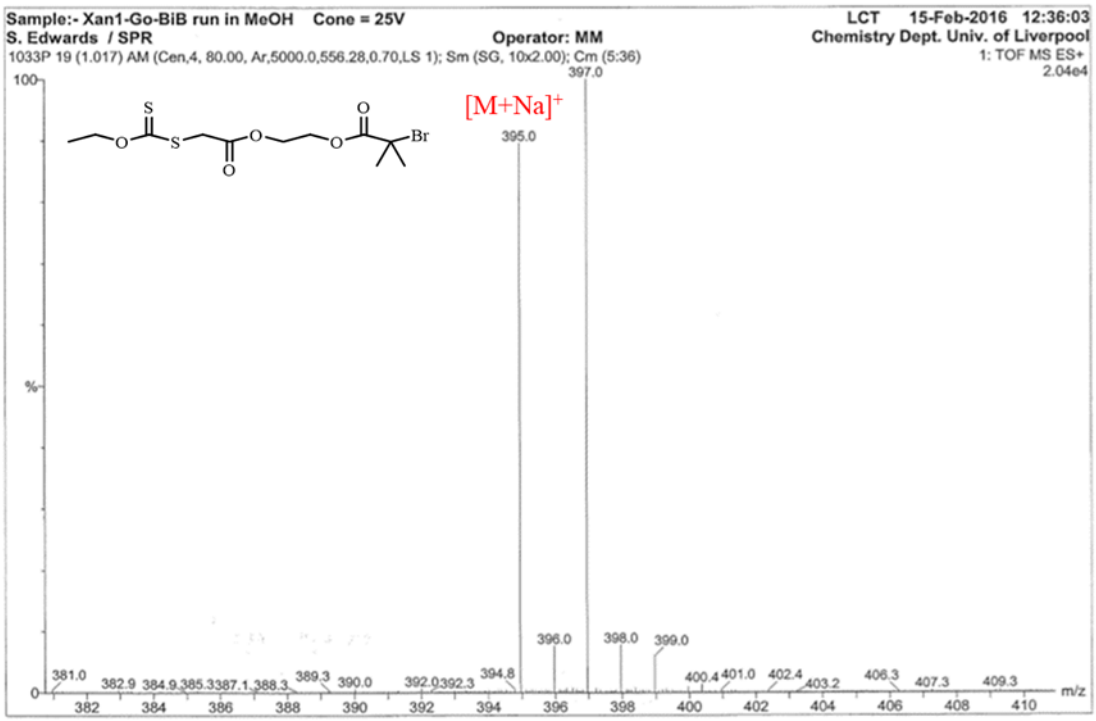

Figure 4.9 MS-ES (MeOH) analysis of XanBiB.

4.2.1 Linear Polymer and Branched Copolymer Synthesis

Linear polymers were synthesised from OEGMA using XanBiB by employing the same ATRP conditions as the linear polymers initiated by DBiB and PBiB detailed in Chapters 2 and 3. Again, a CuCl:bpy catalytic system (1:2:1 ratio with initiator group) was used and linear polymerisations targeted DP_n = 50 monomer units were conducted in a IPA/water (92.5/7.5 % v/v) co-solvent mixture at 55 % w/v (monomer:solvent) at 40 °C, Scheme 4.2. Polymer reactions were monitored *via* ^{1}H NMR, analysing the conversion of vinyl monomer peaks in reference to an internal standard (anisole) and all reactions were considered successful if very high monomer conversion (> 99 %) was achieved. Removal of copper catalyst was performed in all cases *via* a neutral

alumina column and the polymers were purified by precipitation into petroleum ether (40/60).

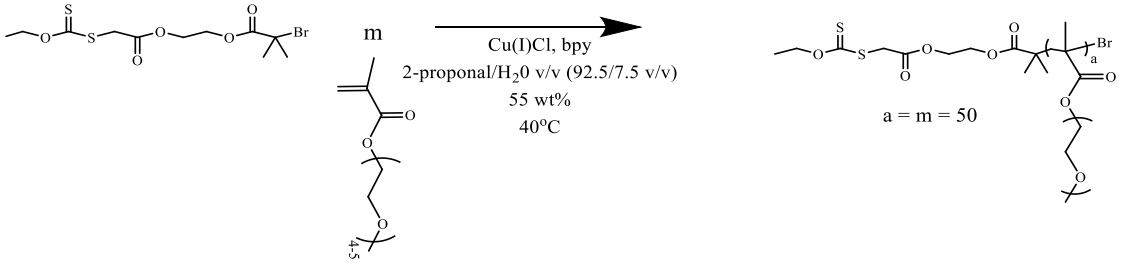

Scheme 4.2 Synthesis of a linear *p*(OEGMA) polymer initiated with XanBiB, targeting $DP_n = 50$.

As with previous studies reported in Chapters 2 and 3, branched XanBiB-initiated copolymers were also synthesised under the same conditions described above with addition of an EGDMA branching monomer at a ratio of 0.80:1.00 ($[EGDMA]_0$ / $[I]_0$ = 0.80) to yield branched copolymers after 24 hours reaction time.

Again, following the procedures and strategy for branched copolymer co-initiation described in Chapter 3, branched copolymers were synthesised by varying the molar ratio of initiator groups DBiB and XanBiB. Across the series of co-initiated branched copolymers, the molar ratio of DBiB:XanBiB was varied over a wide range spanning 1:0 and 0:1, Scheme 4.3, yielding final polymer compositions of $DBiB_xXanBiB_y$*p(*$OEGMA_{50}$-*co*-$EGDMA_{0.8}$) where x + y = 1; the resulting copolymer library, therefore, represents complex macromolecules with systematically varying molar ratios of hydrophobic and functional chain ends whilst maintaining the same hydrophilic OEGMA based polymer core, Figure 4.4. The specific DBiB:XanBiB co-initiation ratios employed here were: 0.92:0.08, 0.75:0.25, 0.5:0.5, 0.25:0.75, 0.1:0.9 and 0.05:0.95.

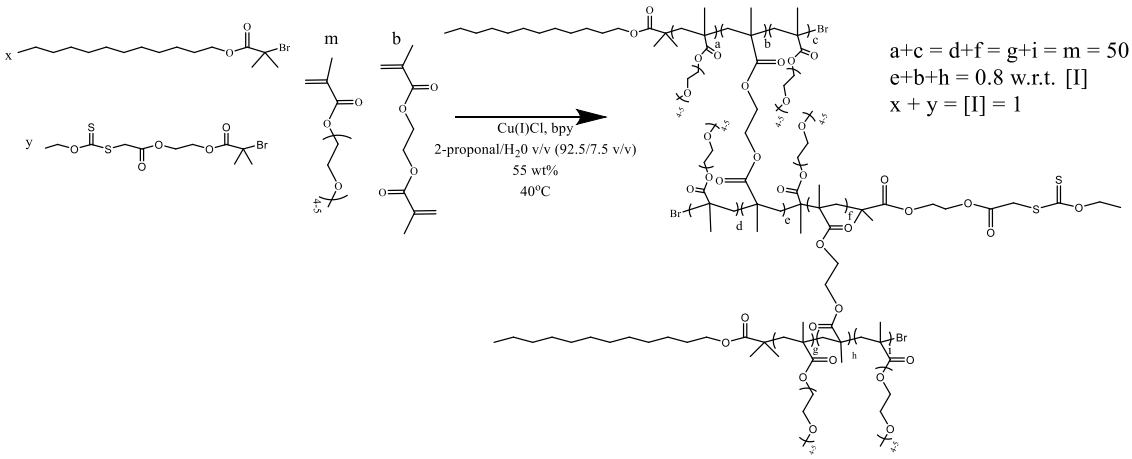

Scheme 4.3 Co-initiated branched copolymerisation of OEGMA and EGDMA with varying ratios of DBiB:XanBiB.

4.2.2 Post-polymerisation Functionalisation of Co-Initiated Branched Copolymers

Post-polymerisation deprotection/functionalisation was carried out on the xanthate-containing linear and branched macromolecules *via* a one-pot removal of the xanthate group with 10:1 excess of *n*-butylamine with respect to xanthate groups, as previously reported, Scheme 4.4.[108,138,144] Thiolated polymer samples were isolated by precipitation of crude polymer samples twice into cold hexane.

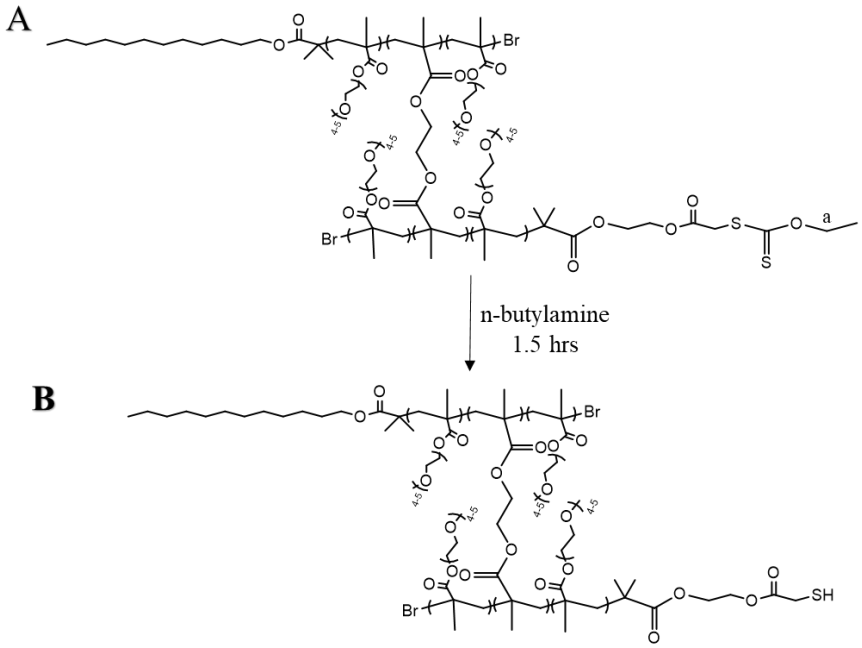

Scheme 4.4 Deprotection of $XanBiB_xDBiB_y$-*p(*$OEGMA_{50}$-*co*-$EGDMA_{0.8}$) in the presence of n-butylamine (anhydrous THF, room temperature, 1.5 hrs) to yield SH_xDBiB_y-*p(*$OEGMA_{50}$-*co*-$EGDMA_{0.8}$) where x+y = 1 = [I].

Removal of the protecting group was characterised and confirmed by ^{1}H NMR, Figure 4.10. Loss of the quartet at 4.65 ppm attributed to $CH_3C\underline{H_2}$-O (labelled a) is observed, which is characteristic of the deprotection of all polymers.

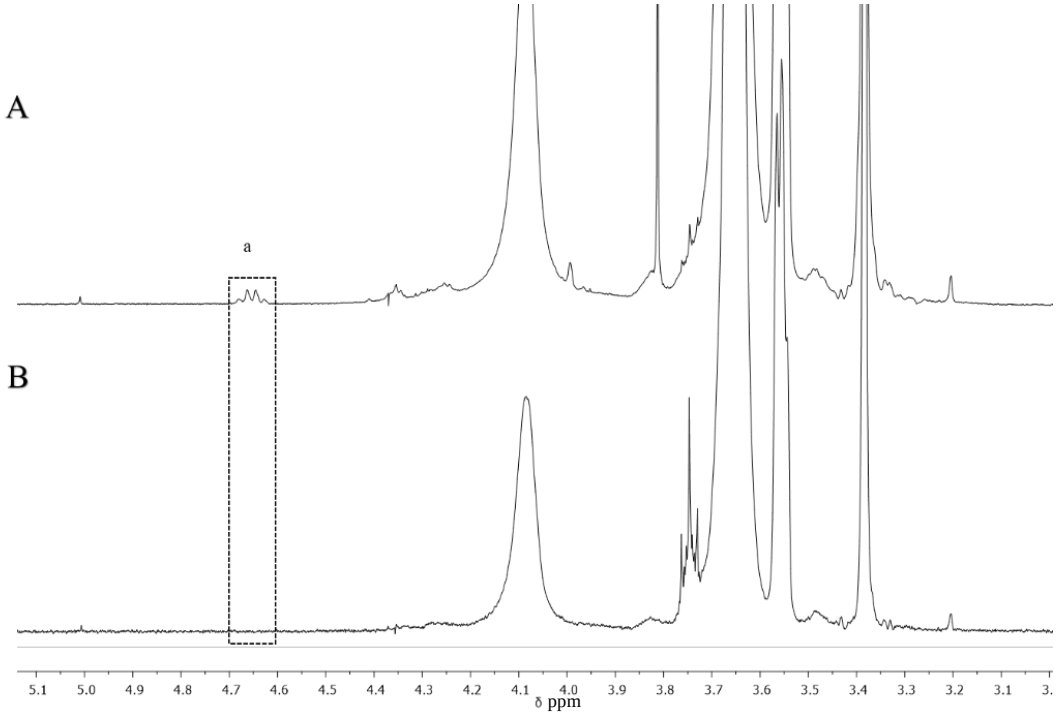

Figure 4.10 ^{1}H NMR (400 MHz, $CDCl_3$) A) $XanBiB_{0.75}DBiB_{0.25}$-*p(*$OEGMA_{50}$-*co*-$EGDMA_{0.8}$) and $SH_{0.75}DBiB_{0.25}$-*p(*$OEGMA_{50}$-*co*-$EGDMA_{0.8}$) showing loss of xanthate protecting group.

4.2.3 Polymer Characterisation

As with the polymers synthesised in Chapters 2 and 3, all xanthate linear and branched copolymers were characterised by GPC and ^{1}H NMR to determine success of each polymerisation, Table 4.1. ^{1}H NMR end-group analysis allows number average molecular weight to be determined for linear polymer samples, but provides little useful information for co-initiated branched copolymers.

Table 4.1 GPC and ^{1}H NMR characterisation of OEGMA-derived polymers co-initiated with XanBiB:DBiB in varying molar ratios.

Target Polymer Composition	^{1}H NMR[b]		GPC[a]		
	Conversion (%)	Theoretical M_n	M_w (g/mol)	M_n (g/mol)	Đ
XanBiB-*p(*$OEGMA_{50}$)	99	15, 373	39,300	22,800	1.7
$DBiB_{0.92}XanBiB_{0.08}$-*p(*$OEGMA_{50}$-*co*-$EGDMA_{0.8}$)	>99	-	297,024	45,856	6.3
$DBiB_{0.75}XanBiB_{0.25}$-*p(*$OEGMA_{50}$-*co*-$EGDMA_{0.8}$)	>99	-	147,522	38,240	3.8
$DBiB_{0.50}XanBiB_{0.50}$-*p(*$OEGMA_{50}$-*co*-$EGDMA_{0.8}$)	>99	-	401,500	52,000	7.7
$DBiB_{0.25}XanBiB_{0.75}$-*p(*$OEGMA_{50}$-*co*-$EGDMA_{0.8}$)	>99	-	281,893	70,749	3.9
$DBiB_{0.10}XanBiB_{0.90}$-*p(*$OEGMA_{50}$-*co*-$EGDMA_{0.8}$)	>99	-	134,501	37,151	3.6
$DBiB_{0.05}XanBiB_{0.95}$-*p(*$OEGMA_{50}$-*co*-$EGDMA_{0.8}$)	>99	-	367,200	64,800	5.7
XanBiB-*p(*$OEGMA_{50}$-*co*-$EGDMA_{0.8}$)	99	-	50,818	23,824	2.1

[a] GPC (DMF/0.01 M LiBr Eluent 60ºC); [b] ^{1}H NMR ($CDCl_3$,400 MHz)

As shown in previous Chapters, the inclusion of a low concentration of EGDMA leads to a broadening of dispersity and considerable increase in weight average molecular weight. This can be readily seen in the refractive index and right angle light scattering chromatograms of the branched copolymers, Figure 4.11, and was previously seen for the branched copolymers of Chapters 2 and 3. All polymers co-initiated with DBiB:XanBiB reached 99 % or greater conversion which is important for intramolecular branching in these copolymerisation strategies.

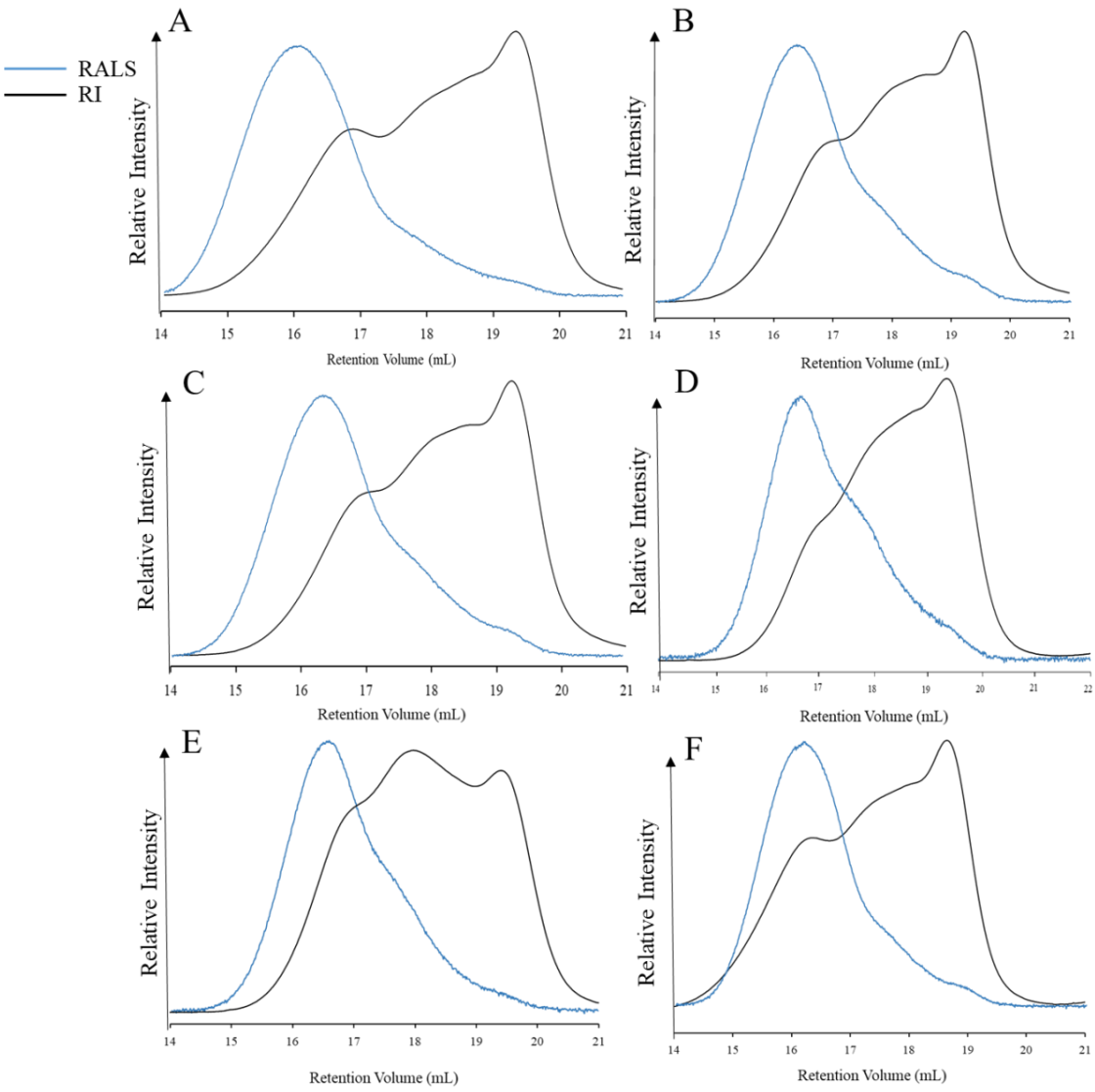

Figure 4.11 Overlay of RI (black) and RALS (blue) chromatograms of A) DBiB$_{0.92}$XanBiB$_{0.08}$-*p*(OEGMA$_{50}$-*co*-EGDMA$_{0.8}$), B) DBiB$_{0.75}$XanBiB$_{0.25}$-*p*(OEGMA$_{50}$-*co*-EGDMA$_{0.8}$), C) DBiB$_{0.50}$XanBiB$_{0.50}$-*p*(OEGMA$_{50}$-*co*-EGDMA$_{0.8}$), D) DBiB$_{0.75}$XanBiB$_{0.25}$-*p*(OEGMA$_{50}$-*co*-EGDMA$_{0.8}$), E) DBiB$_{0.10}$XanBiB$_{0.90}$-*p*(OEGMA$_{50}$-*co*-EGDMA$_{0.8}$) and F) DBiB$_{0.05}$XanBiB$_{0.95}$-*p*(OEGMA$_{50}$-*co*-EGDMA$_{0.8}$).

Interestingly, comparison of the linear XanBiB-*p*(OEGMA$_{50}$) and branched XanBiB-*p*(OEGMA$_{50}$-*co*-EGDMA$_{0.8}$), Figure 4.12, did not display the same dramatic and characteristic increase in M_w and M_n as expected for the inclusion of a EGDMA into the copolymerisation. The linear polymer contained a high molecular weight shoulder on the RI chromatogram, showing a small amount of intermolecular coupling during the polymerisation, as discussed in Section 2.2.2 resulting in the higher than expected

dispersity value of 1.7 and the higher M_w value of 39,370 g/mol. The lack of branching in this copolymerisation, utilising just the single XanBiB initiator is unclear, but these polymers were not studied for emulsion formation.

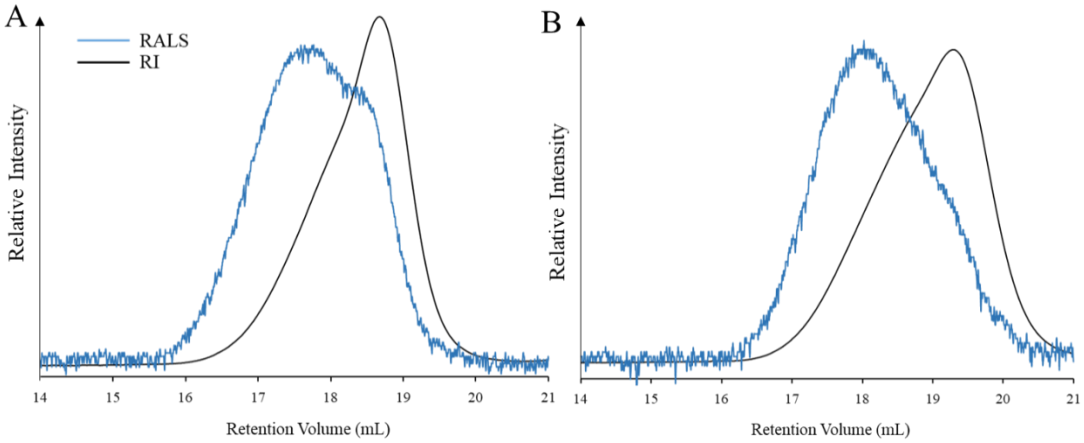

Figure 4.12 Overlay of RI (black) and RALS (blue) traces of A) XanBiB-*p*(OEGMA$_{50}$) and B) XanBiB-*p*(OEGMA$_{50}$-*co*-EGDMA$_{0.8}$).

As described in Chapter 3 Section 3.2.2, the data collected by the GPC analysis allows the determination of the cumulative weight fraction *vs.* molecular weight relationship for each polymer studied. This analysis was conducted for the xanthate containing branched copolymers and the three same nominal molecular weights of 500,000, 750,000 and 1,000,000 g/mol were chosen to illustrate the fraction of very highly branched material in each sample, Table 4.2. These molecular weight values represent structures that have approximately 19, 28 and 37 conjoined primary chains assuming an average M_n of the primary chains as 26,775 g/mol (average of the linear polymer primary chain M_n values for XanBiB-*p*(OEGMA)$_{50}$ and DBiB-*p*(OEGMA)$_{50}$).

Unfortunately, no direct trend was observed for the branched copolymers, however a range of values from 5.6 wt % (DBiB$_{0.10}$XanBiB$_{0.90}$-*p*(OEGMA$_{50}$-*co*-EGDMA$_{0.8}$)) to 18.9 wt % (DBiB$_{0.50}$XanBiB$_{0.50}$-*p*(OEGMA$_{50}$-*co*-EGDMA$_{0.8}$)) of the samples were shown to contain a minimum of 19 conjoined chains and statistically, these high molecular weight species would be bearing at least one thiol group, even at the lowest ratio of XanBiB used within the co-initiated copolymerisations (8 mol %).

Table 4.2 Percentage of polymer weight fraction above 500,000, 750,000 and 1,000,000 g/mol analysed from cumulative weight fraction graph plotted from GPC data (DMF/0.01 M LiBr Eluent 60 ºC, 1 mL/min).

Polymer Composition	Weight % >500,000 (g/mol)	Weight % >750,000 (g/mol)	Weight % >1,000,000 (g/mol)
$DBiB_{0.92}XanBiB_{0.08}$-*p(*$OEGMA_{50}$-*co*-$EGDMA_{0.8}$)	17.7	11.6	8
$DBiB_{0.75}XanBiB_{0.25}$-*p(*$OEGMA_{50}$-*co*-$EGDMA_{0.8}$)	7.7	3.4	1.7
$DBiB_{0.50}XanBiB_{0.50}$-*p(*$OEGMA_{50}$-*co*-$EGDMA_{0.8}$)	18.9	13	9.4
$DBiB_{0.25}XanBiB_{0.75}$-*p(*$OEGMA_{50}$-*co*-$EGDMA_{0.8}$)	7.7	3.9	2.1
$DBiB_{0.10}XanBiB_{0.90}$-*p(*$OEGMA_{50}$-*co*-$EGDMA_{0.8}$)	5.6	2.1	0.9
$DBiB_{0.05}XanBiB_{0.95}$-*p(*$OEGMA_{50}$-*co*-$EGDMA_{0.8}$)	15.6	9.9	6.6

The lack of any discernible trends is further exemplified in Figure 4.13. The polymer containing the highest weight of high molecular weight species, fraction across all of the nominal molecular weights, is $DBiB_{0.50}XanBiB_{0.50}$-*p*($OEGMA_{50}$-*co*-$EGDMA_{0.8}$), where the weight fraction of the polymer >1,000,000 g/mol (> 37 primary chains) was 9 %.

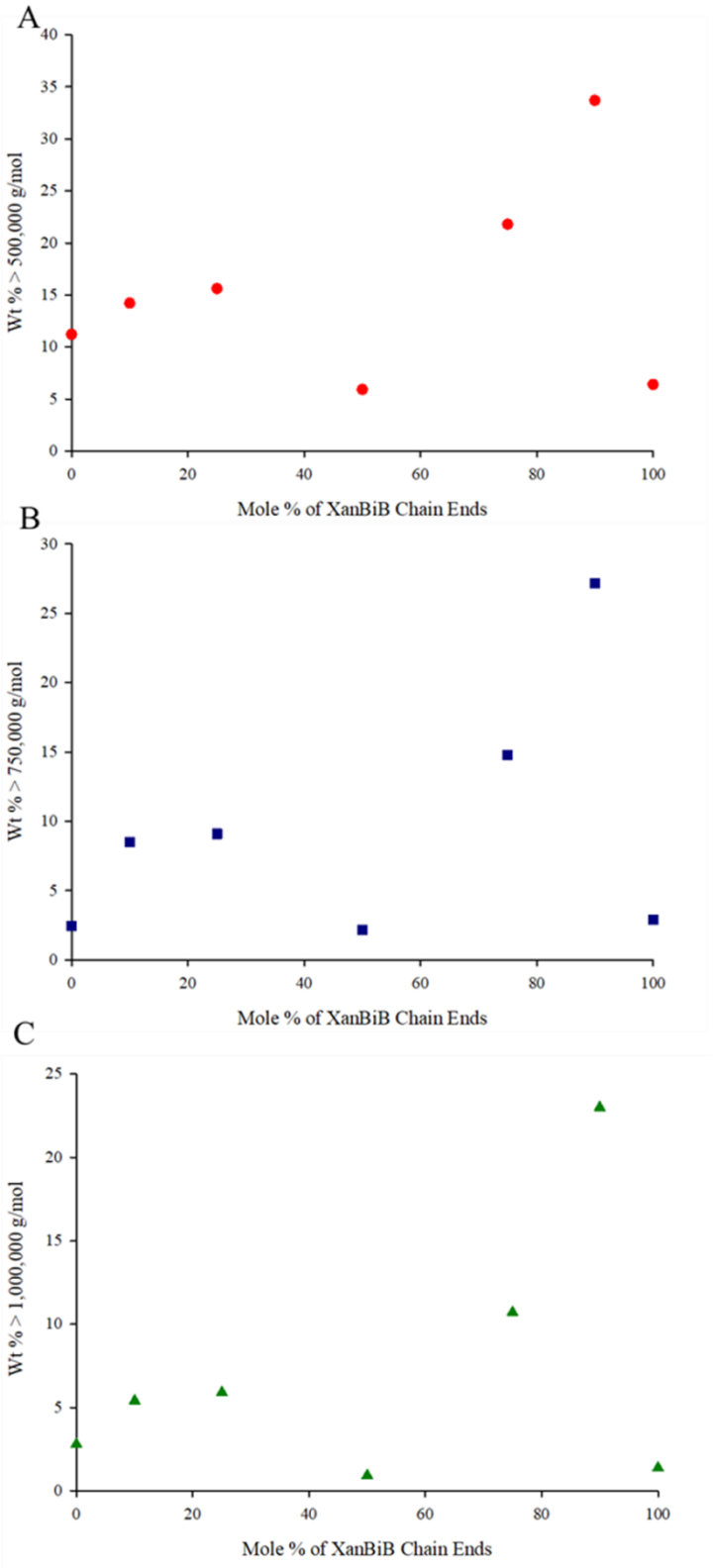

Figure 4.13 Weight fraction of co-initiated XanBiB$_x$DBiB$_y$-*p*(OEGMA$_{50}$-*co*-EGDMA$_{0.8}$) branched copolymers with molecular weights greater than A) 500,000, B) 750,000 and C) 1,000,000 g/mol, plotted against molar percent of XanBiB initiator used in the co-initiated copolymerisation.

4.2.2 Kinetic Evaluation of Singly Initiated and Coinitiated Linear Polymerisations of OEGMA.

The kinetics of a XanBiB initiated linear polymerisation of OEGMA was compared with the formation of a mixture of linear polymers through the simultaneous co-initiation of OEGMA using a 1:1 ratio of DBiB and XanBiB. The polymerisations were monitored by ^{1}H NMR, Figure 4.14, and monomer conversion was determined by the ratio between OEGMA vinyl peaks at 6.13 and 5.58 ppm and *p(*OEGMA) pendant chain at 3.4 ppm.

Polymerisations were studied over 7 hours, with samples taken and studied hourly. As shown by the ^{1}H NMR spectra, vinyl peaks could not be distinguished after 6 hours for the reaction forming XanBiB-*p(*OEGMA); after 5 hours reaction within the co-initiated polymerisation, only a very weak signal for the vinyl protons was observable and no residual vinyl bonds were detectable after 6 hours. The similarity of the consumption of monomer in these reactions suggests that the polymerisations are not affected by the mixture of initiators and that the two initiators appear to lead to similar overall rates of polymerisation.

The ^{1}H NMR data may also be plotted to generate a kinetic plot showing both conversion vs time and the semi-logarithmic plot that is regularly used to confirm a consistent concentration of radicals within the ATRP reaction, Figure 4.15.

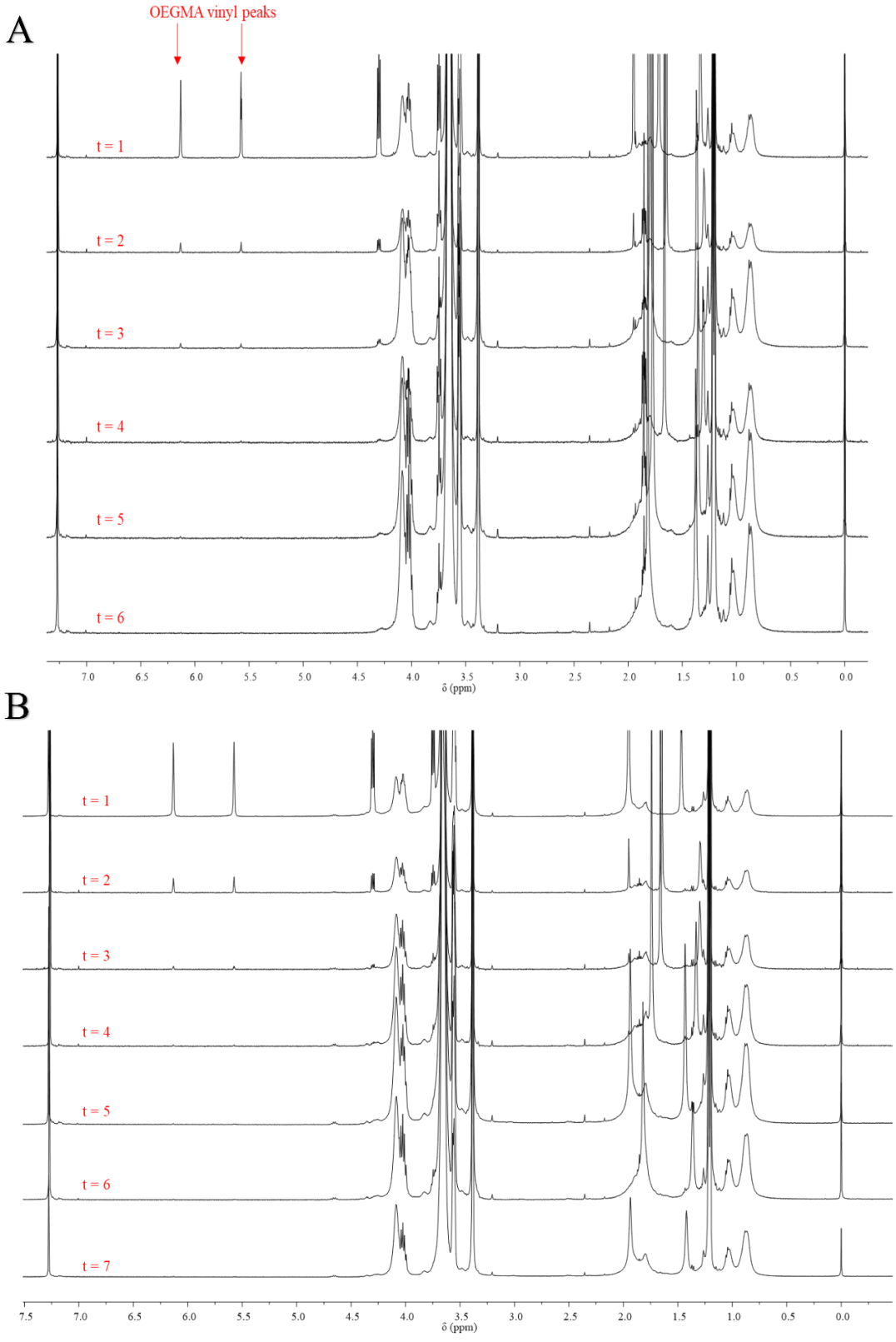

Figure 4.14 Kinetic analysis of ATRP polymerisations using xanthate-functional initiators: ^{1}H NMR ($CDCl_3$, 400 MHz) spectra for the synthesis of A) XanBiB-*p*(OEGMA$_{50}$) and B) the simultaneous formation of DBiB-*p*(OEGMA$_{50}$) and XanBiB$_{0.5}$-*p*(OEGMA$_{50}$) (1:1 molar ratio).

The graphical representations of the kinetic studies are shown in Figure 4.15. First order reactions are indicated in both cases, with high conversion being achieved at a similar time and comparable rates of monomer consumption.

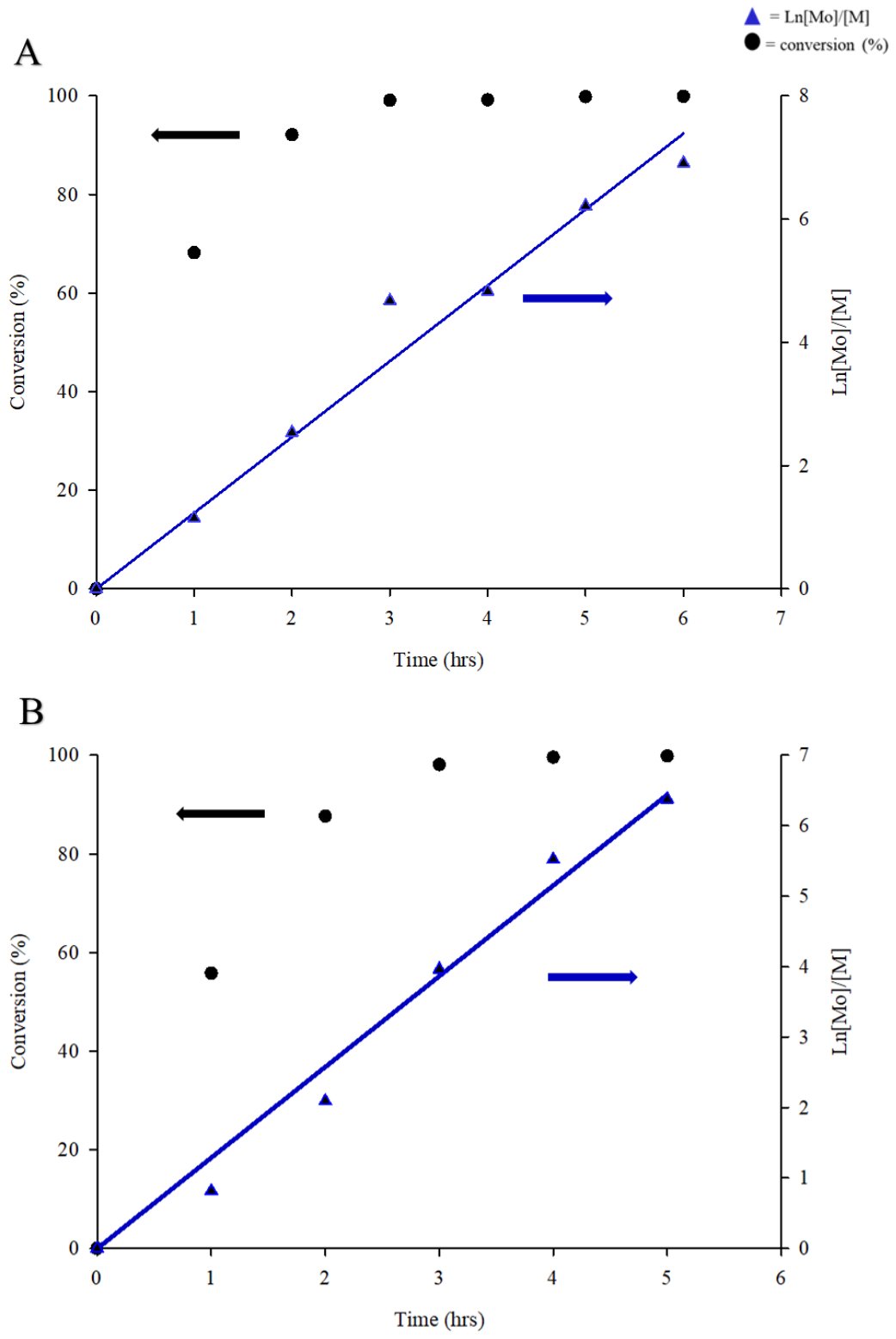

Figure 4.15 Kinetic analysis of A) XanBiB-*p*(OEGMA$_{50}$) synthesis and B) the simultaneous formation of DBiB-*p*(OEGMA$_{50}$) and XanBiB$_{0.5}$-*p*(OEGMA$_{50}$).

4.2.4 Critical Micelle Concentration Measurements of Thiol-functional Branched Copolymers

As the thiol-functional branched copolymers were designed to be utilised as functional stabilisers for macro- and nano-emulsions, the study of the aqueous solutions of the copolymers was conducted to determine self-assembly behaviour and critical micelle concentrations as detailed in Section 3.2.4.1, for the analogous copolymers that were co-initiated by DBiB and PBiB. The CMC values were obtained by calculating the intercept between the lines of best fit for the linear decrease in surface tension and the first plateau area, Figure 4.16.

All, surface tension measurements were conducted as outlined in Chapter 3, Section 3.2.4.1 using a Kibron Delta-8 surface tensiometer at 20 °C. Aqueous polymer solutions were prepared at 30 wt % and subsequent dilutions gave 30 different concentrations down to 6.9 x 10^{-9} wt %. Use of a 96 well-plate allowed for high throughput analysis of samples after 50 μL of each copolymer surfactant (n=8) was added to each well, with pure water as a control. The measured surface tension values were plotted against the surfactant concentration (logarithmic scale).

Interestingly, the thiol-functional branched copolymer solutions also showed the same multiple plateau regions as copolymer concentrations were increased. This complex surfactant behaviour was previously interpreted in Chapter 3 as potentially resulting from the diverse mixture of macromolecular architectures, molecular weights and chain end compositions within each sample containing both PBiB and DBiB initiator residues; it is rational to assume the same behaviour would be seen here.

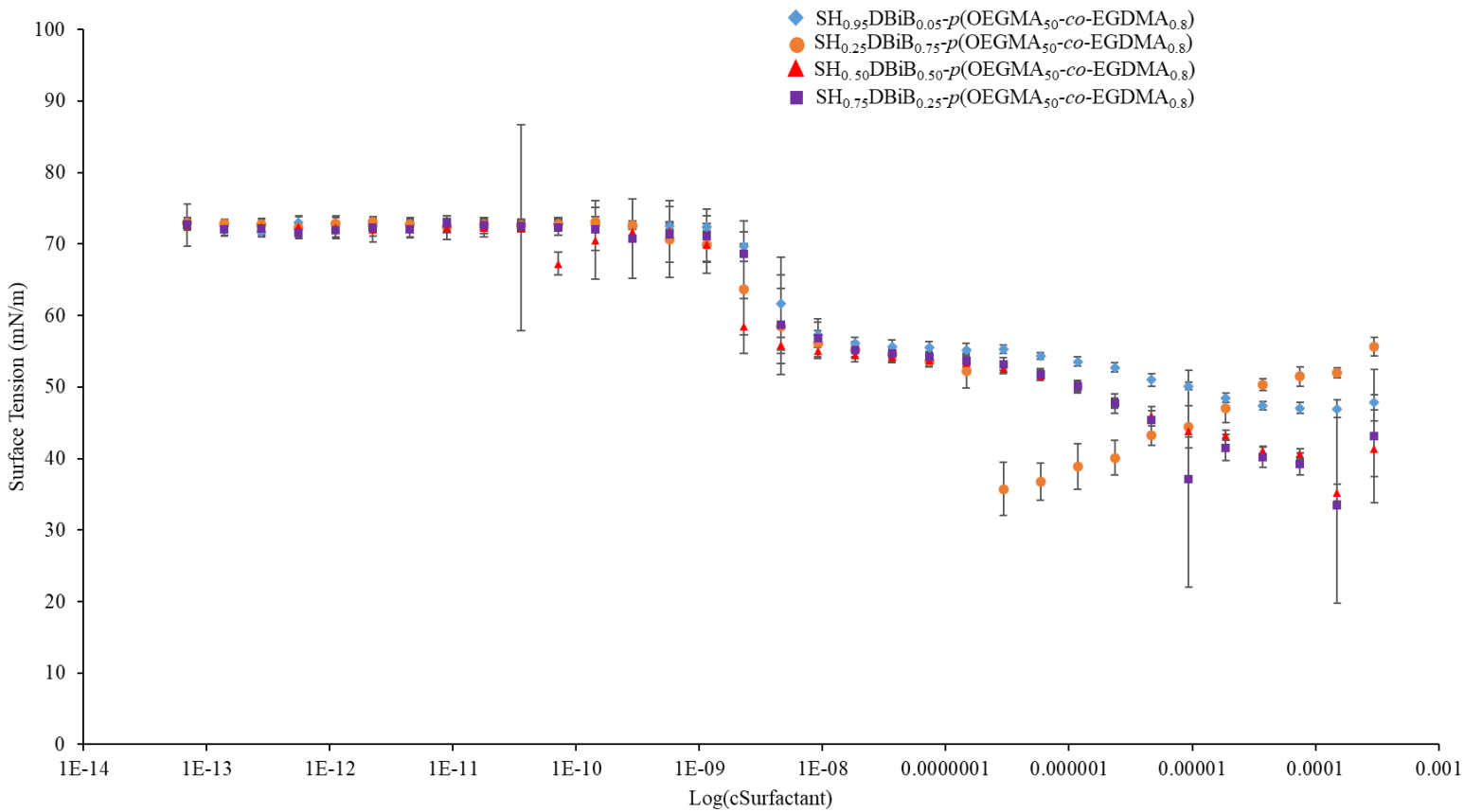

Figure 4.16 CMC data for thiol-functional branched copolymers; $SH_{0.05}DBiB_{0.95}$-*p*(OEGMA$_{50}$-*co*-EGDMA$_{0.8}$) (♦), $SH_{0.25}DBiB_{0.75}$-*p*(OEGMA$_{50}$-*co*-EGDMA$_{0.8}$) (●), $SH_{0.50}DBiB_{0.50}$-*p*(OEGMA$_{50}$-*co*-EGDMA$_{0.8}$) (▲), and $SH_{0.75}DBiB_{0.25}$-*p*(OEGMA$_{50}$-*co*-EGDMA$_{0.8}$) (■). n = 8, error bars = standard deviation.

The range of thiol functional SH_xDBiB_y-*p(*$OEGMA_{50}$-*co*-$EGDMA_{0.8}$) branched copolymer emulsifiers, studied here, show remarkably similar surface tension behaviour with nearly identical ST_{min} values and a narrow range of observed CMC values. ST_{min} is a relatively arbitrary and non-standard value that is reported here for completeness and, as can be seen in Figure 4.16, the behaviour at higher copolymer concentrations is difficult to interpret. The CMC values of these macromolecules, ranging between 9.12 $x10^{-6}$ and 1.83 $x10^{-5}$ mg/L are in marked contrast to those determined in Chapter 3 for $DBiB_xPBiB_y$-*p(*$OEGMA_{50}$-*co*-$EGDMA_{0.8}$) branched copolymers (1.08 $x10^{-8}$ to 4.74 $x10^{-8}$ mg/L); nearly three orders of magnitude in concentration difference is seen. This would indicate the $DBiB_xPBiB_y$-*p(*$OEGMA_{50}$-*co*-$EGDMA_{0.8}$) copolymers are a more surface active series of materials, and are potentially more able to align the hydrophobic chain ends at the air-water interface.

Table 4.3 CMC measurements determined from surface tensiometer measurements for branched thiol-functional copolymers and concentration where surface tension is lowest (ST_{min}). Error = graphical percentage error.

Polymer	CMC (mg/L)	ST_{min} (mg/L)
$SH_{0.25}DBiB_{0.75}$-*p(*$OEGMA_{50}$-*co*-$EGDMA_{0.8}$)	9.12 x 10^{-6} (± 8.7 %)	1.46 x 10^{-4}
$SH_{0.50}DBiB_{0.50}$-*p(*$OEGMA_{50}$-*co*-$EGDMA_{0.8}$)	9.13 x 10^{-6} (± 8.4 %)	1.50
$SH_{0.75}DBiB_{0.25}$-*p(*$OEGMA_{50}$-*co*-$EGDMA_{0.8}$)	1.55 x 10^{-5} (± 16.2 %)	1.50
$SH_{0.95}DBiB_{0.05}$-*p(*$OEGMA_{50}$-*co*-$EGDMA_{0.8}$)	1.83 x 10^{-5} (± 2.0 %)	1.50

4.2.5 Contact Angle Measurements of Thiol-functional Branched Copolymers

Contact angle measurements of aqueous thiol-functional branched copolymer solutions (5 wt % concentration) were taken using the same DSA instrument and static sessile drop method as described in Chapter 3. Also, as previously described, a hydrophobic PTFE substrate in tape form was applied to a glass slide, and 5 µL droplets of polymer solution were applied and the contact angle measured (n = 10), Figure 4.17.

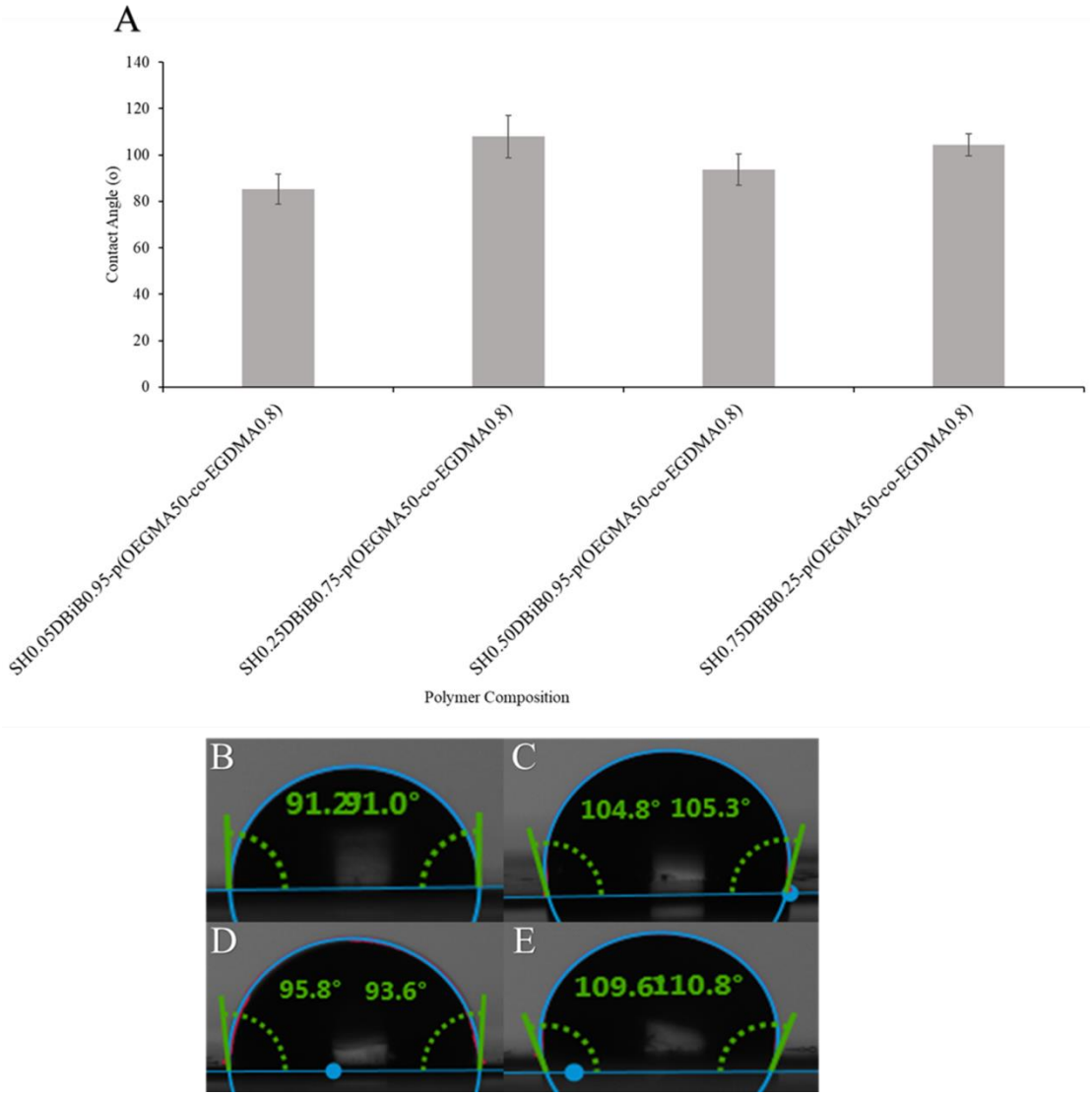

Figure 4.17 A) Contact angle measurements of thiol-functional branched copolymers and pictures of contact angle on PTFE substrate of B) $SH_{0.05}DBiB_{0.95}$-*p*($OEGMA_{50}$-*co*-$EGDMA_{0.8}$), C) $SH_{0.25}DBiB_{0.75}$-*p*($OEGMA_{50}$-*co*-$EGDMA_{0.8}$), D) $SH_{0.50}DBiB_{0.50}$-*p*($OEGMA_{50}$-*co*-$EGDMA_{0.8}$), and E) $SH_{0.75}DBiB_{0.25}$-*p*($OEGMA_{50}$-*co*-$EGDMA_{0.8}$).

The contact angle values obtained for solutions of thiol-functional branched copolymers, Table 4.5, are all below the observed value of pure water of 125° ± 3.6°, described in Chapter 3, suggesting improved wetting of the PTFE surface and presentation of hydrophobic groups to the air/water interface. The lowest contact angle was observed for $SH_{0.05}DBiB_{0.95}$-*p*($OEGMA_{50}$-*co*-$EGDMA_{0.8}$) as expected (median value = 85.03°), and this is highly comparable to the value obtained for the fully hydrophobic DBiB-*p*($OEGMA_{50}$-*co*-$EGDMA_{0.8}$) of 79.38 ° (median). Additionally, contact angle values for solutions containing branched copolymers with nominally

identical 75 mole percent DBiB-derived chain ends, namely $SH_{0.25}DBiB_{0.75}$-*p*(OEGMA$_{50}$-*co*-EGDMA$_{0.8}$) and $DBiB_{0.75}PBiB_{0.25}$-*p*(OEGMA$_{50}$-*co*-EGDMA$_{0.8}$), are also correspondingly higher than their counterparts at approximately 108 ° and 102 ° (median) showing a reduction in wetting with a reduced number of hydrophobic chain ends as expected.

Table 4.5 Contact angles measured for aqueous solutions of thiol-functional branched copolymer surfactants.

Branched Copolymer	Contact Angle (°)		
	Mean	Median	Std. Dev. (±)
DBiB-*p*(OEGMA$_{50}$-*co*-EGDMA$_{0.8}$)	79.59	79.38	2.16
$SH_{0.05}DBiB_{0.95}$-*p*(OEGMA$_{50}$-*co*-EGDMA$_{0.8}$)	85.28	85.03	6.39
$SH_{0.25}DBiB_{0.75}$-*p*(OEGMA$_{50}$-*co*-EGDMA$_{0.8}$)	107.95	108.36	9.09
$SH_{0.50}DBiB_{0.50}$-*p*(OEGMA$_{50}$-*co*-EGDMA$_{0.8}$)	93.71	93.62	6.66
$SH_{0.75}DBiB_{0.25}$-*p*(OEGMA$_{50}$-*co*-EGDMA$_{0.8}$)	104.33	104.26	4.72

Despite the significant difference in CMC values, reported in Section 4.2.4., the two libraries of branched copolymer surfactants derived from mixtures of DBiB with either PBiB or the deprotected XanBiB (thiol functionality) were clearly surface active and comparable within their chemistry and solution behaviour. Studies of emulsification were therefore conducted to establish the potential to form thiol-functional macroemulsions and nanoemulsions.

4.3 MUCOADHESIVE MACROEMULSIONS

The targeted mucoadhesive macroemulsions and nanoemulsions must contain biologically relevant oil phases and therefore all studies using the SH_xDBiB_y-*p*(OEGMA$_{50}$-*co*-EGDMA$_{0.8}$) branched copolymer surfactants as emulsifiers were conducted using either squalene or castor oil, Figure 4.18.

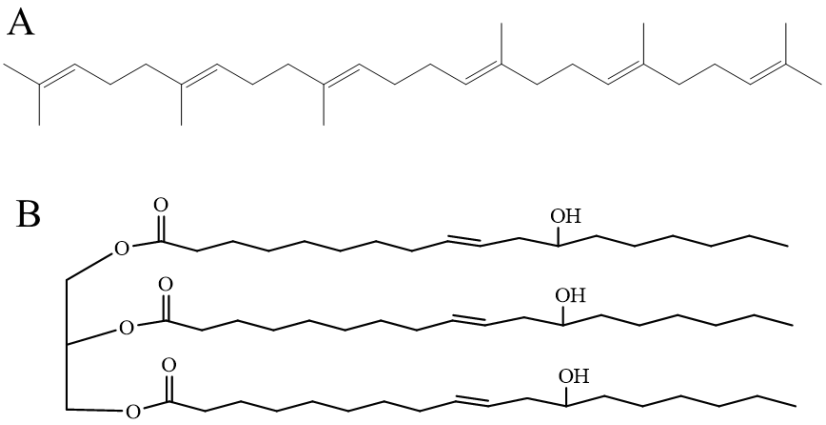

Figure 4.18 Chemical structures of A) Squalene and B) Castor oil.

4.3.1 Macroemulsion Formation using Mucoadhesive Branched Copolymer Emulsifiers

Macroemulsions were generated *via* mechanical shear using an overhead homogeniser (Ultra-Turrax 25, IKA) and aqueous branched copolymer polymer solutions (5 mg/mL) and squalene in a 1:1 volume ratio for 2 minutes at 24,000 rpm in a procedure identical to previous emulsion studies reported in Chapter 3. The resulting emulsions were left to stand overnight and equilibrate before quantitative analysis by laser diffraction spectroscopy. The $SH_{0.75}DBiB_{0.25}$-*p*($OEGMA_{50}$-*co*-$EGDMA_{0.8}$) branched copolymer was selected for detailed study as this polymer had shown to have a good overall balance of molecular weight, thiol functionality and significant weight fractions of highly branched species, Tables 4.1 and 4.2.

For completeness, and as seen for linear PBiB-initiated materials, linear SH-*p*($OEGMA_{50}$) did not form stable macroemulsions, with the minimal emulsion layer that could be retrieved after 24 hours displaying a bimodal distribution determined from laser diffraction analysis, Figure 4.19. The samples rapidly creamed and separated and, after 3 days of storage, full separation of the oil and aqueous phases was observed.

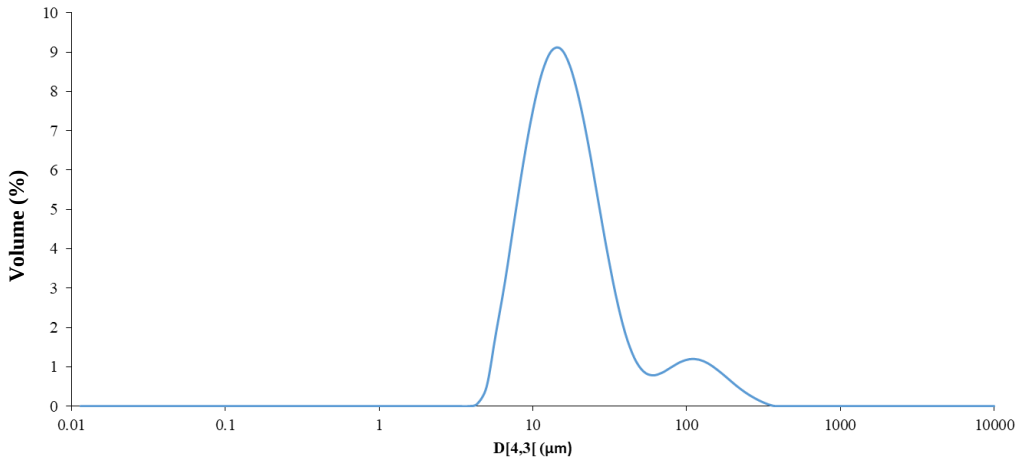

Figure 4.19 $D_{[4,3]}$ trace of SH-*p(*OEGMA$_{50}$) stabilised squalene macroemulsion layer present within a rapidly separating sample.

4.3.2 Mucoadhesive Branched Copolymer Stabilised Macroemulsion Characterisation

As stated above, SH$_{0.75}$DBiB$_{0.25}$-*p*(OEGMA$_{50}$-*co*-EGDMA$_{0.8}$) branched copolymer stabilised squalene macroemulsions were selected for detailed study; the samples were characteristically white and opaque in appearance, with creaming of the emulsion but no apparent separation of the oil phase. Laser diffraction spectroscopy was used to assess the long term stability of the emulsion when stored at ambient temperature. The volume weighted $D_{[4,3]}$ after 24 hrs of equilibration was 15.4 µm and maintained a very similar size when measured repeatedly over 5 days, 2, 3 and 4 weeks ($D_{[4,3]}$ = 15.2, 15.8, 15.9 and 16.2 µm respectively), Figure 4.20.

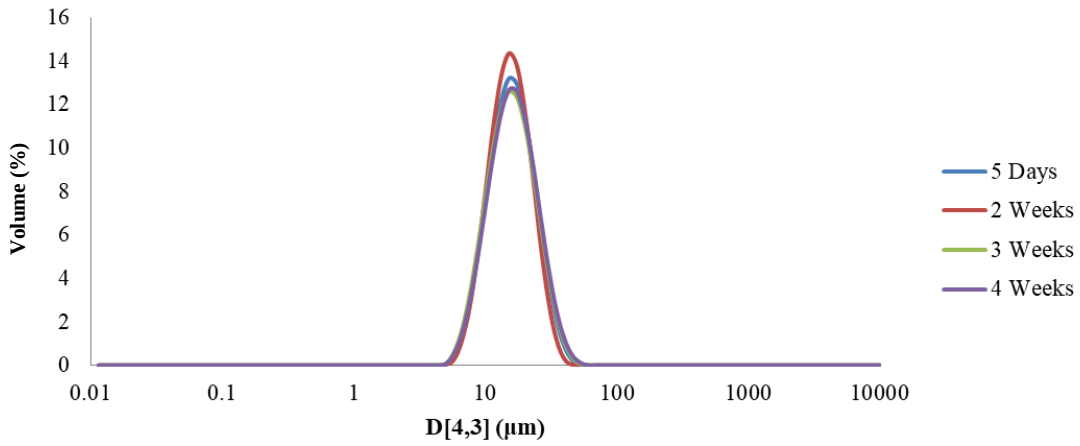

Figure 4.20 Overlay of $D_{[4,3]}$ traces showing stability of thiolated branched copolymer, $SH_{0.75}DBiB_{0.25}$-*p*($OEGMA_{50}$-*co*-$EGDMA_{0.8}$), stabilised squalene macroemulsions stored at ambient temperature for up to 4 weeks.

The stability of these macroemulsions was somewhat surprising due to the potential for thiol-thiol coupling reactions to occur under these conditions and the lack of oxygen exclusion within the stored samples. The apparent lack of disulphide formation, expected to lead to considerable emulsion droplet growth, is indicative of considerable steric repulsions between the emulsion droplets derived from the branched copolymer emulsifiers. This is noteworthy as it also suggests that the thiol groups are somewhat hidden from each other and do not readily come into contact. Intra-droplet disulphide bonds cannot be ruled out, however, and the resulting increase in branched copolymer molecular weight may lead to increased macroemulsion emulsion stability. This possibility would also lead to loss of surface thiol functionality and potential diminishing of mucoadhesive properties. Although the $D_{[4,3]}$ values did increase slightly over time, the emulsion measurements consistently gave a monomodal distribution with no observable oil release.

For subsequent studies of mucoadhesion, $SH_{0.75}DBiB_{0.25}$-*p*($OEGMA_{50}$-*co*-$EGDMA_{0.8}$) stabilised macroemulsions were loaded with one of two hydrophobic dyes; Oil red O or Oil blue A. The dyes were incorporated into emulsions at 0.1 wt % for ease of visualisation on the mucosal surface, as shown in Figure 4.20. Dye-loaded macroemulsions stabilised by DBiB-*p*($OEGMA_{50}$-*co*-$EGDMA_{0.8}$) were also generated to allow comparison with thiol-functional macroemulsions, Figure 4.21 B.

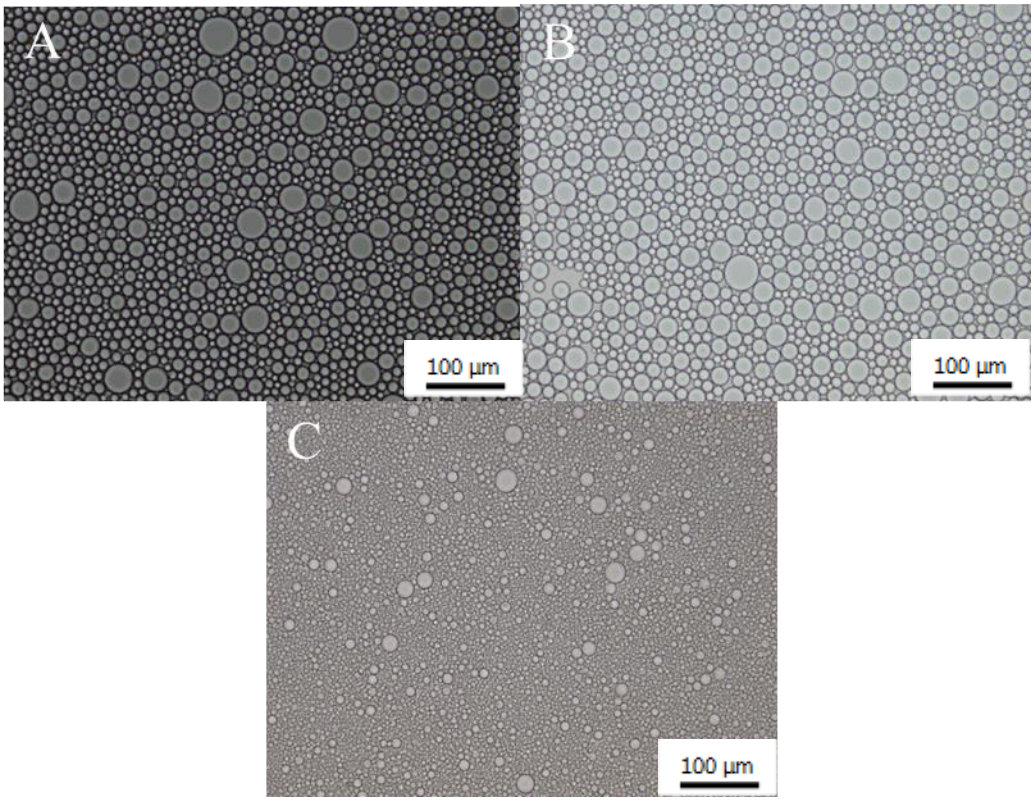

Figure 4.21 Optical microscopy images of various squalene macroemulsions at 20x zoom magnification; A) blank emulsion stabilised with $SH_{0.75}DBiB_{0.25}$-*p*($OEGMA_{50}$-*co*-$EGDMA_{0.8}$), B) oil blue A-loaded (0.1 wt %) emulsion stabilised with DBiB-*p*($OEGMA_{50}$-*co*-$EGDMA_{0.8}$), and C) Oil red O-loaded (0.1 wt %) emulsion stabilised with $SH_{0.75}DBiB_{0.25}$-*p*($OEGMA_{50}$-*co*-$EGDMA_{0.8}$).

In these experiments, and probably due to slight experimental variation, the resulting macroemulsions had a $D_{[4,3]}$ value of 13 µm, compared to that of the blank emulsion which was 15.2 µm. The optical images were analysed by FIJI (V 1.51n) to generate number distributions of droplet diameters, plotted as histograms to provide an indication of the breadth and frequency within each sample, Appendix A12-15. Oil red O and Oil blue A containing macroemulsions showed comparable distributions, indicating that approximately 90 and 95 % of the droplet populations were of diameters below 15 µm for Oil blue A and Oil red O respectively, Figure 4.22.

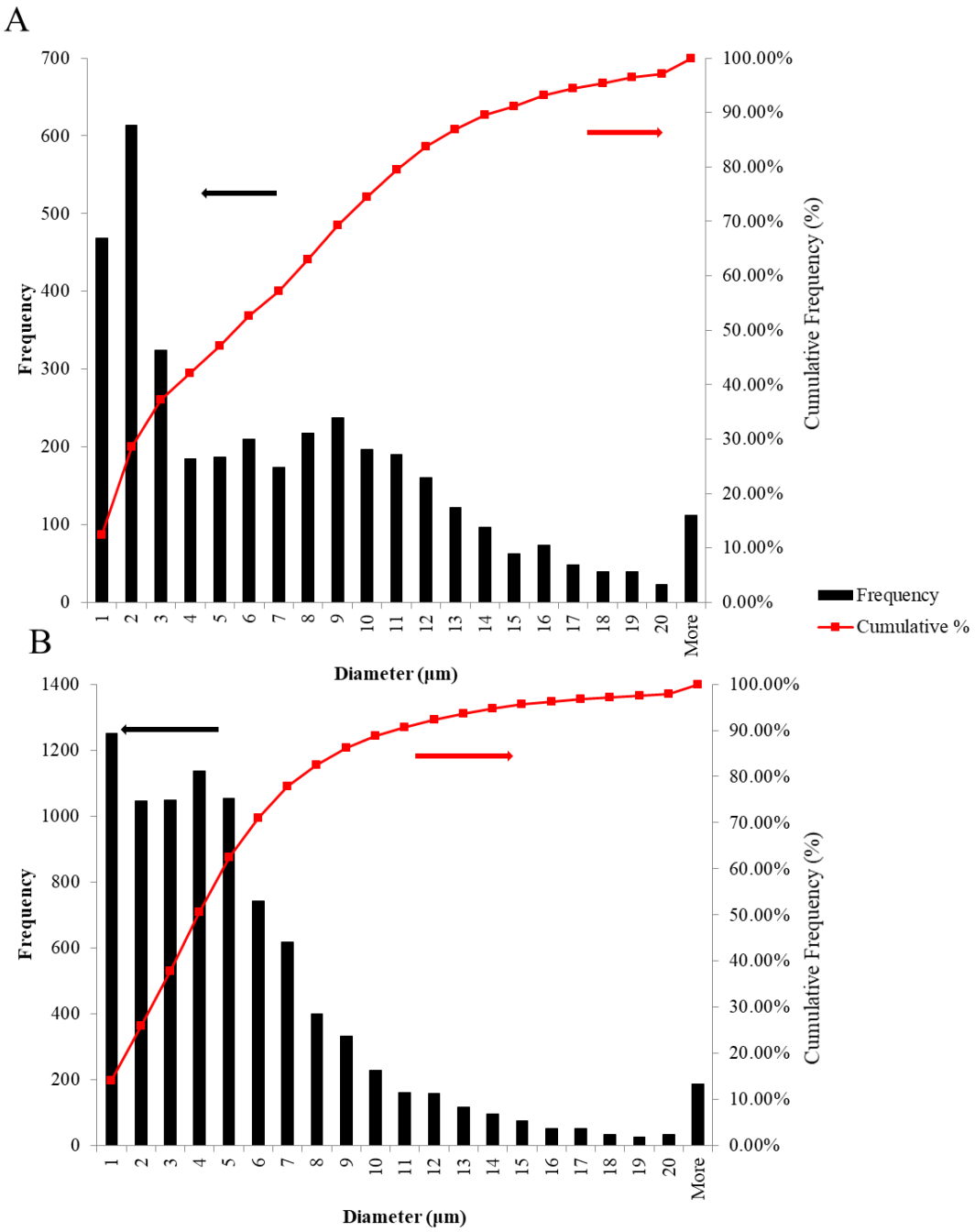

Figure 4.22 Histogram representation of optical microscopy analysed by FIJI (V 1.51n) data for A) Oil blue A and B) Oil red O encapsulated squalene macroemulsion stabilised with the $SH_{0.75}DBiB_{0.25}$-*p*($OEGMA_{50}$-*co*-$EGDMA_{0.8}$) branched copolymer surfactant.

4.3.3 Thiol-functional Macroemulsion Muco-interactive Studies

The assessment of muco-interactions, including mucoadhesion, requires either biological mucus samples or synthetic equivalents of natural mucus. Several biosimilar mucus preparations have been reported and a preparation outlined by Boegh *et al.*[145] was selected for these studies as the rheological profile of this synthetic equivalent was reportedly optimised to strongly resemble natural porcine intestinal mucus. As previously discussed in Chapter 1, mucins are high molecular weight, heavily glycosylated natural molecules which are responsible for the rheological properties of mucus. Commercially available mucins are limited to those sourced from porcine stomach or bovine submaxillary glands and purification leads to large reduction in the molecular weight of the mucins[146]. Boegh *et al.* determined that the inclusion of the high molecular weight poly(acrylic acid), Carbopol 940, led to modification of the biosimilar mucus to mimic the rheological shear-thinning dominant elastic behaviour of porcine intestinal mucus with similar viscosity. The resulting biosimilar mucus, Figure 4.23, contained porcine mucin (5 % w/v), poly(acrylic acid) (0.9 % w/v), bovine serum albumin (BSA) (0.65 w/v %) and a lipid mixture (0.46 % cholesterol, 0.18 % phosphatidylchloine and 0.11 % linoleic acid) with polysorbate 80 (0.16 %).

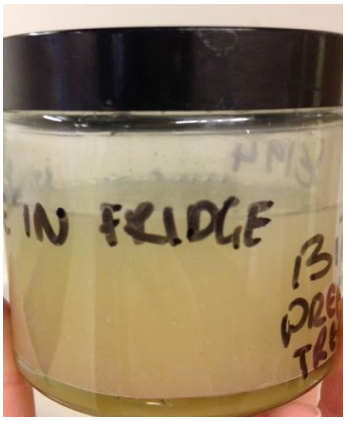

Figure 4.23 Synthetic biosimilar mucus mimicking porcine intestinal secretions.

To establish the potential for thiol-functional macroemulsions to demonstrate varying behaviour in the presence of mucus, two stable macroemulsions were generated using either the non-functional branched copolymer DBiB-*p(*$OEGMA_{50}$-*co*-$EGDMA_{0.8}$), described in Chapter 3, or the heavily thiol-functionalised $SH_{0.75}DBiB_{0.25}$-*p(*$OEGMA_{50}$-*co*-$EGDMA_{0.8}$).

These initial muco-interactive studies were conducted *via* optical microscopy using biosimilar mucus (500 µL) spread across a glass side and additional of a concentrated emulsion (100 µL) to the mucosal surface. The sample were viewed immediately by optical microscopy and monitored over a 10-minute time period, Figure 4.23. Non-functional DBiB-*p(*OEGMA$_{50}$-*co*-EGDMA$_{0.8}$) stabilised macroemulsions appeared to spread evenly across the mucus, with individual droplets easily observed, Figure 4.23A, and no observable aggregation of droplets or emulsion instability. This was in stark contrast to the thiol-functionalised macroemulsion, which upon contact with the mucus showed aggregation of droplets, Figure 4.24 B and C, and rupture of dye-loaded oil at several points over the 10-minute time period; additionally, no migration of emulsion droplets was observed across the sample.

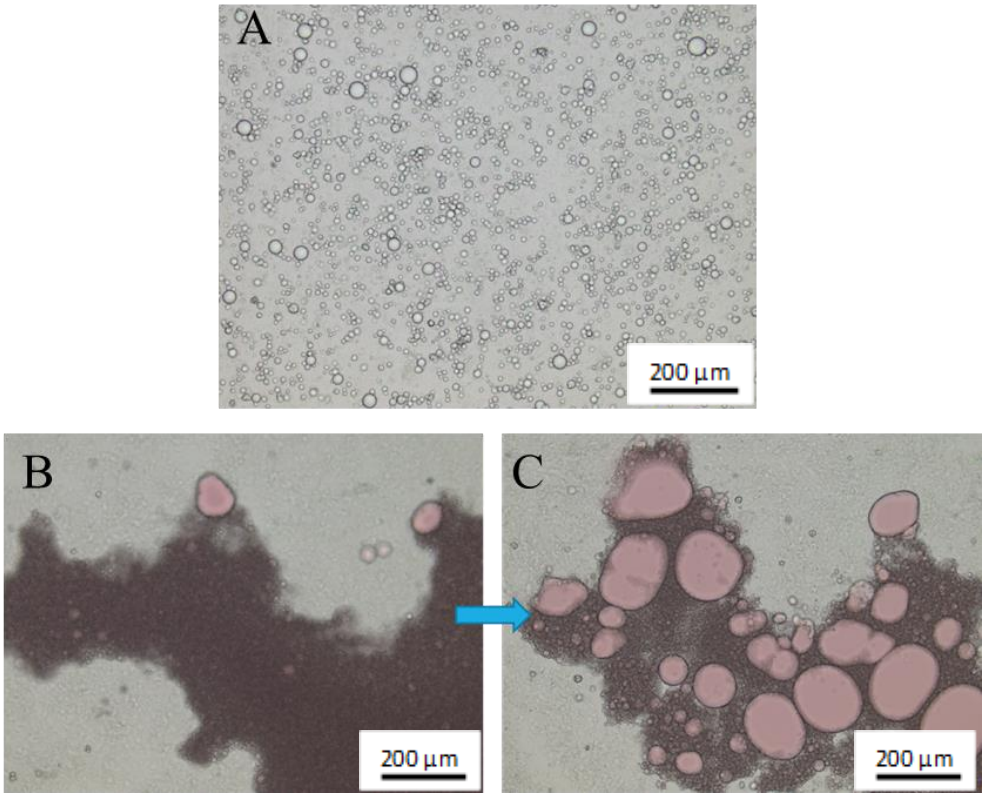

Figure 4.24 Optical microscopy images of branched copolymer stabilised emulsions in contact with biosimilar mucus; A) Oil blue A-loaded DBiB-*p*(OEGMA$_{50}$-*co*-EGDMA$_{0.8}$) stabilised squalene macroemulsion after 10 minutes; and Oil red O-loaded SH$_{0.75}$DBiB$_{0.25}$-*p*(OEGMA$_{50}$-*co*-EGDMA$_{0.8}$) stabilised squalene macroemulsions after B) immediate application and C) 10 minutes in contact with the substrate. 10x zoom magnification, scale bars = 200 µm.

The lack of motion within the thiol-functionalised macroemulsion suggested strong mucoadhesive behaviour, potentially through rapid oxidative disulphide bond formation between the cysteine regions of the biosimilar mucus and the thiolated branched copolymer surfactant. Furthermore, the general theory of mucoadhesion involves two stages which are loosely defined as the contact and consolidation stages. Chemical bond formation during the consolidation stage is characteristic of the so-called "second generation" mucoadhesive materials and disulphide bond formation is the basis of most thiolated mucoadhesive macromolecules. Here, we hypothesise that the formation of disulphide bonds at the contact point leads to a disturbance of the macroemulsion stabilisation, affecting the contact angle at the mucus-emulsion interface and causing the droplet to rupture with subsequent release of encapsulated material. This was further probed by the addition of $SH_{0.75}DBiB_{0.25}$-*p*($OEGMA_{50}$-*co*-$EGDMA_{0.8}$) stabilised squalene macroemulsions loaded with Oil red O and Oil blue A to biosimilar mucus, where again the triggered release of dye was observed, Figure 4.25 A and B. The demulsification of macroemulsion droplets was readily visualised with consequent blending of the dye loaded oil droplets creating a third purple oil phase while still maintaining individual blue and red areas. This behaviour opens up the possibility for these macroemulsions to be used as a dual treatment system which could be studied further in the future.

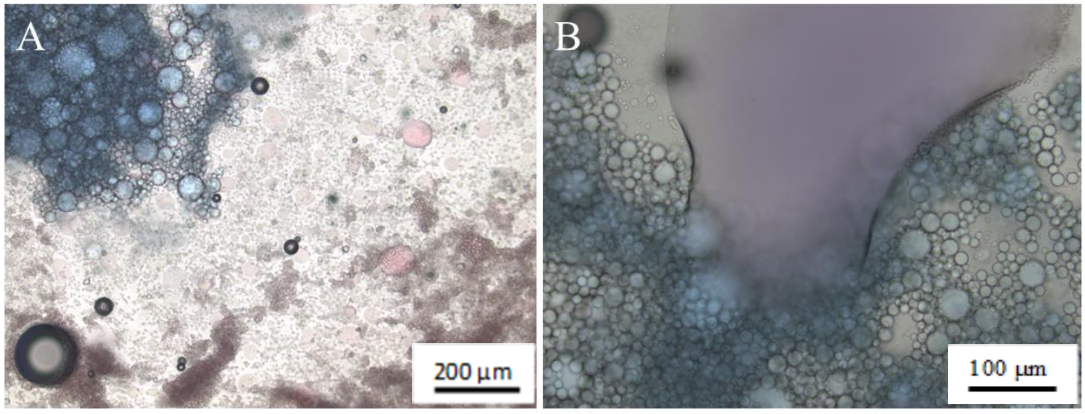

Figure 4.25 Burst release studies visualised by optical microscopy of Oil red O and Oil blue A loaded $SH_{0.75}DBiB_{0.25}$-*p*($OEGMA_{50}$-*co*-$EGDMA_{0.8}$) stabilised squalene macroemulsions in the presence of biosimilar mucus at time intervals of A) 0 mins and B) 10 mins. A = 10x zoom magnification, scale bar = 200 µm, B = 20x zoom magnification, scale bar = 100 µm.

This dramatic mucus-interacting behaviour of the thiol-functional macroemulsions was unexpected as the 4-week storage study suggested no instability or thiol-thiol coupling between polymer chains. Furthermore, the non-functional macroemulsion behaviour suggested no stability issues following interaction with the biosimilar mucus surface, although as full recovery of the emulsion from the mucus surface was not possible this could not be fully established. Previous reports of mucoadhesive thiomers did not suggest mucus-triggered release may occur in these systems, however, the potential for a triggered/mucus-interacting drug delivery system was considered as particularly useful for delivery to sites such as the eye, where the mucus turnover time is rapid and long term stability of commercial therapies is a known issue, see Chapter 5.

The potential for similar behaviour from thiol-functionalised nanoemulsions led to similar studies. A range of adhesive and release behaviour would be ideal, to allow targeting of specific benefits as required by different disease states or administration routes; for example, increasing the retention time of orally-dosed drug delivery systems, without immediate release, may improve absorption of drug molecules into the blood stream.

4.4 MUCOADHESIVE STUDIES OF THIOL-FUNCTIONAL BRANCHED COPOLYMER STABILISED NANOEMULSIONS

4.4.1 Nanoemulsion Formation

For this study $SH_{0.75}DBiB_{0.25}$-*p*($OEGMA_{50}$-*co*-$EGDMA_{0.8}$) was again selected as the branched copolymer stabiliser to directly compare behaviour with similar macroemulsions and nanoemulsions stabilised with this macromolecule. O/w nanoemulsions were generated using the same solvent evaporation methodology described in Chapter 3, where the ratio of volatile:non-volatile oil was varied to tailor the droplet size. In this study, castor oil was selected as the non-volatile oil phase due to previous research published within the group showing successful nanoemulsion size tailoring;[107] castor oil is also known to be non-toxic and a safe drug delivery vehicle within the body. Nanoemulsions were left at ambient temperature following homogenisation, allowing for full removal of volatile co-solvent by evaporation which was monitored gravimetrically. Similar observations were made for macroemulsions generated using linear homopolymer showed that, stable nanoemulsions were not able

to be formed using SH-*p*(OEGMA$_{50}$) and rapid demulsification was observed. As expected, SH-*p*(OEGMA$_{50}$-*co*-EGDMA$_{0.8}$) was also unsuccessful as an emulsifier for nanoemulsion formation.

4.4.2 Nanoemulsion Characterisation

A study was undertaken to evaluate whether SH$_{0.75}$DBiB$_{0.25}$-*p*(OEGMA$_{50}$-*co*-EGDMA$_{0.8}$) stabilised nanoemulsions would exhibit the triggered demulsification seen for macroemulsions stabilised by the same branched copolymer. A SH$_{0.75}$DBiB$_{0.25}$-*p*(OEGMA$_{50}$-*co*-EGDMA$_{0.8}$) stabilised nanoemulsion was generated using the methodology outlined in Chapter 3, utilising ethyl acetate:castor oil in a 99:1 ratio incorporating Oil red O (0.05 wt % loading) for ease of observation against a biosimilar mucus substrate, Figure 4.26.

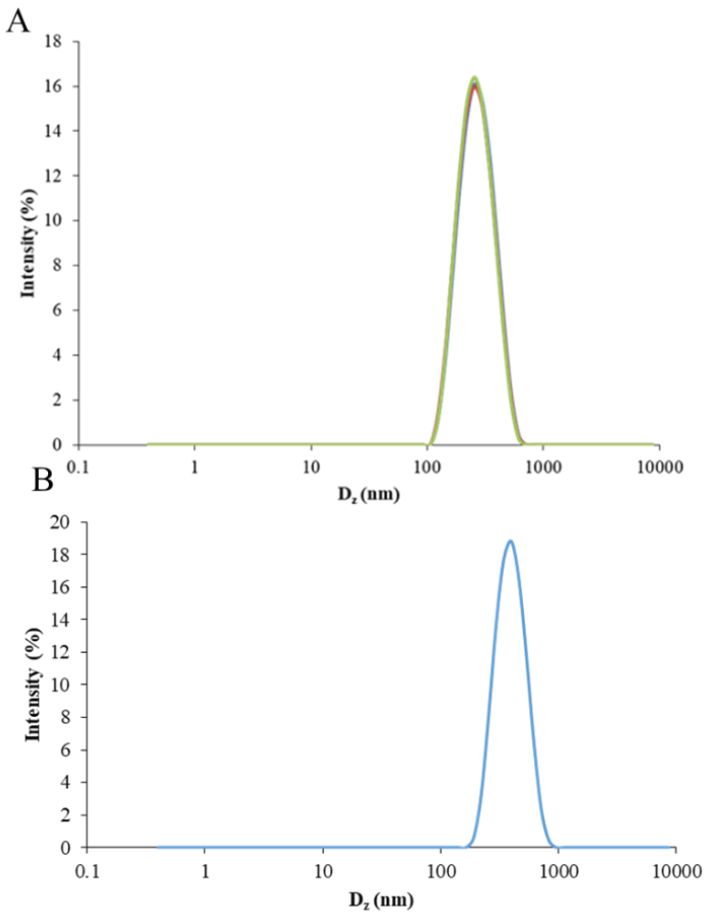

Figure 4.26 DLS nanoemulsion size distributions of castor oil-based nanoemulsions: A) loaded with Oil red O (0.05 wt %) and with SH$_{0.75}$DBiB$_{0.25}$-*p*(OEGMA$_{50}$-*co*-EGDMA$_{0.8}$) as polymeric surfactant and B) SH$_{0.75}$DBiB$_{0.25}$-*p*(OEGMA$_{50}$-*co*-EGDMA$_{0.8}$) as polymeric surfactant, unloaded.

DLS analysis of the $SH_{0.25}DBiB_{0.75}$-*p*($OEGMA_{50}$-*co*-$EGDMA_{0.8}$) stabilised castor oil nanoemulsion with Oil red O yielded a D_z value of 250 nm and a low PdI of 0.10, Table 4.4. No visual indication of instability was observed during storage before evaluation for mucus-interacting properties with biosimilar mucus. Characterisation of the nanoemulsion containing Oil red O was almost indistinguishable an analogous nanoemulsion generated in the absence of Oil red O, showing a lack of influence from the encapsulated dye on the nanoemulsion formation process or the branched copolymer surfactant.

Table 4.4 DLS analysis of castor oil nanoemulsion with $SH_{0.75}DBiB_{0.25}$-*p*($OEGMA_{50}$-*co*-$EGDMA_{0.8}$) as polymeric surfactant, loaded with Oil red O (0.05 wt %) or unloaded.

Polymer	Oil Red O wt %	D_z (nm)	D_n (nm)	PdI
$SH_{0.75}DBiB_{0.25}$-*p(*$OEGMA_{50}$-*co*-$EGDMA_{0.8}$)	0.05	250	230	0.10
$SH_{0.75}DBiB_{0.25}$-*p(*$OEGMA_{50}$-*co*-$EGDMA_{0.8}$)	-	249	230	0.10

A sample of the Oil red O containing nanoemulsion (10 μL) was applied to the biosimilar mucus and monitored visually for any triggered release of oil and dye, which may indicate similar behaviour to the thiol-functional macroemulsion; no release of dye-containing oil was observed visually over 10 minutes, with the nanoemulsion appearing to be predominantly static on the mucosal surface throughout. Figure 4.27 shows the behaviour of the thiol-functional nanoemulsion following immediate addition to biosimilar mucus and after 10 minutes. The thiol-functionalised nanoemulsions appeared, therefore, to display mucoadhesive behaviour but no triggering of demuslification. This may be due to the reduced droplet diameter limiting the number of disulphide bonds formed between polymer stabiliser and the mucus surface and a lack of sufficient perturbation of the oil/water interface which would lead to rupturing of the oil droplets.

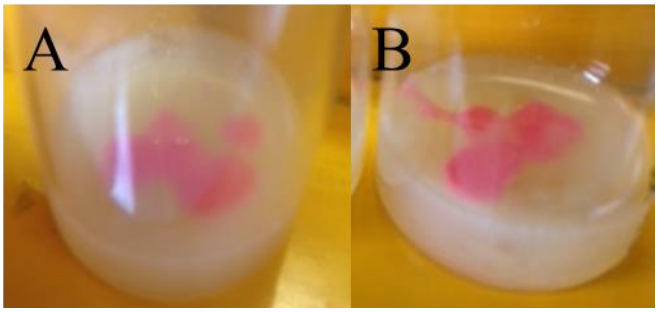

Figure 4.27 Mucus-interaction studies of $SH_{0.25}DBiB_{0.75}$-*p*($OEGMA_{50}$-*co*-$EGDMA_{0.8}$) nanoemulsion on biosimilar mucus after A) 0 minutes and B) 10 minutes.

As no triggered release was shown by a 250 nm $SH_{0.25}DBiB_{0.75}$-*p*($OEGMA_{50}$-*co*-$EGDMA_{0.8}$) stabilised nanoemulsion, in stark contrast to the corresponding macroemulsion (13 µm), the relationship of release behaviour and droplet diameter would be an interesting area of future research. Tailoring of nanoemulsion droplet size was evaluated to establish whether thiol functional emulsifiers were able to act similarly to the non-thiol containing branched copolymers. $SH_{0.75}DBiB_{0.25}$-*p*($OEGMA_{50}$-*co*-$EGDMA_{0.8}$) was used to stabilise nanoemulsions with varying ratios of volatile solvent to non-volatile solvent leading to tailored droplet sizes, as outlined in Chapter 3. To tailor droplet diameters the ratio of ethyl acetate:castor oil was varied in ratios of 50:50, 60:40, 70:30, 80:20, 90:10 and 99:1, Figure 4.28, Appendix Table A1. These nanoemulsions were studied for mucus-triggered release but no such behaviour was seen in this size range.

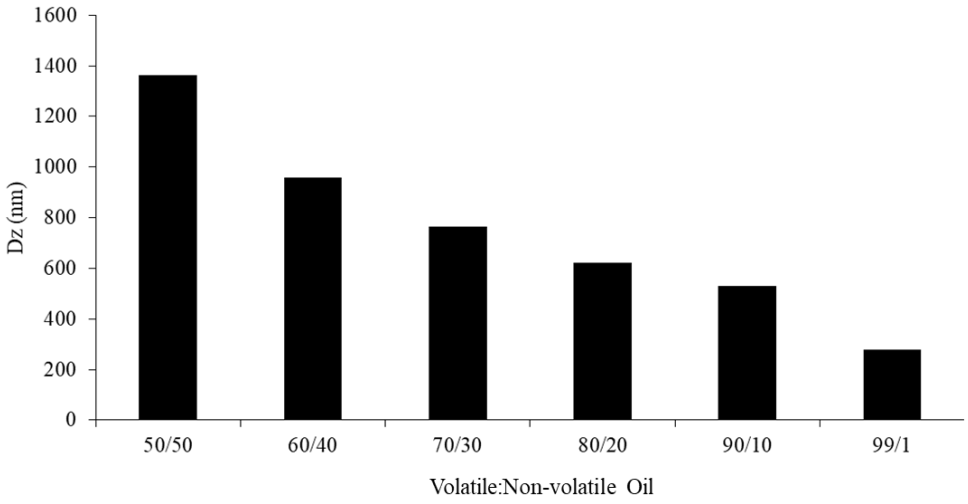

Figure 4.28 Tailored droplet size (Dz) of thiol-functional copolymer $SH_{0.75}DBiB_{0.25}$-*p*($OEGMA_{50}$-*co*-$EGDMA_{0.8}$) stabilised nanoemulsions were varying ethyl acetate:castor oil ratios.

The trend seen in Figure 4.28 is highly analogous to the previous tailoring of nanoemulsion droplet size presented in Chapters 2 and 3 for analogous branched copolymer stabilisers. It is important to compare and contrast the tailoring of nanoemulsion droplet size to establish if clear trends can be seen and insight into the mechanism of branched copolymer emulsifiers can be determined. As detailed in Table 4.5, thiol-functional droplet diameters were able to be tailored from 1300 nm to 270 nm by increasing the amount of volatile solvent present in the oil phase/decreasing the amount of non-volatile oil.

Table 4.5 DLS analysis of tailored nanoemulsion droplets by varying the ratio of volatile:non-volatile oil and varying branched block copolymer stabiliser.

	Nanoemulsion hydrodynamic diameter using different branched copolymer stabilisers D_z (nm)		
EtOAc:castor oil volume ratio	$DBiB_{0.25}PBiB_{0.75}$-*p*($OEGMA_{50}$-*co*-$EGDMA_{0.8}$)	$SH_{0.75}DBiB_{0.25}$-*p*($OEGMA_{50}$-*co*-$EGDMA_{0.8}$)	DBiB-*p*($OEGMA_{50}$-*co*-$EGDMA_{0.8}$)
50:50	2500	1370	1036
60:40	1290	960	766
70:30	960	706	635
80:20	820	620	481
90:10	540	530	486
99:1	270	280	211

Comparison with data generated from similar tailoring using $DBiB_{0.25}PBiB_{0.75}$-*p*($OEGMA_{50}$-*co*-$EGDMA_{0.8}$) and DBiB-*p*($OEGMA_{50}$-*co*-$EGDMA_{0.8}$) showed an interesting trend where DBiB-*p*($OEGMA_{50}$-*co*-$EGDMA_{0.8}$) stabilised nanoemulsions consistently exhibited the smallest hydrodynamic diameters across all ratios of volatile and non-volatile oil; $DBiB_{0.25}PBiB_{0.75}$-*p*($OEGMA_{50}$-*co*-$EGDMA_{0.8}$) stabilised

nanoemulsions were consistently the largest with $SH_{0.25}DBiB_{0.75}$-*p*($OEGMA_{50}$-*co*-$EGDMA_{0.8}$) stabilised nanoemulsions remaining intermediate at all ratios, Figure 4.29

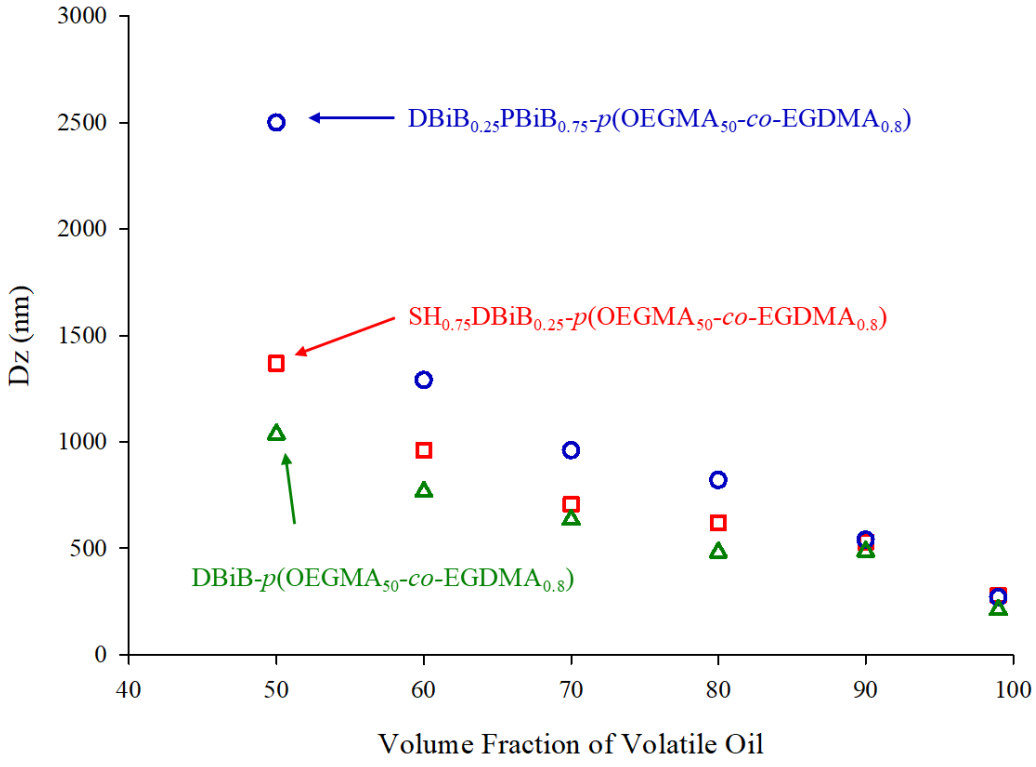

Figure 4.29 Comparison of D_z values for nanoemulsions with different volume fraction of volatile oil (ethyl acetate). Nanoemulsions stabilised with branched copolymers; $DBiB_{0.25}PBiB_{0.75}$-*p*($OEGMA_{50}$-*co*-$EGDMA_{0.8}$), ($SH_{0.75}DBiB_{0.25}$-*p*($OEGMA_{50}$-*co*-$EGDMA_{0.8}$) and DBiB-*p*($OEGMA_{50}$-*co*-$EGDMA_{0.8}$).

This trend suggests that the high density of hydrophobic DBiB-derived chain ends within DBiB-*p*($OEGMA_{50}$-*co*-$EGDMA_{0.8}$) are most efficient at stabilising the interfacial tension of the remaining non-volatile oil phase. The same volume of non-volatile oil is present in each sample derived from identical volatile/non-volatile oil ratios in each series, therefore, the thiol-functional branched copolymer stabiliser is more closely aligned to the behaviour of branched copolymers containing high ratios of DBoB-derived chain ends. This may be due to the lack of steric crowding at the chain end when compared to the PBiB initiator residue but may also point to a difference in the arrangement of chains at the surface of the oil droplets; for example, the presence of dangling chains or density of packing of hydrophobic chain ends, which may have implications for interpretation of data from later studies.

4.5 MUCOADHESIVE BEHAVIOUR OF NANOEMULSIONS AS DETERMINED BY FLOW THROUGH MODEL WITH BIOSIMILAR MUCUS

The ‘gutter’ model previously described in Section 4.1.2, is a valid experimental design for liquid dosing systems, however it is more commonly used to test the adhesive strength of semi-solid dosing systems. Typically, an *ex vivo* sample of mucosal tissue is treated with simulated biological fluids that flow over the sample to ‘wash’ the adhesive substrate. As the ‘gutter’ model design requires the use of *ex vivo* tissues, it is somewhat inaccessible for research groups working outside of a biological laboratory. It is also suffers from tissue sample-to-sample variation, as with any evaluation utilising biological samples, and does not lend itself to rapid evaluation of a range of material options without multiple repeated experiments.

For the studies reported here, a model was therefore designed to incorporate the ‘gutter’ flow model concepts but utilising biosimilar mucus to replace tissue samples, and allowing for ease of studies within non-biological laboratories and without the requirement for tissue sampling. The model design aimed to study the flow of nanoemulsion samples over a biosimilar mucus surface and allow the quantification of adhesion through gravimetric analysis of the liquids passing across the surface; a reduction in mass would equate to loss of nanoemulsion from the flow and therefore be directly interpreted as mucoadhesion. By selecting a sealed system, rather than the typical open gutter model, repeatable coverage of the biosimilar mucosal surface could be accomplished and the potential for the nanoemulsion to flow outside of the tissue boundaries was avoided.

The “flow-through” mucoadhesion model was, therefore, adapted from a novel flow-through cell culture chamber (Kirstall QV500), Figure 4.30A and C. The model is made up of four components; an inlet chamber, a sealed chamber, an outlet chamber and a peristaltic pump. The inlet chamber is attached *via* tubing to the peristaltic pump, which is in turn attached to the sealed chamber. The pump is set at the desired speed for flow (mL/min), and then the system flows the inlet liquid over the sealed chamber and back into the inlet chamber in a ‘recycling’ mode. As the model has various joints throughout the tubing, they can be easily detached to allow for flow into an outlet vessel, allowing for collection of the inlet liquid and ultimately quantification.

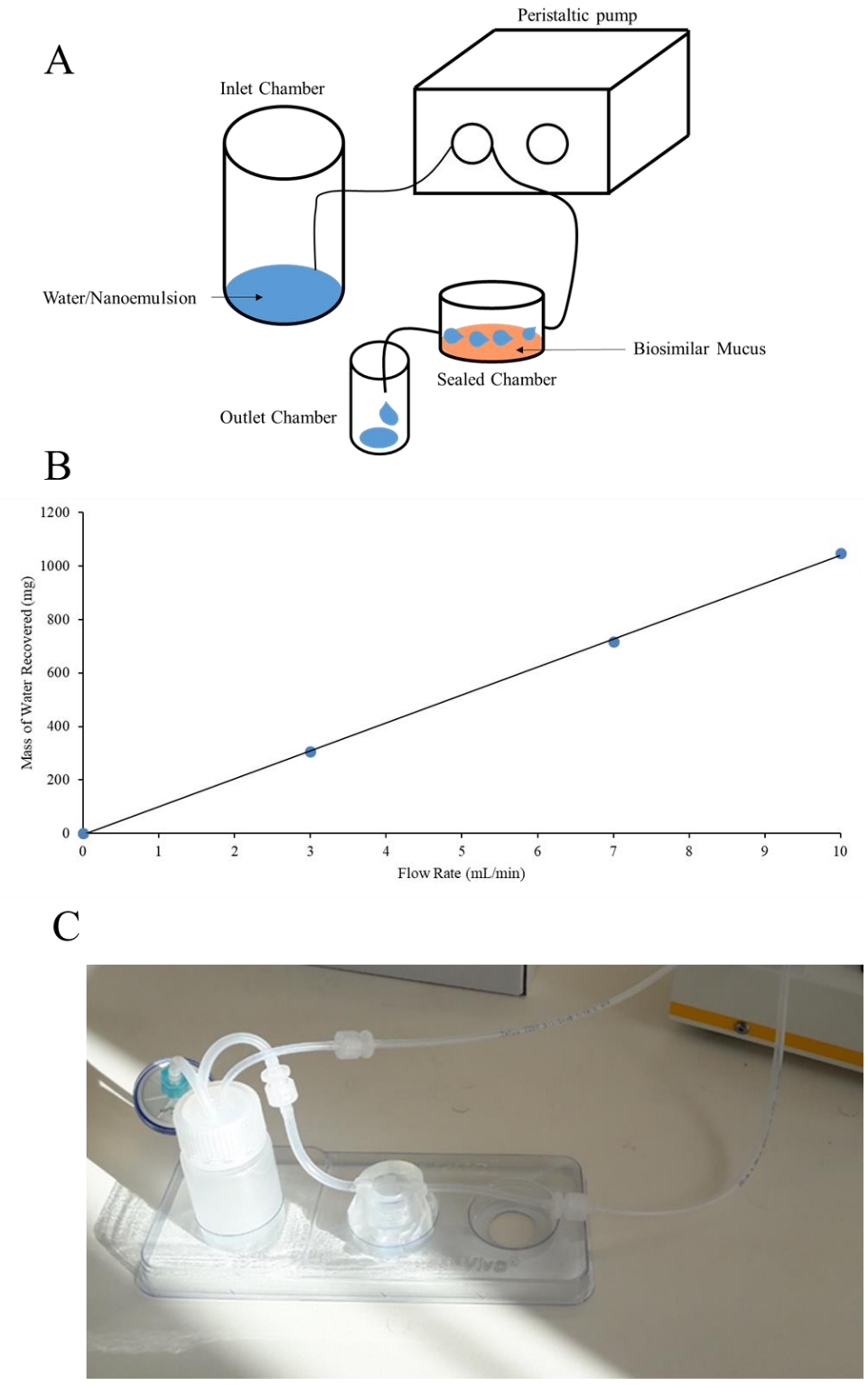

Figure 4.30 Flow through mucoadhesive model: A) Diagrammatic representation of the model showing inlet, outlet and sealed chamber containing biosimilar mucus with attachment to peristaltic pump. B) Validation of pump settings by flow of water over biosimilar mucus at 3 speed settings. C) Photograph of sealed chamber set up.

In this study biosimilar mucus (1 mL) was placed in the sealed chamber and weighed before attachment to the pump. The inlet chamber was also pre-weighed and weighed again upon addition of nanoemulsion (2 mL); the inlet, sealed chamber and pump are then attached together. Once the pump setting is selected, the nanoemulsion will flow from the inlet over the biosimilar mucus at a rate of 1 mL/min, and repeated. Upon the second flow the sealed chamber was detached from the system and fed into a pre-weighed outlet chamber, thereby allowing for quantification of mucoadhesion by gravimetric measurements of nanoemulsion regained from the model in comparison to the amount originally added to the inlet. The weight of the biosimilar mucus plus emulsion was also taken to account for adhesion; the inlet chamber was also weighed to account for any loss of emulsion due to experimental error.

A validation study was initially conducted to check that any loss of emulsion during flow can be attributed solely to the potential adhesive behaviour of the nanoemulsions and not due to swelling of the mucus in the presence of water. Pure water (1 mL) was flowed over the biosimilar mucus at 3 different speed settings for 1 minute each to create a three-point calibration. The peristaltic pump was able to administer flow rates of 100 μL/min to 1000 μL/min; for this study flow rates of 300 μL/min, 700 μL/min and 1000 μL/min were used. Water was collected *via* an outlet chamber, and the amount of water regained from the model monitored gravimetrically. As shown in Figure 4.30 B, the study confirmed that the amount of water recovered from the model was consistent with the pump speed settings, therefore showing that the biosimilar mucus did not have an adverse effect on the amount of mass of liquid flowing through the cell; if the weight had increased, the flow may be diluting and removing biosimilar mucus into solution/suspension, and if the weight had decreased, the biosimilar mucus would be potentially swelling and removing water from the flow. Validation prior to the mucoadhesive study was important as the expected mass differences between nanoemulsions are small, and any loss of emulsion due to mucus swelling would nullify the experiment.

4.5.1 Impact of Droplet Diameter on Mucoadhesive Behaviour of Nanoemulsions

As stated above, the flow-through method required the nanoemulsion to be flowed directly over a known volume of biosimilar mucus, with quantification of adhesion

measured gravimetrically by the reduction of mass of the sample; a so-called "mass-loss" experiment.

A series of different nanoemulsions (2 mL) stabilised with the same branched copolymer surfactant, $SH_{0.75}DBiB_{0.25}$-*p*($OEGMA_{50}$-*co*-$EGDMA_{0.8}$), but created with varying droplet sizes, Table 4.6, were flowed over the biosimilar mucus using methodology as described above in Section 4.5 and results are shown in Figure 4.31.

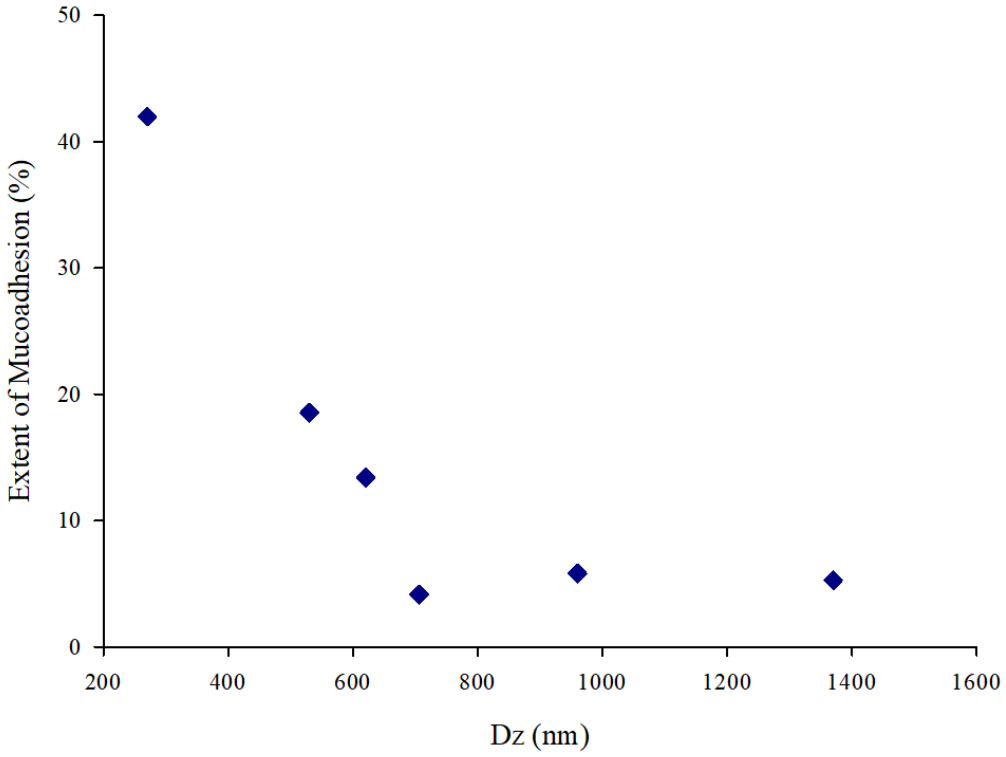

Figure 4.31 Extent of mucoadhesion (%) of tailored nanoemulsions with $SH_{0.75}DBiB_{0.25}$-*p*($OEGMA_{50}$-*co*-$EGDMA_{0.8}$) as polymeric surfactant.

As shown in Figure 4.28, nanoemulsions stabilised by $SH_{0.75}DBiB_{0.25}$-*p*($OEGMA_{50}$-*co*-$EGDMA_{0.8}$) with droplet diameters between 1300 and 700 nm showed no apparent difference in mucoadhesive behaviour (approximately 95 % mass recovery). However, nanoemulsion droplet diameters < 600 nm showed a measurable and increasing mucoadhesion. The smallest nanoemulsions (530 nm and 280 nm) exhibited 19 and 42 % adhesion respectively. This initial investigation utilised nanoemulsions of varying size but stabilised with the same thiol-functional branched copolymer, therefore the same number of thiols were spread over a varying surface area.

Table 4.6 Extent of mucoadhesion (%) of tailored nanoemulsions stabilised with $SH_{0.75}DBiB_{0.25}$-*p*($OEGMA_{50}$-*co*-$EGDMA_{0.8}$).

Polymer	D_z (nm)	Extent of Adhesion (%)
$SH_{0.75}DBiB_{0.25}$-*p*($OEGMA_{50}$-*co*-$EGDMA_{0.8}$)	1370	5.2
	960	5.8
	706	4.1
	620	13.4
	530	18.5
	280	42.0

The collected (post-flow) nanoemulsion samples were analysed by DLS to assess the effect of mucosal contact on the size distributions to assess whether a particular droplet size within each sample was preferentially adhering to the biosimilar mucus. With the exception of largest nanoemulsion droplets, a general trend of slightly increased droplet D_z values diameters was observed post flow-through, Figure 4.32 This increase is most probably derived from the preferential adherence of the smallest droplets within each distribution leading to a larger hydrodynamic diameter being measured for the samples; the considerable difference between the mucoadhesion of the tailored nanoemulsions, Figure 4.31, would support this assumption and the largest samples would not have a distribution that extends very far into 500 nm range.

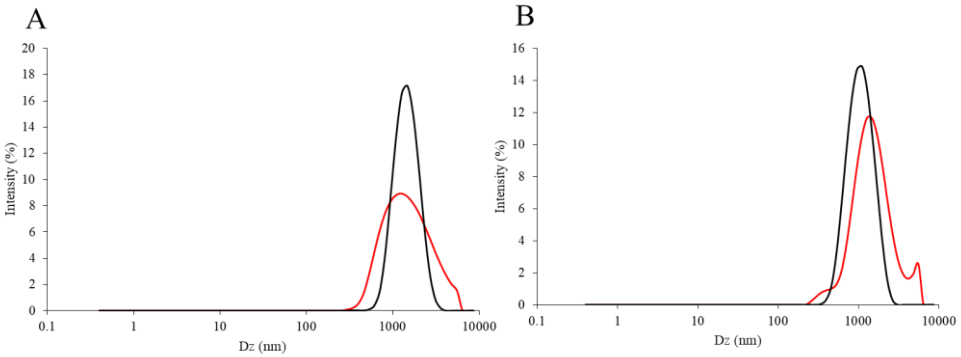

Figure 4.32 DLS traces of $SH_{0.75}DBiB_{0.25}$-*p*($OEGMA_{50}$-*co*-$EGDMA_{0.8}$) stabilised nanoemulsions initial (black) and post-flow (red) at ethyl acetate:castor oil ratios of A) 50:50 and B) 60:40.

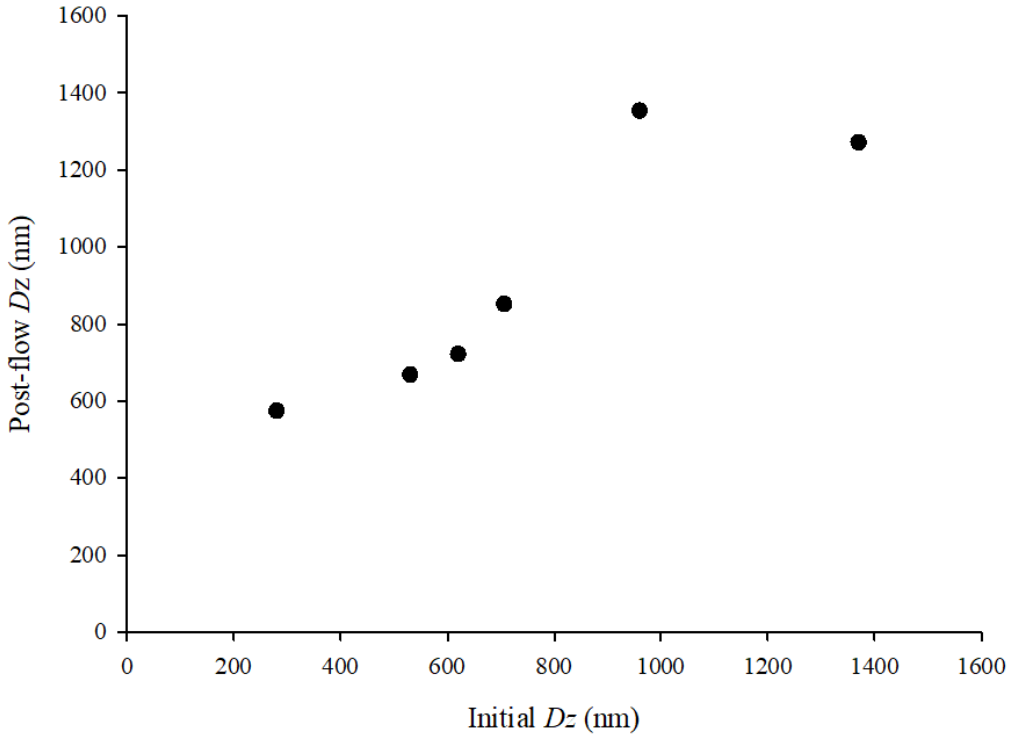

Figure 4.33 Comparison of D_z (nm) of tailored nanoemulsions with $SH_{0.75}DBiB_{0.25}$-*p*($OEGMA_{50}$-*co*-$EGDMA_{0.8}$) as branched copolymer stabiliser with castor oil as non-volatile oil, pre- and post-mucoadhesive studies with flow-through model.

The variation of nanoemulsion sizes within the tailored droplet experiments does utilise varying oil volumes and, therefore, the amount of oil within each flow-through experiment varies by a factor of 50 for any given sample volume. Typically, reports of nanoparticles strongly refer to the considerable increase in surface area at the nanoscale but this is only true for comparative materials at equal mass.

Nanoemulsions would also exhibit a considerable increase in surface area as the droplet size decreases for any fixed mass; however, the decrease in oil volume used to generate each tailored nanoemulsion sample does lead to a systematically decreasing oil volume (1.5 mL to 0.03 mL) and potentially, fewer actual droplets although this has not been established; a simple "increased surface area" explanation of the increased mucoadhesion as size decreases is not applicable. To understand the impact of size on the observed mucoadhesion, the packing of spheres onto surfaces was also considered, however, this is known to be radius independent and has a theoretical maximum packing density of 0.9069 on a Euclidean surface.

The DLS analysis of the tailored nanoemulsions provides hydrodynamic diameter (D_z) data for the average droplet within each sample. This may be used to calculate the surface area of the average droplet, if we assume that the droplets are perfectly spherical, Equation 4.1.

$$A = 4\pi r^2 \qquad (4.1)$$

The percentage of the total surface area of each nanoemulsion droplet that contacts the emulsion is governed by the evenness of the biosimilar mucus surface, but assuming a flat surface and non-deformable oil droplets, the actual surface area of contact may be assumed to be relatively similar (approximates to a point contact) and independent of oil droplet diameter. If we also assume a statistical distribution of thiols at the surface of all oil droplets, a comparative interaction of different sized nanoemulsion droplets may be envisaged as shown in Figure 4.34. This would suggest that a considerably higher fraction of the thiols present are available for surface interactions with decreasing droplet diameter and this may explain the improved mucoadhesion of smaller nanoemulsion droplets.

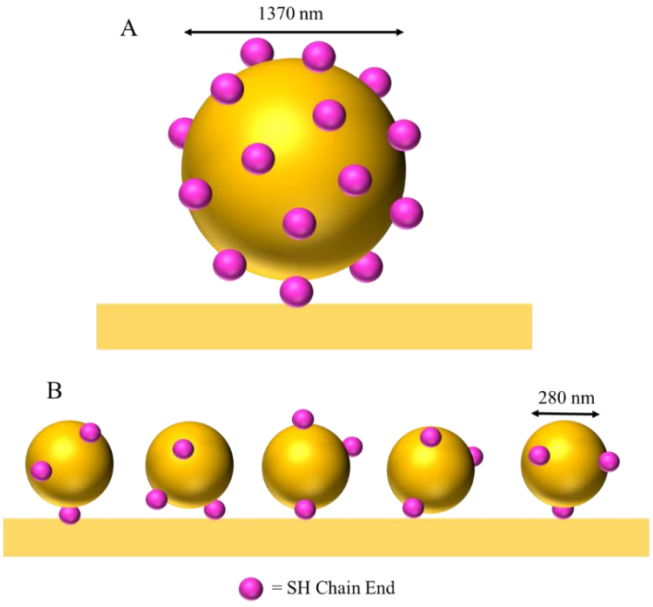

Figure 4.34 Comparative interaction between nanoemulsion oil droplets at two different diameters and biosimilar mucus surface, where a statistical distribution of thiols (pink spheres) leads to a higher fraction of thiols present at droplet surface for interaction at a smaller droplet diameter. Schematically pictured is the distribution of 15 chain ends over nanoemulsion droplet diameters of; A) 1370 nm and B) 280 nm.

An alternative explanation is that the biosimilar mucus is flexible, uneven and the nanoemulsion droplets are slightly deformable. This would lead to a contact area that is considerably higher than a point-contact and potentially involving increased numbers of thiols per nanoemulsion droplet. One complication is that smaller droplets would potentially be able to access more of the available surface area of an uneven biosimilar mucous due to size exclusion of the larger droplets, however, if we assume the contact area is considerably larger than a point contact and discount any size exclusion effects, the interaction with the mucosal substrate may be represented as shown in Figure 4.35.

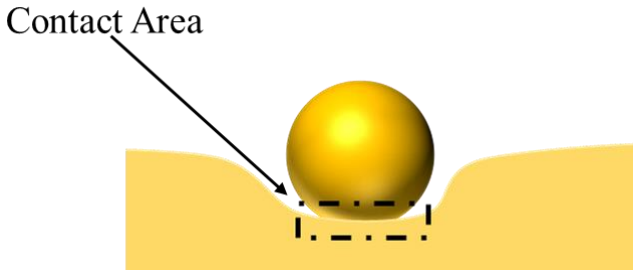

Figure 4.35 Hypothetical contact area of nanoemulsion droplet with biosimilar mucosal surface.

If we assume a circular contact area with a diameter of 25 nm, a surface area of contact is calculated to be 1960 nm^2. Different contact areas can also be considered, however this large contact area is taken as an extreme value; for context, the excluded surface area of a PEG chain with an M_n = 2000 g/mol tethered to a nanoparticle surface has been reported as 12.25 nm^2. The D_z value measured by DLS also allows the calculation of average droplet volume which may be used to determine the relative number of droplets in each nanoemulsion sample as the amount of oil used to create each sample at tailored diameters is known.

For example, the nanoemulsion created using a 50:50 ratio of ethyl acetate:castor oil displayed a D_z value of 1370 nm, and therefore a radius of 685 nm, surface area per droplet of 5.96×10^6 nm^2 and a volume per droplet of 1.35×10^9 nm^3; similarly the D_z = 280 nm nanoemulsion created from the 99:1 ethyl acetate:castor oil ratio has a radius of 140 nm, a subsequent droplet surface area of 2.46×10^5 nm^2 and droplet volume of 1.15×10^7 nm^3, Table 4.7 The volume of each droplet, or the relative number of droplets, is not critical to the consideration of the individual droplet contact, however,

it is interesting to note that there are nearly 120 droplets with a D_z = 280 nm for each D_z = 1370 nm droplet.

Table 4.7 Variation in droplet volume (nm^3), droplet surface area (nm^2) and droplet consumed by a set area (%) with change in D_z (nm).

D_z (nm)	Droplet volume (nm^3)	Droplet surface Area (nm^2)	Droplet area consumed by 1960nm^2 (%)
1370	$1.35x10^9$	$5.96x10^6$	0.03
960	$4.63x10^8$	$2.90x10^6$	0.07
706	$1.84x10^8$	$1.57x10^6$	0.13
620	$1.25x10^8$	$1.21x10^6$	0.16
530	$7.80x10^7$	$8.82x10^5$	0.22
280	$1.15x10^7$	$2.46x10^5$	0.81

When considering the percentage of each individual droplet surface area that does contact the surface, the relationship that can be derived is particularly illuminating. If we accept a contact surface area of 1960 nm^2 per droplet, the fraction of the droplet surface area that is in contact with the surface scales by 24-fold, Table 4.7. The actual surface area of contact is not important for this relative ratio as the values scale accordingly; for example, if a 500 nm^2 contact area is considered as more representative, the droplet area consumed by contact with the biosimilar mucus for the 1370 nm diameter nanoemulsion droplets is 0.03 % and a value of 0.81 % is derived for the 280 nm sample (a 24-fold difference). This is graphically represented in Figure 4.36 where the mucoadhesion data and relative percentage of individual droplet surface area utilised for mucoadhesion contact are plotted against nanoemulsion hydrodynamic diameter.

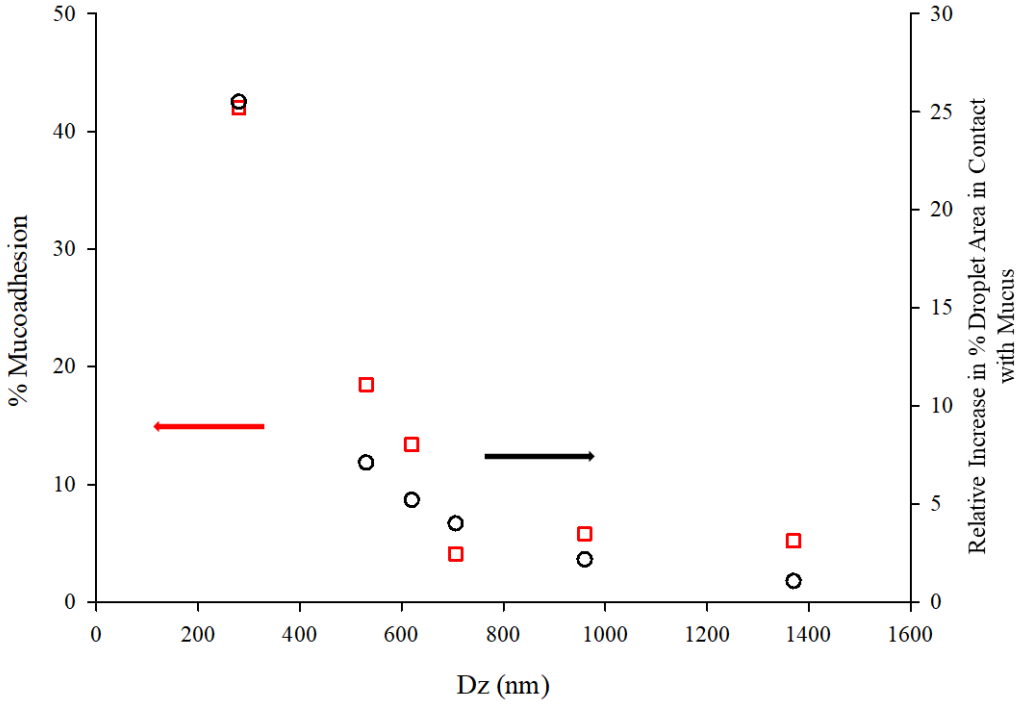

Figure 4.36 Relative increase in droplet area (%) in contact with mucus (○) against the percentage mucoadhesion determined by flow through model as nanoemulsion droplet diameter (D_z) increases (□).

4.5.2 Impact of Increasing Thiol-Functionality on Mucoadhesive Behaviour of Nanoemulsions

The size of nanoemulsion droplets clearly has an impact on the mucoadhesion of thiol-functional samples stabilised by branched copolymer stabilisers. The library of branched copolymers synthesised with varying thiol-functionalities provides an opportunity to study the impact of the concentration of thiols on the mucoadhesion of nanoemulsions of similar sizes. In order to generate a systematically varying nanoemulsion library, samples were generated using the same aqueous polymer concentration of each thiol functional branched copolymer (5 wt %) at two volatile:non-volatile oil volume ratios (ethyl acetate:castor oil) of 90:10 and 99:1, Table 4.7.

Table 4.7 Tailored nanoemulsions using varying ethyl acetate:castor oil ratios and different thiol-functional branched copolymer stabilisers.

Polymer	EtOAc:castor oil ratio	D_z (nm)	D_n (nm)	PdI
DBiB-*p*(OEGMA$_{50}$-*co*-EGDMA$_{0.8}$)	90.10	351	305	0.06
	99:1	228	209	0.07
SH$_{0.08}$DBiB$_{0.92}$-*p*(OEGMA$_{50}$-*co*-EGDMA$_{0.8}$)	90:10	530	209	0.19
	99:1	241	217	0.05
SH$_{0.25}$DBiB$_{0.75}$-*p*(OEGMA$_{50}$-*co*-EGDMA$_{0.8}$)	90:10	-	-	-
	99:1	260	221	0.14
SH$_{0.50}$DBiB$_{0.50}$-*p*(OEGMA$_{50}$-*co*-EGDMA$_{0.8}$)	90:10	460	221	0.08
	99:1	251	218	0.05
SH$_{0.75}$DBiB$_{0.25}$-*p*(OEGMA$_{50}$-*co*-EGDMA$_{0.8}$)	90:10	530	480	0.12
	99:1	280	270	0.13
SH$_{0.90}$DBiB$_{0.10}$-*p*(OEGMA$_{50}$-*co*-EGDMA$_{0.8}$)	90:10	660	634	0.02
	99:1	345	290	0.16

At the higher ratio of volatile ethyl acetate (99% v/v), the branched copolymer SH$_{0.08}$DBiB$_{0.92}$-*p*(OEGMA$_{50}$-*co*-EGDMA$_{0.8}$), SH$_{0.50}$DBiB$_{0.50}$-*p*(OEGMA$_{50}$-*co*-EGDMA$_{0.8}$) and SH$_{0.75}$DBiB$_{0.25}$-*p*(OEGMA$_{50}$-*co*-EGDMA$_{0.8}$) generated comparable nanoemulsions of 240 – 250 nm; however, the use of SH$_{0.90}$DBiB$_{0.10}$-*p*(OEGMA$_{50}$-*co*-EGDMA$_{0.8}$) led to a larger nanoemulsion of D_z = 345 nm. As expected from previous observations, variation in the branched copolymer stabiliser at higher castor oil content (10 % v/v) showed a greater variance of droplet diameter and D_z varying from 460 nm to 750 nm. Nanoemulsions generated using SH$_{0.75}$DBiB$_{0.25}$-*p*(OEGMA$_{50}$-*co*-EGDMA$_{0.8}$) and SH$_{0.90}$DBiB$_{0.10}$-*p*(OEGMA$_{50}$-*co*-EGDMA$_{0.8}$) at this ratio led to D_z values ~200 nm greater than that of nanoemulsions with lower thiol content. This again would suggest that the increase in thiol chain ends, or lack of hydrophobic chain ends, changes the packing of the polymer at the oil interface; a greater number of DBiB chain ends on the branched copolymer may be able to facilitate a more dense packing around the oil droplet, creating a *p*(OEGMA) interfacial layer that is held closer to the droplet surface resulting in lower hydrodynamic diameters. Importantly, DLS

measures the hydrodynamic diameter of the swept volume of the entire entity, Figure 4.37, not the specific diameter of the oil droplet itself that is surrounded by the tethered branched *p(*OEGMA) stabiliser.

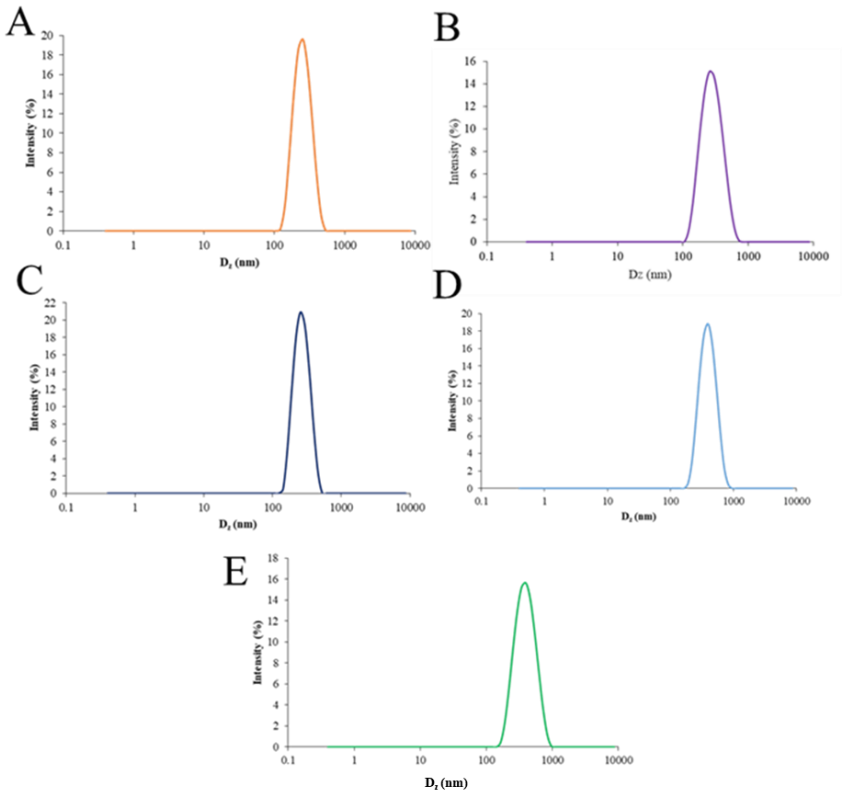

Figure 4.37 DLS traces for SH_xDBiB_y-*p*($OEGMA_{50}$-*co*-$EGDMA_{0.8}$) stabilised nanoemulsions formulated with a 99:1 ratio of EtOAc:castor oil; A) $SH_{0.08}DBiB_{0.92}$-*p*($OEGMA_{50}$-*co*-$EGDMA_{0.8}$), B) $SH_{0.25}DBiB_{0.75}$-*p*($OEGMA_{50}$-*co*-$EGDMA_{0.8}$), C) $SH_{0.50}DBiB_{0.50}$-*p*($OEGMA_{50}$-*co*-$EGDMA_{0.8}$), D) $SH_{0.75}DBiB_{0.25}$-*p*($OEGMA_{50}$-*co*-$EGDMA_{0.8}$) and E) $SH_{0.90}DBiB_{0.10}$-*p*($OEGMA_{50}$-*co*-$EGDMA_{0.8}$).

Due to the consistent D_z values (D_z = 228-260 nm; one sample at D_z = 345 nm as described above) of the nanoemulsions derived from a 99:1 ratio of ethyl acetate and castor oil, Table 3.8, these samples with varying thiol content were selected for the flow-through mucoadhesion investigation. The nanoemulsions (2 mL) were flowed over the previously described biosimilar mucus at a rate of 1 mL/min, with the extent of mucoadhesion again monitored by the mass loss calculation. A non-functional nanoemulsion stabilised with polymeric surfactant, DBiB-*p*($OEGMA_{50}$-*co*-$EGDMA_{0.8}$), was also included as a control which theoretically should not interact with the mucus.

Figure 4.38 shows the results of the flow-through model experiment; the number of thiol-functional chain ends within the branched copolymer stabiliser is clearly correlated with the observed mucoadhesive behaviour of these nanoemulsions with substantially similar D_z values. A sigmoidal relationship is observed with a significant increase from 3 % of the nanoemulsion being retained when no thiol functionality is present, to 42 % retention when $SH_{0.75}DBiB_{0.25}$-*p*($OEGMA_{50}$-*co*-$EGDMA_{0.8}$) is used as the stabiliser. A small additional increase to 43% retention is seen when $SH_{0.90}DBiB_{0.10}$-*p*($OEGMA_{50}$-*co*-$EGDMA_{0.8}$) is used but this appears to be a plateu of retention that may be derived from saturation of the mucosal surface. Interestingly, no meaningful change in retained nanoemulsion was seen between nanoemsulsions stabilised with either the non-functional DBiB-*p*($OEGMA_{50}$-*co*-$EGDMA_{0.8}$) or the $SH_{0.25}DBiB_{0.75}$-*p*($OEGMA_{50}$-*co*-$EGDMA_{0.8}$) lightly functional branched copolymer. This may be due to the stochastic nature of the adhesion and the probability of a nanoemulsion presenting a statistically placed thiol at the contact point and at the time of contact, Figure 4.34.

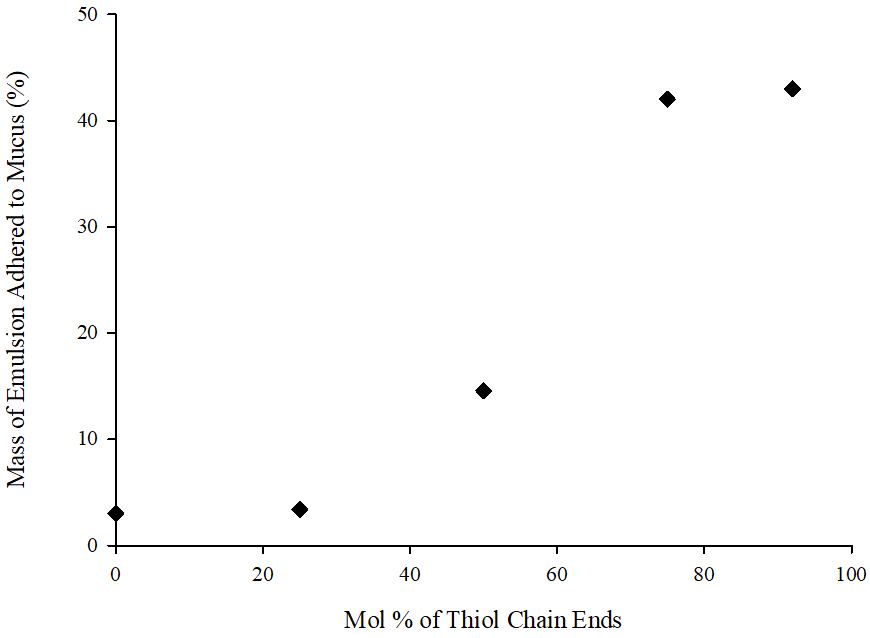

Figure 4.38 Mucoadhesive behaviour of nanoemulsions stabilised with polymeric surfactants DBiB-*p*($OEGMA_{50}$-*co*-$EGDMA_{0.8}$), $SH_{0.25}DBiB_{0.75}$-*p*($OEGMA_{50}$-*co*-$EGDMA_{0.8}$), $SH_{0.50}DBiB_{0.50}$-*p*($OEGMA_{50}$-*co*-$EGDMA_{0.8}$), $SH_{0.75}DBiB_{0.25}$-*p*($OEGMA_{50}$-*co*-$EGDMA_{0.8}$) and $SH_{0.90}DBiB_{0.10}$-*p*($OEGMA_{50}$-*co*-$EGDMA_{0.8}$) as determined by a flow of nanoemulsion over biosimilar mucus, measuring the amount of mucoadhesion (%).

DBiB-*p(*$OEGMA_{50}$-*co*-$EGDMA_{0.8}$) surprisingly showed very slight mucoadhesive behaviour which could be attributed to the mesh nature of mucus, where some entrapment of particles can be noted. When 50 % of the chain ends of the branched copolymer are thiol-bearing, statistically half of the droplet is coated in thiol functional chains which are more likely to successfully bind to the mucus. As the functionality of the particles is changed from no thiol to $SH_{0.75}DBiB_{0.25}$-*p(*$OEGMA_{50}$-*co*-$EGDMA_{0.8}$) the probability of binding to the cysteine rich areas of the mucus is increased. The actual values of mucoadhesion are presented in Table 4.8.

Table 4.8 Extent of mucoadhesion (%) by non-functional and thiol-functional branched copolymer surfactant stabilised nanoemulsions formulated with a 99:1 ratio of EtOAc:castor oil.

Polymer	D_z (nm)	Mucoadhesion (%)
DBiB-*p(*$OEGMA_{50}$-*co*-$EGDMA_{0.8}$)	228	3.0
$SH_{0.25}DBiB_{0.75}$-*p(*$OEGMA_{50}$-*co*-$EGDMA_{0.8}$)	288	3.4
$SH_{0.50}DBiB_{0.50}$-*p(*$OEGMA_{50}$-*co*-$EGDMA_{0.8}$)	251	14.5
$SH_{0.75}DBiB_{0.25}$-*p(*$OEGMA_{50}$-*co*-$EGDMA_{0.8}$)	249	42.0
$SH_{0.90}DBiB_{0.10}$-*p(*$OEGMA_{50}$-*co*-$EGDMA_{0.8}$)	345	43.0

4.6 *EX VIVO* MULTIPLE PARTICLE TRACKING

To probe the mucoadhesive properties of the nanoemulsions further, an *ex vivo* multiple particle tracking (MPT) study was conducted to detail their diffusive or adhesive behaviour through biologically-derived mucus. The studies were carried out in collaboration with the Gumbleton group in the School of Pharmacy and Pharmacology at Cardiff University, with the procedure detailed in preceding publications[39] and previously described mathematical methods detailed below.[147–149]

A fluorescent dye, Lumogen Red 305 (BASF), was encapsulated into nanoemulsions stabilised with the branched copolymer surfactants containing a varying amount of thiol functionality: DBiB-*p(*$OEGMA_{50}$-*co*-$EGDMA_{0.8}$), $SH_{0.25}DBiB_{0.75}$-*p(*$OEGMA_{50}$-*co*-$EGDMA_{0.8}$), $SH_{0.50}DBiB_{0.50}$-*p(*$OEGMA_{50}$-*co*-$EGDMA_{0.8}$), $SH_{0.75}DBiB_{0.25}$-

p($OEGMA_{50}$-*co*-$EGDMA_{0.8}$) and $SH_{0.90}DBiB_{0.10}$-*p(*$OEGMA_{50}$-*co*-$EGDMA_{0.8}$) at 0.1 wt % concentration, with respect to the final nanoemulsion volume. Nanoemulsions were formulated as described above using homogenisation (24,000 rpm for 2 minutes) of a 1:1 ratio of each aqueous polymer solution (5 wt %) to oil phase and a 99:1 v/v ratio of ethyl acetate:castor oil. Following overnight solvent evaporation of the volatile solvent, luminous pink emulsions were produced and characterised *via* DLS, Table 4.9 the nanoemulsions were stored at ambient temperature away from direct light. For MPT studies, porcine intestinal ileum (2 m) was obtained from a local abattoir and stored in ice-cold oxygenated phosphate buffered saline (PBS) prior to sample processing. The ileum was processed into 25 cm lengths and incised longitudinally to allow for waste to be gently rinsed away using ice-cold PBS. The mucus layer was subsequently harvested by gentle scraping, to increase the yield of the loose mucus layer but also include a high content of the adhered layer.[150] Previous reports have shown that the structure of mucus can be significantly damaged if gentle handling is not employed. The harvested mucus was divided into aliquots (0.5 g) and stored at -20 °C until required for use.[151,152]

Table 4.9 DLS analysis of lumogen red loaded nanoemulsions with varying polymeric surfactants. All nanoemulsions were formulated with an oil phase in a ratio of 99:1 EtOAc:Castor Oil.

Polymer	D_z (nm)	D_n (nm)	PdI	ζ (mV)
DBiB-*p(*$OEGMA_{50}$-*co*-$EGDMA_{0.8}$)	226	187	0.129	-19
$SH_{0.25}DBiB_{0.75}$-*p(*$OEGMA_{50}$-*co*-$EGDMA_{0.8}$)	203	156	0.148	-16
$SH_{0.50}DBiB_{0.50}$-*p(*$OEGMA_{50}$-*co*-$EGDMA_{0.8}$)	363	336	0.238	-8
$SH_{0.75}DBiB_{0.25}$-*p(*$OEGMA_{50}$-*co*-$EGDMA_{0.8}$)	479	371	0.330	-18
$SH_{0.90}DBiB_{0.10}$-*p(*$OEGMA_{50}$-*co*-$EGDMA_{0.8}$)	568	466	0.321	-16

The fluorescently labelled nanoemulsions were inoculated into a sample of mucus (0.5 g) at a concentration confirmed not to cause particle aggregation (0.001 %). This concentration was confirmed by inoculating porcine intestinal mucus with three volumes of nanoemulsions (0.05, 0.02 and 0.001 %) and conducting MPT studies where individual droplets could not be easily defined at concentrations of 0.05 and 0.02 %.

All samples were incubated for 2 hours at 37°C before particle tracking was studied, to ensure a good particle distribution throughout the sample. 2-dimensional imaging (Lecia DM IRB wide-field epi-fluorescence microscope, x63 magnification oil immersion lens) using a high speed camera (Allied Vision Technologies, UK), allowed video capture at a frame rate of 33 ms (30 frames/s), and each resulting video contained 300 frames. For each sample of mucus containing nanoemulsion, approx. 120 individual particles were tracked; each sample was repeated three times, therefore 360 nanoemulsion particles were tracked over 3 separate mucus samples. Fluorescent dye that appeared to dissociate from the nanoemulsions did not detract from individual droplet tracking, but was part of the background fluorescence. Videos were processed using Fiji ImageJ plugin mosaic to track individual droplet trajectories through the mucus sample.

The 10 second videos were reduced to 30 frame videos (1 second) where individually tracked particles were continuously maintained within the X-Y focal plane throughout the 30 frames, (see supporting USB). Limiting videos to 30 frames minimises the impact of mucin movement on particle diffusive calculations.[147] Individual particle trajectories were converted into numeric pixel data also using the Mosaic Particle Tracker plugin within Fiji ImageJ, which was able to be converted into metric distance based on microscope and video capture settings.

Distance moved by an individual particle over a selected time interval (Δt) in the X-Y trajectory is expressed as a squared displacement (SD). The mean squared displacement (MSD)[153], detailed in equation 4.2 of any particle (n) is the geometric mean of the particles SD through the 30-frame period.

$$MSD_{(n)} = (X_{\Delta})^2 + (Y_{\Delta})^2 \qquad (4.2)$$

MSD was calculated for the 360 particles over the three mucus samples and the Effective Diffusion Coefficient (Deff), equation 4.3 for each nanoemulsion was calculated:

$$Deff = MSD/ (4*\Delta t) \qquad (4.3)$$

where 4 is a constant relating to the 2D mode of video, and Δt known.

The particle diffusion across various time intervals can therefore be measured; and the number of particles that are diffusive through the mucus evaluated.[147] A diffusivity factor (DF), equation 4.4 expresses the Deff across time intervals chosen to be 1 s and 0.2 s.

$$DF = Deff_{\Delta t=1s} / Deff_{\Delta t=0.2s} \qquad (4.4)$$

From this calculation, a particle with a DF value of over 0.9 was determined to be diffusive, this is then further expressed as a percentage of diffusive particles. The diffusion in mucus is compared against that of particle diffusion in water (D^o), equation 4.5 which is calculated using the Stokes-Einstein equation at 37°C.

$$D^o = kT/ 6\pi\eta r \qquad (4.5)$$

Where k is the Boltzmann constant, T is absolute temperature, η is water viscosity and r the radius of the particles.

This also allows for diffusion of all particles to be expressed as the parameter percentage ratio of $Deff/D^o$.

Lumogen Red stability in the nanoemulsions appeared to decrease as the thiol content within the branched copolymer stabiliser increased and measured D_z values ranged from 226 to 568 nm across the samples, with PdI values increasing with the apparent released dye seeming to interfere with the DLS measurements slightly, Figure 4.39, and the formation of additional peaks which were not seen in the absence of the encapsulated dye.

.

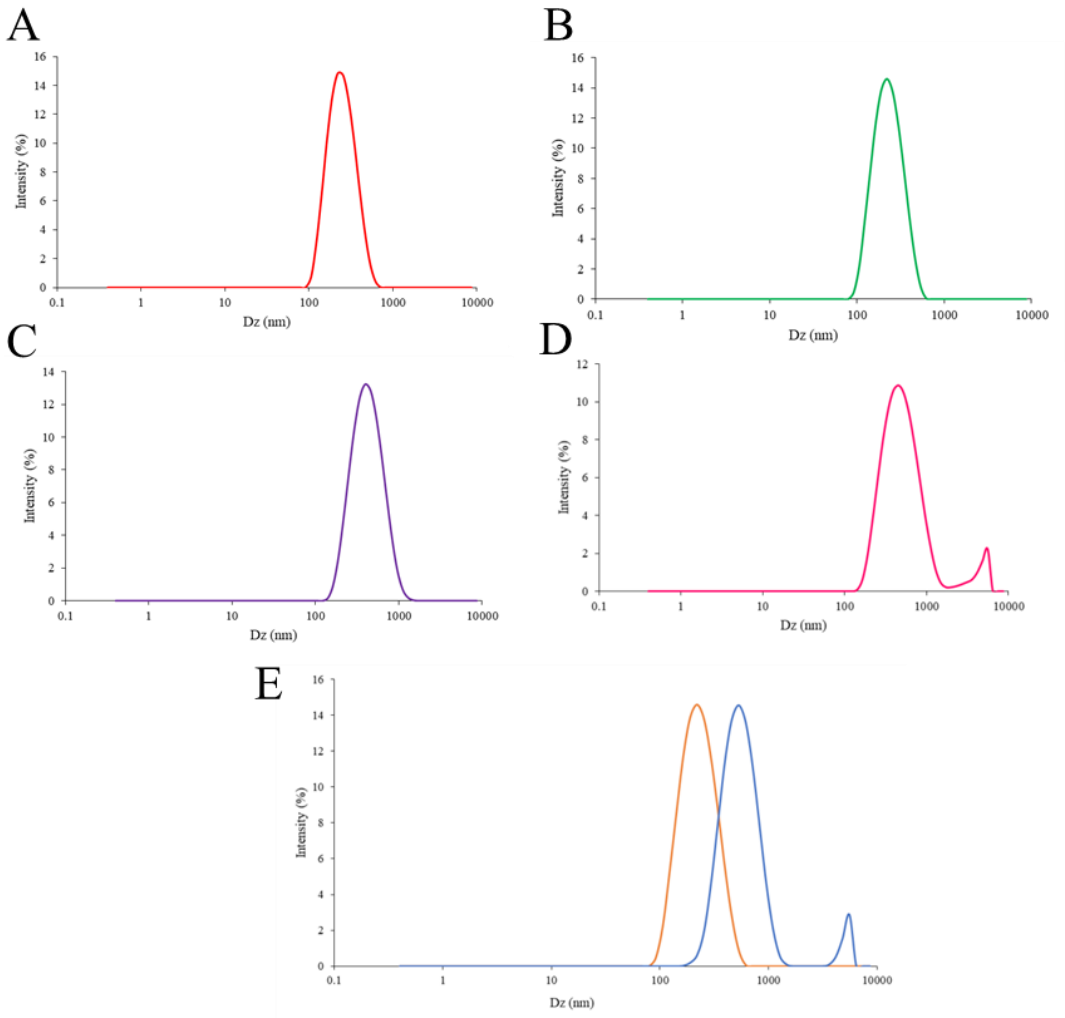

Figure 4.39 DLS traces of lumogen red nanoemulsions stabilised with A) DBiB-*p*(OEGMA$_{50}$-*co*-EGDMA$_{0.8}$) (red), B) SH$_{0.25}$DBiB$_{0.75}$-*p*(OEGMA$_{50}$-*co*-EGDMA$_{0.8}$) (green), C) SH$_{0.50}$DBiB$_{0.50}$-*p*(OEGMA$_{50}$-*co*-EGDMA$_{0.8}$) (purple), D) SH$_{0.75}$DBiB$_{0.25}$-*p*(OEGMA$_{50}$-*co*-EGDMA$_{0.8}$) (pink) and overlay of E) SH$_{0.25}$DBiB$_{0.75}$-*p*(OEGMA$_{50}$-*co*-EGDMA$_{0.8}$) (orange) with SH$_{0.90}$DBiB$_{0.10}$-*p*(OEGMA$_{50}$-*co*-EGDMA$_{0.8}$) (blue).

As mentioned above MPT is not affected by background fluorescence and individual nanoemulsion droplets were readily observed. Images taken from MPT videos, Figure 4.40, show the individual fluorescently labelled particles of similar diameters in the mucosal tissue. In Figure 4.34B, clouds of lumogen red are visible, most noticeably in the top left hand corner coinciding with the aggregation shown within DLS traces.

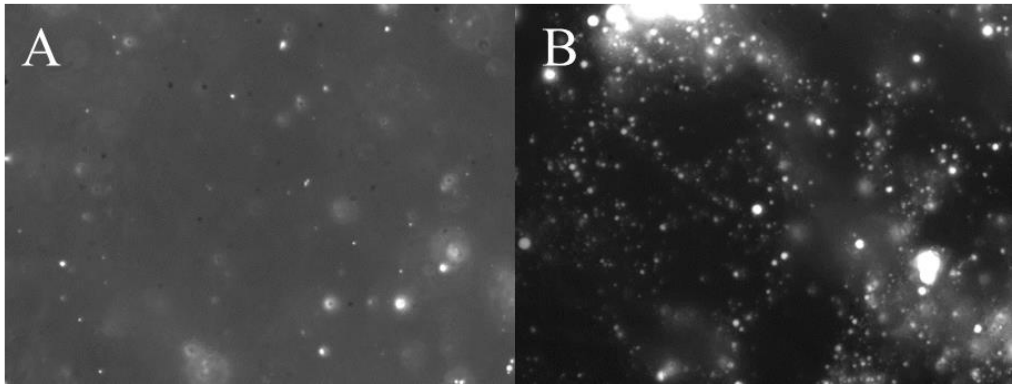

Figure 4.40 Images taken from MPT videos, of nanoemulsion with polymeric surfactants A) DBiB-*p(*OEGMA$_{50}$-*co*-EGDMA$_{0.8}$) and B) SH$_{0.90}$DBiB$_{0.10}$-*p(*OEGMA$_{50}$-*co*-EGDMA$_{0.8}$).

Following video capture of MPT, the individual nanoemulsion droplet trajectories are able to be visualised as shown in Figure 4.41, (video capture included on supporting disk). DBiB-*p(*OEGMA$_{50}$-*co*-EGDMA$_{0.8}$) and SH$_{0.25}$DBiB$_{0.75}$-*p(*OEGMA$_{50}$-*co*-EGDMA$_{0.8}$) stabilised nanoemulsions were readily able to diffuse through the mucus, Figure 4.35A and B, but increasing the thiol content of the branched copolymer stabiliser, using SH$_{0.50}$DBiB$_{0.50}$-*p(*OEGMA$_{50}$-*co*-EGDMA$_{0.8}$), led to a higher percentage of fully adhered and poorly diffusing nanoemulsion droplets in the mucus.

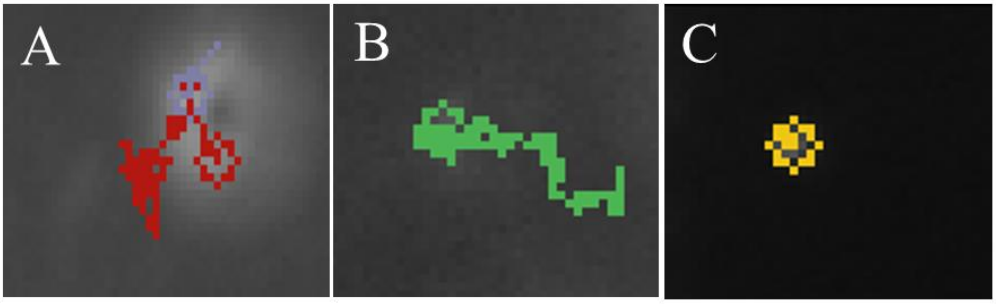

Figure 4.41 Typical MPT trajectories taken from Mosaic individual particle trajectory plugin on FIJI. Trajectories of nanoemulsions with polymeric surfactants; A) DBiB-*p*(OEGMA$_{50}$-*co*-EGDMA$_{0.8}$), B) SH$_{0.25}$DBiB$_{0.75}$-*p*(OEGMA$_{50}$-*co*-EGDMA$_{0.8}$) and SH$_{0.90}$DBiB$_{0.10}$-*p*(OEGMA$_{50}$-*co*-EGDMA$_{0.8}$)

For each nanoemulsion a D_{eff} value was calculated for each of the 360 particles, over a time interval of 1 second. Diffusion kinetics are detailed in Table 4.10

Table 4.10 Diffusion kinetics of nanoemulsions stabilised with polymeric surfactants with general composition SH_xDBiB_y-*p*(OEGMA$_{50}$-*co*-EGDMA$_{0.8}$) where x+y = 1 and DBiB-*p*(OEGMA$_{50}$-*co*-EGDMA$_{0.8}$), through native porcine mucus, n = 3, ± standard deviation.

Polymer	D_z (nm)	Diffusion in water D° (cm^2/sec *10^{-9})	Diffusion in Mucus Deff (cm^2/sec *10^{-9})	Deff/ D° (%)	Diffusive particles (%)
DBiB-*p*(OEGMA$_{50}$-*co*-EGDMA$_{0.8}$)	228	19.71	0.22390 (±0.0496)	1.1359	42
$SH_{0.25}DBiB_{0.75}$-*p*(OEGMA$_{50}$-*co*-EGDMA$_{0.8}$)	203	22.14	0.12148 (±0.0363)	0.5487	31
$SH_{0.50}DBiB_{0.50}$-*p*(OEGMA$_{50}$-*co*-EGDMA$_{0.8}$)	363	12.38	0.05074 (±0.0234)	0.4099	21
$SH_{0.75}DBiB_{0.25}$-*p*(OEGMA$_{50}$-*co*-EGDMA$_{0.8}$)	479	9.38	0.00244 (±0.0005)	0.0261	14
$SH_{0.90}DBiB_{0.10}$-*p*(OEGMA$_{50}$-*co*-EGDMA$_{0.8}$)	568	7.91	0.00085 (±0.0002)	0.0107	6

The DBiB-*p*(OEGMA$_{50}$-*co*-EGDMA$_{0.8}$) stabilised nanoemulsion showed significant diffusion through the mucus, with 42 % of particles diffusing rapidly, twice as fast as a nanoemulsion stabilised with $SH_{0.25}DBiB_{0.75}$-*p*(OEGMA$_{50}$-*co*-EGDMA$_{0.8}$) which also sees an 11 % drop in diffusive nanoemulsion droplets. The rate of diffusion in mucus continues to drop by half as the thiol chain end content is increased to 50 and 75 mole %. The $SH_{0.90}DBiB_{0.10}$-*p*(OEGMA$_{50}$-*co*-EGDMA$_{0.8}$) stabilised nanoemulsion has the most dramatic increase in mucoadhesion, with only 6 % of the particles showing diffusive behaviour and these nanoemulsion droplets only diffusing at a rate of 0.00085×10^{-9} cm^2/sec .

Heterogenity of particle diffusion is calculated to assess the diffusive properties of each individual particle. This means that outliers to the population can be determined, which may follow alternative pathways through the mucus. For the percentile data shown in Figure 4.42, the effective diffusion coefficient values, Deff, were calculated for n = 360 particles over 1 second, $Deff_{\Delta t=1s}$, and ranked; the 90th percentile shows the Deff value below which 90 % of the nanoemulsion droplet reside.

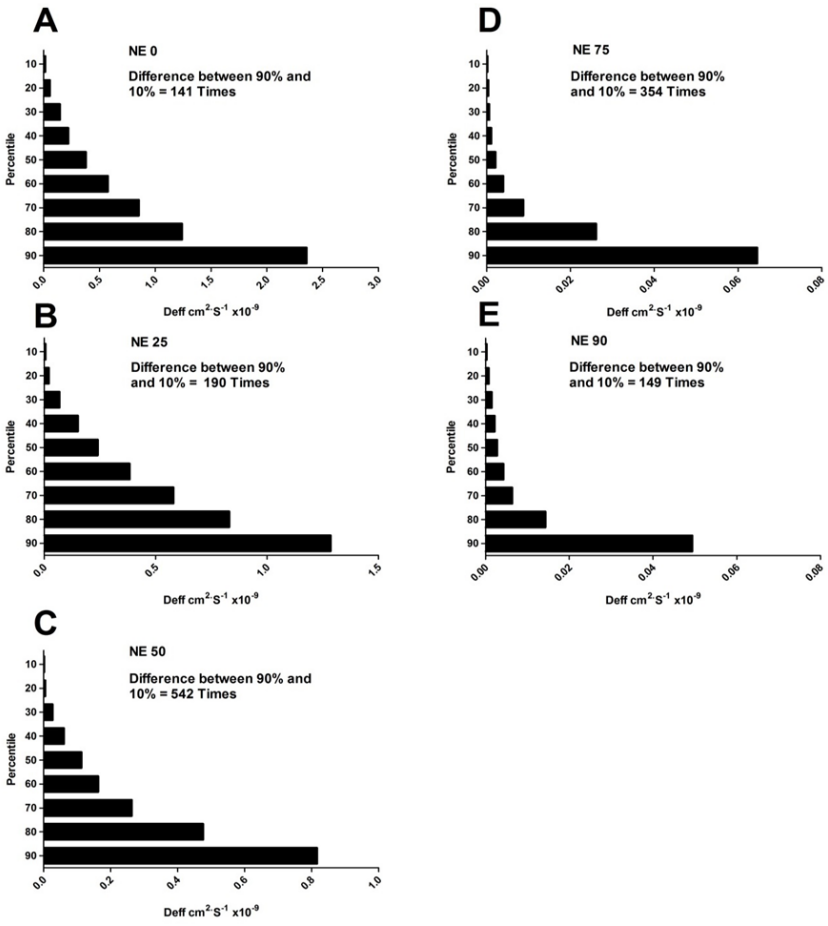

Figure 4.42 Heterogenity of movement through mucus of nanoemulsions over a range of different thiolated polymers. Deff was calculated over n = 360 particles over 1 second, percentiles ranked from the 10th to the 90th, where the 90th percentile shows the Deff value within which 90 % of the particles are below. A) DBiB-*p*(OEGMA-*co*-$EGDMA_{0.8}$), B) $SH_{0.25}DBiB_{0.75}$-*p*($OEGMA_{50}$-*co*-$EGDMA_{0.8}$), C) $SH_{0.50}DBiB_{0.50}$-*p*($OEGMA_{50}$-*co*-$EGDMA_{0.8}$), D) $SH_{0.75}DBiB_{0.25}$-*p*($OEGMA_{50}$-*co*-$EGDMA_{0.8}$) and E) $SH_{0.90}DBiB_{0.10}$-*p*($OEGMA_{50}$-*co*-$EGDMA_{0.8}$)

Heterogenity of particle diffusion shows the distinct difference between the diffusive behaviour of DBiB-*p(*$OEGMA_{50}$-*co*-$EGDMA_{0.8}$) and $SH_{0.90}DBiB_{0.10}$-*p(*$OEGMA_{50}$-

co-EGDMA$_{0.8}$) where the 90th percentile Deff values are 2.5 x10^{-9} and 0.05x10^{-9} cm^2 S^{-1} respectively. This highlights not only the difference in diffusive speed between nanoemulsions stabilised with branched copolymers containing 0 and 90 mole% thiol functional chain ends but also aligns with the trend showing decreasing diffusion speed in the 90th percentile as the amount of thiol is increased.

4.7 OIL BLUE A RELEASE FROM NON-FUNCTIONAL AND THIOL-FUNCTIONAL NANOEMULSIONS

MPT studies have shown that by increasing the number of thiol chain ends present in the branched copolymer stabilisers, the rate of diffusion through mucus steadily declines, and the amount of particles showing diffusive character is reduced, Table 4.10; this correlates strongly with the results seen using the flow-through mucoadhesion model. DBiB-*p*(OEGMA$_{50}$-*co*-EGDMA$_{0.8}$) showed rapid diffusion and limited mucoadehsion whilst the thiol-containing branched copolymer stabilisers created nanoemulsions with carrying properties.

A clear indication of the density of packing and the physical conformations of the varying branched copolymer surfactants has been building with each study. It appears that decreasing the number of DBiB chain ends within the stabilising branched copolymers leads to a variation in the homogeneity of the hydrophilic branched *p*(OEGMA) chains.

When all chain ends of the branched copolymer are hydrophobic, the stabilised nanoemulsion droplets can be considered as being stabilised by a dense arranegement of close-packed DBiB chains at the oil water interface and, therefore, each primary chain of the branched stabiliser is held within a limited distance from the oil droplet surface, Figure 4.43A. This allows the droplets to pass quickly through the mucus due to the stealth like qualities of *p(*OEGMA),[48] with 58 % of the particles showing limited diffuse probably due to the mesh like nature of mucus (200+ nm particles would be expected to be trapped to some extent) and the distribution of pore sizes being heterogeneous.

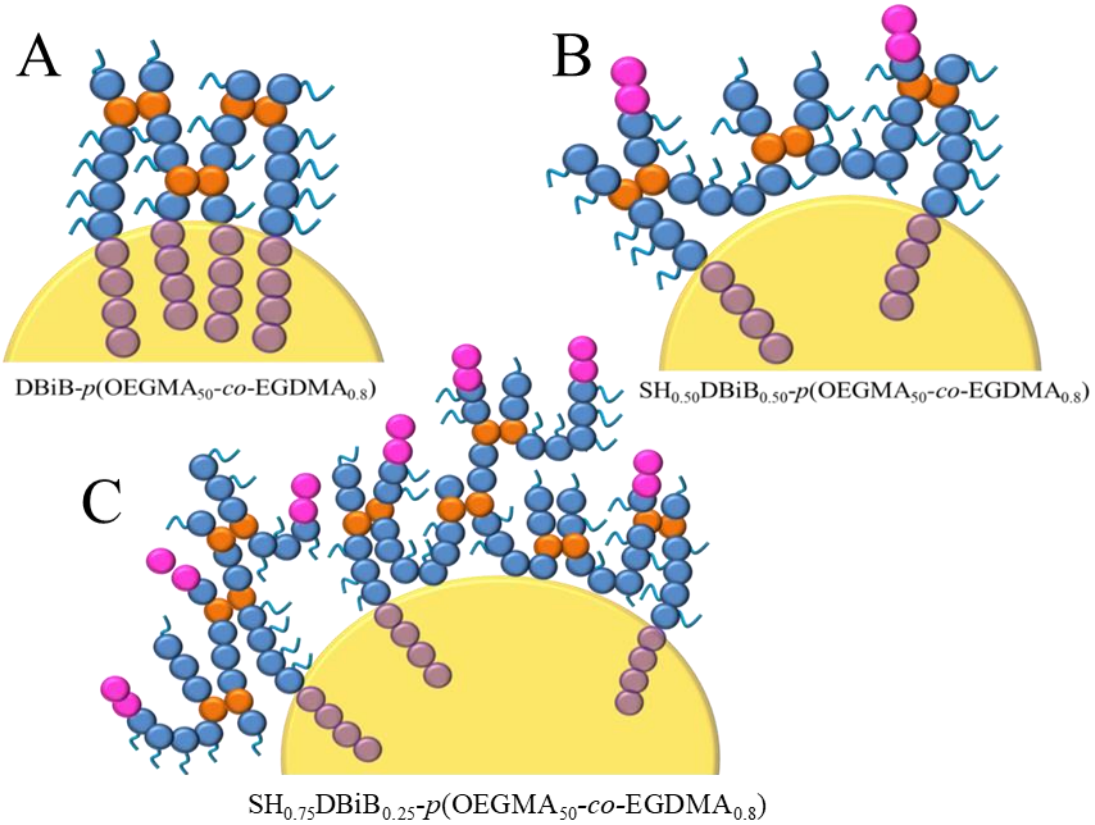

Figure 4.43 Potential arrangement of thiol-functional branched copolymers around an oil droplet; A) DBiB-*p*(OEGMA$_{50}$-*co*-EGDMA$_{0.8}$), B) SH$_{0.50}$DBiB$_{0.50}$-*p*(OEGMA$_{50}$-*co*-EGDMA$_{0.8}$) and C) SH$_{0.75}$DBiB$_{0.25}$-*p*(OEGMA$_{50}$-*co*-EGDMA$_{0.8}$).

SH$_{0.25}$DBiB$_{0.75}$-*p*(OEGMA$_{50}$-*co*-EGDMA$_{0.8}$) stabilised nanoemulsions have a slight decrease in particle diffusion which can be attributed to disulphide bonds being formed between the free thiol groups on the droplet surface and the cysteine rich areas of mucus; this correlates with the slight, but limited mucoadhesion observed.

Further increases in thiol functionality within the branched copolymers leads to a subsequent decrease in the number of hydrophobic chain ends and therefore the number and density of anchoring points for the branched copolymers at the oil droplet interface. Hypothetically, this would also lead to an expansion of the hydrodynamic diameter as the branched copolymer primary chains are more able to extend into the aqueous surrounding medium, Figure 4.43 B and C. A decrease in diffusion would be expected (ie those nanoemulsions that are diffusing would diffuse slower as they have a larger hydrodynamic diameter) and the increased concentration of thiols would lead to an increase in mucoadehesion (as observed in the flow-through experiment) and a decrease in the number of diffusing nanoemulsion droplet.

The apparent release of Lumogen red from the nanoemulsions with higher thiol functionality, seen during the MPT studies, also suggested that the decreasing density of DBiB-derived chain ends may lead to "leaky" nanoemulsion droplet interfaces. This is schematically shown in Figure 4.43 where the thiol functional branched copolymers are extending into the aqueous continuous phase and the density of DBiB chain ends decreases. If this is occurring, the hydrophobic dye may be able to release from the oil droplet and release would be expected to be mediated by DBiB content in the branched copolymer stabiliser.

To investigate this hypothesis, a radiochemical dialysis experiment was undertaken to monitor release of a hydrophobic dye from nanoemulsions stabilised with either $SH_{0.75}DBiB_{0.25}$-*p(*$OEGMA_{50}$-*co*-$EGDMA_{0.8}$) or DBiB-*p(*$OEGMA_{50}$-*co*-$EGDMA_{0.8}$). Nanoemulsions were generated as described previously (1:1 ratio of aqueous polymer solution (5 wt %), 99:1 ratio of EtOAc:castor oil), yielding a final emulsion volume of 1.5 mL. Table 4.12 and Figure 4.44. The nanoemulsions were loaded with tritiated Oil blue A (0.1 wt %) as a radiolabelled hydrophobic dye, rather than Lumogen red, as Oil blue A has a very low water-solubility and therefore was expected to accentuate any differences in release; radiological studies were chosen as detection and quantification is very sensitive and may be adjusted without changing the concentrations of materials used. DLS evaluations showed D_z values of 230 nm for nanoemulsions generated using DBiB-*p*($OEGMA_{50}$-*co*-$EGDMA_{0.8}$) D_z = 353 nm when using the $SH_{0.75}DBiB_{0.25}$-*p*($OEGMA_{50}$-*co*-$EGDMA_{0.8}$) stabiliser. This difference is consistent with the size increases previously described in this chapter and the rationale explained above.

Table 4.12 Comparison of hydrophobic dye loaded nanoemulsions compared to blank nanoemulsions, with the oil phase composed of 99:1ethyl acetate:castor oil.

Polymer	Dye Loaded	D_z (nm)	D_n (nm)	PdI
DBiB-*p*(OEGMA$_{50}$-*co*-EGDMA$_{0.8}$)	^{3}H Oil blue	230	206	0.066
SH$_{0.75}$DBiB$_{0.25}$-*p*(OEGMA$_{50}$-*co*-EGDMA$_{0.8}$)	^{3}H Oil blue	353	248	0.244
DBiB-*p*(OEGMA$_{50}$-*co*-EGDMA$_{0.8}$)	Oil blue	225	195	0.057
DBiB-*p*(OEGMA$_{50}$-*co*-EGDMA$_{0.8}$)	Lumogen	226	187	0.129
SH$_{0.75}$DBiB$_{0.25}$-*p*(OEGMA$_{50}$-*co*-EGDMA$_{0.8}$)	Lumogen	479	371	0.330
DBiB-*p*(OEGMA$_{50}$-*co*-EGDMA$_{0.8}$)	-	228	209	0.079
SH$_{0.75}$DBiB$_{0.25}$-*p*(OEGMA$_{50}$-*co*-EGDMA$_{0.8}$)	-	249	230	0.100

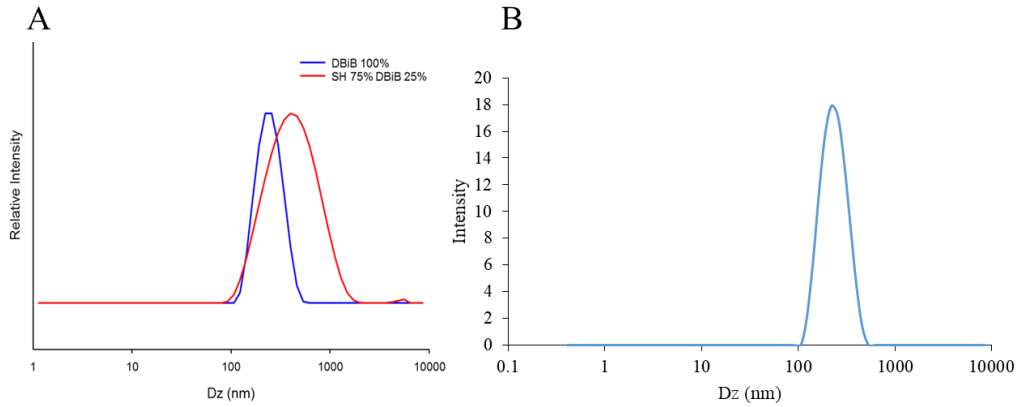

Figure 4.44 A) DLS trace of DBiB-*p*(OEGMA$_{50}$-*co*-EGDMA$_{0.8}$) (blue) and SH$_{0.75}$DBiB$_{0.25}$-*p*(OEGMA$_{50}$-*co*-EGDMA$_{0.8}$) (red) stabilised nanoemulsions with tritiated Oil blue A (0.1 wt %) and B) DBiB-*p*(OEGMA$_{50}$-*co*-EGDMA$_{0.8}$) stabilised nanoemulsion loaded with oil blue A (0.1 wt %).

A schematic of the dialysis experimental is shown in Figure 4.45, where a 3.5 kDa molecular weight cut off membrane was used and distilled water was employed as the reservoir solvent. Release of Oil blue A was monitored for 24 hrs with 1 mL sampled at t = 0.5 hrs and 1 hr, then subsequent 1 hr time points for 8 hrs. After each sample, the full reservoir was replaced to maintain sink conditions throughout the experiment. Quantification of dye release was conducted using liquid scintillation counting.

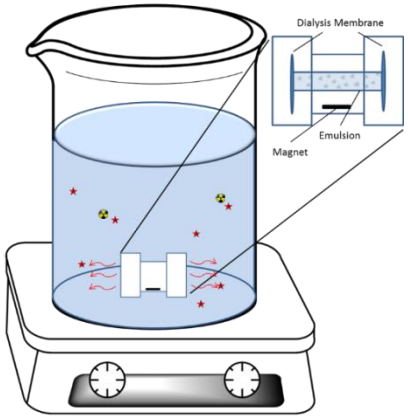

Figure 4.45 Diagram of dialysis experimental set-up, with distilled water as reservoir.

The dialysis study described above appears to confirm the previously described hypothesis; when using $SH_{0.75}DBiB_{0.25}$-*p*(OEGMA$_{50}$-*co*-EGDMA$_{0.8}$) as the nanoemulsion stabiliser, an increase rate of dye release was observed in comparison to the non-functional nanoemulsion stabilised with DBiB-*p*(OEGMA$_{50}$-*co*-EGDMA$_{0.8}$). After 24 hrs the thiol functionalised nanoemulsion had released 26 % more dye, Figure 4.46, compared to the un-functionalised counterpart.

The lack of anchoring DBiB chain ends does seem to lead to a "leaky" interface which is consistent with the Lumogen red loading observations and many of the observations described during this Chapter including contact angle studies and varying DLS measurements over systematically varying nanoemulsions.

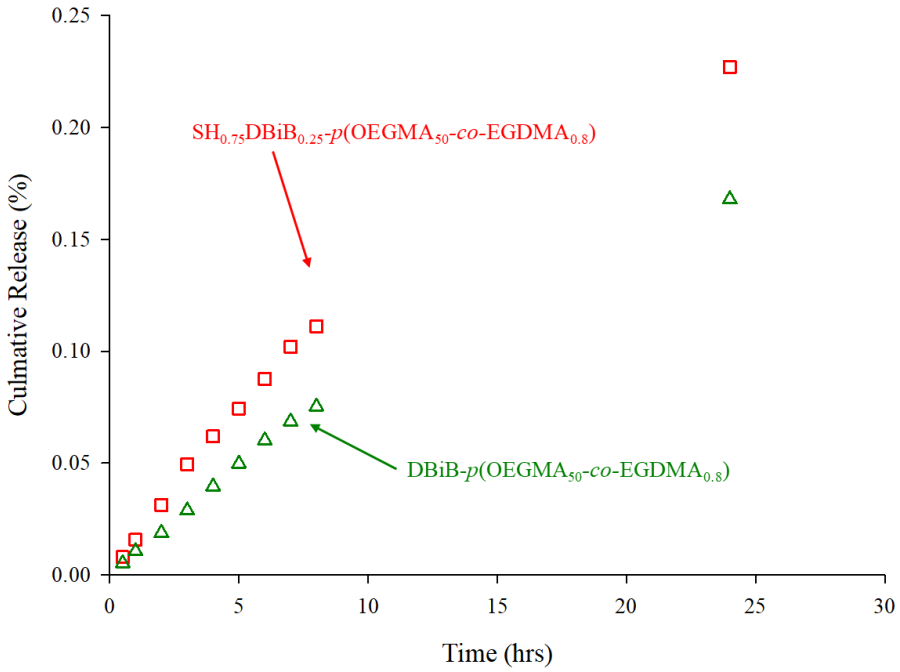

Figure 4.46 Cumulative release (percentage) of oil blue A (0.1 wt %) from nanoemulsions stabilised with DBiB-*p*(OEGMA$_{50}$-*co*-EGDMA$_{0.8}$) (green) and SH$_{0.75}$DBiB$_{0.25}$-*p*(OEGMA$_{50}$-*co*-EGDMA$_{0.8}$) (red).

4.8 CONCLUSIONS

In this study, branched copolymers with the general composition XanBiB$_x$DBiB$_y$-*p*(OEGMA$_{50}$-*co*-EGDMA$_{0.8}$) have been synthesised with variation of x and y varying systematically from 0:1 through to 1:0 respectively. Deprotection of the copolymers exposed the thiol groups and yielded branched copolymers with the general composition SH$_x$DBiB$_y$-*p*(OEGMA$_{50}$-*co*-EGDMA$_{0.8}$). The library of materials successfully generated macroemulsions and nanoemulsions which demonstrated interactions with biosimilar and biologically-derived mucus samples. The instability of the macroemulsions when presented to mucus substrates appears to offer the potential for triggered release from samples that are very stable in the absence of the mucosal surface.

The ability to modify the number of thiols within the branched copolymer stabilisers and resulting macro and nanoemulsions has been substantially demonstrated with variations of behaviour being observed in a number of different studies. Very interestingly, the strategy presented here allows both control over the size of emulsion droplets at constant thiol content and the number of thiols present at constant emulsion

droplet size, with the subsequent control of emulsion droplet behaviour. Unexpectedly, the influence of droplet diameter on mucoadhesion at constant thiol content, also allows a tailoring of behaviour in mucosal environments.

Mucoadhesive studies using MPT and *ex vivo* porcine mucus also identified DBiB-*p*(OEGMA$_{50}$-*co*-EGDMA$_{0.8}$) stabilised nanoemulsions as extremely diffusive with a demonstrated 263-fold difference between the diffusion speed of DBiB-*p*(OEGMA$_{50}$-*co*-EGDMA$_{0.8}$) stabilised nanoemulsions and nanoemulsions formed using the high thiol counterpart SH$_{0.90}$DBiB$_{0.10}$-*p*(OEGMA$_{50}$-*co*-EGDMA$_{0.8}$). The Cardiff University team commented that these nanoemulsions were amongst the fastest diffusing particles they have studied.

Overall, this investigation has shown that the increase in thiol chain ends within the branched copolymers leads to a controllable increase in mucoadhesive behaviour. However, the impact of reducing the number of hydrophobic chain ends on the hydrodynamic diameter of the nanoemulsions and the potential robustness of the oil-water interface, has also become apparent. This suggests that the thiol-content, where mucoadhesion is maintained, may need to be balanced by the ability to retain hydrophobic guest molecules in any drug delivery applications. Following confirmation that these emulsions do indeed exhibit mucoadhesive properties, the potential for them to be used as for drug delivery requires biological evaluation and this will be the subject of the next Chapter.

CHAPTER 5

Evaluation of Mucoadhesive and Non-Mucoadhesive Emulsions for Medical Applications

5.1 INTRODUCTION

The aim of this chapter is to evaluate the benefits of mucoadhesive emulsions for drug delivery *via* two routes of administration; ophthalmic topical application and *in vivo* oral delivery. In Chapter 4 the successful mucoadhesive characteristics of the polymeric surfactant $SH_{0.75}DBiB_{0.25}$-*p(*$OEGMA_{50}$-*co*-$EGDMA_{0.8}$*)* was determined therefore this polymer was chosen to formulate a mucoadhesive emulsion for further study as a drug delivery vehicle. DBiB-*p(*$OEGMA_{50}$-*co*-$EGDMA_{0.8}$*)* will be used to compare the efficacy between a fully diffusive and mostly mucoadhesive emulsion. Both mucoadhesive and non-mucoadhesive emulsions at the nano- and macro-scale will be biologically evaluated using two cell lines, human corneal epithelial cells (HCE-T) and human conjunctival epithelial cells (HCjE-Gi). In previous studies HCjE-Gi cells have shown to secrete mucus, MUC5AC, once a monolayer of cells has been established.[154] The structure of intestinal mucus is well documented and covers the epithelial cell layer in the gut.[1,155] Mucoadhesive properties of emulsions will be assessed in order to overcome mucus binding inefficiencies and penetration of emulsion through mucus layers will be studied. Emulsions will be loaded with relevant drugs for ophthalmic diseases, Amphotericin B and Cyclosporin A, as well as FTC-prodrug a poorly water soluble drug compound to be absorbed through the gut to understand loading, stability, delivery and finally release.

5.1.1 Structure of the Eye

The human eye (Figure 5.1) consists of two regions: the anterior section including cornea to lens and posterior section, lens to optic nerve. The cornea is the eye's outermost layer and a transparent structural part of the eye that allows light into the lens and acts as a barrier against dirt and germs, and has been extensively reviewed elsewhere for these properties.[156] The cornea consists of five layers, of which three are cellular; epithelium, stroma and endothelium and two interface layers; Bowman membrane and Descement membrane.[157] The human tear film coats the surface of the eye and works to regulate the health of the eye as well as maintaining the surface. The tear film coats the anterior surface of the eye and is composed of three layers and is discussed in greater detail below in Section 5.1.2. The lacrimal gland supplies the aqueous layer[158], while the lipid layer is supplied by the meibomian glands[159] and the mucus layer by the goblet cells in the conjunctiva, which all make up the tear film.

However, studies have also highlighted that the lacrimal gland also supplies mucins to the tear film layer as well.[160] The meiboman glands are sebaceous glands located in the upper and lower eyelids, while the lacrimal glands are situated in upper lateral section of the eye orbit.

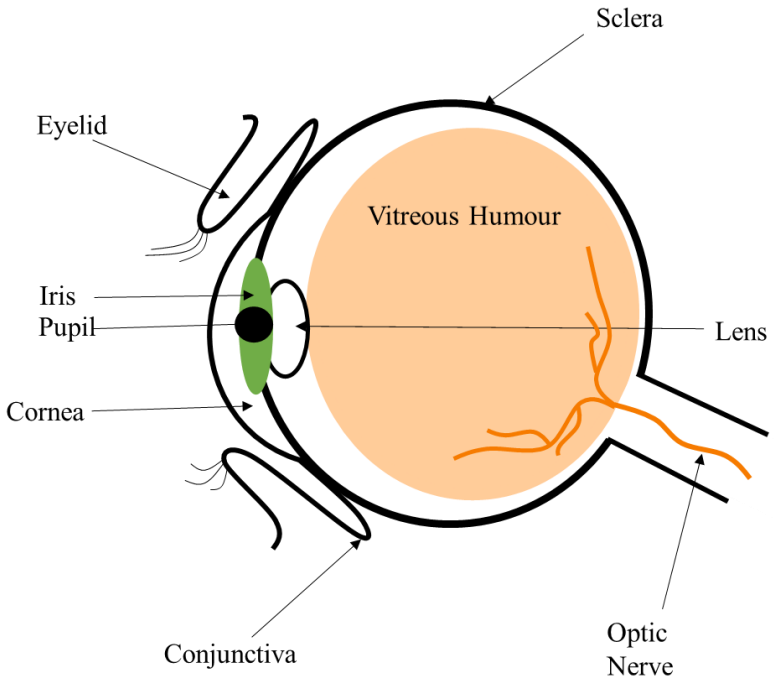

Figure 5.1 Structure of the human eye.

5.1.2 Mucus Production in the Eye

Mucus is produced via two pathways in the eye: 1) Conjunctival goblet cells located within the conjunctiva, Figure 5.1 secrete mucins which spread over the surface of the cornea and conjunctiva, 2) Epithelial cells secrete mucins which form a gel-like matrix, binding loosely to the surface of the microvilli of the epithelium as a stationary layer.[10]

The mucin layer secreted directly by epithelial cells has a thickness of 0.035 μm[9], but the tear film has been shown to vary in thickness from 5 – 40 μm,[9–11] with the middle aqueous layer being ~ 7 μm thick.[161,162] The tear film is composed of three layers; the mucin, aqueous and lipid layers,[10] Figure 5.2. For normal vision to occur the tear film must form a smooth even layer over the surface of the cornea. The phenomena of blinking is used not only to clear the eye of any foreign bodies, but also acts to spread the tear film and mucins over the surface of the cornea. Every time blinking occurs,

the tear film is reformed, mucus layer is resurfaced and the lipid layer redistributed across the preocular surface.[11] The mucus layer helps form and maintain the tear film layer, making the epithelial surface wettable by tears therefore further helping trap contamination.

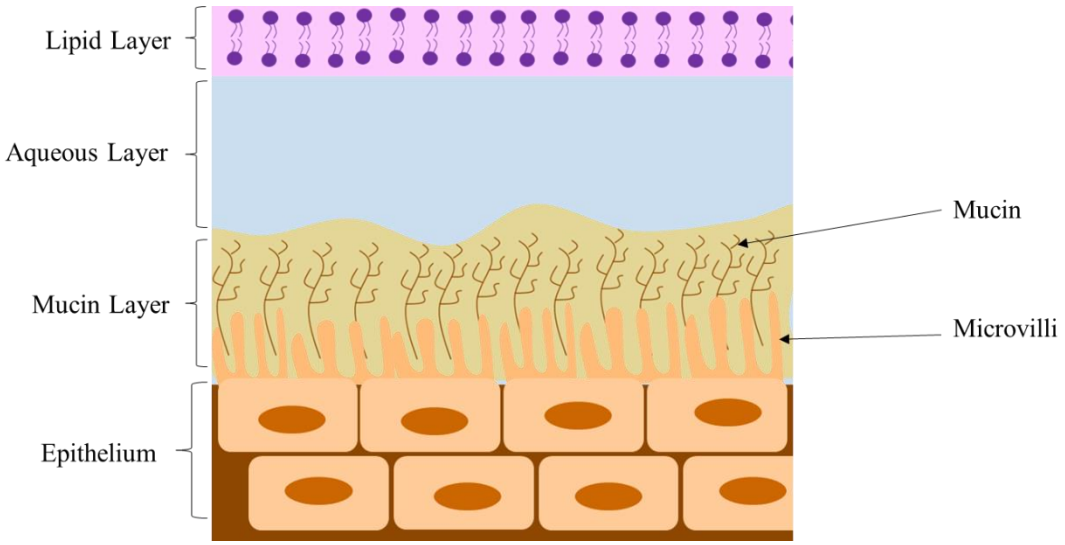

Figure 5.2 Tear film structure consists of three layers: lipid, aqueous and mucin. The mucins are secreted by epithelium cells and stick to the microvilli forming a gel-like matrix.

5.1.3 Corneal Diseases and Current Treatments

There are a variety of conditions which can affect the cornea, including injuries which can heal on their own or cause deep scarring, allergies such as hayfever and corneal dystrophies, where the cornea loses its normal clarity due to a build-up of material. In this investigation two of the most common corneal diseases will be focused on; fungal keratitis and kertaconjuctivitis sicca (dry eye syndrome).

Fungal keratitis is a condition more commonly found in tropical countries and is a potentially blinding condition if not properly treated. Symptoms include blurred vision, redness as well as pain and are a significant cause of ocular morbidity and unilateral blindness globally. Fungal keratitis is an infection of the cornea that can develop quickly from eye injury or even contact lens use; it can be caused by filamentous fungi such as *Fusarium* or *Aspergillus* species or non-filamentous yeasts *candida* species. Fungal keratitis is a common cause of corneal ulcers in developing countries, in India the estimated incidence is 113 in 100,000.[163] In less economically developed countries ocular trauma is common among agricultural workers and is the

most common site of infection of fungal keratitis.[163] Fungal spores within the environment enter through epithelia defects, often caused by the trauma but can also be due to contact lens wear or ocular surgery. In the US fungal keratitis is a rare condition, however it is found more typically in the southern states with *Candida* being the more prevalent cause with 30,000 new cases reported annually.[163] Due to the prevalence of contact lens use and the reduction of agriculture in the US there is a risk factor of 37 % for people who wear contact lenses and a 25 % risk factor for ocular trauma.[163] *Candida* usually causes keratitis in eyes which have a pre-existing ocular surface disease, previous treatment with topical steroids or systemic illnesses.[164]

Amphotericin B (Amp B), Figure 5.3, is an antifungal drug used to treat fungal keratitis;[165] it is applied as a topical solution and has previously shown good activity against *Aspergillus* and *Candida* strains and continues to be the first choice of treatment against *Candida.*[163] Amp B works by binding to the fungal cell membrane, forming pores causing rapid ion leakage and therefore fungal cell death with the mechanism well studied elsewhere.[166,167]

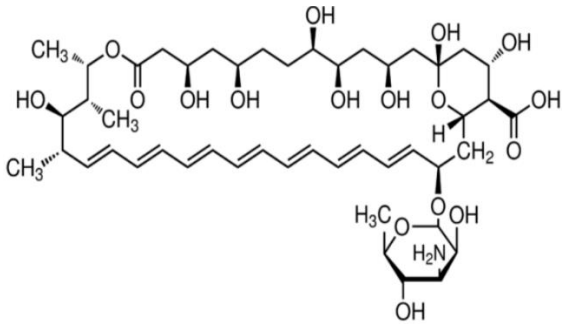

Figure 5.3 Chemical structure of Amphotericin B an anti-fungal agent used to treat keratitis.

Cyclosporin A (CsA), see Figure 5.4, is an anti-inflammatory and immunosuppressant which can be used to treat a number of ocular conditions including uveitis (inflammation of the middle layer of the eye), corneal healing, vernal keratoconjunctivitis (an allergic response) as well as helping prevent rejections of corneal transplants.[168–171]

Another disease which affects the cornea is keraticonjunctivitis sicca, or as more commonly referred to, dry eye syndrome. This is a common condition which affects the tear film causing either a lack of formation of tears or rapid evaporation of tears from the ocular surface.[172] Patients who have dry eye syndrome are prone to

potentially blinding infections as well as increased risk of complications following procedures. Dry eye syndrome is associated with a variety of causes including environmental conditions, hormone imbalance and contact lenses.[173] Previous treatments for dry eye syndrome included the use of artificial tears, ointments and environmental control, however research concluded that dry eye syndrome could successfully be treated by an anti-inflammatory agent. Studies showed that decreased tear secretion, turnover and desiccation promote inflammation on the ocular surface.[174]

CsA in an emulsion form was the first FDA approved anti-inflammatory treatment for dry eye syndrome in 2002. Through multiple clinical trials[175,176] CsA was shown to be able to treat dry eye syndrome *via* stimulating the production of aqueous tears as well as reducing the symptoms of blurred vision and reducing the need for artificial tears. Through these studies it was shown that ocular surface and lacrimal gland inflammation had been identified which play a role in the pathogenesis of dry eye syndrome.[172]

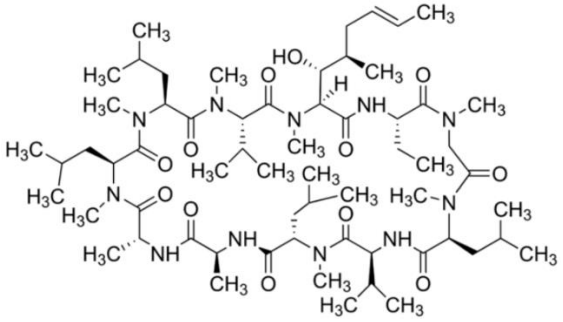

Figure 5.4 Chemical structure of Cyclosporin A an immunosuppressant used to treat a variety of ocular conditions including dry eye syndrome.

The most common topical administration of ophthalmic treatments is eye drops, providing patients with ease of application as well as being a non-invasive system. However, a drawback to the use of eye drops is that they are rapidly cleared from the site of administration by the eyes defensive mechanisms; blinking, tear drainage and tear formation.[156] This leads to poor penetration for drugs applied topically, with contact time with the ocular surface being low, leading to less than 5 % of the applied dose reaching the intraocular tissues.[177,178] Due to this rapid clearance alongside the low levels of permeation across the cornea, the efficacy of eye droplets is low, leading to repetitive dosing. Further issues with eye drops include that the volume administered typically exceeds the capacity of the conjunctival sac, leading to

overspill onto the cheeks.[179] There is potential to mitigate these effects by utilising a mucoadhesive system as a topical ophthalmic treatment, increasing the retention time of the drug at the site of administration due to bonding of the mucoadhesive system to the mucins present in the tear film.

CsA is currently administered as an ophthalmic emulsion for topical dosing (0.05 %, Restasis®), which is composed of glycerin, castor oil, polysorbate 80, carbomer copolymer type A in water to improve the solubility and adjusted to pH using NaOH.[158] Restasis® as an eye drop treatment has the same issues with retention time at the target site. Amp B was previously formulated as Fungizone®, a micellar formulation of the drug, however this formulation contained deoxycholate to improve the solubility of Amp B which was shown to be an irritant for the cornea.[156] Eye drops have recently been produced from the liposomal Amp B (AmBisome®), however this also has formulation problems as it is stated to only have a one week shelf life after reconstitution.[165]

5.1.4 *In-vitro* Cytoxicity Assays

In-vitro assays were performed on two cell lines, human corneal epithelial cells (HCE-T) and human conjunctival epithelial cells (HCjE-Gi) to determine the cytotoxic effects of both mucoadhesive and non-mucoadhesive emulsions at the nanoscale. HCE-T cells are a transformed cell line from a 49 year old female donor which were donated by JCHO Hohigaoka Medical Centre and HCjE-Gi are a human immortalised cell line which were donated by Gibson laboratory to the University of Liverpool. Both cell lines were used as they are well established and have similar structural and functional properties of corneal cells *in vivo* as well as having an active role in mucus production.

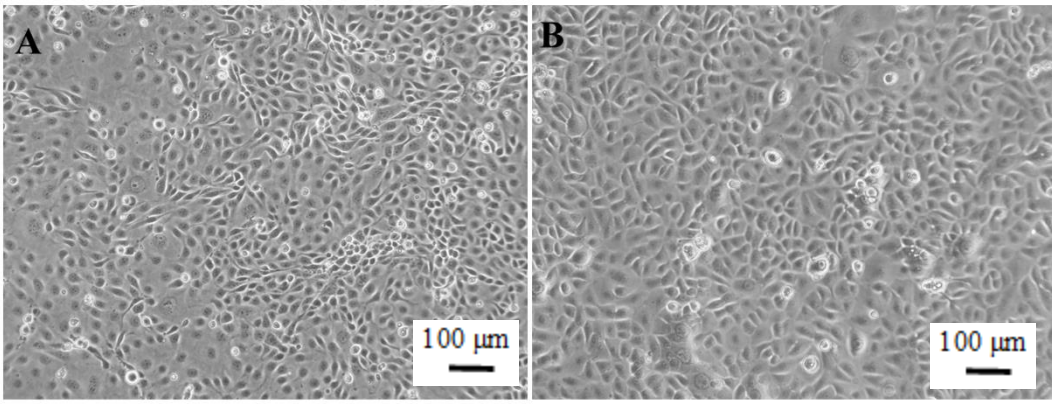

Figure 5.5 Optical microscopy image example of A) HCE-T and B) HCjE-Gi cells after 7 days of growth, scale bar = 100 µm.

There are many assays that can be carried out to evaluate the cytotoxic effects of a drug and/or an emulsion to a cell. In this section the assays used to biologically evaluate blank emulsions (emulsion not containing a drug payload) and loaded emulsions (emulsion containing drug) are discussed. It is important to perform multiple cytotoxicity assays on cells to confirm cytotoxic responses due to different criteria of cells being assessed.

5.1.4.1 Resazurin Assay

The resazurin assay measures the mitochondrial activity of a cell and is therefore indicative of cytotoxicity. The mitochondria have many functions within the cell, the most prominent being energy conversion and regulation of cell metabolism.[180] In this assay the mitochondria reduce resazurin to fluorescently active resorufin, see Scheme 5.1, which can be measured on a fluorescent plate reader. An advantage of this assay over the common MTT assay is that the cells remain alive after the assay, allowing for further studies on the same samples, including staining.

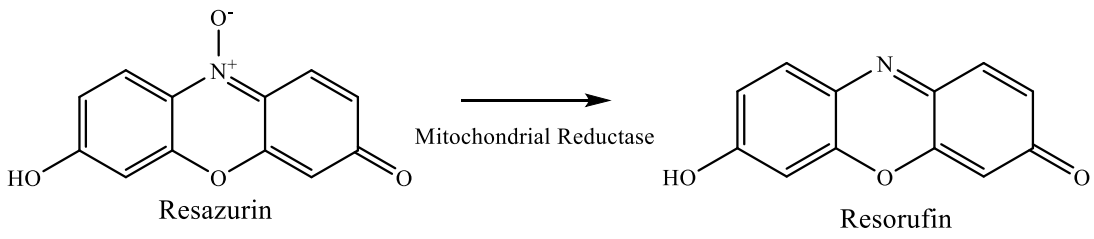

Scheme 5.1 Resazurin reduction to resorufin.

As mentioned it is important to perform multiple cytotoxicity assays on cells to confirm cytotoxic responses, for example a resazurin assay may indicate that there is

no cytotoxic response if the mitochondria of cells are not affected, however other components of the cell may be being affected.

5.1.4.2 Phalloidin Assay

Phalloidin is conjugated to a fluorophore and used to stain the F-actin of the cellular cytoskeleton so the structural integrity of the cell can be determined by fluorescent microscopy. Alongside phalloidin, the nuclei of the cells are also stained with 4′,6-diamidino-2-phenylindole (DAPI). DAPI is a fluorescent DNA stain, which binds to adenine-thymine rich areas making it an ideal stain for nuclei.[181] Figure 5.6 shows an image of HCE-T cells stained with phalloidin (green) and DAPI (blue), after 7 day growth to reach confluency. This is defined as the percentage at which the surface of the culture dish is covered in adherent cells.

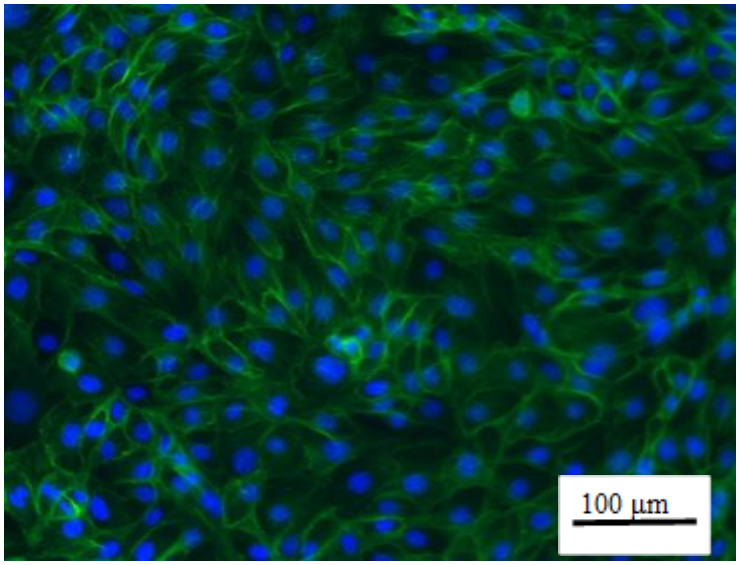

Figure 5.6 Phalloidin staining of HCE-T cells. DAPI staining of the nuclei (blue) and phalloidin staining of the cell cytoskeleton (green). 20 x zoom magnification, scale bar = 100 µm.

5.1.4.3 Live/Dead Assay

The live/dead assay determines cell viability in response to treatment, compared to the resazurin assay and phalloidin staining the number of dead cells can also be determined. In this assay live cells are distinguished from dead cells by the presence of intracellular esterase activity, shown by the enzymatic conversion of non-fluorescent calcein AM to intensely fluorescent calcein. The calcein dye is well retained within live cells, yielding an intense green fluorescence (ex/em ~495/~515

nm). Ethidium homodimer-1 (EthD-1) enters cells with damaged membranes and undergoes a 40-fold enhancement of fluorescence upon binding to the nucleic acids. This thereby produces a bright red fluorescence in dead cells (excitation/emission ~495/~635 nm), see Figure 5.7. EthD-1 is excluded from the live cells by the intact plasma membrane. Live/dead cell count was completed post-experimentation using an image processing package for unstitching of cell images and cell counting (FIJI, ImageJ 1.51n).

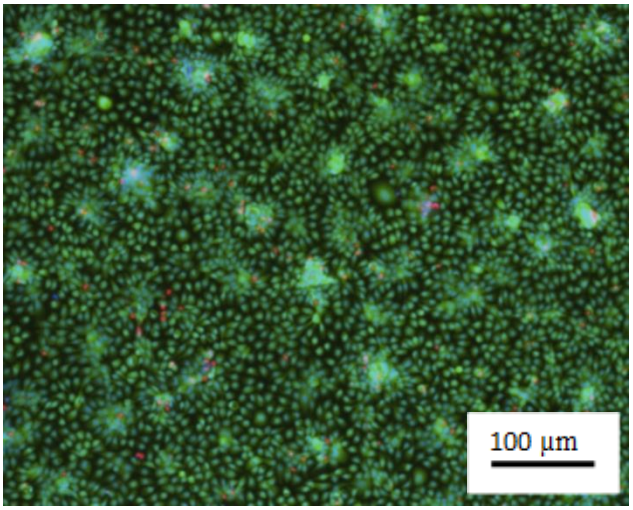

Figure 5.7 Live/dead assay performed on HCjE-Gi cell line. Live cells stained by enzyme activated calcein AM (green), dead cells by EthD-1 (red) and nuclei by DAPI (blue). 10 x zoom magnification, scale bar = 100 µm.

5.2 GENERATION OF DRUG LOADED MACROEMULSIONS

As discussed two drugs currently used to treat ophthalmic conditions were selected for encapsulation into emulsions: Amphotericin B (Amp B) an antifungal drug used to treat fungal keratitis[165] and Cyclosporin A (CsA) an immunosuppressant used to treat keratoconjunctivitis sicca (Dry Eye Syndrome).

Currently formulations of Amp B have stability issues leading to a short shelf life as well as low solubility in a range of solvent systems being problematic. Amp B has partial solubility in water at low pH values of 2-3 at approximately 0.1 mg/mL.[182] A variety of oils were tested to determine which could successfully solubilise Amp B and CsA to the greatest extent. Solubility was tested by blending drugs into the oils at a known mass and left for 3 days to stir. For castor, peanut, sesame, soybean and squalene, partial solubility at 7 mg/ mL was observed, however, as previously reported

Amp B has a critical aggregation concentration of (1 μg/mL)[183] so the presence of insoluble aggregates was noted in all oils tested. Squalene was selected as the oil phase for all drug loaded macroemulsion formulations due to its natural presence in the human eyelid lipid,[184] and also within the tears.[185] CsA has known aqueous solubility of 27.67 μg/mL[186] and was determined to be soluble in castor, peanut, soybean, sesame and squalene oils at 7 mg/mL. The drugs were loaded at topical dose concentrations into the emulsions *via* blending with the oil phase. As discussed earlier, Section 5.1.2., the current clinical formulations include concentrations of: Amp B at 0.15 % w/v[165] and CsA at 0.05 % w/v.[154]

Initially macroemulsions were formulated with the clinically relevant drug concentrations for biological evaluation, due to the interesting behaviour shown in Chapter 4, Section 4.3 where macroemulsions produced a burst release effect of encapsulated hydrophobic dye when in contact with a mucosal surface. This would be an interesting dynamic to explore as a topical ophthalmic treatment system with potential rapid release to the target site.

Macroemulsions were formulated *via* mechanical shearing, using an overhead shear homogeniser (Ultra-Turrax 25, IKA). Aqueous polymer solutions (5 mg/mL) were homogenised with squalene in a 1:1 ratio for 2 minutes at 24,000 rpm and left overnight to equilibrate before quantitative analysis by laser diffraction spectroscopy. Six macroemulsions were generated, unloaded or drug loaded with Amp B or CsA using unfuctionalised, DBiB-*p(*$OEGMA_{50}$-*co*-$EGDMA_{0.8}$) and thiol functionalised, $SH_{0.75}DBiB_{0.25}$-*p(*$OEGMA_{50}$-*co*-$EGDMA_{0.8}$) polymers for mucoadhesion.

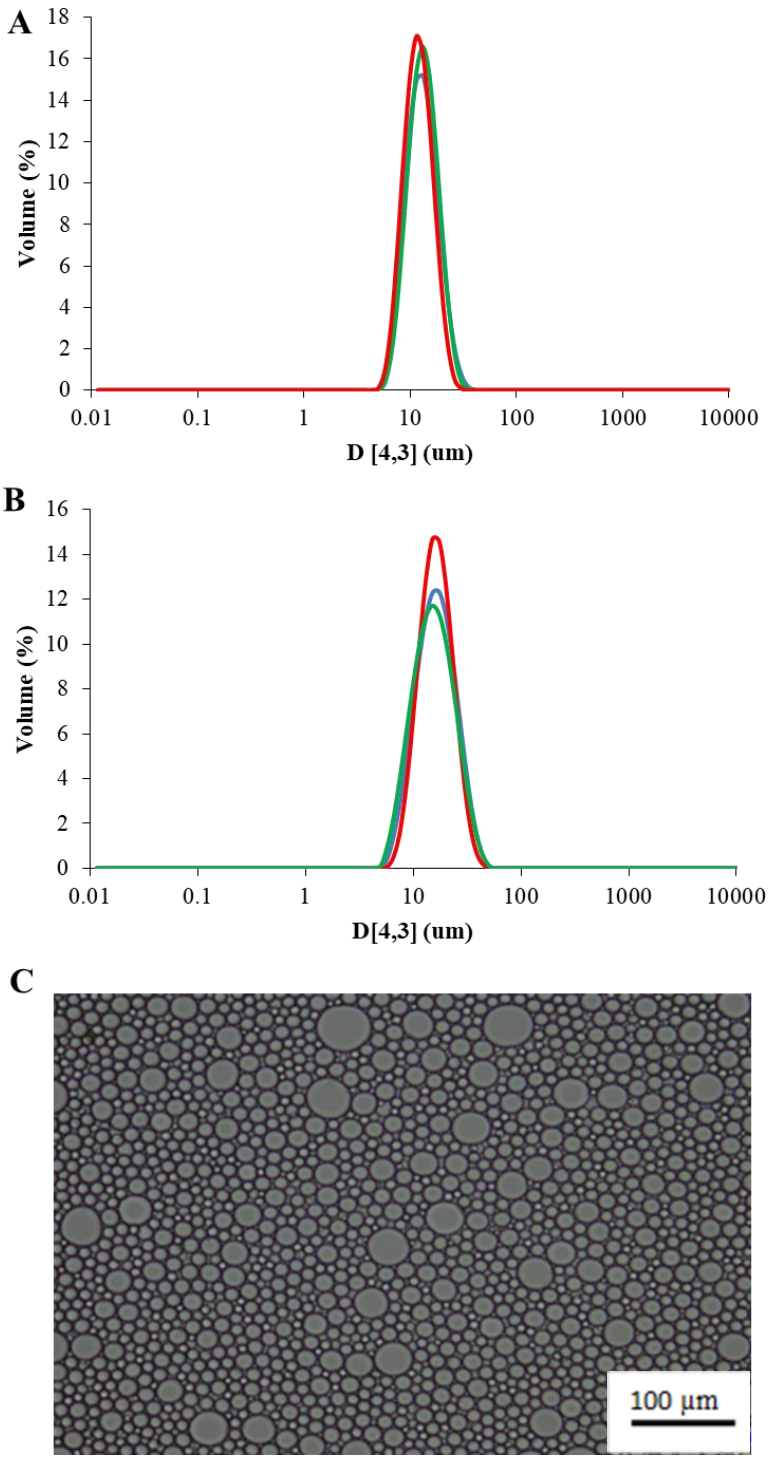

Figure 5.8 Laser diffraction measurements of A) non-mucoadhesive, DBiB-*p*(OEGMA$_{50}$-*co*-EGDMA$_{0.8}$) with B) mucoadhesive SH$_{0.75}$DBiB$_{0.25}$-*p*(OEGMA$_{50}$-*co*-EGDMA$_{0.8}$) macroemulsions loaded with AmpB (green), CsA (blue) and a blank emulsion (red) and C) Optical microscopy image of Amphotericin B loaded macroemulsion stabilised with DBiB-*p*(OEGMA$_{50}$-*co*-EGDMA$_{0.8}$), 20 x zoom magnification, scale bar = 100 µm.

As shown in Figure 5.8 and Table 5.1, inclusion of CsA and Amp B in non-mucoadhesive, DBiB-*p(*$OEGMA_{50}$-*co*-$EGDMA_{0.8}$), emulsions produced monodispersed droplets with the same $D_{[4,3]}$ for both drug loaded and blank emulsions. Mucoadhesive, $SH_{0.75}DBiB_{0.25}$-*p(*$OEGMA_{50}$-*co*-$EGDMA_{0.8}$), macroemulsions also had the same $D_{[4,3]}$ following encapsulation of both drugs compared to the unloaded emulsion analogue. Optical microscopy further confirmed the presence of well-defined oil droplets, with no drug aggregates able to be observed.

Table 5.1 Comparison of the volume mean diameter of macroemulsions loaded with Amphotericin B, Cyclosporin A and an unloaded emulsion. Emulsions were stabilised with either $SH_{0.75}DBiB_{0.25}$-*p(*$OEGMA_{50}$-*co*-$EGDMA_{0.8}$) (mucoadhesive) or DBiB-*p(*$OEGMA_{50}$-*co*-$EGDMA_{0.8}$) (non-mucoadhesive).

Polymer	Loading	$D_{[4,3]}$ (μm)
$SH_{0.75}DBiB_{0.25}$-p(OEGMA50-*co*-$EGDMA_{0.8}$)	Blank	14.6
	Amp B	16.0
	CsA	15.9
DBiB-p($OEGMA_{50}$-*co*-$EGDMA_{0.8}$)	Blank	11.4
	Amp B	13.2
	CsA	13.2

Macroemulsions were generated for completeness of the study, where encapsulation of Amp B and CsA at topical dose concentrations was possible. However, as macroemulsions were shown to demulsify in contact with a mucosal surface as seen in Chapter 4, releasing the drug payload rapidly, it was decided to only proceed with nanoemulsions for biological evaluation.

5.3. BIOLOGICAL EVALUATION OF NANOEMULSIONS

5.3.1. Cytotoxicity of Unloaded Nanoemulsions

Aqueous polymer solutions at 5 wt% of both DBiB-*p*(OEGMA$_{50}$-*co*-EGDMA$_{0.8}$) (non-mucoadhesive) and SH$_{0.75}$DBiB$_{0.25}$-*p*(OEGMA$_{50}$-*co*-EGDMA$_{0.8}$) (mucoadhesive) were prepared for nanoemulsion formulations. These polymers were selected following the multiple particle tracking studies in Chapter 4 to reflect a highly adhesive system and a highly mucous penetrating one. These potentially provide alternative drug delivery routes, permeation through the mucus layer and epithelial cells to deliver drugs to the underlying cells or complete adhesion to the ocular surface, which would improve the retention time of ocular topical administration routes such as eye drops. As these nanoemulsions have been shown to have long term stability in previous chapters, there is potential to increase the shelf life of an Amp B treatment from one week as discussed in Section 5.1.2.

Nanoemulsions were generated in a 1:1 ratio of oil:aqueous polymer solution; the oil phase was a mixture of volatile solvent and non-volatile oil. In this instance, the non-volatile oil was biologically relevant castor oil mixed with ethyl acetate as the volatile solvent in a 99:1 ratio. Castor oil was selected as it has previously been shown to be a good vehicle for CsA ophthalmic emulsions (0.05 %, Restasis®, Allergan), where it is thought that upon release of the oil it interacts with the tear film lipid layer[187], stabilising the tear film and reducing tear evaporation.[188] In one study, castor oil was shown to decrease tear evaporation after two weeks of treatment.[189] Similar to macroemulsions, nanoemulsions were also formulated *via* over-head shear homogenisation for 2 minutes at 24,000 rpm, utilising a solvent evaporation method. Emulsions were left at ambient temperature following homogenisation, allowing for full removal of the volatile oil phase which was monitored gravimetrically. The DLS traces for blank nanoemulsions stabilised with SH$_{0.75}$DBiB$_{0.25}$-*p*(OEGMA$_{50}$-*co*-EGDMA$_{0.8}$) and DBiB-*p*(OEGMA$_{50}$-*co*-EGDMA$_{0.8}$) is shown in Figure 5.9, with full characterisation outlined in Table 5.2. This therefore allows for the evaluation of a system which could potentially permeate through the mucus layer and towards the underlying epithelial cells as well as one which could provide complete adhesion to the ocular surface, improving the retention time of a dosing system such as eye drops.

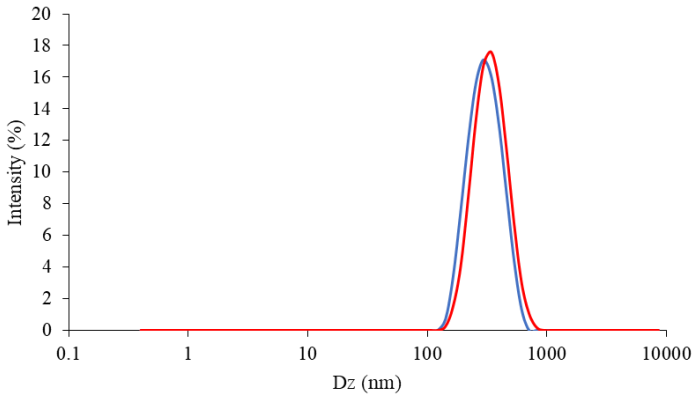

Figure 5.9 Overlay of DLS traces for nanoemulsions stabilised with $SH_{0.75}DBiB_{0.25}$-*p(*$OEGMA_{50}$-*co*-$EGDMA_{0.8}$) (blue) and DBiB-*p(*$OEGMA_{50}$-*co*-$EGDMA_{0.8}$) (red), generated with a 99:1 ratio of ethyl acetate:castor oil.

Table 5.2 Comparison of D_z and PdI of castor oil nanoemulsions. Emulsions stabilised with either $SH_{0.75}DBiB_{0.25}$-*p(*$OEGMA_{50}$-*co*-$EGDMA_{0.8}$) (mucoadhesive) or DBiB-*p(*$OEGMA_{50}$-*co*-$EGDMA_{0.8}$) (non-mucoadhesive).

Polymer	D_z (nm)	PdI
$SH_{0.75}DBiB_{0.25}$-*p(*$OEGMA_{50}$-*co*-$EGDMA_{0.8}$)	277	0.13
DBiB-*p(*$OEGMA_{50}$-*co*$EGDMA_{0.8}$)	250	0.06

As discussed in section 5.1, the assays used to determine cytotoxicity of blank nanoemulsions stabilised with DBiB-*p*($OEGMA_{50}$-*co*-$EGDMA_{0.8}$) (non-mucoadhesive) and $SH_{0.75}$DBiB-*p*($OEGMA_{50}$-*co*-$EGDMA_{0.8}$) (mucoadhesive) were resazurin, phalloidin staining and live/dead. HCE-T and HCjE-Gi cells were treated with non-mucoadhesive and mucoadhesive nanoemulsions and exposure time was varied between 1, 4 and 24 hours. This time points were selected to reflect potential treatment times for topical dosing to the eye, with 24 hours being the maximum time for dosing. Cells were cultured for 7 days and monitored by optical microscopy to assure approximately 80 % confluency and a monolayer had been established prior to treatment with each nanoemulsion. It is important that cells reached this level of

confluency to ensure they are able to communicate successfully but do not inhibit cell growth due to being over-confluent.

Nanoemulsions were successfully diluted in culture media to obtain concentrations of 50.0, 25.0, 10.0, 9.1, 8.3, 7.7, 7.1, 5.0 and 3.3 v/v % (nanoemulsion in media) for exposure to cells. Following previous research within the group it was determined that dilution of nanoemulsions stabilised with copolymers analogous to DBiB-*p*(OEGMA$_{50}$-*co*-EGDMA$_{0.8}$) from a 2 – 4096 fold dilution in distilled water did not cause nanoemulsion instability or change in droplet diameter.[107]

For each treatment the same material was tested on the same cell line of same passage number in triplicate, alongside controls to confirm the assay was working correctly and ensure validity of the experiment. The two controls were:

- Negative Control – represents healthy, confluent cells treated with culture media only, expected to observe no adverse effects
- Positive Control – cells treated with 10 % DMSO to induce cell death. A high DMSO concentration was used to adverse effects within 1 hr.

For the reszaurin assay, the above controls were studied, alongside wells with media and media with cells so background signals detected by the fluorescent plate reader could be removed.

Results from resazurin assays are shown in Figure 5.10 for HCjE-Gi cells and Figure 5.11 for HCE-T cell line. Statistical analyses were carried out on SPSS Statistics V22 software; one-way test of homogeneity of variances and analysis of variance (ANOVA) as well as Dunnett's T3 post-hoc evaluation were conducted, $p \leq 0.05$ was regarded to be statistically significant.

The assay was deemed to be working correctly as a significant difference between the negative and positive controls for both cell lines was observed, therefore cytotoxicity was clearly observed with the positive control and no adverse effects were observed with the negative control. Overall no significant difference was observed between the negative control and all concentrations of nanoemulsions gained by diluting with media. Therefore no cytotoxicity was observed for all concentrations of both mucoadhesive and non-mucoadhesive nanoemulsions tested.

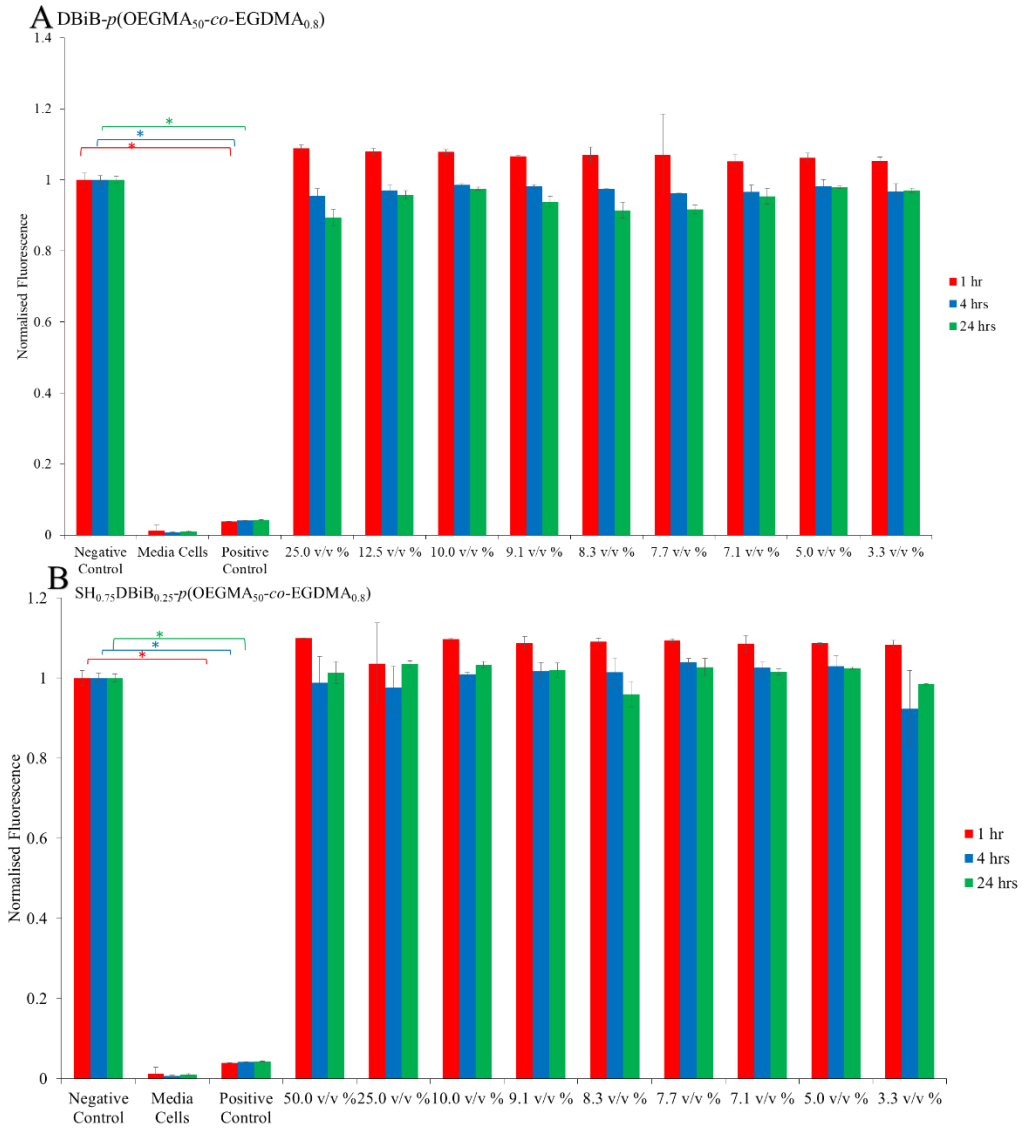

Figure 5.10 Overall cytotoxicity of nanoemulsions stabilised with A) DBiB-*p*(OEGMA$_{50}$-*co*-EGDMA$_{0.8}$) (non-mucoadhesive) and B) SH$_{0.75}$DBiB$_{0.25}$-*p*(OEGMA$_{50}$-*co*-EGDMA$_{0.8}$) (mucoadhesive) determined from resazurin assays. HCjE-Gi cells were exposed to different concentrations of blank castor oil emulsions 50 - 3.3 v/v %, grown and treated for different time scales. Confluent cells (grown for 7 days) were exposed to emulsions for 1 hour (red), 4 hours (blue) and 24 hours (green). (mean error bars represent ± 1 standard deviation); n=3. *, Significance by ANOVA and Dunnett's T3 post-hoc evaluation ($p \leq 0.05$).

Mucoadhesive emulsions tested on HCE-T cells observed cytotoxicity after 24 hrs at a 50 v/v % concentration, however dilutions of 25.0 – 3.3 v/v % mucoadhesive emulsion had no cytotoxic effect on the cells, however, non-mucoadhesive emulsions showed cytotoxic effects after 24 hours at concentrations of 50 – 12.5 v/v %. 10.0 v/v

% dilution showed no significant difference from the negative control, however due to this concentration having a greater cytotoxic impact, a 9.1 v/v % emulsion concentration was taken forward for future studies.

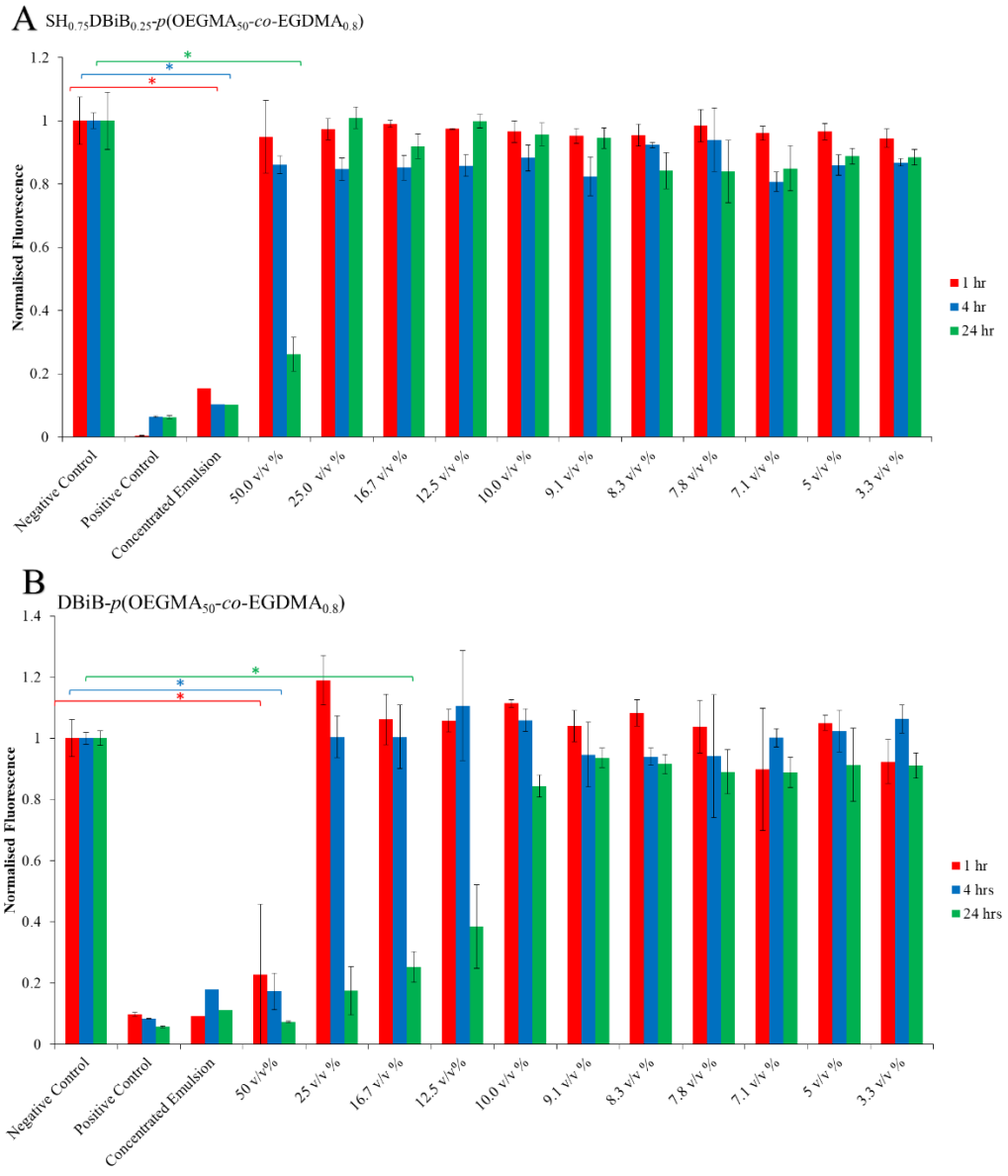

Figure 5.11 Overall cytotoxicity of nanoemulsions stabilised with A) $SH_{0.75}DBiB_{0.25}$-*p*(OEGMA$_{50}$-*co*-EGDMA$_{0.8}$) (mucoadhesive) and B) DBiB-*p*(OEGMA$_{50}$-*co*-EGDMA$_{0.8}$) (non-mucoadhesive) polymeric surfactants determined from resazurin assays. HCE-T cells were exposed to different concentrations of blank castor oil emulsions, 100 % emulsion – 3.3 v/v %, grown and treated for different time scales. Confluent cells (grown for 7 days) were exposed to emulsions for 1 hr (red), 4 hrs (blue) and 24 hrs (green). (mean error bars represent ± 1 standard deviation); n=3. *, Significance by ANOVA and Dunnett's T3 post-hoc evaluation ($p \leq 0.05$).

As discussed previously it is important to perform numerous assays to confirm cytotoxicity. A live/dead assay was performed on the HCjE-Gi cell line for mucoadhesive emulsion and for non-mucoadhesive emulsions, see Figure 5.12 A and B respectively. Emulsions were dosed at dilutions of 12.5 – 5.0 v/v %, a smaller range than the resazurin as this had indicated cytotoxicity at higher concentrations. Cells were exposed to emulsions for 1, 24 and 48 hour time points and run in technical triplicates. As cells exposed to a 9.1 v/v % and above dilution of nanoemulsions were shown to be non-toxic over a 24 hr exposure time, a 48 hr time point was included as an extreme condition. Mucoadhesive emulsions showed no cytotoxic effect on cells, with 24 and 48 hour time points yielding increased cell growth in comparison to the negative control. At 24 hours there was significant difference between the negative control and 9.1 v/v %, with the cells treated with emulsion showing an increased live cell number but cell death was not induced.

Non-mucoadhesive emulsions were dosed again at a smaller range of dilutions than resazurin, 12.5 – 5.0 v/v % over 1, 24 and 48 hour time points and run in technical triplicates. Non-mucoadhesive emulsions showed no cytotoxic effect on cells after 1, 24 and 48 hr time points yielding no significant difference between the negative control and all emulsion concentrations. Therefore this confirmed that concentrations of emulsions at 9.1 v/v % had no toxic effect on the cells.

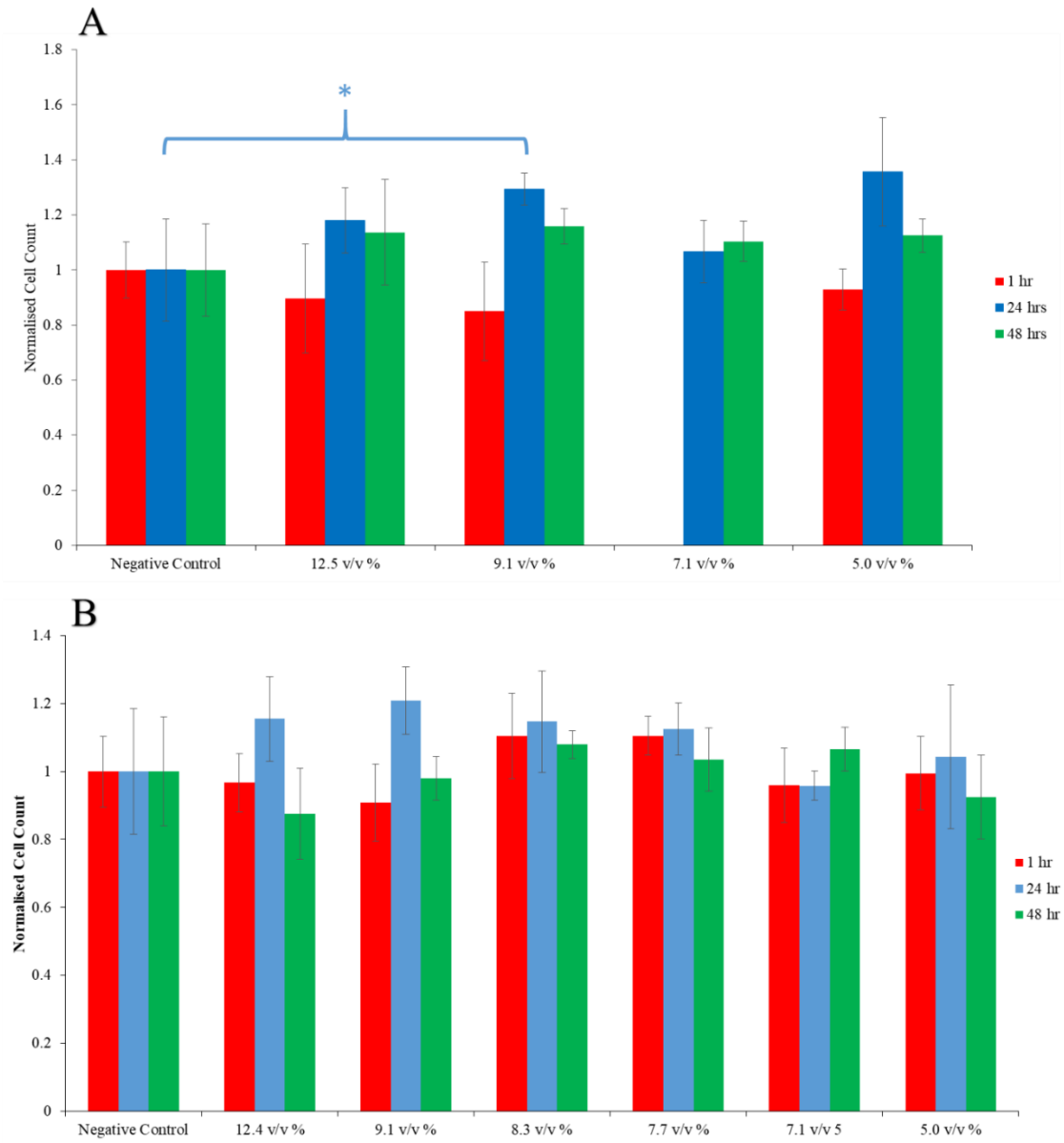

Figure 5.12 Overall cytotoxicity of nanoemulsions stabilised with polymeric surfactants A) $SH_{0.75}DBiB_{0.25}$-*p*($OEGMA_{50}$-*co*-$EGDMA_{0.8}$) (mucoadhesive) and B) DBiB-*p*($OEGMA_{50}$-*co*-$EGDMA_{0.8}$) (non-mucoadhesive) determined by live/dead assays. HCjE-Gi cells were exposed to different concentrations of blank emulsions, 12.5 – 5.0 v/v %, grown and treated for different time scales. Confluent cells (grown for 7 days) were exposed to blank castor oil emulsions for 1 hour (red), 24 hours (blue) and 48 hours (green). (mean error bars = ± 1 standard deviation), n = 3. *, Significance by ANOVA and Dunnett's T3 post-hoc evaluation ($p \leq 0.05$).

5.4 DRUG LOADED NANOEMULSIONS FOR BIOLOGICAL EVALUATION

5.4.1 Loading emulsions with Amphotericin B

To determine the need for an oil phase to encapsulate Amp B and eliminate the potential of a purely aqueous polymer solution stabilising Amp B particles, Amp B (0.15 w/v %) was homogenised with an aqueous polymer solution of DBiB-*p*(OEGMA$_{50}$-*co*-EGDMA$_{0.8}$) (5 wt %) for 2 minutes at 24,000 rpm analogous to the emulsion formulation method. An Amp B (0.15 w/v %) and water solution was also homogenised to assess Amp B behaviour without the presence of branched copolymer surfactants. As shown in Figure 5.13, DLS studies for Amp B and an aqueous polymer solution of DBiB-*p*(OEGMA$_{50}$-*co*-EGDMA$_{0.8}$) (5 wt %), produced a bimodal distribution, whereas the DLS trace for Amp B in water produced a multimodal distribution. Therefore, the presence of an oil phase as well as a branched copolymer stabiliser in the formulation is key for the loading and stabilisation of Amp B.

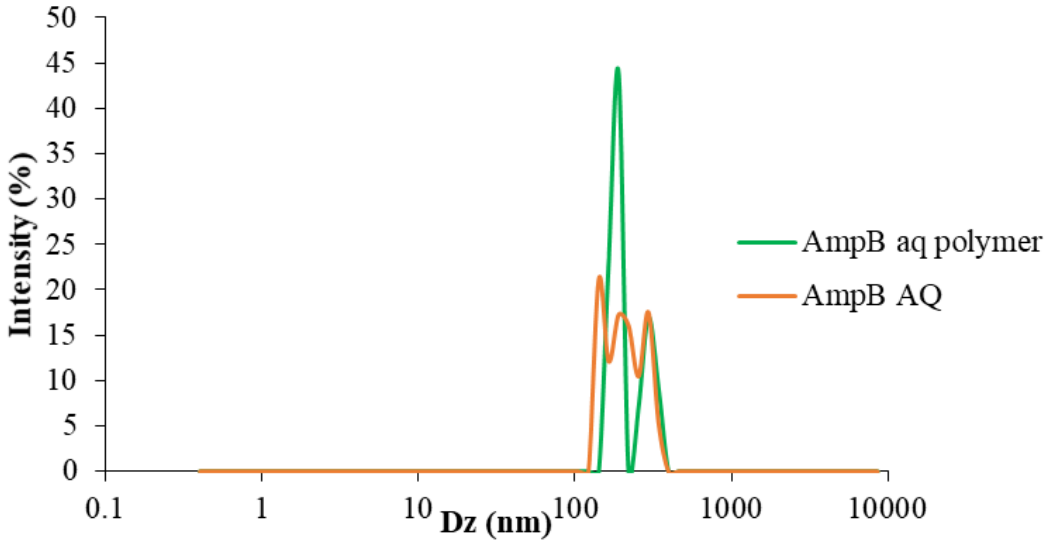

Figure 5.13 Overlay of DLS traces of homogenised suspensions of Amp B and aqueous polymer solution of DBiB-*p*(OEGMA$_{50}$-*co*-EGDMA$_{0.8}$) (5 wt %) (green) and Amp B in pure water (orange).

As discussed in Section 5.2., the use of Amp B led to some fundamental encapsulation issues. Nanoemulsions were generated in a 99:1 ratio of ethyl acetate:castor oil with DBiB-*p*(OEGMA$_{50}$-*co*-EGDMA$_{0.8}$) as polymeric surfactant and following solvent evaporation, sedimentation of a small amount of Amp B aggregates was observed. However, following gentle agitation of the emulsion, resuspension of Amp B sediment

was observed. The emulsion was characterised *via* DLS, see Table 5.3, and a 290 nm emulsion was successfully formulated, with no secondary population to coincide with free aggregates in the sample.

To further investigate this issue, Amp B nanoemulsion with DBiB-*p*(OEGMA$_{50}$-*co*-EGDMA$_{0.8}$) as polymeric surfactant was centrifuged for 15 minutes at 5000 G to remove the aggregates and assess the effect of this on the formulation. As shown in Figure 5.14, DBiB-*p*(OEGMA$_{50}$-*co*-EGDMA$_{0.8}$) stabilised Amp B nanoemulsion both before and after centrifugation produce a singular peak which overlays fully showing no breakdown of emulsion. Post centrifugation a pellet of what was suspected to be unencapsulated Amp B was collected and ^{1}H NMR was used. This confirmed the presence of pure Amp B recovered post-centrifugation (Appendix 16).This indicates that unencapsulated Amp B may be suspended within the nanoemulsion.

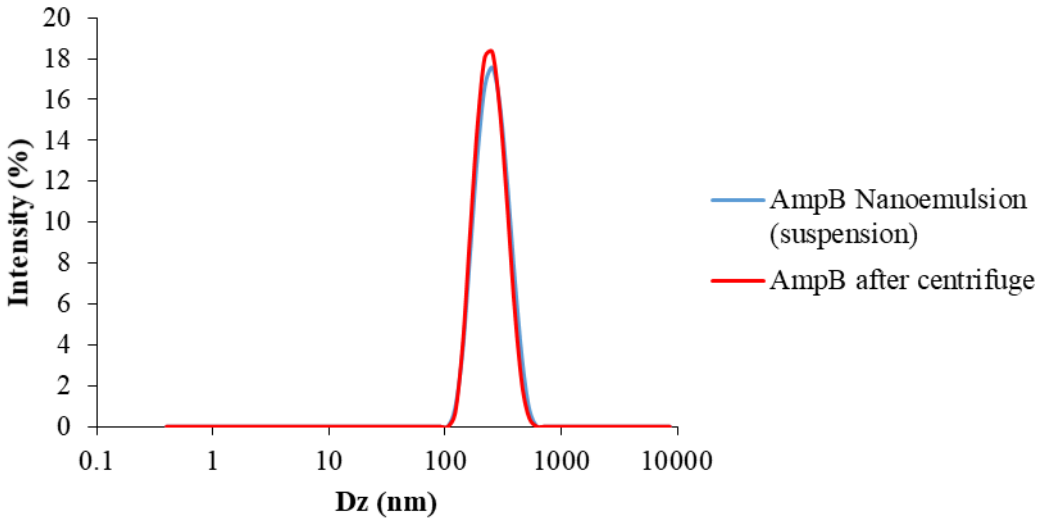

Figure 5.14 Overlay of DLS traces for DBiB-*p(*OEGMA$_{50}$-*co*-EGDMA$_{0.8}$) stabilised Amp B nanoemulsions (0.15 w/v %) with castor oil as non-volatile oil, for 15 mins at 5000 G.

Nanoemulsions were generated with an aqueous solution of SH$_{0.75}$DBiB$_{0.25}$-*p*(OEGMA$_{50}$-*co*-EGDMA$_{0.8}$) or DBiB-*p*(OEGMA$_{50}$-*co*-EGDMA$_{0.8}$) as branched copolymer surfactants (5 wt %) and a 99:1 ratio of ethyl acetate:castor oil. The mixtures were homogenised for 2 minutes at 24,000 rpm and the volatile solvent left to evaporate. Amp B and CsA were loaded into the emulsions by solubilising the drugs in castor oil overnight at topical dose concentrations of 0.15 and 0.05 w/v % respectively. A small amount of Amp B aggregates were present at this concentration,

however as it was shown that Amp B could be successfully suspended these nanoemulsions were used without centrifugation. Figure 5.15 shows the overlay of DLS trace for Amp B loaded non-mucoadhesive and mucoadhesive nanoemulsions, where both nanoemulsions yielded D_z sizes of 290 nm, with PdIs of 0.15 and 0.17 respectively. The inclusion of drug into the emulsion led to a slight increase in diameter, from 250 nm for both blank emulsions made using the different polymeric surfactants.

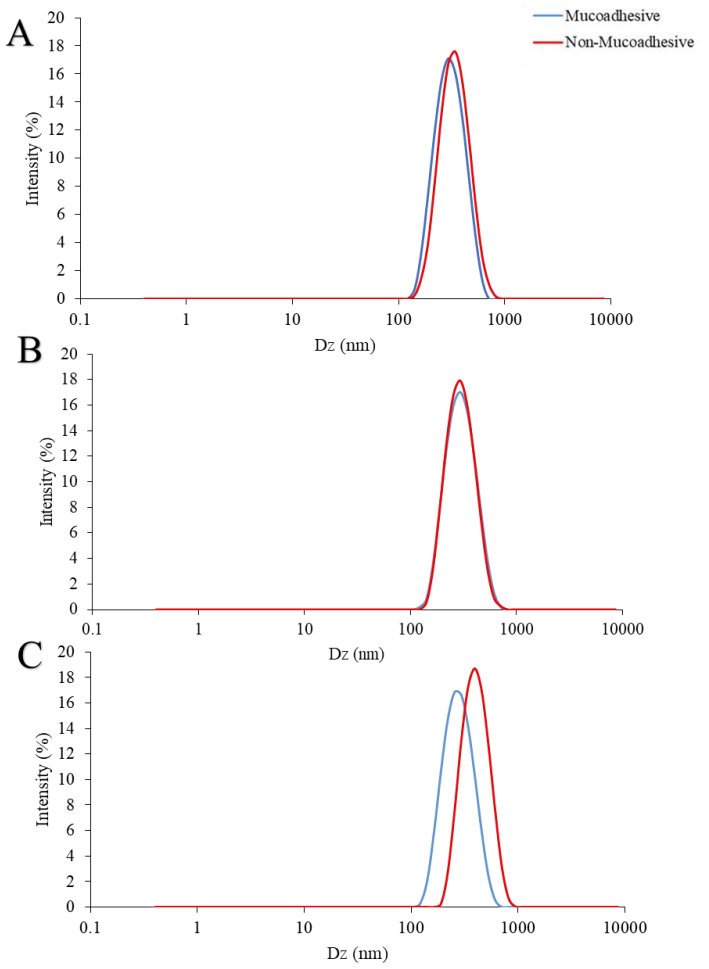

Figure 5.15 Comparison of nanoemulsion droplet diameters stabilised with non-mucoadhesive, DBiB-*p*(OEGMA$_{50}$-*co*-EGDMA$_{0.8}$) (red) and mucoadhesive, SH$_{0.75}$DBiB$_{0.25}$-*p*(OEGMA$_{50}$-*co*-EGDMA$_{0.8}$) (blue) branched copolymers with castor oil as non-volatile oil. A) Blank emulsions, B) Amp B at topical dose concentration (0.15 w/v %) and C) CsA at topical dose concentration (0.05 w/v %).

CsA nanoemulsion formulated with a non-mucoadhesive polymeric surfactant DBiB-*p*(OEGMA$_{50}$-*co*-EGDMA$_{0.8}$) with castor oil as non-volatile oil, produced droplets

with larger D_z values of 370 nm compared to the previously formulated unloaded emulsion, of 250 nm, however the PdI remained low at 0.08. The mucoadhesive castor oil based nanoemulsion with $SH_{0.75}DBiB_{0.25}$-*p*($OEGMA_{50}$-*co*-$EGDMA_{0.8}$) as branched copolymer surfactant showed an increase to 260 nm from 250 nm of the unloaded emulsion, with the inclusion of CsA but still maintaining a low PdI value at 0.07, as detailed in Table 5.3.

Table 5.3 Comparison of D_z and PdI of nanoemulsions loaded with Amphotericin B, Cyclosporin A and an unloaded emulsion. Emulsions stabilised with either $SH_{0.75}DBiB_{0.25}$-*p(*$OEGMA_{50}$-*co*-$EGDMA_{0.8}$) (mucoadhesive) or DBiB-*p(*$OEGMA_{50}$-*co*-$EGDMA_{0.8}$) (non-mucoadhesive) with castor oil as non-volatile oil.

Polymer	Loading	D_z (nm)	PdI
$SH_{0.75}DBiB_{0.25}$-*p(*$OEGMA_{50}$-*co*-$EGDMA_{0.8}$)	Blank	277	0.13
	AmpB	290	0.15
	CsA	264	0.07
DBiB-*p(*$OEGMA_{50}$-*co*-$EGDMA_{0.8}$)	Blank	250	0.06
	AmpB	290	0.17
	CsA	371	0.08

5.4.2 HCjE-Gi Secretion of Mucus

As described in section 5.1, HCjE-Gi cells were chosen because after a monolayer of cells is established, MUC5AC mucins are secreted and allow the mucoadhesive properties of the nanoemulsions formulated with the thiol functionalised polymers to be tested. To determine the mucoadhesive properties of the thiol-functionalised branched copolymer surfactants, a series of nanoemulsions were generated incorporating Oil red O into the castor oil phase as described below. The dye then allowed a fluorescent plate reader to be used to quantify nanoemulsions.

Two nanoemulsions were formulated using $SH_{0.75}DBiB_{0.25}$-*p(*$OEGMA_{50}$-*co*-$EGDMA_{0.8}$) and DBiB-*p(*$OEGMA_{50}$-*co*-$EGDMA_{0.8}$) as polymeric surfactants. Oil red

o (0.1 w/v %) was solubilised in castor oil over night and nanoemulsions formulated in a 1:1 ratio of aqueous polymer solution (5 wt %) to oil phase, where the oil phase was a 99:1 ratio of ethyl acetate:castor oil. Following homogenisation and volatile oil evaporation DLS analysis of the two nanoemulsions was carried out: D_z diameters of 280 nm, with PdIs of 0.11 – 0.13, as detailed in Table 5.4, Figure 5.16. HCjE-Gi cells were treated with non-mucoadhesive, DBiB-*p(*$OEGMA_{50}$-*co*-$EGDMA_{0.8}$) and mucoadhesive $SH_{0.75}DBiB_{0.25}$-*p(*$OEGMA_{50}$-*co*-$EGDMA_{0.8}$) stabilised oil red O loaded nanoemulsions (9.1 v/v %) for 24 hrs, and cells analysed using a fluorescent plate reader, following removal of the nanoemulsion. It was hypothesised that due to the presence of mucins the mucoadhesive emulsions would adhere to the cell surface and the non-functionalised emulsion would not and this would be reflected by the fluorescence readings taken using a fluorescence plate reader.

Table 5.4 DLS analysis of nanoemulsions loaded with oil red O (0.1 wt %).

Polymer	Oil Red O Conc. (wt %)	D_z (nm)	D_n (nm)	PdI
$SH_{0.75}DBiB_{0.25}$-*p*($OEGMA_{50}$-*co*-$EGDMA_{0.8}$)	0	250	230	0.100
$SH_{0.75}DBiB_{0.25}$-*p*($OEGMA_{50}$-*co*-$EGDMA_{0.8}$)	0.1	280	260	0.11
DBiB-p($OEGMA_{50}$-*co*-$EGDMA_{0.8}$)	0	228	209	0.07
DBiB-*p*($OEGMA_{50}$-*co*-$EGDMA_{0.8}$)	0.1	280	260	0.13

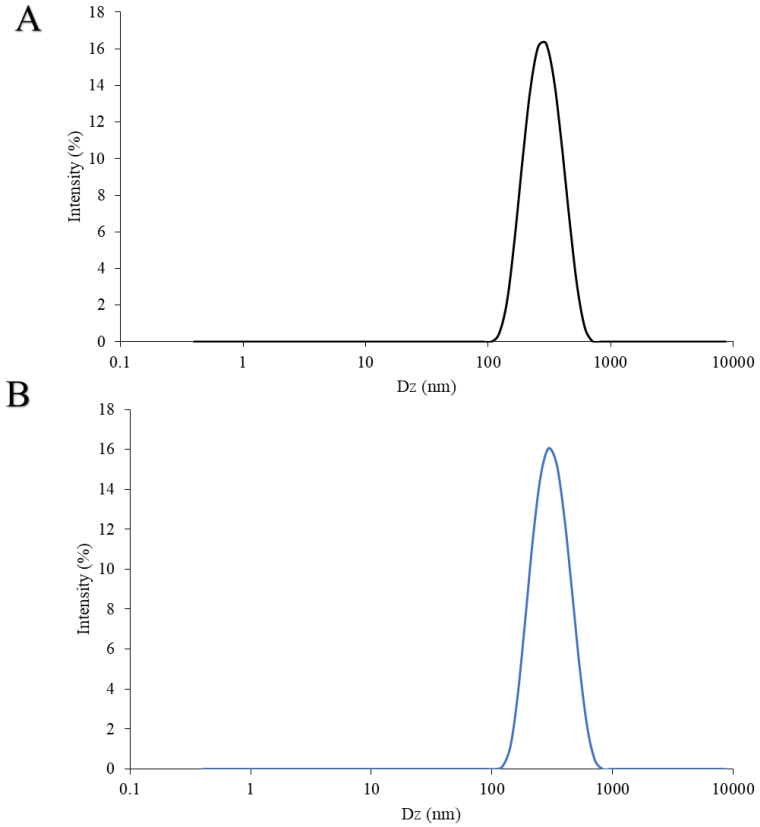

Figure 5.16 DLS traces of oil red O (0.1 wt %) nanoemulsions stabilised with A) $SH_{0.75}DBiB_{0.25}$-*p*($OEGMA_{50}$-*co*-$EGDMA_{0.8}$) and B) DBiB-*p*($OEGMA_{50}$-*co*-$EGDMA_{0.8}$) branched copolymers with castor oil as non-volatile oil.

Nanoemulsions were also dosed to HCjE-Gi cells in the presence of commercially available contrived tears (Ursa Bioscience), which contain mucins found naturally in the tear film. It was hoped that the inclusion of biosimilar tears would increase the concentration of mucins present in the sample and induce mucoadhesion. As shown in Figure 5.17, the mucoadhesive emulsions showed no preferential absorbance to that of a non-mucoadhesive emulsion. The addition of tears to the cells also did not affect the absorbance, with again no difference between a non-mucoadhesive and mucoadhesive emulsion.

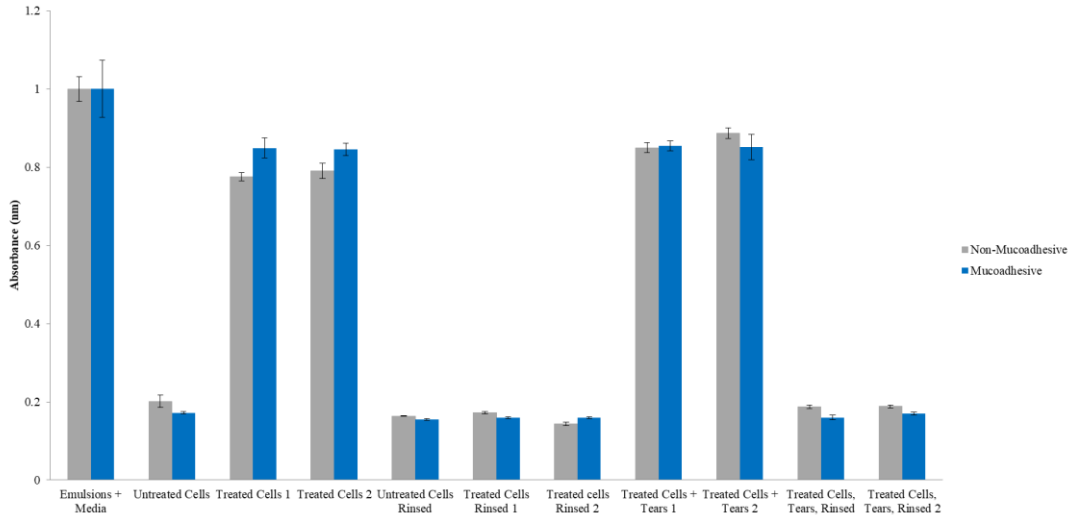

Figure 5.17 HCjE-Gi cells treated with oil red O (0.1 wt %) castor oil based nanoemulsions, stabilised with DBiB-*p(*OEGMA$_{50}$-*co*-EGDMA$_{0.8}$) (grey) and SH$_{0.75}$DBiB$_{0.25}$-*p(*OEGMA$_{50}$-*co*-EGDMA$_{0.8}$) (blue) branched copolymers to assess their adhesive properties. Cells were treated with nanoemulsions only and in the presence of biosimilar tears, n = 2.

Due to the lack of adhesion shown to HCjE-Gi, the amount of mucus secreted by the cells in this cell culture was not deemed to be sufficient to test for adhesive properties of emulsions. Following this it was decided the, DBiB-*p(*OEGMA$_{50}$-*co*-EGDMA$_{0.8}$) system and its potential ability to permeate through mucus and epithelium cells to treat the two ocular diseases highlighted in Section 5.1.2. would be focused on. HCE-T cells was therefore used for the remainder of the biological evaluation studies described below, as these cells replicate the drug delivery route i.e. permeation through the epithelial cells lining the corneal surface for increased drug delivery and efficacy.

5.4.3 Phalloidin Staining of Drug Loaded Nanoemulsions

Phalloidin staining was carried out on HCE-T cells using negative (media only) and positive controls (10 % DMSO) as well as DBiB-*p*(OEGMA$_{50}$-*co*-EGDMA$_{0.8}$) stabilised nanoemulsions of castor oil with varying concentrations of Amp B and CsA. As described in Section 5.1.2. nanoemulsions were formulated with Amp B and CsA at topical doses of 0.15 and 0.05 w/v % respectively using castor oil as the non-volatile oil phase. HCE-T cells were exposed to 100 % nanoemulsion with either Amp B or CsA i.e. no culture media, and subsequent dilutions of nanoemulsion in media reflecting the blank nanoemulsion concentrations used in the previous resazurin study, 50.0 – 3.3 v/v %. Staining confirmed that the cytoskeleton and cellular structure was

the correct morphology for HCE-T cells in the negative control, and as expected the positive control of 10% DMSO was unable to be stained as cells had detached from the well due to cell death. Figure 5.18, shows the results of Amp B loaded nanoemulsions dosed to confluent HCE-T cells for 24 hrs at concentrations of 100 % nanoemulsion – 3.3 v/v % diluted in culture media, with relevant drug concentrations stated in Table 5.5. Cells exposed to 100 % emulsion lead to cell death i.e. cells lifted from the well; cells still present were stained and could be seen to be rounded and/or not resembling a healthy cell. Cells exposed from emulsion dilution of 25.0 v/v % in media (184 µg Amp B or 62 µg CsA), concentrations onwards are comparable to the negative control.

Table 5.5 Nanoemulsion dilutions (v/v % in media) and their relevant Amp B and CsA concentrations in µg as dosed to HCE-T cells.

Emulsion Dilution (v/v %)	Amp B Concentration (µg)	CsA Concentration (µg)
100	735	250
50.0	367	125
25.0	184	62
16.7	123	42
12.5	92	31
10.0	73	25
9.1	67	23
8.3	68	23
7.8	57	19
7.1	52	18
5.0	37	13
3.3	24	8

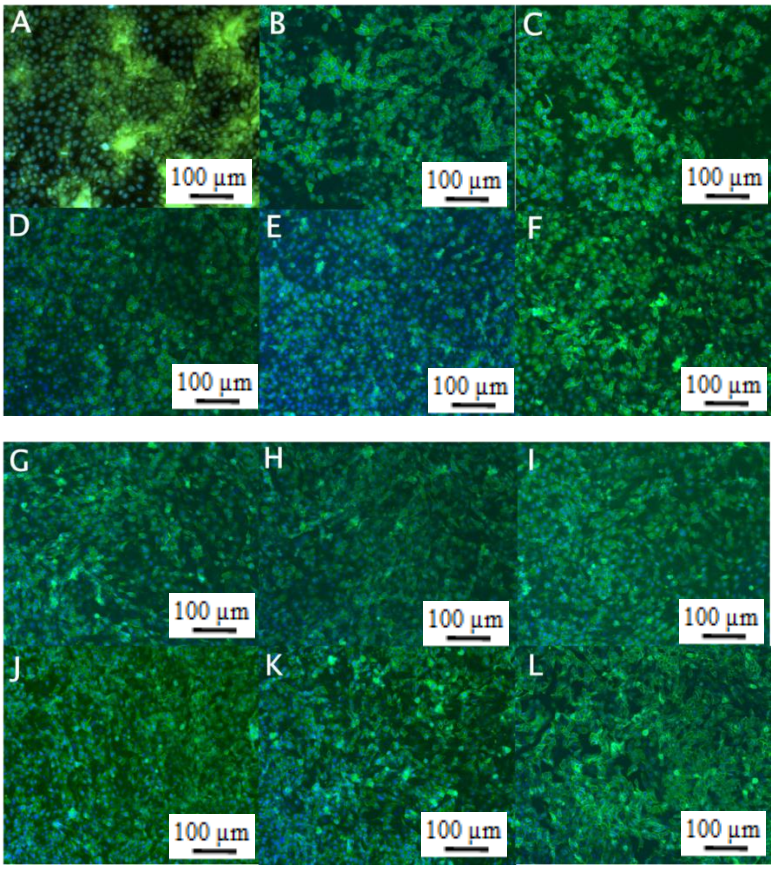

Figure 5.18 Phalloidin staining of HCE-T cells treated with Amp B loaded DBiB-*p*(OEGMA$_{50}$-*co*-EGDMA$_{0.8}$) stabilised nanoemulsions with castor oil as non-volatile oil at concentrations of: A) 100 % nanoemulsion, B) 25.0 v/v %, C) 16.7 v/v %, D) 12.5 v/v %, E) 10.0 v/v % , F) 9.1 v/v %, G) 8.3 v/v %, H) 7.8 v/v %, I) 7.1 v/v %, J) 5.0 v/v %, K) 3.3 v/v % and L) negative control. 20x zoom magnification, scale bars = 100 µm.

Figure 5.19 shows phalloidin staining of HCE-T cells exposed to CsA loaded nanoemulsions from 100 % nanoemulsion to 3.3 v/v % diluted in culture media i.e. 250 µg – 8 µg CsA. 100 % nanoemulsion led to cell death; cells round and lift from the baseplate through a process called mesenchymal transition, meaning few cells were remaining to be imaged. Those cells that were imaged appeared unhealthy and rounded in comparison to the negative control (unexposed cells). Cells exposed to 50.0 v/v %, 125 µg CsA nanoemulsion and subsequent dilutions were comparable to the negative control.

These results combined with resazurin and live/dead assay, confirms that a 9.1 v/v % concentration of nanoemulsion to media is viable for further biological testing with drug loading of CsA (23 µg) and Amp B (67 µg) as dosed to HCE-T cells or 46 µg/mL

and 137 µg /mL respectively. Phalloidin staining also confirms that the inclusion of CsA and Amp B does not induce cell death at higher nanoemulsion concentrations of 50.0 (125 µg CsA) and 25.0 (184 µg Amp B) v/v %.

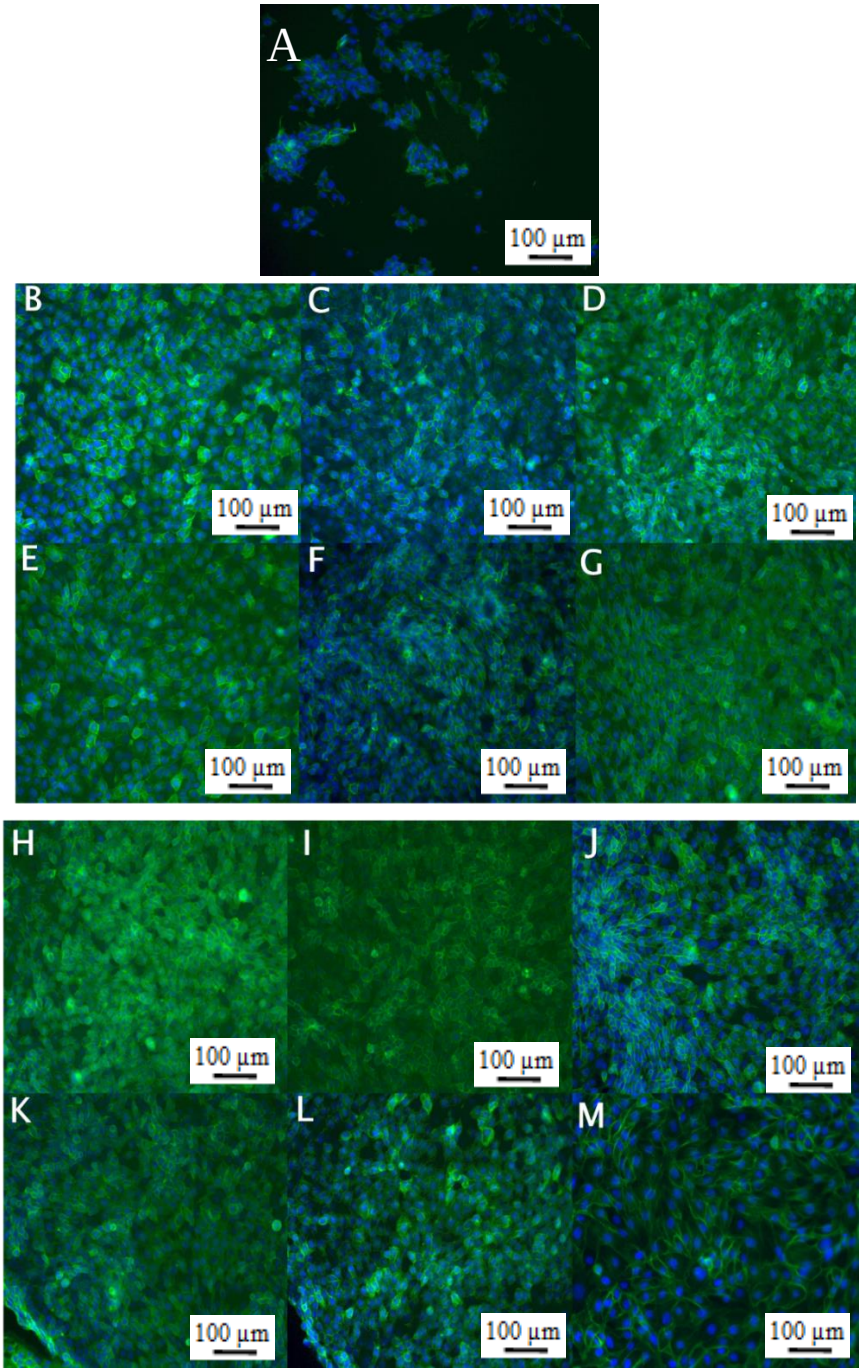

Figure 5.19 Phalloidin staining of HCE-T cells treated with CsA loaded nanoemulsions stabilised DBiB-*p*(OEGMA$_{50}$-*co*-EGDMA$_{0.8}$) with castor oil as non-volatile oil at concentrations of: A) 100 % nanoemulsion, B) 50.0 v/v %, C) 25.0 v/v %, D) 16.7 v/v %, E) 12.5 v/v %, F) 10.0 v/v % , G) 9.1 v/v %, H) 8.3 v/v %, I) 7.8 v/v %, J) 7.1 v/v %, K) 5.0 v/v %, L) 3.3 v/v % and M) negative control.

5.3.4 Antifungal Activity of Amphotericin B Loaded Nanoemulsions

As discussed in Section 5.1.2., *Candida* is one of the fungal species which leads to keratitis. Agricultural workers in developing countries such as India, are most likely to contract fungal keratitis as ocular traumas frequently occur and lead to the fungal infection.[163] *Candida* is an opportunistic species and can also cause infection post ocular surgery. Despite antifungal therapy this can occasionally lead to corneal grafting, and accounts for more fungal corneal infections at temperature latitudes[172], but has a worldwide incidence of approximately 1 per 1,000,000.[164] In this study, Amp B loaded nanoemulsions were tested for efficacy to inhibit the growth of the *Candida albicans (C. albicans)* yeast strain.

For this study, DBiB-*p(*$OEGMA_{50}$-*co*-$EGDMA_{0.8}$) was used as the polymeric surfactant and the nanoemulsions formulated at a 99:1 ratio of ethyl acetate:castor oil. Nanoemulsions were loaded with Amp B at an overall concentration of 194 mg/mL, 282 mg/mL and 4118 mg/mL. The controls used were an unloaded nanoemulsion, expected to have no effect on the *C. albicans*, and fungizone (f), a current Amp B marketed product with drug concentration of 250 μg/mL expected to demonstrate a considerable effect.

A 194 mg/mL concentration of Amp B was formulated by saturating a castor oil and ethyl acetate mix with Amp B before homogenisation with aqueous polymer solution (5 wt %). Following emulsion formulation (homogenisation for 2 minutes at 24,000 rpm and removal of volatile oil phase), excess Amp B was removed by centrifugation and final concentration determined gravimetrically by the loss of Amp B. To further increase the drug concentration in the sample, the continuous phase (water) was evaporated to generate a higher internal phase volume isolate higher oil droplet content.

Table 5.6 DLS analysis of Amp B loaded nanoemulsions: DBiB-*p(*$OEGMA_{50}$-*co*-$EGDMA_{0.8}$) as polymeric surfactant and castor oil as non-volatile oil phase for zone of inhibition study of *candida albicans*.

Polymer	AmpB Conc. (mg/mL)	D_z (nm)	D_n (nm)	PdI
DBiB-*p(*$OEGMA_{50}$-*co*-$EGDMA_{0.8}$)	194	260	225	0.15
	282	221	190	0.09
	4118	225	192	0.10

Preparation of the *C. alibcans* culture was completed as followed: *C. albicans* strain SC5314 was revived from -80 °C storage on potato dextrose-agar (PD-agar) (Formedium Ltd., Norfolk, England) and streak plates incubated at 37 °C overnight. *C. albicans* was sub-cultured by inoculating a PD-agar streak plate with one colony taken from a previous PD-agar plate and incubated overnight at 37 °C. Colonies were maintained on PD-agar stored at 5 °C. Broth cultures were initiated by inoculating potato dextrose media (10 mL) with one colony of *C. albicans* taken from a PD-agar plate. Cultures were incubated overnight at 37 °C with constant shaking at 100 RPM. These were sub-cultured by taking an aliquot of *C. albicans* broth culture (0.5 mL) and diluting it in sterile PD broth (10 mL). An initial optical density, OD_{600}, measured between 0.1 - 0.2 and was monitored until an OD_{600} 0.5 - 0.6 was obtained. This was the working stock dilution of *C. albicans* for the following experiments.

An aliquot (20 μL) of each sample was pipetted carefully to minimise spreading on to potato dextrose agar plates. Samples were spaced to avoid cross-contamination and agar plates left at room temperature for 20 minutes to allow the samples to dry. An aliquot of *C. albicans* stock solution (1 mL) was pipetted onto the centre of each agar plate. A glass spreader sterilised with ethanol and following aseptic technique was used to uniformly spread the culture broth around the agar plate. The plate was again allowed to dry for 30 minutes before turning the plates upside down and placing in an

incubator at 37 °C for 24 hours. The samples were then checked for a zone of inhibition and measurements taken of the diameter of each zone if applicable.

Figure 5.20 Amp B zone of inhibition study with *C. albicans,* assessing the inhibition level of nanoemulsions with DBiB-*p*(OEGMA$_{50}$-*co*-EGDMA$_{0.8}$) as polymeric surfactant and castor oil as non-volatile oil phase. Nanoemulsions were dosed at varying concentrations; F) Fungizone, negative control, 1) 194 mg/mL, 2) 282 mg/mL, 3) 4117 mg/mL and B) 0 mg/mL (unloaded nanoemulsion).

As shown in Figure 5.20, blank emulsions showed no inhibiting effect on the *C. albicans,* whereas all concentrations of AmpB nanoemulsions displayed an inhibition level similar to that of Fungizone.

As Amp B loaded nanoemulsions were at a much higher concentration than that of Fungizone, a further two samples were formulated at lower Amp B concentrations for testing alongside the previously tested 194 mg/mL concentration nanoemulsion. The 194 mg/mL sample was diluted in water to 9.1 v/v % to reflect the non-toxic dose, yielding a final concentration of 17.65 mg/mL of Amp B. A second sample was formulated with an original concentration of 2750 μg/mL, which after dilution to the non-toxic range yielded a final concentration of 250 μg/mL for dosing. A third nanoemulsion was prepared at a concentration of 250 μg/mL and was dosed without further dilution. As shown in Figure 5.21, the unloaded emulsion showed no inhibition of *c. albicans* growth as expected, and the two diluted samples showed a slight inhibition effect. However, the concentrated sample, 3, had a zone of inhibition level comparable to Fungizone.

Table 5.7 DLS analysis of Amp B loaded non-mucoadhesive nanoemulsions, with DBiB-*p(*$OEGMA_{50}$-*co*-$EGDMA_{0.8}$) as polymeric surfactant and castor oil as non-volatile oil phase, for zone of inhibition study.

Polymer	Amp B Conc. (μg/mL)	D_z (nm)	D_n (nm)	PdI
DBiB-*p(*$OEGMA_{50}$-*co*-$EGDMA_{0.8}$)	1,765	260	225	0.15
	250	240	210	0.22
	250	240	220	0.07

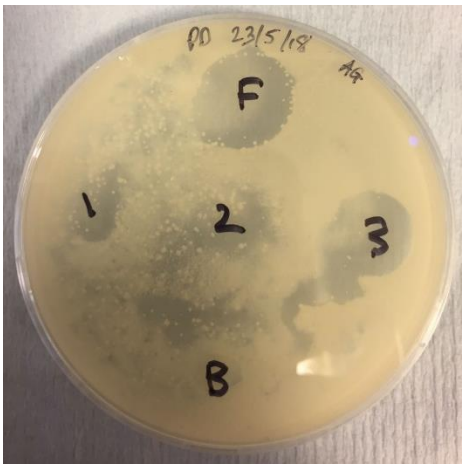

Figure 5.21 Amp B inhibition study with *C. albicans,* assessing the zone of inhibition of nanoemulsions with DBiB-*p*($OEGMA_{50}$-*co*-$EGDMA_{0.8}$) as polymeric surfactant and castor oil as non-volatile oil phase at varying drug concentrations. F) Fungizone as negative control (250 μg/mL), 1) 17,654 μg/mL, 2) 250 μg/mL, 3) 250 μg/mL (concentrated) and B) blank emulsion as positive control.

Nanoemulsions with Amp B concentrations comparative to Fungizone showed promising efficacy against the growth of *C. albicans* however it should be noted that a concentrated dosing of Amp B at 250 μg/mL led to the biggest zone of inhibition, with diluted nanoemulsions not providing as greater effect against the yeast strain. As shown in Figure 5.22, when the number of droplets dosed to *C. albicans* is calculated, assuming fully spherical droplets and using D_z values as average droplet diameter, by diluting the emulsions to the non-toxic range the amount of droplets dosed is

drastically reduced. Therefore, less Amp B is effectively dosed per 1 µL sample, further experimentation would benefit from increased drug concentration per droplet to match the Fungizone concentration after taking into account the loss of droplets due to dilution. Further studies would need to evaluate the effect of a nanoemulsion containing high oil droplet concentration with lower drug loading against a nanoemulsion with low oil concentration and high drug loading. This would therefore determine which system would have their greatest inhibiting effect on *c. albicans* and be the optimum dosing option.

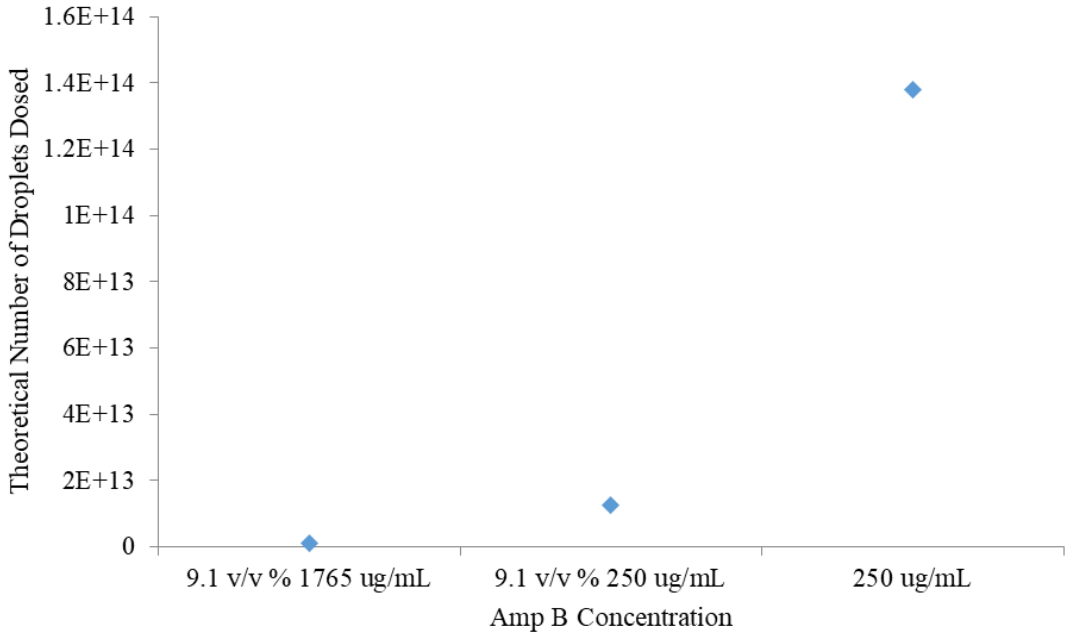

Figure 5.22 Theoretical number of droplets dosed to *c. albicans* per 1 µL aliquot of Amp B loaded nanoemulsions with DBiB-*p*(OEGMA$_{50}$-*co*-EGDMA$_{0.8}$) as polymeric surfactant and castor oil as non-volatile oil phase.

5.3.5 Release Study of Radiolabelled CsA Loaded Nanoemulsion

To determine if CsA was being released from nanoemulsions, a dialysis experiment was designed to quantify the release of CsA from nanoemulsions over time using tritiated CsA so low concentrations could be determined. Tritium isotope was chosen as the radionuclide as it has a long half-life (12.43 years) and decay during experimental time periods would not need to be accounted for, it is also a relatively safe beta emitter as it produces a maximum energy of 0.0186 MeV which only penetrates 4 mm of air and is incapable of passing through the dead outermost layer of skin (0.05 mm). Due to the nature of radiometrics, the amount of drug released can

be quantified very accurately; down to extremely small quantities. This is possible if the specific activity used is sufficient. Specific activity is the amount of radiolabelled drug added to unlabelled drug i.e. the concentration of activity. Due to the low energy emitted by tritium the only way to detect radiation from this isotope is liquid scintillation counting. This study determined CsA release from a nanoemulsion *via* radioactivity measurements.

Liquid scintillation counting (LSC) relies upon the use of a scintillation cocktail which contains scintillants; the most common scintillants used in liquid scintillation cocktails is 2,5-diphenyloxazole (PPO) which exhibits luminescence when excited by ionising radiation. The solvent molecules absorb energy emitted from radioactive beta particles and transfer energy until it reaches a scintillant. The scintillants then emits photons after the energy absorption which are detectable by a scintillation counter.

Tritiated CsA (specific activity 54 µCi/mg) and castor oil were solubilised in ethyl acetate at ambient temperature overnight, with the oil phase in a 99:1 ratio of ethyl acetate:castor oil. DBiB-*p*(OEGMA$_{50}$-*co*-EGDMA$_{0.8}$) was used as the polymeric surfactant (5 wt % in the aqueous phase) and the nanoemulsion was generated *via* homogenisation (24000 rpm, 2 minutes) followed by evaporation of volatile oil phase (ethyl acetate). Emulsion size was analysed by DLS, see Figure 5.23.

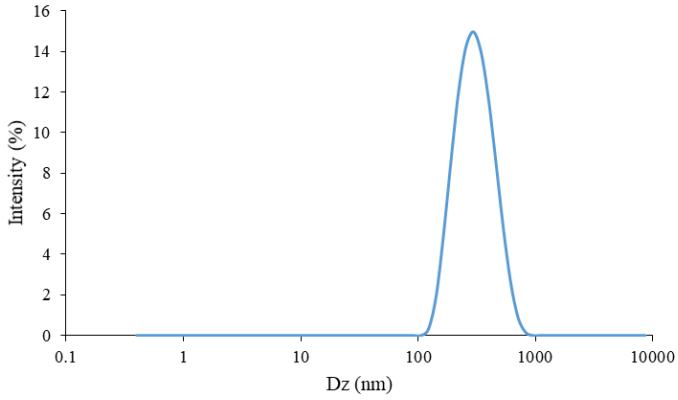

Figure 5.23 DLS trace of nanoemulsion stabilised by DBiB-*p*(OEGMA$_{50}$-*co*-EGDMA$_{0.8}$) with castor oil as non-volatile oil and loaded with CsA and tritiated CsA for dialysis release study.

For dialysis, 1 mL of nanoemulsion was added to a double sided biodialyser and sealed with a 3,500 Da molecular weight cut off membrane and placed in a reservoir of 100

mL deionised water heated to 37 °C. A biodialyser is used for dialysis experiments involving radiolabelled substances as it is a more secure container compared to traditional dialysis tubing. It also increases the reproducibility of experiments as the surface area 1 mL of sample is exposed to is consistently 2 cm^3. 1 mL samples of the reservoir were taken hourly for eight hours and then further samples were taken at 24 and 144 hours and the reservoir was replaced. The sample was measured by LSC and radioactivity measured converted to mass of CsA released.

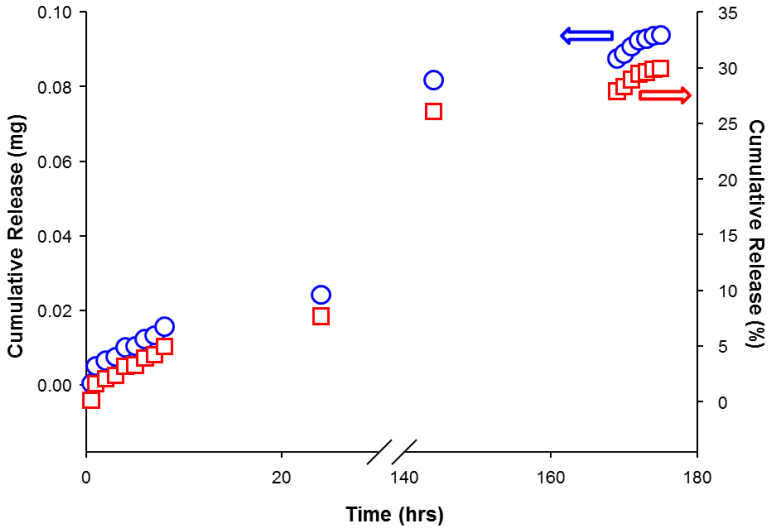

Figure 5.24 Release of radiolabelled CsA from castor oil based nanoemulsions stabilised with DBiB-*p*(OEGMA$_{50}$-*co*-EGDMA$_{0.8}$) through a 3500 Da MWCO membrane into a deionised water reservoir at 37 °C; red open boxes cumulative release (%), blue open squares cumulative release (mg).

Figure 5.24 shows the release of CsA from the nanoemulsion over time; a linear release profile of CsA through the dialysis membrane is determined not only over the initial 8 hours but also at 24 and 144 hours. Another 8 hour time period was tested between 172 – 180 hours, and again the linear release profile was seen. Overall 30 % of the encapsulated CsA was released after 180 hours, therefore, it may be necessary to make nanoemulsions more potent and have a higher loading to have a therapeutic benefit in the eye as currently the therapeutic dose is only 0.05 % w/v.

5.4 *IN-VIVO* EVALUATION OF MUCOADHESIVE NANOEMULSIONS

Improved delivery and pharmacokinetics of oral therapeutic compounds is of great importance in the development of drug formulations. This is particularly true for chronic, life-long conditions such as human immunodeficiency virus, where there is an associated pill burden and high dosage for patients, with the need for strict compliance with antiretroviral regimens. Advances have been made in the nanoformulation of hydrophobic drug compounds, however, water soluble anti-retrovirals are not suitable for common nanoformulation approaches, such as milling or o/w emulsion templating.[190] Here we describe the formation of nanoemulsions consisting of hydrophobic emtricitabine (FTC) prodrugs, for use as oral formulations, Figure 5.25. The FTC-prodrug was selected as it has converted a hydrophilic drug into a novel hydrophobic drug compound; this change in solubility of the FTC to the hydrophobic FTC-prodrug allowed solubilisation into oil and therefore formulation into nanoemulsions. FTC-prodrug was synthesised by Amer from Johns Hopkins Medical School as part of an ongoing NIH funded collaboration with Dr Caren Freel-Meyers. It was hypothesised that an orally administered mucoadhesive emulsion would improve the retention time of the FTC-prodrug in the gut due to its binding capabilities with the mucosal surface in the GI tract. The aim of this study was to establish if nanoemulsions can deliver drugs through the gut and to then determine if there was any difference in the release profiles of a mucoadhesive nanoemulsion to that of a non-mucoadhesive, highly penetrating nanoemulsion. This study will also establish whether the oral dosing of an oil-soluble prodrug in a nanoemulsion formulation would be substantially different to the FTC parent drug solubilised in water. Finally, this experiment will determine whether the nanoemulsion system can be orally administered and provide good drug exposure.

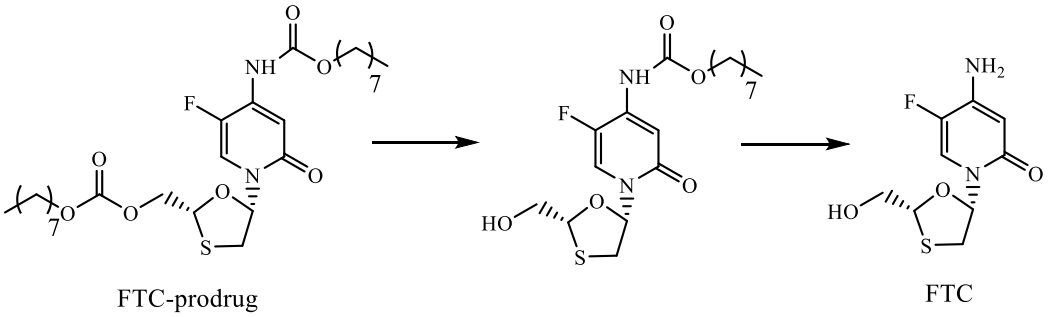

Figure 5.25 Chemical structure of FTC-prodrug, and subsequent hydrolysis to FTC as observed in plasma. FTC-prodrug was synthesised by researchers at Johns Hopkins Medical School.

FTC-prodrug nanoemulsions were formulated using polymeric surfactants $SH_{0.75}DBiB_{0.25}$-*p*(OEGMA$_{50}$-*co*-EGDMA$_{0.8}$) or DBiB-*p*(OEGMA$_{50}$-*co*-EGDMA$_{0.8}$) to formulate mucoadhesive and non-mucoadhesive nanoemulsions respectively. FTC-prodrug was solubilised into the oil phase, 99:1 ethyl acetate:castor oil and underwent homgenisation (2 minutes, 24,000 rpm) followed by evaporation of the volatile oil phase produced the nanoemulsions to yield a final concentration of 4.875 mg/mL. As detailed in Table 5.8 and Figure 5.26, the inclusion of FTC-prodrug produced larger nanoemulsions than their unloaded counterparts at 390 and 340 nm for mucoadhesive and non-mucoadhesive formulations respectively.

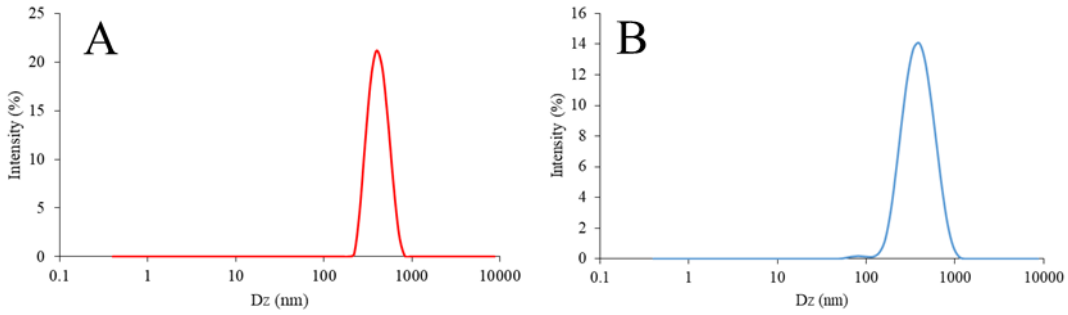

Figure 5.26 DLS analysis of FTC-prodrug loaded nanoemulsions (4.875 mg/mL) with A) $SH_{0.75}DBiB_{0.25}$-*p*(OEGMA$_{50}$-*co*-EGDMA$_{0.8}$) B) DBiB-*p*(OEGMA$_{50}$-*co*-EGDMA$_{0.8}$) as polymeric surfactants with castor oil as non-volatile oil.

Table 5.8 DLS characterisation of FTC-prodrug (4.085 mg/mL) loaded nanoemulsions formulated using $SH_{0.75}DBiB_{0.25}$-*p(*$OEGMA_{50}$-*co*-$EGDMA_{0.8}$*)* or DBiB-*p(*$OEGMA_{50}$-*co*-$EGDMA_{0.8}$*)* as the polymeric surfactant and castor oil as the non-volatile oil phase.

Polymer	D_z (nm)	D_n (nm)	PdI	Zeta (mV)
$SH_{0.75}DBiB_{0.25}$-*p(*$OEGMA_{50}$-*co*-$EGDMA_{0.8)}$	390	380	0.11	-9.40
DBiB-*p(*$OEGMA_{50}$-*co*-$EGDMA_{0.8}$*)*	340	250	0.12	-10.4

FTC was dosed orally to male wistar rats at 5 mg/kg as conventional FTC as well as the formulated FTC-prodrug in nanoemulsions. All treatment conditions were reproduced (n=4) to validate results and overcome experimental error inherent with *in vivo* work. The three treatments tested during this study were hydrophilic FTC solubilised in water, a mucoadhesive nanoemulsion loaded with FTC-prodrug and a non-mucoadhesive nanoemulsions loaded with FTC-prodrug. Following habituation (7 days) where food and water were provided *ad libitum*, the rats received a single dose of either FTC or the FTC-prodrug nanoemulsions (5 mg/Kg FTC) *via* oral gavage. Blood samples were collected to determine plasma concentrations of FTC at 0.5, 1, 2, 4, 6, 8 hours post dosing from the tail vein. Bioanalysis of the blood samples was performed by measurement of FTC parent drug by liquid chromatography followed by combination of two mass spectrometry analysers (LC-MS/MS). At the 24 hour time point, the rats were sacrificed using cardiac puncture under terminal anaesthesia.

As mentioned, the FTC parent drug was measured by LC-MS/MS, therefore the concentration of FTC-prodrug in systemic circulation which has not yet been metabolised to the parent drug cannot be determined. Plasma concentrations of the FTC measured over 8 and 24 hour time points are highlighted in Figure 5.27. Although the formulation of FTC-prodrug into mucoadhesive or non-mucoadhesive

nanoemulsions seems to have no great effect on the concentration of FTC in the blood plasma compared to dosed, unformulated FTC it does show that the FTC-prodrug nanoemulsions permeate through the gut and are able to deliver prodrug and parent FTC to the body, and release profiles mimic those of the pure drug.

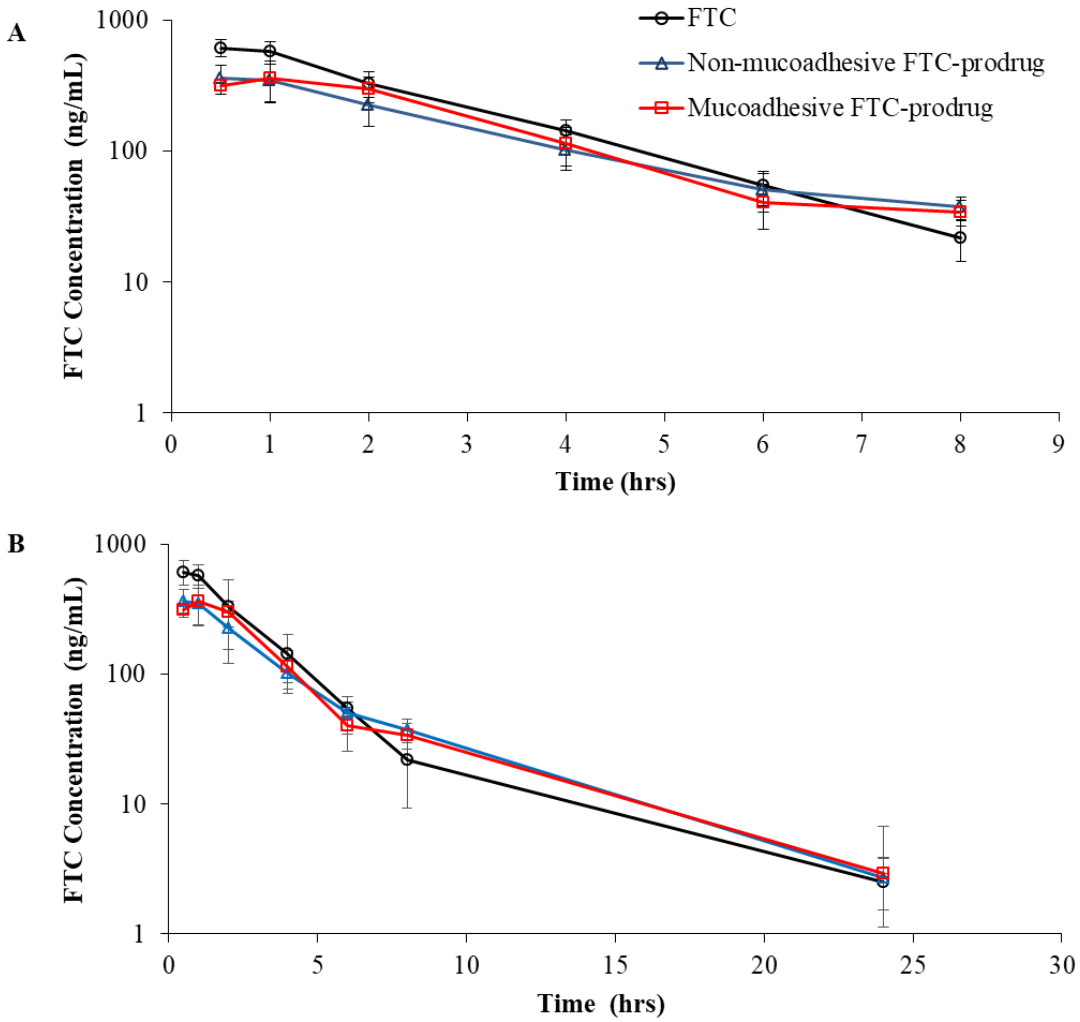

Figure 5.27 Oral dosing of unformulated FTC in water dispersant (black circle), DBiB-*p*(OEGMA$_{50}$-*co*-EGDMA$_{0.8}$) stabilised non-mucoadhesive nanoemulsion (blue triangle) and SH$_{0.75}$DBiB$_{0.25}$-*p*(OEGMA$_{50}$-*co*-EGDMA$_{0.8}$) stabilised mucoadhesive nanoemulsion (red square). FTC-prodrug loaded nanoemulsions dosed to rats at 5 mg/Kg, n=4 at A) 8 hours and B) 24 hours. Bioanalysis was performed by LC-MS/MS.

Pharmacokinetic parameters calculated in the blood plasma are: the maximum, minimum and average FTC concentration achieved after dosage (C_{max}, C_{min} and C_{avg}), the area under the curve which is dependent on clearance time (AUC_{0-24}) and the half-life of the drug which is the time required for the concentration of FTC to be reduced

by one half ($t_{1/2}$), Table 5.9. Although the release profiles of the unformulated FTC and FTC-prodrug nanoemulsions were comparable the C_{max} achieved from the nanoemulsions was lower than parent FTC meaning a lower concentration was reached, however the AUC is only slightly lower meaning retention in the blood plasma for a similar time period. This is similar for C_{avg} and C_{min} which were comparable for both nanoemulsions studied, with almost identical C_{mins} for the FTC parent drug as well. However, the C_{avg} was over 100 ng/mL higher than both nanoemulsions meaning a greater average drug concentration of parent FTC was observed.

Table 5.9 *In vivo* oral pharmacokinetic parameters comparing plasma concentrations of FTC from unformulated FTC and FTC-prodrug in mucoadhesive and non-mucoadhesive nanoemulsions.

PK Parameter	FTC	Non-mucoadhesive FTC-prodrug Emulsion	Fold Change	Mucoadhesive FTC-prodrug Emulsion	Fold Change
C_{max} (ng/mL)	618.76	376.81	0.61	393.31	0.64
C_{min} (ng/mL)	2.49	2.69	1.08	2.93	1.17
C_{avg} (ng/mL)	248.44	160.94	0.65	166.96	0.67
AUC_{0-24} (ng.h/mL)	1842.19	1439.77	0.78	1518.95	0.82
Half-life ($t_{1/2}$) (h)	3.87	4.10	1.06	3.76	0.97

5.5 CONCLUSIONS

Mucoadhesive, $SH_{0.75}DBiB_{0.25}$-*p*($OEGMA_{50}$-*co*-$EGDMA_{0.8}$), and non-mucoadhesive, DBiB-*p*($OEGMA_{50}$-*co*-$EGDMA_{0.8}$) polymeric surfactants were used to formulate macroemulsions and nanoemulsions using squalene and castor oil as the non-volatile oil phase. Analogous emulsions were successfully formulated which included Amp B and CsA at varying concentrations around the topical dose currently used in clinic. Nanoemulsions were taken forward for biological evaluation to assess their potential as ophthalmic treatments for corneal disease. Blank nanoemulsions were tested for the

cytotoxic effect on two corneal cell lines, HCjE-Gi and HCE-T, and a non-toxic concentration of 9.1 v/v % was determined. Phalloidin staining confirmed no drug loaded nanoemulsions induced cell death apart from when 100 % nanoemulsion i.e. undiluted was dosed. Unfortunately, the mucoadhesive character of the emulsion did not show any signs of adhesion when exposed to HCjE-Gi cells. It is thought that the secretion of mucus was not great enough to show any benefit of adhesive character, and the concentration of mucins too low in comparison to the data shown in the previous chapter. The mucus penetrating characteristics of nanoemulsions formulated using DBiB-*p*(OEGMA$_{50}$-*co*-EGDMA$_{0.8}$) was then studied. Amp B loaded nanoemulsions were tested for their ability inhibit the growth of *C. albicans*, which causes fungal infections in the cornea. It was successfully shown to be able to inhibit the growth of yeast culture at the same concentrations as a current fungal treatment (250 μg/mL), however it is worth noting that the undiluted nanoemulsion had the greatest effect on *C. albicans* growth. This highlights the difference in oil droplet number between diluted and non-diluted Amp B nanoemulsions, where further experimentation could look at increasing the amount of Amp B per droplet to mitigate the effects of dilution. CsA loaded nanoemulsions were successfully formulated and the release of CsA confirmed *via* dialysis using tritium labelled CsA to measure small quantities. It was shown that CsA was steadily released from the emulsion over a 180 hrs, time period.

Finally, an *in vivo* experiment confirmed that the nanoemulsions can deliver drugs through the gut and into systemic circulation and an FTC-prodrug delivered orally *via* an emulsion can be metabolised in the body. FTC concentrations in the blood plasma were unchanged when hydrophilic FTC in water or FTC-prodrug formulated into nanoemulsions were dosed. There was also no significant difference in the release profiles of the two nanoemulsions, however as a proof of concept study of the prodrug against pure FTC, it was shown that the prodrug was well metabolised.

CHAPTER 6

Conclusions and Future Work

6.1 CONCLUSIONS

The aim of this research was to investigate the nature of linear and branched polymeric architectures as surfactants for o/w macroemulsions and nanoemulsions. Our hypothesis was that functionality could be introduced at the chain ends of the copolymer structures, with an emphasis on thiol functionality to allow the potential development of mucoadhesive drug delivery vehicles. Initially, the principle of mixing chain end chemistries was established by studying the systematic replacement of hydrophobic chain ends with hydrophilic PEG groups within branched copolymers. The minimum number of hydrophobic chain ends required to generate stable emulsions was determined using DBiB and PBiB co-initiation and shown to be approximately 25 mol %. The potential to include functionality was then established using a XanBiB initiator containing a masked thiol group, in place of PBiB in the co-initiated branched polymerisations, with the aim of xanthate cleavage and formation of thiol-functional stabilisers able to create mucoadhesive macroemulsions and nanoemulsions. The response of these macro- and nanoemulsions to mucus substrates was established using a novel flow-through model with biosimilar mucus and an *ex vivo* MPT system with porcine intestinal mucus. The different sized emulsions were also shown to encapsulate drugs and enable studies of drug delivery for ophthalmic treatments and, in *in vivo* tests as oral administration options.

To assess the effect of polymeric architecture on the ability of polymers to act as surfactants, a number of linear and branched copolymers with varying hydrophilicity were synthesised. The branched architecture was repeatedly shown to be critical to the emulsion formation and stability, where branched copolymers were able to successfully stabilise emulsions (macro and nano) over sustained periods of time when stored under ambient conditions. The role of the multiple-anchoring points derived from the numerous conjoined chains, appears to be key, suggesting the branched architecture holds desorbed polymer chain ends close to the surface of the oil droplet rather than allowing a dynamic equilibrium with the continuous phases that would be seen in linear polymer analogues.

The thiol-functional branched copolymer stabilisers were synthesised to generate a range of chain end group ratios (DBiB:SH) Surprisingly, thiol-functionalised emulsions displayed high levels of stability with no observation of emulsion

breakdown or aggregation due to an expected inter-droplet disulphide bond formation between neighbouring polymers; four week stability was observed, however this is not believed to be a limiting timeframe and longer stabilities may be achieved. Macroemulsions and nanoemulsions generated with thiol-functional stabilisers exhibited an unexpected size-dependent interaction with mucosal surfaces. When tested with a biosimilar mucus, a burst release, captured *via* optical microscopy, was seen on contact of macroemulsions with the substrate; this was not seen when nanoemulsions were tested (up to approximately 1 micron) and was hypothesised as being due to the larger perturbations of the oil-water interface when multiple disulphide bonds are formed. For nanoemulsions, decreasing droplet diameters led to an increase in mucoadhesion, which was interpreted as being due to the larger percentage of surface area per droplet that contacts the mucosal surface when droplets are small; this is yet to be verified

Varying the number of thiols at the nanoemulsion surface, whilst attempting to maintain the size of the droplets, showed a clear correlation between thiol chain end concertation increasing mucoadhesion using the flow-model. Similar results were seen when using an *ex vivo* MPT analysis to track and quantify the diffusive properties of thiol-functional nanoemulsions through porcine intestinal mucus

A conceptual model of the behaviour of the branched copolymers and the resulting nanoemulsions has transpired when considering the different behaviour across the varying structures and emulsions that have been studied. Decreasing the number of hydrophobic chain ends potentially leads to a subsequent decrease in the density of packing of the branched copolymer at the surface of the oil droplet. As the number of hydrophobic anchoring chain ends are reduced, there is fewer anchoring points per oil droplet, but also fewer primary chains within the branched structure actually tethered to the oil/water interface. This would also correspond to some of the primary chains being able to extend further into the surrounding aqueous medium. The difference between the DLS measured hydrodynamic diameters (D_z values) that are seen for DBiB, PBiB and SH containing nanoemulsions formed under controlled conditions but using varying ratios of volatile to non-volatile oils is certainly pointing to this potential interpretation, Figure 6.1 (from Chapter 4).

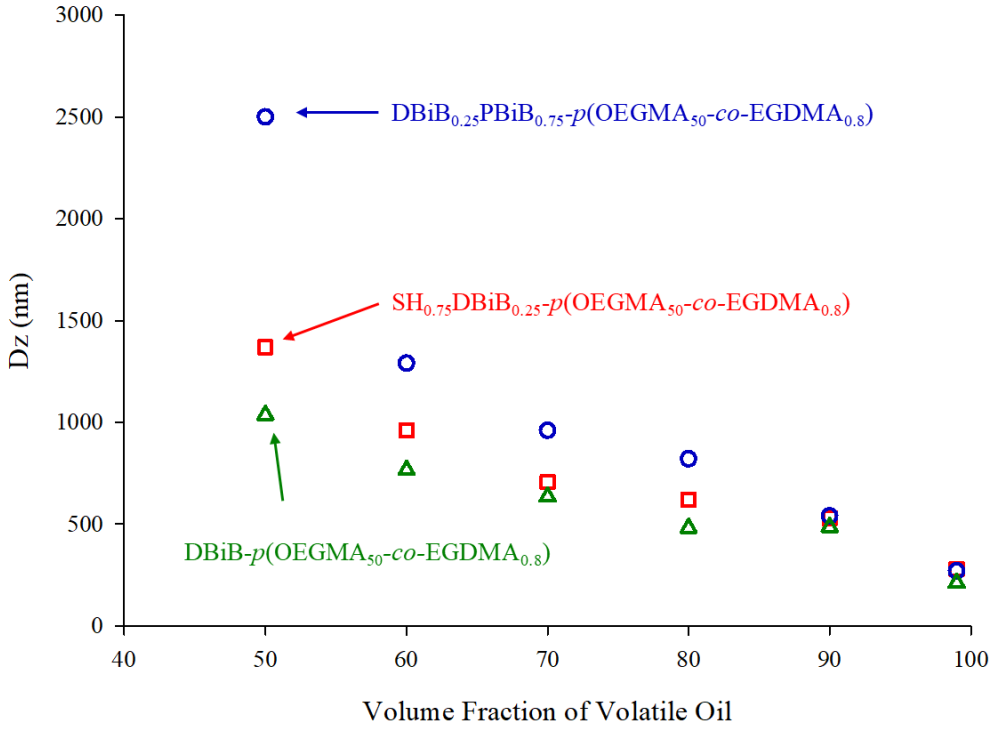

Figure 6.1 Comparison of D_z values for nanoemulsions with different volume fraction of volatile oil (ethyl acetate). Nanoemulsions stabilised with branched copolymers; $DBiB_{0.25}PBiB_{0.75}$-*p*($OEGMA_{50}$-*co*-$EGDMA_{0.8}$), ($SH_{0.75}DBiB_{0.25}$-*p*($OEGMA_{50}$-*co*-$EGDMA_{0.8}$) and DBiB-*p*($OEGMA_{50}$-*co*-$EGDMA_{0.8}$).

Also, the different diffusion speeds of the nanoemulsions stabilised by branched copolymers with varying thiol content that were tracked through porcine mucus, suggests the difference in speed is due to variation in hydrodynamic diameter and potentially not due to varying chemical interactions with the mucus. This due to the fact that the difference in thiol content varies the physical hydrodynamic size of the nanoemulsions. This interpretation is also supported by the study that aimed to investigate the 'leakiness' of the oil/water interface. The release of Oil blue A from DBiB-*p*($OEGMA_{50}$-*co*-$EGDMA_{0.8}$) and $SH_{0.75}DBiB_{0.25}$-*p*($OEGMA_{50}$-*co*-$EGDMA_{0.8}$) stabilised nanoemulsions, shows a considerable impact that is not chemistry-derived, but rather a physical effect, Figure 6.2.

Finally, drug loading of nanoemulsions was shown to be possible, to high loading, with two different drug classes. The route of administration was also shown to be variable from topical, ophthalmic candidate therapy, to oral, HIV prodrug delivery. Cytotoxicity appeared to show that the fully formulated nanoemulsions would be tolerated well *in vivo*.

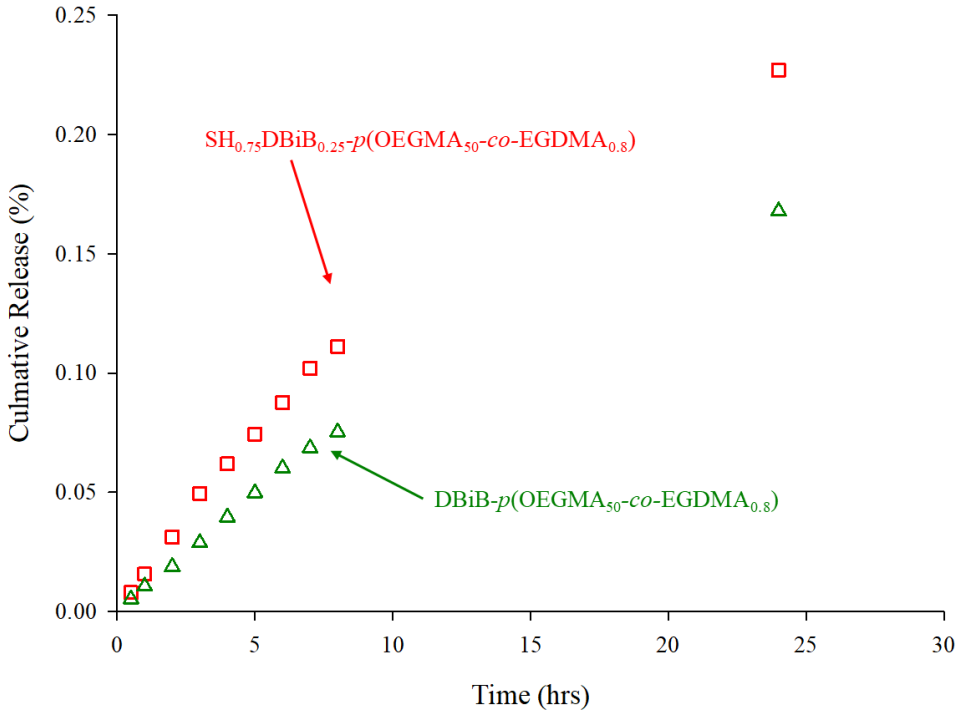

Figure 6.2 Cumulative percentage release of oil blue A (0.1 wt %) from nanoemulsions stabilised with DBiB-*p*(OEGMA$_{50}$-*co*-EGDMA$_{0.8}$) (green) and SH$_{0.75}$DBiB$_{0.25}$-*p*(OEGMA$_{50}$-*co*-EGDMA$_{0.8}$) (red).

Interestingly, efficacy testing of Amp B nanoemulsions against a yeast strain, *candida albicans*, also showed the potential for drug release, as also seen in the radiochemical dialysis experiments of CsA and Oil blue A.

6.2 FUTURE WORK

Further study into the cytotoxic limits of the drug loaded nanoemulsions could be carried out on HCE-T cells, to determine a more precise toxic limit with a secondary technique to confirm the non-toxic levels. An enzyme-linked immunosorbent assay (ELISA) for determining the efficacy of CsA loaded nanoemulsions would prove beneficial to show that the nanoemulsions could be successful as therapeutic treatment systems. A future study could also look at the benefit of macroemulsions as drug delivery systems to the eye, with the burst release in the presence of mucosa potentially leading to an improved topical treatment route to the cornea. The cytotoxic limits and also efficacy testing again would have to be performed on these macroemulsions, where the oil phase could be further varied to determine the most biologically relevant oil for these studies.

An interesting prospect from this research would be to determine the emulsion droplet size at which the burst release is not shown, potentially between 1 – 15 μm, further tailoring the mucoadhesive properties observed. Another development could involve zoning the thiol groups within the polymeric structure, where instead of a statistical distribution of thiol-chain ends across the surface, each chain end could contain up to 8 thiol groups. This could be done by including a xanthate-based dendritic initiator, as reported previously within the group and discussed in Chapter 4, Section 4.1. Zoning of thiol groups could potentially alter the mucoadhesive properties of the nanoemulsions, with a question of whether zoning increases the likelihood of thiol-cysteine bonding at lower mole percent thiol chain ends.

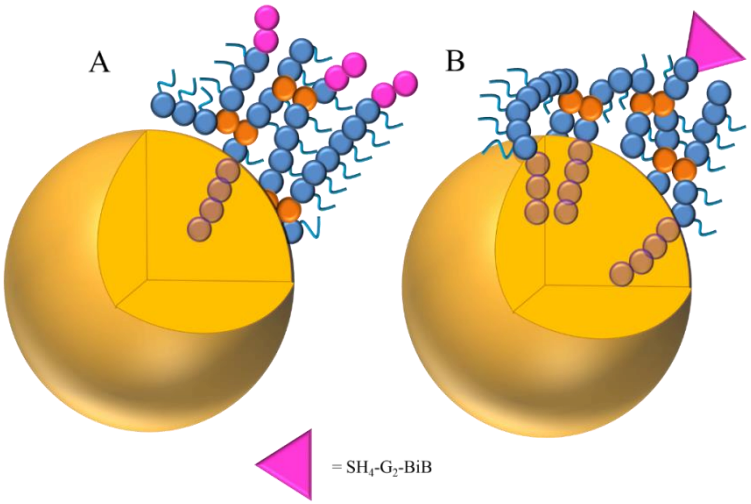

Figure 6.3 A) Non-zoned thiol functional branched copolymer stabilised oil droplet with one thiol group per chain end with respect to molar ratio of initiating group and B) oil droplet stabilised with zone thiol functional branched copolymer, where one primary chain can have four thiol groups.

Due to the large amount of mucosal surfaces covering the body, the potential for these materials is vast. These materials could be loaded with therapeutic agents typical for treatment of diseases observed for example, in the nasal cavity, respiratory tract or reproductive organs. The tailoring of mucus diffusive properties through the manipulation of the polymeric structure as well as emulsion droplet diameter mean that these materials could be specifically designed for use, where a highly diffusive or a highly adhesive system would be more beneficial.

CHAPTER 7

Experimental

7.1 CHARACTERISATION

7.1.1 NMR Spectroscopy

NMR spectra were recorded using a Bruker DPX-400 spectrometer operating a 400 MHz for ^{1}H NMR and 100 MHz for ^{13}C NMR. Solvents used for NMR spectroscopy were $CDCl_3$, D_2O and DMSO-*d6.*

7.1.2 Mass Spectrometry

Chemical ionisation (CI) and electrospray (ES) mass spectrometry data was recorded at the University of Liverpool in the Mass Spectrometry Laboratory. The CI-MS was obtained using an Agilent GCQTOF 7200 using methane gas CI. ES-MS was analysed using a MicroMass LCT mass spectrometer using electron ionisation and direct infusion syringe pump sampling.

7.1.3 Gel Permeation Chromatography (GPC)

Double and Triple detection GPC was performed to measure molecular weights and molecular weight distributions using Malvern Viscotek instruments. The first GPC was equipped with GPCmax VE2001 auto sampler, two Viscotek T600 columns, guard column, a refractive index (RI) detector VE3580 and a 270 Dual Detector (light scattering and viscometer) with a mobile phase of THF containing 2 v/v % of trimethylamine at 35 ^{o}C with a flow rate of 1 mL/min.

The second instrument was equipped with GPCmax VE2001 auto sampler, two Viscotek D6000 columns, guard column and a triple detector array TDA305 (refractive index, light scattering and viscometer) and a mobile phase of DMF containing 0.01 M lithium bromide at 60 ^{o}C with a flow rate of 1 mL/min.

GPC determines molecular weight by separating different polymeric chain lengths within a molecular weight distribution. The GPC columns contain porous beads with different pore sizes;larger polymeric materials cannot pass through the pores therefore a shorter pathway is taken through the column and results in earlier elution. Whereas smaller polymeric materials are able to pass through the porous beads, this longer pathway through the column, results in longer retention and later elution times. The triple detection GPC uses refractive index, viscometry and light scattering detectors to calculate the absolute molecular weight of the polymer.

Due to technical problems with the DMF viscometer, Chapter 2 and 3 polymeric materials molecular weights were determined without the viscometer analysis.

7.1.4 Contact Angle Measurement

Drop shape analysis (DSA) was performed using a Kruss DSA100E located in the Materials Innovation Factory (MIF) formulation laboratory. DSA used a manual static sessile drop method, using PTFE tape as a hydrophobic substrate. An advanced digital camera (x20 magnification) attachment was used to capture water/aqueous polymer solution droplets.

7.1.5 Surface Tensiometer Measurements

Surface tension measurements were performed using a Kibron Delta 8 located in the MIF formulation laboratory. This equipment is a high throughput platform for surface tension measurements using a standard 96-well microlitre plate format; cross contamination between measurements is eliminated by the probes being cleaned using a 600 ^{o}C furnace between measurements. Surface tension measurements are resolved to 0.01 mN/m, using the Du Nouy-Padday method. This is a minimised version of the Du Nouy ring technique, which uses a small size rod to determine surface tension, allowing for use in small volumes of liquid, which in this experiment was 50 µL. The rod is lowered to the surface of the sample until a meniscus is formed and then raised till the bottom edge of the rod lies on the plane of the undisturbed surface and the surface tension is determined by the programme.

7.1.6 Mastersizer Analysis

All macroemulsions were characterised using a Malvern Mastersizer 3000A, which uses static light scattering to measure the average droplet volume ($D_{[4,3]}$). Samples are dispersed within water and a combination of red (633 nm) and blue (432 nm) lasers are used with a series of detectors at set angles to accurately measure particle size from 1 – 3500 µm.

7.1.7 Dynamic Light Scattering

All nanoemulsions were characterised by dynamic light scattering (DLS) using Malvern Zetasizer ZS. This equipment measures particle size in the range of 0.3 – 10000 nm, measuring the diffusion of particles moving under Brownian motion which

the software converts into size and size distribution using the Stokes-Einstein relationship.

7.1.8 Scintillation Counter

ProSafe+ scintillation cocktail (Meridian Biotechnologies Ltd.) was used as received. All radiation measurements were carried out using a liquid scintillation counter (Packard Tri-carb 3100TR; Isotech).

Liquid scintillation counting relies upon the use of a scintillation cocktail which contain scintillators (materials which exhibit luminescence when excited by ionising radiation). The solvent molecules absorb energy emitted from beta particles and transfer this energy until it is transferred to a scintillant. The scintillant then emits photons following the energy absorption which are detectable by the scintillation counter.

7.2 MATERIALS

All deuterated solvents were purchased from Sigma Aldrich apart from DMSO-*d6* which was purchased from Goss Scientific, and used as received apart from $CDCl_3$ where 0.1 % TMS was added. All solvents were reagent grade and purchased from Fisher Scientific. Dodecane, squalene and castor oil were purchased from Sigma Aldrich and used as received. Lumogen F Red 305 was donated by Cardiff University and BASF and used as received. Resazurin was purchased from Sigma Aldrich and used as received. Alex Fluro 488 Phalloidin (Phallodin) and Live/dead^{TM} full viability/cytotoxicity kit was purchased from Invitrogen and used as received. Amphotericin B (Amp B) and Cyclosporin A (CsA) were purchased from ChemLeader and used as received.

7.3 CHAPTER 2

7.3.1 Chapter 2 Materials

Magnesium sulphate ($MgSO_4$), sodium hydrogen carbonate ($NaHCO_3$), timethylamine (TEA) were purchased from Fischer and used as received. 1-dodecanol, α-bromoisobutyl bromide (98 %), anisole, poly(ethylene glycol)methyl ether methacrylate (average M_n = 300 g/mol) (98 %) (OEGMA), ethylene glycol dimethacylate (EGDMA), 2,2'-bipyridyl (bpy), copper (I) chloride (Cu(I)Cl) (97 %),

activated neutral alumina and basic alumina were purchased from sigma Aldrich and used as received.

7.3.2 Synthesis of ATRP Initiator DBiB

1-dodecanol (9.32 g, 50 mmol, 1.0 equiv) and trimethylamine (TEA) (6.07 g, 60 mmol, 1.2 equiv) were dissolved in dichloromethane (70 mL). α-bromoisobutyl bromide (13.80 g, 60 mmol, 1.2 equiv) was added dropwise to the mixture via a pressure equalising dropping funnel and stirred in an ice bath under nitrogen. After addition the reaction vessel was left to warm to ambient temperature and left to stir for 24 hours. The solution was washed once with $NaHCO_3$ (50 mL) and distilled water (4 x 50 mL). The organic layer was dried over anhydrous $MgSO_4$, filtered, and concentrated *in vacuo.* If ^{1}H NMR showed the need for additional purification by the inclusion of environments assigned to impurities, the product was passed through a basic alumina column.

Yield: 3.155 g, yellow oil, (19 %). ^{1}H NMR (400 MHz, $CDCl_3$) δ (ppm) = 0.81 (t, 3H), 1.19 (m, 18H), 1.61 (m, 2H), 1.86 (s, 6H, C$\underline{H}_3$C$\underline{H}_3$), 4.08 (t, 2H). ^{13}C NMR (100 MHz, $CDCl_3$) δ (ppm) = 14.1, 22.7, 25.8, 28.4, 29 - 30, 32.0, 56.0, 66.2, 171.8. Mass Spectrometry: $[M+H]^+$ ($C_{16}H_{32}BrO_2$) m/z = 335.0. Experimentally: ES MS $[M+H]^+$ m/z = 335.2. Elemental Analysis:Calculated (%): ($C_{16}H_{31}O_2Br$) = C, 57.31; H, 9.32. Experimental (%) = C, 57.33; H, 9.20.

7.3.3 ATRP of DBiB-*p*(OEGMA$_{50}$)

OEGMA (5.00 g, 16 mmol, 50 eq.), 2,2'-bipyridyl (0.100 g, 0.64 mmol, 2 eq.) and DBiB (0.0268 g, 0.08 mmol, 0.25 eq.) were added to a RBF equipped with magnetic stirrer and IPA/H_2O (92.5:7.5 v/v, 4.39:0.36 mL, 55 wt%) added as solvent. Anisole was added as internal standard for ^{1}H NMR conversion of monomer peaks. The vessel was sealed and degassed with dry nitrogen for 5 minutes, CuCl(I) (0.032 g, 0.32 mmol, 1 eq.) was added and the reaction vessel sealed. RBF was immersed in silicone oil bath at 40 ^{o}C and left to react until complete conversion, approx. 8 hrs. The polymerisation was terminated by exposure to air and dilution in THF and purified by: removal of copper catalyst by a neutral alumina column, removal of solvent *in vacuo* and crude polymer precipitated twice into cold hexane. Residual solvent was removed at 40^{o}C in a vacuum oven overnight.

7.3.4 ATRP of DBiB-*p(*OEGMA$_{50}$-*co*-EGDMA$_{0.8}$)

OEGMA (5.00 g, 16 mmol, 50 eq.), EGDMA (0.051 g, 0.26 mmol, 0.8 eq.), 2,2'-bipyridyl (0.100 g, 0.66 mmol, 2 eq.), DBiB (0.111 g, 0.34 mmol, 1 eq.) were added to a RBF equipped with magnetic stirrer and IPA/H_2O (92.5:7.5 v/v, 4.39:0.36 mL, 55 wt%) added as solvent. Anisole was added as an internal standard for ^{1}H NMR conversion of monomer peaks. The vessel was sealed and degassed with dry nitrogen for 5 minutes, CuCl(I) (0.032 g, 0.32 mmol, 1 eq.) was added and the reaction vessel sealed. RBF was immersed in silicon oil bath at 40 ^{o}C and left to react until complete conversion, approx. 24 hrs. The polymerisation was terminated by exposure to air and dilution in THF and purified by: removal of copper catalyst by a neutral alumina column, removal of solvent *in vacuo* and crude polymer precipitated twice into cold hexane. Residual solvent was removed at 40^{o}C in a vacuum oven overnight.

7.3.5 Kinetic Studies of ATRP

Kinetic studies ($\ln[M]_0/[M]$ = conversion) were performed by taking samples of the polymerisation reaction medium and analysed by ^{1}H NMR spectroscopy and GPC. The monomer conversion was determined by ^{1}H NMR; vinyl protons of monomer located at 6.13 and 5.58 ppm were integrated and compared to integrated values for pendant polymer chain at 3.4 ppm. Conversion was then calculated by:

$$\text{Conversion} = ([I_1/(I_2\text{-}3)]/3)*100$$

Where I_1 = integral at 5.58 ppm and I_2 = 3.4 ppm. The catalytic system was removed from the samples prior to GPC anaylsis by passing through a neutral alumina column. A kinetic plot is produced on a semi-logarithimic scale, plotting monomer conversion against time.

7.3.6 Preparation of Macroemulsion

Aqueous polymer solutions were prepared at a 5 mg/mL concentration of branched and linear polymers. Emulsions were prepared at a 1:1 v:v ratio of oil:water, where the oil phase was *n*-dodecane. Emulsions were homogenised *via* over-head shear homogenisation (IKA T 25 ULTRA-TURRAX) for 2 minutes at 24,000 rpm. Emulsions were left over night to equilibrate before characterisation of droplet using light scattering was carried out (Malvern Mastersizer 2000).

7.3.7 Preparation of Nanoemulsion

Nanoemulsions were generated using the solvent evaporation technique, with aqueous polymer solutions of branched and linear polymers at a 5 wt % concentration. The oil phase is a mixture of two miscible oils with one being a volatile solvent. As the volatile solvent evaporated, the non-volatile section of the oil droplet shrinks to the nanoscale. The oil phase is composed of ethyl acetate: castor oil in a ratio of 50:50, 60:40, 70:30, 80:20, 90:10 or 99:1. The oil: water ratio was 1:1, with the water phase being aqueous polymer solution at 5 wt%. Emulsions formulated *via* homogenisation using an over-head shear homogeniser (IKA T 25 ULTRA-TURRAX) for 2 minutes at 24,000 rpm. Emulsions are left overnight until all ethyl acetate is removed which was followed by gravimetric analysis and emulsions analysed by dynamic light scattering (Malvern, Zetasizer ZS).

7.4 CHAPTER 3

7.4.1 Chapter 3 Materials

Magnesium sulphate ($MgSO_4$), sodium hydrogen carbonate ($NaHCO_3$), timethylamine (TEA) were purchased from Fischer and used as received. Anhydrous THF (99%), 1-dodecanol (99 %), α-bromoisobutyl bromide (98 %), anisole (99 %), poly(ethylene glycol)methyl ether methacrylate (average M_n = 300 g/mol) (98 %) (OEGMA), ethylene glycol dimethacylate (EGDMA), 2,2'-bipyridyl (bpy), Copper (I) chloride (Cu(I)Cl) (97 %), activated neutral alumina and basic alumina were purchased from Sigma Aldrich and used as received. 4-(dimethylamino) pyridine (>99 %) (DMAP), was purchased from Alfa Aesar and used as received. All solvents unless stated were reagent grade, purchased from Fischer Scientific and used as received.

7.4.2 Synthesis of ATRP Initiator PBiB

Monomethoxy poly(ethylene glycol) Mw ~ 750 g/mol, (23.0 g, 30.7 mmol) was dissolved in anhydrous THF (40 ^oC) under dry N_2. DMAP (0.0375 g, 0.3 mmol) and TEA (5.6 g, 53.7 mmol) was added and the reaction mixture stirred in an ice bath. α-bromoisobutyryl bromide (10.6 g, 46.0 mmol) was added dropwise using a dropping funnel over 30 minutes and a white precipitate ($Et_3NH^+Br^-$ salt) was immediately formed. The reaction was conducted over 24 hours, the precipitate removed by filteration, solvent removed *in vacuo* and the resulting crude product was precipitated twice from acetone into petroleum ether (30 – 40 ^oC) to give the final product. Yield:

15 g, 65.2 %. yellow oil. ^{1}H NMR (400 MHz, D_2O) δ ppm = 1.86 (s, 6H), 3.30 (S, 2H), 3.64 (m, 60H), 3.77 (m, 2H), 4.32 (m, 2H). ^{13}C NMR (100 MHz, D_2O) δ ppm = 29.8, 56.8, 65.4, 38.3, 69.5, 69.5, 69.7, 70.9, 173.7. Elemental Analysis: Calculated (%): ($C_{37}H_{73}O_{18}Br$) = C, 50.16; H, 8.24. Experimental (%) = C, 49.25; H, 8.31.

7.4.3 ATRP of PBiB-*p*(OEGMA$_{50}$)

OEGMA (5.00 g, 16 mmol, 50 eq.), 2,2'-bipyridyl (0.100 g, 0.64 mmol, 2 eq.), PBiB (0.25 g, 0.34 mmol, 1 eq.) were added to a RBF equipped with magnetic stirrer and solvent system IPA/H_2O (92.5:7.5 v/v%, 4.39:0.36 mL, 55 wt%) added. Anisole was added as internal standard for ^{1}H NMR conversion of monomer peaks. The vessel was sealed and degassed with dry nitrogen for 5 minutes, CuCl(I) (0.032 g, 0.32 mmol, 1 eq.) was added to the reaction mixture and the vessel sealed. RBF was immersed in a silicone oil bath at 40 ^{o}C and left to react until complete conversion, approx. 8 hrs. The polymerisation was terminated by exposure to air and dilution in THF and purified by: removal of copper catalyst by a neutral alumina column, removal of solvent *in vacuo* and crude polymer precipitated twice into cold hexane. Residual solvent was removed at 40^{o}C in a vacuum oven overnight.

7.4.4 ATRP of PBiB-*p*(OEGMA$_{50}$-*co*-EGDMA$_{0.8}$)

OEGMA (5.00 g, 16 mmol, 50 eq.), EGDMA (0.051 g, 0.32 mmol, 0.8 eq.), 2,2'-bipyridyl (0.100 g, 0.64 mmol, 2 eq.), PBiB (0.25 g, 0.34 mmol, 1 eq.) were added to a RBF equipped with magnetic stirrer and solvent system IPA/H_2O (92.5:7.5 v/v%, 4.39:0.36 mL, 55 wt %) added. Anisole was added as internal standard for ^{1}H NMR conversion of monomer peaks. The vessel was sealed and degassed with dry nitrogen for 5 minutes, Cu(I)Cl (0.032 g, 0.32 mmol, 1 eq.) was added and the reaction vessel sealed. RBF was immersed in silicone oil bath at 40 ^{o}C and left to react until complete conversion, approx. 24 hrs. The polymerisation was terminated by exposure to air and dilution in THF and purified by: removal of copper catalyst by a neutral alumina column, removal of solvent *in vacuo* and crude polymer precipitated twice into cold hexane. Residual solvent was removed at 40^{o}C in a vacuum oven overnight.

7.4.5 ATRP of con-initiated DBiB$_x$/PBiB$_y$-*p*(OEGMA$_{50}$-*co*-EGDMA$_{0.8}$)

DBiB$_x$/PBiB$_y$-*p*(OEGMA$_{50}$-*co*-EGDMA$_{0.8}$) was polymerised where x+y = 1 equiv., and represent the molar ratio of the initiators DBiB:PBiB. This ratio can be varied

and ranges have been generated from 0.9:0.1, 0.75:0.25, 0.5:0.5, 0.25:0.75, 0.1:0.9 DBiB:PBiB as well as the homopolymers of each prepared.

In a typical atom-transfer radical polymerisation reaction, OEGMA (5.00 g, 16 mmol, 50 eq.), EGDMA (0.051 g, 0.32 mmol, 0.8 eq.), 2,2'-bipyridyl (0.100 g, 0.64 mmol, 2 eq.), DBiB (0.0268 g, 0.08 mmol, 0.25 eq.), PBiB (0.185 g, 0.25 mmol, 0.75 eq.) were added to a RBF equipped with magnetic stirrer and solvent system IPA/H_2O (92.5:7.5 v/v, 4.39:0.36 mL, 55 wt%) was added. Anisole was added as internal standard for ^1H NMR conversion of monomer peaks. The vessel was sealed and degassed with dry nitrogen for 5 minutes, CuCl(I) (0.032 g, 0.32 mmol, 1 eq.) was added and the reaction vessel sealed. The RBF was immersed in a silicone oil bath at 40 ^oC and left to react until complete conversion, approx. 24 hrs. The polymerisation was terminated by exposure to air and dilution in THF and purified by: removal of copper catalyst by a neutral alumina column, removal of solvent *in vacuo* and crude polymer precipitated twice into cold hexane. Residual solvent was removed at 40^oC in a vacuum oven overnight.

7.4.6 Kinetic Studies

Same methodology as 7.3.4.

7.4.7 Preparation of Macroemulsions

Same methodology as 7.3.5.

7.4.8 Preparation of Nanoemulsions

Same methodology as 7.3.6.

7.5 CHAPTER 4

Ex vivo testing of nanoemulsions was conducted in collaboration with Cardiff University, in the School of Pharmacy and Pharmacology, with Dr Muthanna Al-Balwadi, within Prof. Mark Gumbleton's group. Radiochemical analysis was conducted in the Radiomaterials Laboratory in the Department of Chemistry at the University of Liverpool by Dr Helen Cauldbeck. Zone of inhibition study was performed by Dr Andrew Gallagher from the Department of Eye and Vision Science in the Department of Microbiology at the University of Liverpool.

7.5.1 Chapter 4 Materials

Magnesium sulphate ($MgSO_4$), sodium hydrogen carbonate ($NaHCO_3$), timethylamine (TEA), hydrochloric acid (1M) (HCl) were purchased from Fischer Scientific and used as received. Ethylene glycol (99.8 %), anhydrous THF (99%), α-bromoisobutyl bromide (98 %), butylamine (99 %), anisole (99 %), poly(ethylene glycol)methyl ether methacrylate (average M_n = 300 g/mol) (98 %) (OEGMA), ethylene glycol dimethacylate (EGDMA), 2,2'-bipyridyl (bpy), Copper (I) Chloride (Cu(I)Cl) (97 %), activated neutral alumina, porcine mucin, bovine serum albumin (> 98 %) (BSA), cholesterol, phosphatidylchloine and polysorbate 80 were purchased from Sigma Aldrich and used as received. Potassium ethyl xanthogenate (96 %), 2-bromoacetic acid, 4-(dimethylamino) pyridine (>99 %) (DMAP), N-N'-dicyclohexylcarbodiimide (>99 %) (DCC), 2-bromoacetic acid were all purchased from Alfa Aesar and used as received. 4-(dimethylamino)pyridinium-4-toluene sulphonate (DPTS) was synthesised Dr Faye Hern of the Rannard research group. Poly acrylic acid (Carbopol 940) was donated by Unilever and used as received. Linoleic acid was donated by researchers in the Department of Pharamacology. All solvents unless stated were reagent grade, purchased from Fischer and used as received.

7.5.2 Preparation of 2-((Ethoxycarbonothioyl)thio) acetic acid

Potassium ethyl xanthogenate (53.06 g, 311 mmol, 1 equiv.) was added to an RBF and stirred in acetone (400 mL). A solution of 2-bromoacetic acid (38.35 g, 276 mmol, 1.12 equiv.) in acetone (100 mL) was added dropwise *via* a dropping funnel to the reaction vessel over 20 minutes and left to stir at ambient temperature for 16 hours. The crude mixture was filtered under vacuum, washed with acetone and solvent removed *in vacuo*. The residual oil was solubilised in a minimum amount of dichloromethane and washed with brine (150 mL). The organic layer was dried over $MgSO_4$ and solvent removed *in vacuo* to give a white solid. Yield: 16.28 g, white solid, (33%). ^{1}H NMR (400 MHz, $CDCl_3$) δ ppm = 1.43 (t, 3H), 3.98 (s, 2H), 4.65 (q, 2H), 9.3 (s, br, –OH). ^{13}C NMR (100 MHz, $CDCl_3$) δ ppm = 13.70, 37.63, 70.93, 173.86, 212.07. Mass Spectrometry: calculated: $[M+H]^+$ ($C_6H_{12}BrO_3$) m/z = 211.0. Experimental: CI MS $[M+Na]^+$ m/z = 211.0. Elemental analysis: Calculated (%): ($C_5H_8O_3S_2$) = C, 33.32; H, 4.47; S, 35.58. Experimental (%) = C, 32.80; H, 4.40; S, 34.59.

7.5.3 Preparation of 2-Hydroxyethyl 2-Bromoisobutyrate

Ethylene glycol (301.35 g, 4855 mmol, 50 equiv.), TEA (20.33 g, 201 mmol, 2 equiv.) were dissolved in anhydrous tetrahydrofuran (100 mL) and the reaction was stirred in an ice bath. α-bromoisobutyl bromide (22.32 g, 97.1 mmol, 1 equiv.) was added dropwise over 30 minutes and the reaction was left stirring under nitrogen atmosphere at ambient temperature for 16 hours. The reaction mixture was poured into distilled water (800 mL) and extracted with dichloromethane (6 x 100 mL), the retrieved layers were washed with 1M HCl (2 x 300 mL), dried over $MgSO_4$ and solvent removed *in vacuo*. Yield: 18.60 g, yellow oil, (90.80%). ^{1}H NMR (400 MHz, $CDCl_3$) δ ppm = 1.96 (s, 6H), 3.87 (t, 2H), 4.31 (t, 2H). ^{13}C NMR (100 MHz, $CDCl_3$) δ ppm = 30.7, 55.8, 60.7, 63.3, 67.4, 171.8. Elemental Analysis: calculated (%) = ($C_6H_{11}BrO_3$) = C, 34.14; H, 5.25. Experimental (%) = C, 34.09; H, 5.24.

7.5.4 Synthesis of ATRP Initiator XanBiB

2-((Ethoxycarbanothioyl)thio) acetic acid, XanCOOH (3.85 g, 21.2 mmol, 1 equiv), 2-hydroxyethyl 2-bromoisobutyrate (4.5 g, 21.2mmol, 1 equiv) and DPTS (6.86g, 23.32 mmol, 1.1 equiv) were dissolved in anhydrous dichloromethane (40 mL) under nitrogen. DCC (4.81 g, 23.32 mmol, 1.1 equiv) was dissolved in anhydrous dichloromethane (10 mL) under nitrogen flow and transferred to the main reaction vessel *via* syringe and the reaction was left to stir at ambient temperature for 16 hours. The resulting crude mixture was filtered, diluted in dichloromethane (100 mL) and washed with distilled water (2 x 100 mL) and once with brine (100 mL). The organic layer was dried over $MgSO_4$. After removal of solvents *in vacuo* the xanthate initiator was purified by automated liquid chromatography (silica, eluting hexane increasing the polarity to hexane:ethyl acetate 70:30) to give pure product. Yield: 5.08 g, yellow oil, (25%). ^{1}H NMR (400 MHz, $CDCl_3$) δ ppm = 1.43 (t, 3H), 1.94 (s, 6H), 3.96 (s, 4H), 4.41 (m, 4H), 4.66 (q, 2H). ^{13}C NMR (100 MHz, $CDCl_3$) δ ppm = 13.70, 30.7, 37.7, 63.0, 63.3, 70.8, 167.8, 171.5, 212.5. Mass spectrometry calculated: $[M+Na]^+$ ($C_{11}H_{17}BrO_5S_2Na$) m/z = 395.28. Experimental: ES MS $[M+Na]^+$ m/z = 395.Elemental Analysis: calculated (%): ($C_{11}H_{17}BrO_5S_2$) = C, 35.39; H, 4.59; S, 17.18. Experimental (%) = C, 36.29; H, 4.79; S, 17.06.

7.5.5 ATRP of XanBiB-*p*(OEGMA$_{50}$)

OEGMA (5.00 g, 16 mmol, 50 eq.), 2,2'-bipyridyl (0.100 g, 0.64 mmol, 2 eq.), XanBiB (0.089 g, 0.24 mmol, 0.75 eq.) were added to a RBF equipped with a magnetic stirrer and the solvent system IPA/H_2O (92.5:7.5 v/v%, 4.39:0.36 mL, 55 wt%) was added. Anisole was added as internal standard for ^{1}H NMR conversion of monomer peaks. The reaction vessel was sealed and degassed with dry nitrogen for 5 minutes, CuCl(I) (0.032 g, 0.32 mmol, 1 eq.) was added and the reaction vessel sealed again. The RBF was immersed in a silicone oil bath at 40 ^{o}C and left to react until complete conversion, approx. 8 hrs. The polymerisation was terminated by exposure to air and dilution in THF and purified by: removal of copper catalyst by a neutral alumina column, removal of solvent *in vacuo* and crude polymer precipitated twice into cold hexane. Residual solvent was removed at 40^{o}C in a vacuum oven overnight.

7.5.6 ATRP of Mixed Initiator System DBiB$_x$/Xan$_1$-G$_0$-BiB$_y$-*p*(OEGMA$_{50}$-*co*-EGDMA$_{0.8}$)

DBiB$_x$/Xan$_1$-G$_0$-BiB$_y$-*p*(OEGMA$_{50}$-*co*-EGDMA$_{0.8}$) was synthesised where x+y = 1 equiv., and represent the molar ratio of the initiators DBiB:Xan$_1$-G$_0$-BiB. This ratio can be varied and ranges have been generated from 0.9:0.1, 0.75:0.25, 0.5:0.5, 0.25:0.75, 0.1:0.9 DBiB:Xan$_1$-G$_o$-BiB as well as the homopolymers of each.

In a typical atom-transfer radical polymerisation reaction, OEGMA (5.00 g, 16 mmol, 50 eq.), EGDMA (0.051 g, 0.32 mmol, 0.8 eq.), 2,2'-bipyridyl (0.100 g, 0.64 mmol, 2 eq.), DBiB (0.0268 g, 0.08 mmol, 0.25 eq.), Xan-G$_0$-BiB (0.089 g, 0.24 mmol, 0.75 eq.) were added to a RBF equipped with magnetic stirrer and solvent system IPA/H_2O (92.5:7.5 v/v, 4.39:0.36 mL, 55 wt%) was added. Anisole was added as internal standard for ^{1}H NMR conversion of monomer peaks. The vessel was sealed and degassed with dry nitrogen for 5 minutes, CuCl(I) (0.032 g, 0.32 mmol, 1 eq.) was added and the reaction vessel sealed. RBF was immersed in silicone oil bath at 40 ^{o}C and left to react until complete conversion, approx. 24 hrs.

The polymerisation was terminated by exposure to air and dilution in THF and purified by: removal of copper catalyst by a neutral alumina column, removal of solvent *in vacuo* and crude polymer precipitated twice into cold hexane. Residual solvent was removed at 40^{o}C in a vacuum oven overnight.

7.5.7 Deprotection of $DBiB_x/Xan_1$-G_o-BiB_y(*p*$OEGMA_{50}$-*co*-$EGDMA_{0.8}$)

In a typical experimental procedure to remove the xanthate protecting group, $DBiB_x/Xan_1$-G_o-BiB_y(*p*$OEGMA_{50}$-*co*-$EGDMA_{0.8}$) (0.599 g, 1.66 mmol, 1 equiv.) was dissolved in tetrahydrofuran (10 mL) and degassed with dry nitrogen for ~5 minutes. Butyl amine (0.38 mL, 4.15 mmol, 2.5 equiv.) was added to the reaction vessel and left to stir for 1.5 hours at ambient temperature. The solvent was removed *in vacuo* and crude product precipitated twice into cold hexane to purify. Residual solvent was removed *in vacuo.*

7.5.8 Preparation of Macroemulsions

Same methodology as Section 7.3.4.

7.5.9 Preparation of Nanoemulsions

Same methodology as Section 7.3.5.

7.5.10 Preparation of Macroemulsions with Encapsulated Hydrophobic Dyes

Aqueous polymer solutions were prepared at 5 mg/mL and used as the water phase of the emulsion. Emulsions were prepared at a 1:1 v:v ratio of oil:water, where the oil phase was dodecane or squalene. Oil red O or Oil blue A (0.5 wt% with respect to oil) were used as a hydrophobic drug mimic. Emulsions were generated *via* homogenisation using an over-head shear homogeniser (IKA T 25 ULTRA-TURRAX) for 2 minutes at 24,000 rpm. Emulsions were left over night before characterisation of droplets using light scattering was carried out (Malvern Mastersizer 2000).

7.5.11 Preparation of Nanoemulsions with Encapsulated Hydrophobic Dyes

Nanoemulsions were formulated using the solvent evaporation technique, with aqueous polymer solutions of branched copolymers at a 5 wt % concentration. The oil phase is a mixture of two miscible oils, one a volatile solvent and one a non-volatile oil. As the volatile solvent evaporates, the non-volatile section of the oil droplet shrinks to the nanoscale. The oil phase is composed of ethyl acetate:castor oil in a ratio of 50:50, 60:40, 70:30, 80:20, 90:10 or 99:1. The oil:water ratio was 1:1, with the water phase being aqueous polymer solution (5 wt%). Oil blue or oil red O were encapsulated in the oil phase at a concentration (0.1 wt%) with respect to the oil phase. Emulsions were generated *via* homogenisation using an over-head shear homogeniser

(IKA T 25 ULTRA-TURRAX) for 2 minutes at 24,000 rpm. Emulsions were left overnight until all ethyl acetate is removed (monitored gravimetrically) and analysis performed using dynamic light scattering (Malvern, Zetasizer Nano).

7.5.12 Synthesis of Biosimilar Mucus

Carbopol (0.9 g, 0.9 w/v%) was dissolved in HEPES buffer solution (9 mL) using magnetic stirring. A lipid mixture of phosphatidylcholine (0.018 g, 0.18 % w/v), cholesterol (0.0036 g, 0.36 w/v%), polysorbate 80 (0.033 g, 4:1 ratio) and buffer solution (1 mL) was prepared and added to the carbopol solution once ~ 90 % of the carbopol had dissolved. Mucin from porcine stomach (0.5000 g, 5 w/v%) was added to the solution and the pH altered to 7.4 with the addition of NaOH (1 M), this was monitored using a pH probe. BSA (0.3100 g, 3.1 w/v%) was added and the pH once again adjusted to 7.4 with the addition of NaOH (1 M). Biosimilar mucus was stored overnight at 2 – 4 ^{o}C before use, with a four day storage life from day of preparation.

7.5.13 Quantification of Mucoadhesion by Flow-through Model

Biosimilar mucus (1 mL) was placed into the chamber of Kirkstall QV500 weighed and sealed. A set volume of emulsion (1 mL) was flowed over the mucus twice at a rate of 1 mL/min and free emulsion that did not adhere to the mucus was recovered into a pre-weighed outlet chamber. Quantification of mucoadhesion was determined gravimetrically by the amount of emulsion collected post-flow. The other components of the flow through model were also weighed to mitigate any error.

7.5.14 Preparation of Fluorescent Nanoemulsions

Nanoemulsions were generated using the solvent evaporation technique, with aqueous polymer solutions of branched copolymers at a 5 wt % concentration. The oil phase is a mixture of two miscible oils, one a volatile solvent and one a non-volatile oil. As the volatile solvent evaporates, the non-volatile section of the oil droplet shrinks to the nanoscale. The oil phase is composed of ethyl acetate: castor oil in a ratio of 99:1. The oil: water ratio was 1:1, with the water phase being aqueous polymer solution at 5 wt%. Lumogen F red 305 was encapsulated at a concentration (0.1 wt %) with respect to the oil phase. Emulsions formulated *via* homogenisation using an over-head shear homogeniser (IKA T 25 ULTRA-TURRAX) for 2 minutes at 24,000 rpm. Emulsions

were left overnight until all ethyl acetate is removed (monitored gravimetrically) and analysis performed using DLS.

7.5.15 *Ex vivo* Study of Mucoadhesive Nanoemulsions

For multiple particle tracking (MPT) studies mucus from fresh porcine intestinal ileum (2 m in length) was obtained from a local abattoir and stored in ice-cold oxygenated phosphate buffered saline (PBS) prior to sample processing. The ileum was processed into 25 cm lengths, incised longitudinally to allow for waste to be gently rinsed away using ice-cold PBS. The mucus was harvested by gentle scraping, to increase the yield of the loose mucus layer but also include a high content of the adhered layer. Mucus was divided into aliquots (0.5 g) and stored at -20 ^{o}C until required for use. Fluorescently labelled nanoemulsions were inoculated into a sample of mucus (0.5 g) at a concentration confirmed not to cause particle aggregation (0.001 %). Samples were then incubated for 2 hours at 37 ^{o}C before particle tracking, to ensure good particle distribution following incubation. Video capture used 2-dimensional imaging (Lecia DM IRB wide-field epi-fluorescence microscope, x63 magnification oil immersion lens) using a high speed camera (Allied Vision Technologies, UK), at a frame rate of 33 ms (30 frames/s), where each video contained 300 frames. For each sample of mucus, approx. 120 individual particles were tracked for each nanoemulsion, n = 3, therefore, 360 particles were tracked over 3 separate mucus samples. Videos were processed using Fiji ImageJ plugin mosaic to track individual droplet trajectories through mucus. Each 10 second video was cut down to a 30 frame video (1 second) where any individually tracked particle must be continuously in the X-Y plane throughout all 30 frames. Individual particle trajectories were converted into numeric pixel data using Mosaic Particle Tracker plugin within Fiji ImageJ, which based on microscope and video capture settings metric distance was able to be determined.

7.5.16 Preparation of Fluorescent Nanoemulsions

Nanoemulsions were generated using the solvent evaporation technique, with aqueous polymer solutions of branched copolymers at a 5 wt % concentration. The oil phase is a mixture of two miscible oils, one a volatile solvent and one a non-volatile oil. As the volatile solvent evaporates, the non-volatile section of the oil droplet shrinks to the nanoscale. The oil phase is composed of ethyl acetate: castor oil in a ratio of 99:1. The

oil: water ratio was 1:1, with the water phase being aqueous polymer solution at 5 wt%. Tritiated oil blue A was encapsulated at a concentration (0.1 wt %) with respect to the oil phase. Emulsions formulated *via* homogenisation using an over-head shear homogeniser (IKA T 25 ULTRA-TURRAX) for 2 minutes at 24,000 rpm. Emulsions were left overnight until all ethyl acetate is removed (monitored gravimetrically) and analysis performed using DLS.

7.5.17 Release of Hydrophobic Dyes from Nanoemulsions

Dialysis through a 3.5 kDa molecular weight cut off membrane was conducted with distilled water (100 mL) at 37 °C as the reservoir. Release was monitored for 24 hrs with 1 mL sampled at t = 0.5 hrs and 1 hr, then subsequent 1 hr time points for 8 hrs and a final 24 h timepoint. After each time point, the reservoir was replaced to ensure sink conditions remained constant throughout the experiment. Quantification of dye released was calculated from liquid scintillation counting (LSC) radiation released.

LSC of a reservoir sample (1 mL) plus liquid scintillation cocktail (20 mL) provided disintegrations per minute (DPM) which is a measure of the source of radioactivity. DPM is then converted to mass of dye by the following equations:

$$\text{DPM} / 2.22 \times 10^6 = \text{Radioactivity (µCi)} \qquad (1)$$

$$\text{Radioactivity (µCi)} / \text{Specific Activity (µCi/mg)} = \text{Mass of dye within the 1 mL sample (mg)} \qquad (2)$$

$$\text{Mass of dye within the 1 mL sample (mg)} \times 100 = \text{Mass of dye within the 100 mL reservoir (mg)} \qquad (3)$$

7.6 CHAPTER 5

Radiochemical analysis was again conducted in the Radiomaterials Laboratory within the University of Liverpool and experimentation done by Dr Helen Cauldbeck. *In vivo* testing was conducted in collaboration with the Department of Pharmacology in the Materials Innovation Factory, University of Liverpool by Dr Lee Tatham.

7.6.1 Preparation of Macroemulsions with Encapsulated Drugs for Biological Evaluation

Aqueous polymer solutions were prepared at 5 mg/mL of branched amphiphilic polymer for the water phase of the emulsion. Emulsions were prepared at a 1:1 v:v ratio of oil:water, where the oil phase was squalene. Amphotericin B and cyclosporin A were loaded in the oil phase at the clinical topical dose concentration, 0.15 w/v% and 0.05 w/v% respectively. Emulsions were generated *via* over-head shear homogenisation (IKA T 25 ULTRA-TURRAX) for 2 minutes at 24,000 rpm. Emulsions were left over night to equilibrate before characterisation of droplet size using light scattering was conducted using a Malvern Mastersizer 2000.

7.6.2 Preparation of Nanoemulsions with Encapsulated Drugs for Biological Evaluation

Nanoemulsions were formulated using the solvent evaporation technique, with aqueous polymer solutions of branched copolymers at a 5 wt % concentration. The oil phase is a mixture of two miscible oils, one a volatile solvent and one a non-volatile oil. As the volatile solvent evaporates, the non-volatile section of the oil droplet shrinks to the nanoscale. The oil phase is composed of ethyl acetate: castor oil in a ratio of 99:1. Amphotericin B and Cyclosporin A were loaded into the oil phase at the clinical topical dose concentration, 0.15 w/v % and 0.05 w/v % respectively. Emulsions were generated using an over-head shear homogeniser (IKA T 25 ULTRA-TURRAX) for 2 minutes at 24,000 rpm. Emulsions were left overnight until all ethyl acetate is removed (monitored gravimetrically) and analysis performed using DLS.

7.6.3 Preparation of Nanoemulsions for *In Vivo* Testing

Nanoemulsions were formulated using the solvent evaporation technique, with aqueous polymer solutions of branched copolymers at a 5 wt % concentration. The oil phase is a mixture of two miscible oils, one a volatile solvent and one a non-volatile oil. As the volatile solvent evaporates, the non-volatile section of the oil droplet shrinks to the nanoscale. The oil phase is composed of ethyl acetate:castor oil in a ratio of 99:1. FTC-prodrug was incorporated into the nanoemulsions at a concentration of 4.85 mg/mL to yield final concentration of 5 mg/kg for each rat. Emulsions were generated using an over-head shear homogeniser (IKA T 25 ULTRA-TURRAX) for

2 minutes at 24,000 rpm. Emulsions were left overnight until all ethyl acetate is removed, monitored gravimetrically and analysis performed using DLS.

7.6.4 Release Study of CsA from Nanoemulsion

Tritiated CsA (33.7 µCi, specific activity 54 µCi/mg), CsA (0.625 mg, 0.52 µmol) and castor oil (12.5 µL) were added to a 20 mL vial and solubilised in ethyl acetate (1.824 mL) at ambient temperature overnight. DBiB-*p(*$OEGMA_{50}$-*co*-$EGDMA_{0.8}$) was used as the polymeric surfactant 5 wt % in aqueous phase. The emulsion was formulated *via* homogenisation (24000 rpm, 2 minutes) followed by evaporation of volatile oil phase (ethyl acetate) and monitored gravimetrically. DLS measurements were taken to ensure incorporation of tritium did not affect droplets.

Dialysis through a 3.5 kDa molecular weight cut off membrane was conducted with distilled water (100 mL) at 37 °C as the reservoir. Release was monitored with 1 mL sampled at t = 0.5 hrs and 1 hr, then subsequent 1 hr time points for 8 hrs, a 24 hr and 144 hr were taken and finally another 8 hour time period was tested between 172 – 180h hrs. After each time point, the reservoir was replaced to ensure sink conditions remained constant throughout the experiment. Quantification of dye released was calculated from liquid scintillation counting (LSC) radiation released (same as Section 7.5.16).

7.6.5 *In Vivo* Testing

FTC was dosed to male wistar rats at 5 mg/kg. The three samples tested for this study were:

- Conventional FTC (water diluent) n=4
- Non-mucoadhesive emulsion, FTC-prodrug loaded (water diluent) n=4
- Mucoadhesive emulsion, FTC-prodrug loaded (water diluent) n=4

Following habituation (7-days) where food and water were provided ad libitum, the rats received the single dose of either FTC or the FTC-prodrug emulsion (5 mg/Kg FTC) *via* oral gavage. Blood samples were collected (~230 µl) at 0.5, 1, 2, 4, 6, 8 h post dosing from the tail vein (~1.4 ml total blood volume). Bioanalysis of the blood samples was performed by measurement of FTC parent drug by liquid chromatography followed by combination of two mass spectrometry analysers (LC-MS/MS). At the 24 h time point, the rats was sacrificed using cardiac puncture under terminal anaesthesia (AC).

7.7 CELL CULTURE

In vitro testing of nanoemulsions for ophthalmic treatment was conducted in collaboration with Prof. Rachel Williams in the Department of Eye and Vision Science at the University of Liverpool.

All cell culture was carried out under strictly aseptic conditions in a class II laminar flow biological safety cabinet. All cells were incubated at 37 ^{o}C with 5 % CO_2 atmosphere.

7.7.1 Cell Source

Human Conjunctival Cells, HCjE-Gi and Human Corneal Epithelium cells, HCE-T were used throughout. HCE-T cells were donated by Kaura Araki-Sasaki from JCHO Hohigaoka Medical Centre and obtained from in house frozen stocks for experimentation. HCjE-Gi are a human immortalised cell line which were donated by Gibson laboratory at Havard Medical School to the University of Liverpool and obtained from in house frozen stocks for the experiments described.

7.7.2 Media Preparation

The solutions used for media preparation throughout cell culture for this project are summarised in Table 7.1 for HCE-T cells and Table 7.2 for HCjE-Gi cells.

Table 7.1 Solutions used to prepare culture media for HCE-T cells.

Name	Abbreviation	Company	Catalogue Number
Dublecco's Modified Eagle Medium/Ham's Nutrient Mixture F-12 Formulation	DMEM/F12	Sigma Aldrich	D6421
Foetal Calf Serum	FCS	BioSera	S1900

Cells were cultured in a mixture of DMEM/F12 containing 10 % FCS.

Table 7.2 Solutions used to prepare culture media for HCjE-Gi cells.

Name	Abbreviation	Company	Catalogue Number
Keratinocyte Serum Free Media	KFSM	Sigma Aldrich	133-500
Calcium Chloride	$CaCl_2$	Sigma Aldrich	C5670
Bovine Pituitary Extract	BPE	Sigma Aldrich	P1476
Epidermal Growth Factor	EGF	Sigma Aldrich	E4127

7.7.3 Cell Retrieval

HCjE-Gi and HCE-T cells were stored in 1mL cryovials under liquid nitrogen in complete culture media with 10 % DMSO. To retrieve cells, cryovials were warmed in a water bath at 37 ^{o}C then emptied into a 30 mL universal, with 15 mL pre-warmed media. This was split evenly into 3 T75 flasks with an additional 7 mL of media added. Cells were then incubated in a microplasma free incubator at 37 ^{o}C under 5 % CO_2.

7.7.4 Cell Culture Maintenance

HCjE-Gi and HCE-t cell flasks were fed every other day, removing 7 mL of old media and replacing with 8 mL of fresh pre-warmed media. Cells were examined using light microscopy to check for any abnormalities or preliminary infections. For these studies, cells were used between passages 4 – 22 for HCjE-Gi and 15 – 37 for HCE-T.

Both cell lines were split when the flasks reached >80 % confluence, this was checked *via* an optical microscope. T75 flasks were split by removing 10 mL of media, rinsing with 5 mL PBS solution and adding 5 mL Trypsin/PBS (1:10) solution to flask. The flask was incubated at 37 ^{o}C for 5 minutes, with the lifting of cells monitored *via* optical light microscopy. Cells that were rounded but still attached were removed by gently agitation of the flask. Media (5 mL) was added to inactivate and neutralise the trypsin reaction. For HCjE-Gi cells cultured in serum free media, HCE-T culture media was used to neutralise trypsin. For subculture 2.5 mL of the HCE-T cell suspension was placed into a fresh flask with 9 mL fresh culture media, for HCjE-Gi

cells culture media was removed gently to assure no disturbance of the pellet and re-suspended with KSFM. To seed samples for experiments, the cell suspension was pipetted into a centrifuge tube and centrifuged at 1200 rpm for 4 minutes. The supernatant was removed and the cell pellet re-suspended in culture media (1 mL). A haemocytometer was prepared by cleaning all surfaces with 70 % ethanol and dried before the coverslip was centred. 20 µL of cell suspension was pipetted onto the top edge of the coverslip to allow the cells to enter the counting chamber. After cells were counted calculations were made to determine the volumes needed to obtain the desired seeding density for experimental procedures.

7.7.5 Cellular Assays

Multiple assays were carried out on HCE-T and HCjE-Gi cells to study cytotoxicity and effects of different drug concentrations of cells. 15,000 cells/well were seeded into a 48 well tissue culture plate and left for 7 days to adhere to the plate and produce a cell monolayer. The cells were nourished twice a week by replacing 150 µL of old media with 150 µL of fresh culture media. After this the media was removed and replaced with either unloaded nanoemulsion in media or drug loaded nanoemulsion in media.

7.7.6 Resazurin Assay

Resazurin was dissolved in PBS at 0.1 mg/mL and filtered to sterilise, this was stored at 4 °C in the dark. Stock resazurin solution (10 µL per 100 µL media) was added to wells of the assay apart from control wells, plates were incubated at 37 ^{o}C for 4 hours. Media was removed and put in black 96-well plastic plates; resorufin fluorescence was read using a Biotek FLx800 spetrofluorometer (λExcitation = 530 nm; λEmission = 590 nm). All values were normalised to control wells on each plate which contained culture medium from cells.

7.7.7 Phalloidin Staining

In a 48 well tissue culture plate, cells were seeded at 15,000 cells/well then the same protocol as in Section 7.7.6 was followed. After incubation the media was discarded and the cells washed with PBS (500 µL) then fixed for 10 minutes in 10 % neutral buffered formalin (NBF; 10 % formalin, approximately 4 % formaldehyde). NBF was discarded and the cells washed again with PBS. A phalloidin solution was used to

stain the F-actin of the cytoskeleton of the cell. A phalloidin solution was produced at 1 mg powder in 1.5 mL MeOH according to manufacturer's instruction. The solution was then diluted 1 in 100 (in fresh PBS) and 75 µL was placed in each well followed by 30 minutes of incubation at 4 °C. Phalloidin solution was removed and the cells washed with PBS.

4′,6-Diamidino-2-phenylindole dihydrochloride (DAPI, purchased from Invitrogen) was used to stain the nuclei of the cell. A stock solution of DAPI was made at 1:1,000 with PBS, then further diluted to a working solution of 1:10 PBS, 75 µL was placed in each well and incubated for 10 minutes at 4 °C. Cells were washed with PBS and placed under 500 µL PBS.

7.7.8 Zone of Inhibition Study

Preparation of the *C. albicans* culture was done as followed: *C. albicans* strain SC5314 was revived from -80 °C storage on potato dextrose-agar (PD-agar; Formedium Ltd., Norfolk, England) and streak plates incubated at 37 °C overnight. *C. albicans* was sub-cultured by inoculating a PD-agar streak plate with one colony taken from a previous PD-agar plate and incubated overnight at 37 °C. Colonies were maintained on PD-agar stored at 5 °C. Broth cultures were initiated by inoculating PD media (10 cm^3) with one colony of *C. albicans* taken from a PD-agar plate. Cultures were incubated overnight at 37 °C with constant agitation at 100 RPM. These were sub-cultured by taking an aliquot of *C. albicans* broth culture (0.5 cm^3) and diluted in sterile PD broth (10 cm^3). An initial OD_{600} measured between 0.1 - 0.2 and was monitored until an OD_{600} 0.5-0.6 was obtained. This was the working stock dilution of *C. albicans* for the following experiments.

An aliquot (20 mm^3) of each sample was pipetted carefully to minimise spreading on to potato dextrose agar plates. Samples were spaced to avoid cross-contamination and agar plates left at room temperature for 20 minutes to allow the samples to dry. An aliquot of *C. albicans* stock solution (1 cm^3) was pipetted onto the centre of each agar plate. A glass spreader sterilised with ethanol and following aseptic technique was used to uniformly spread the culture broth around the agar plate. The plate was again allowed to dry for 30 minutes before turning the plates upside down and placing in an incubator at 37 °C for 24 h. The samples were then checked for a zone of inhibition and measurements taken of the diameter of each zone if applicable.

APPENDIX

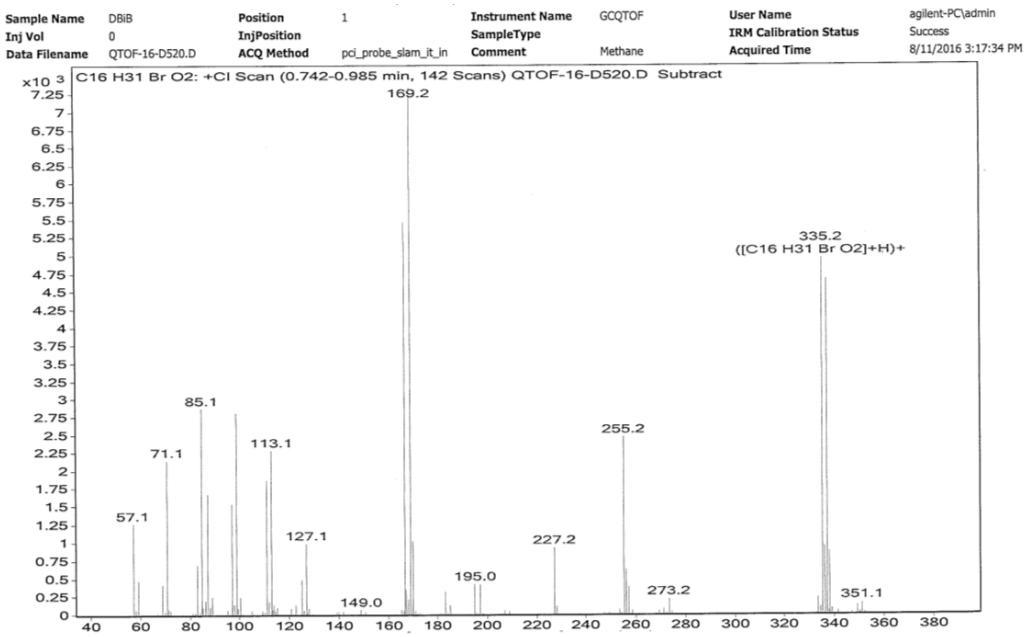

A1 Mass spectrum (CI-MS) of DBiB.

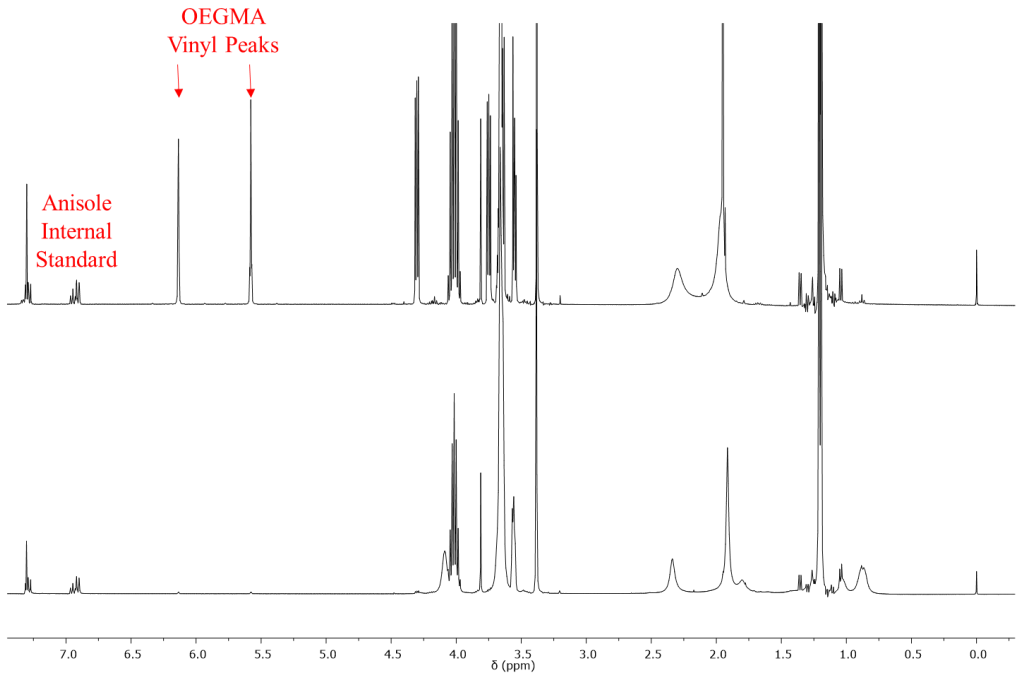

A2 ^{1}H NMR ($CDCl_3$, 400 MHz) of DBiB-*p*($OEGMA_{50}$-*co*-$EGDMA_{0.8}$) at t = 0 and t = 24. Percentage conversion determined by ratio of OEGMA vinyl peaks to internal standard (anisole).

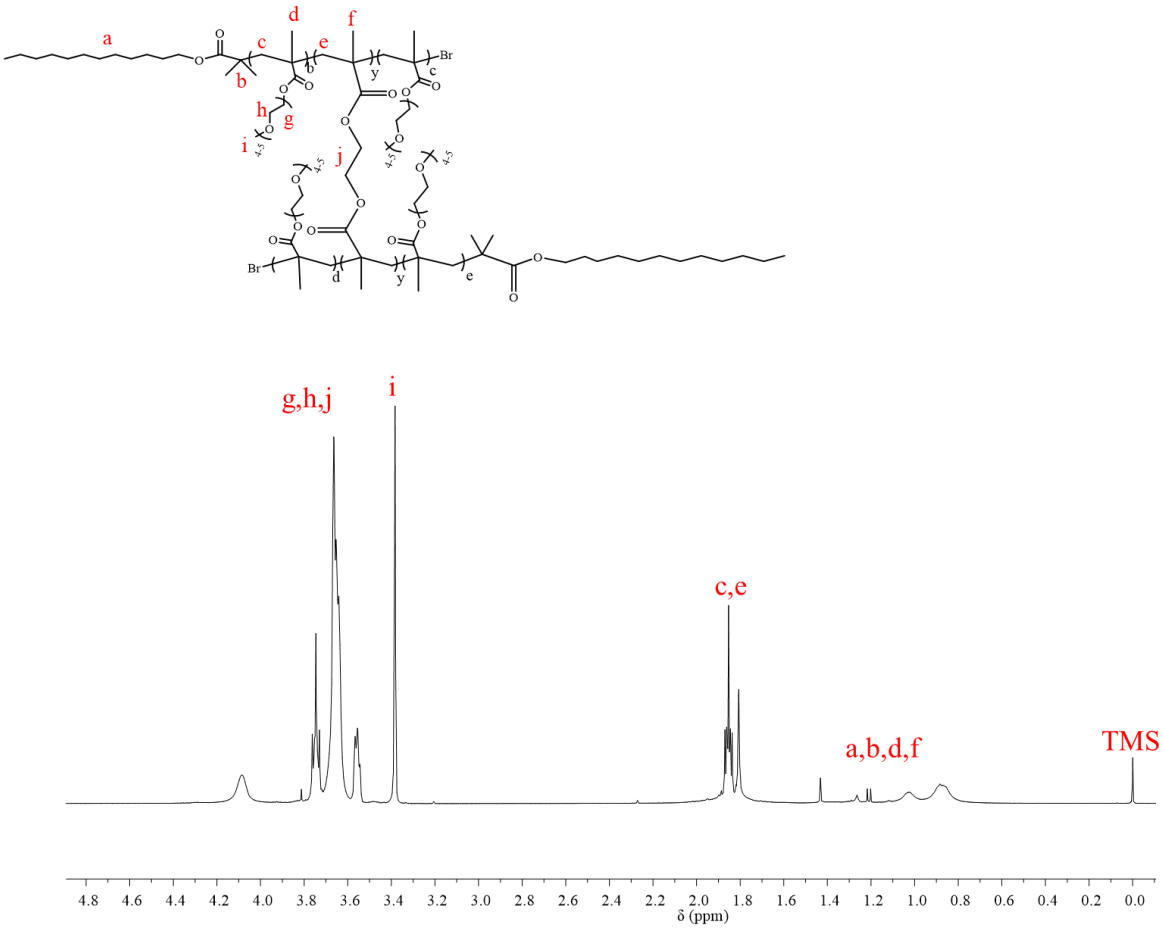

A3 ^{1}H NMR ($CDCl_3$, 400 MHz) of purified DBiB-*p*($OEGMA_{50}$-*co*-$EGDMA_{0.8}$).

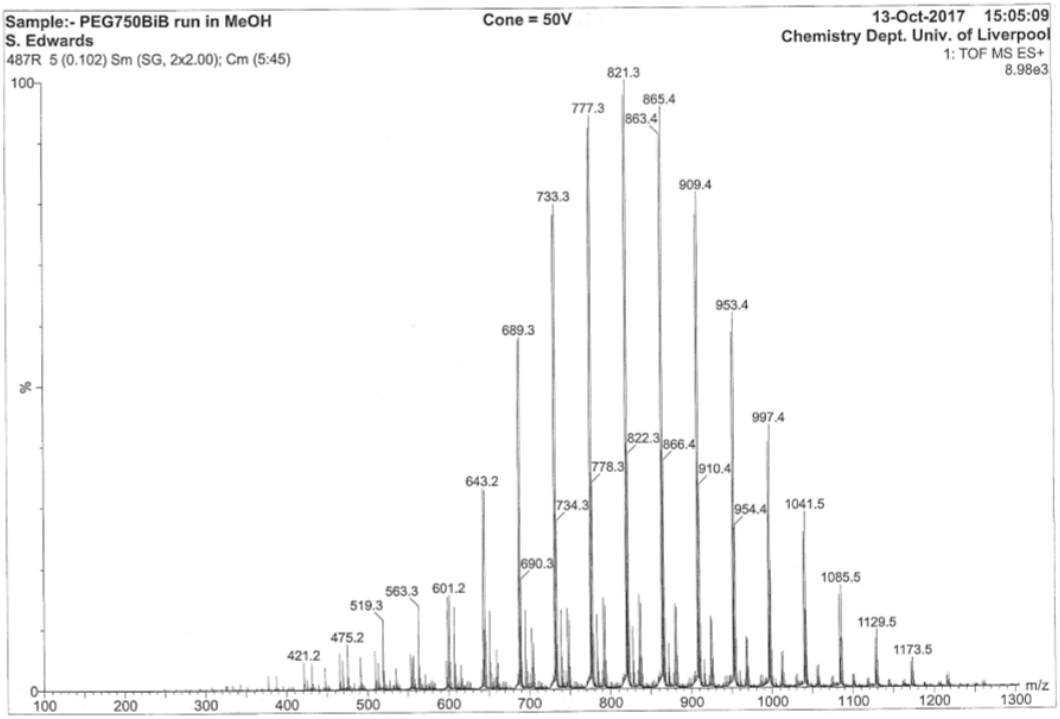

A4 Mass spectrum (ES-MS) of PBiB.

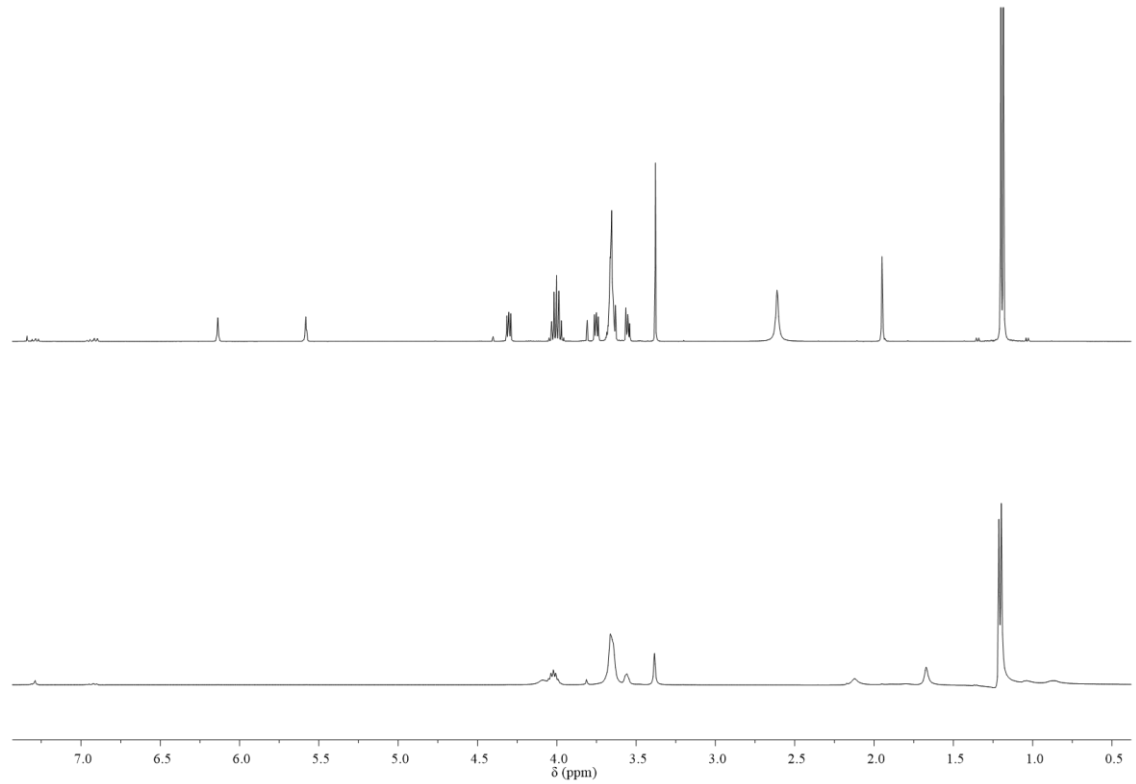

A5 ^{1}H NMR ($CDCl_3$, 400 MHz) of $DBiB_xPBiB_y$-*p*($OEGMA_{50}$-*co*-$EGDMA_{0.8}$) at t = 0 and t = 24. Percentage conversion determined by ratio of OEGMA vinyl peaks to internal standard (anisole).

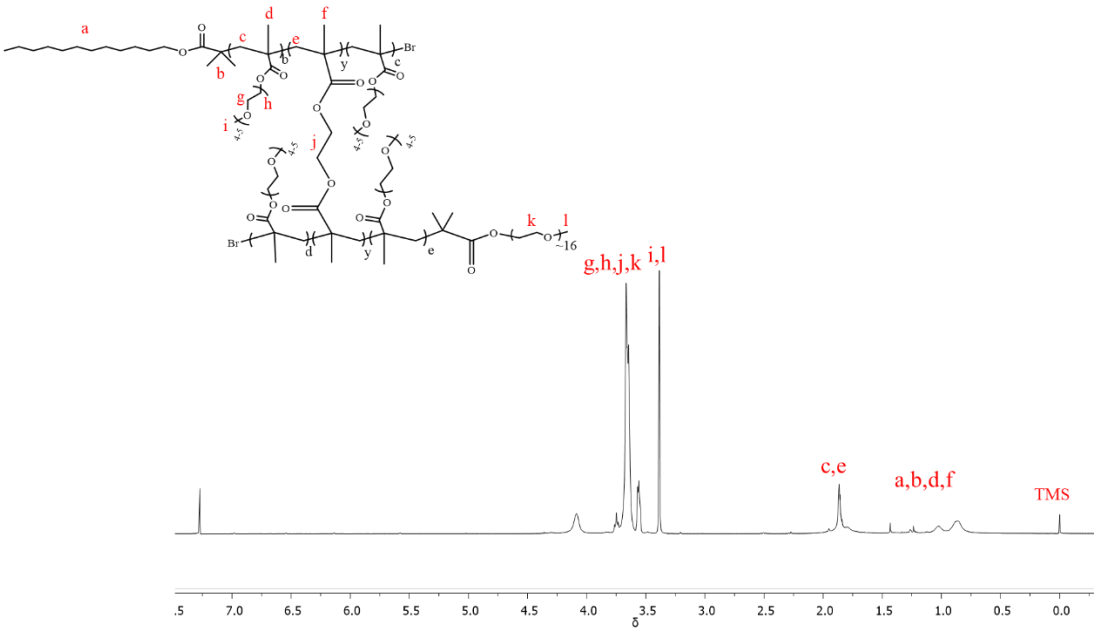

A3 ^{1}H NMR ($CDCl_3$, 400 MHz) of purified $DBiB_{0.50}PBiB_{0.50}$-*p*($OEGMA_{50}$-*co*-$EGDMA_{0.8}$).

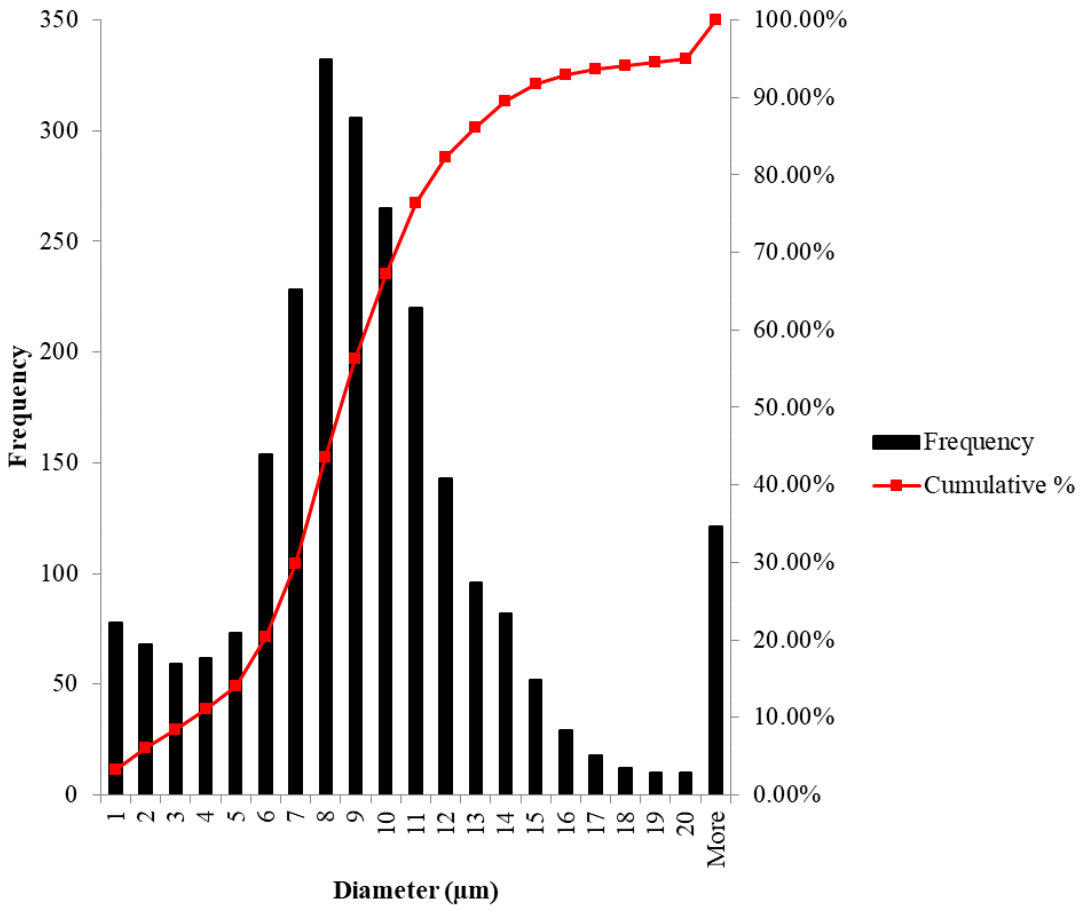

A6 Frequency distribution of $DBiB_{0.75}PBiB_{0.25}$-*p*($OEGMA_{50}$-*co*-$EGDMA_{0.8}$) stabilised squalene macroemulsion.

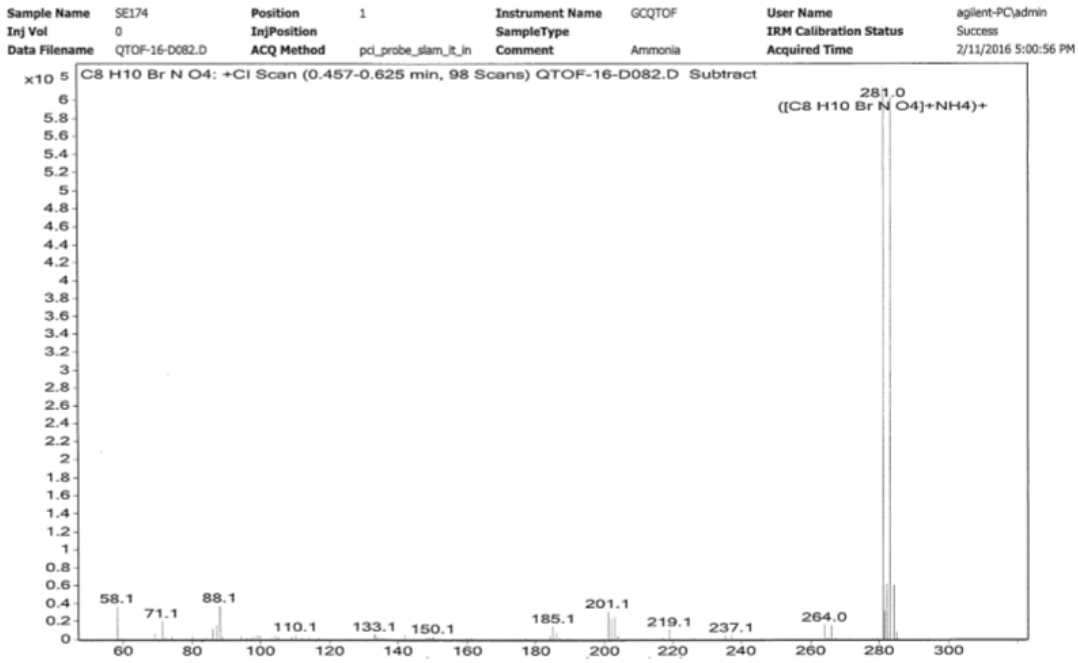

A7 CI-MS of XanCOOH

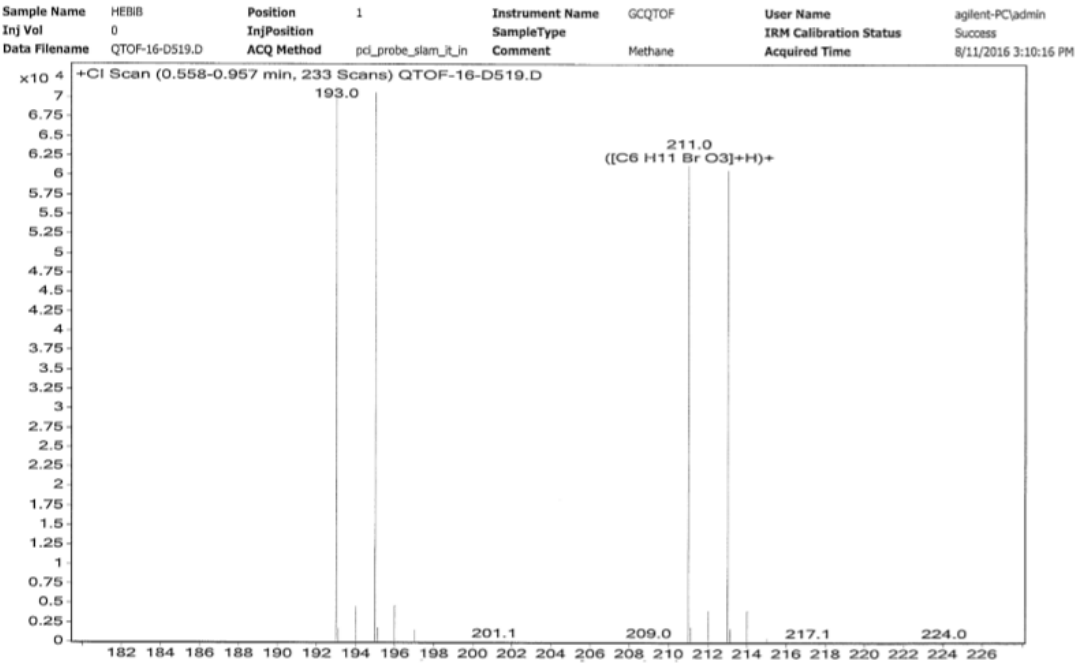

A8 CI-MS of HEBiB

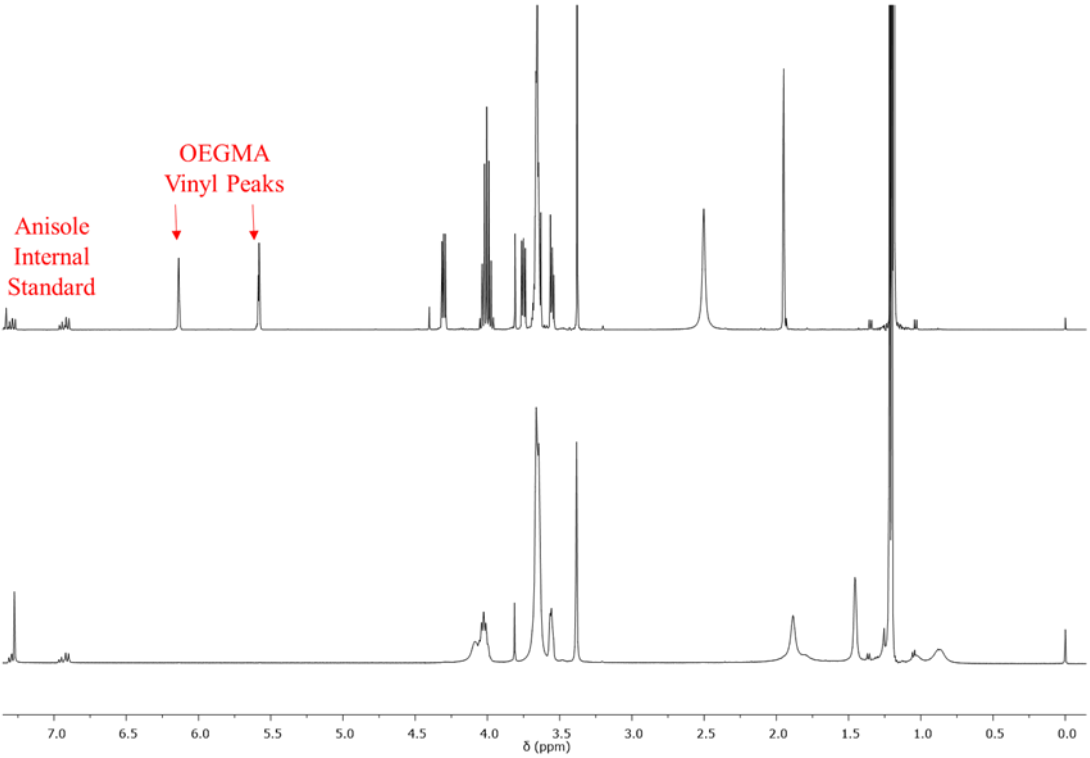

A9 ^{1}H NMR ($CDCl_3$, 400 MHz) of XanBiB-*p*($OEGMA_{50}$-*co*-$EGDMA_{0.8}$) at t = 0 and t = 24. Percentage conversion determined by ratio of OEGMA vinyl peaks to internal standard (anisole).

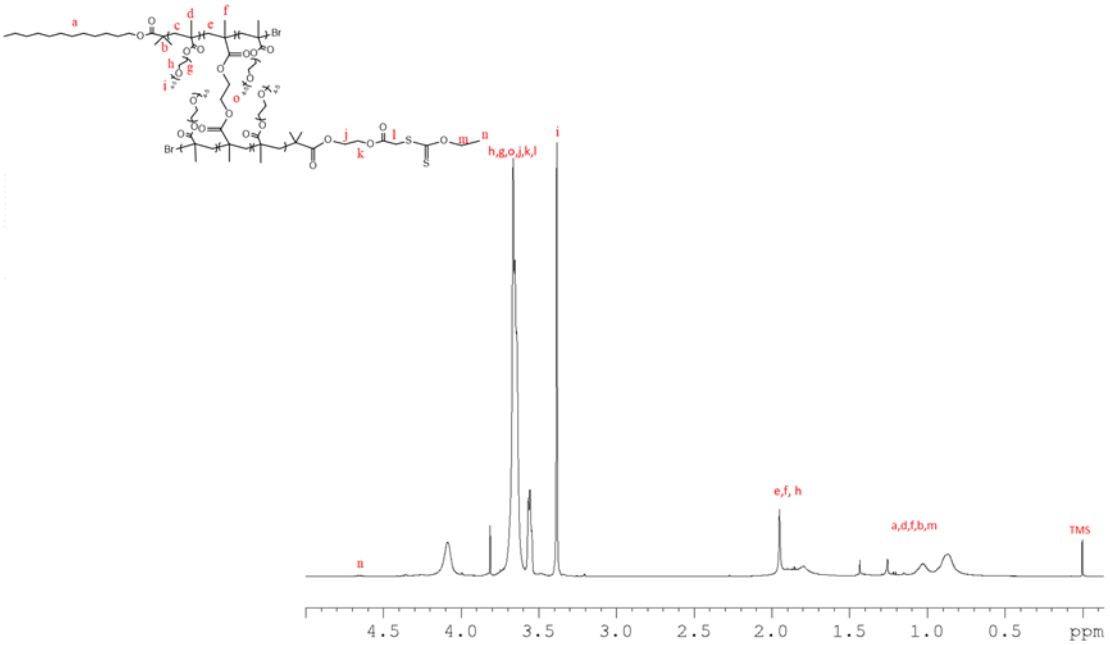

A10 ^{1}H NMR ($CDCl_3$, 400 MHz) of purified $DBiB_{0.50}XanBiB_{0.50}$-*p*($OEGMA_{50}$-*co*-$EGDMA_{0.8}$).

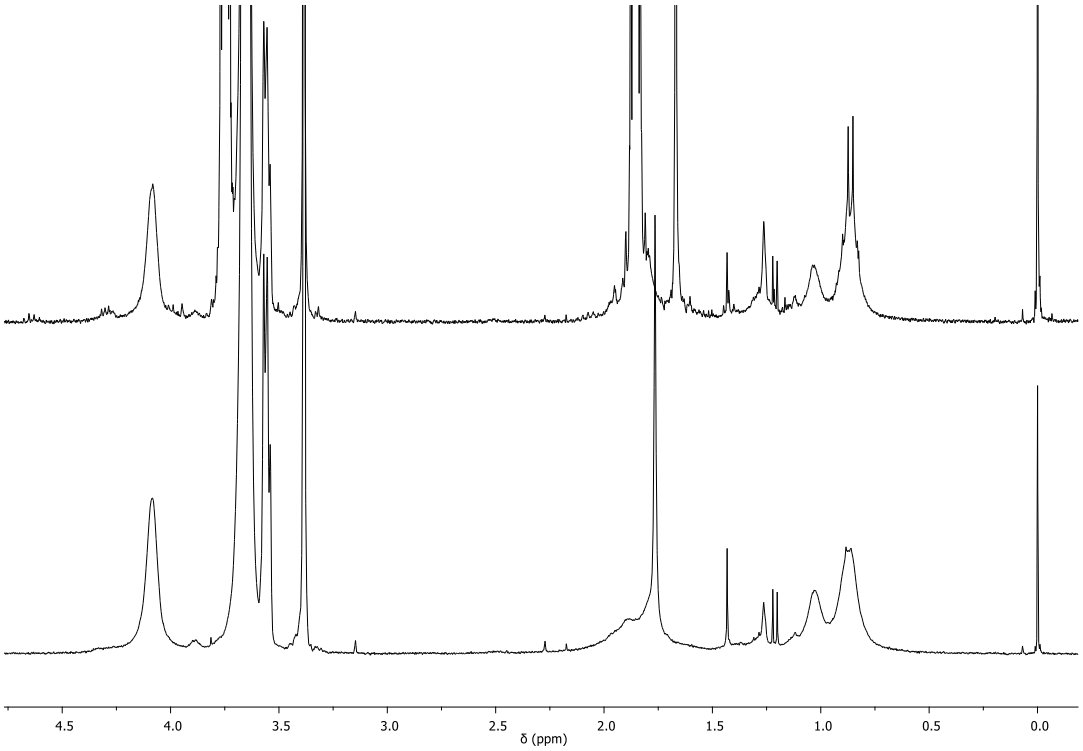

A11 Typical deprotection of XanBiB$_{0.90}$DBiB$_{0.08}$-*p*(OEGMA$_{50}$-*co*-EGMDA$_{0.8}$) to yield SH$_{0.90}$DBiB$_{0.08}$-*p*(OEGMA$_{50}$-*co*-EGDMA$_{0.8}$) in the presence of n-butylamine after reaction for 1.5 hrs.

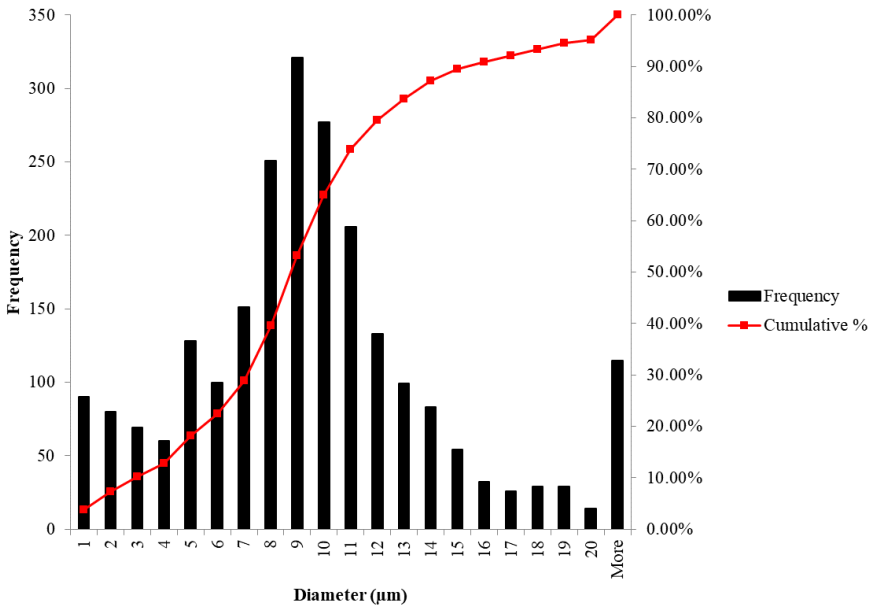

A12 Frequency distribution of SH$_{0.90}$DBiB$_{0.10}$-*p*(OEGMA$_{50}$-*co*-EGDMA$_{0.8}$) stabilised squalene macroemulsion.

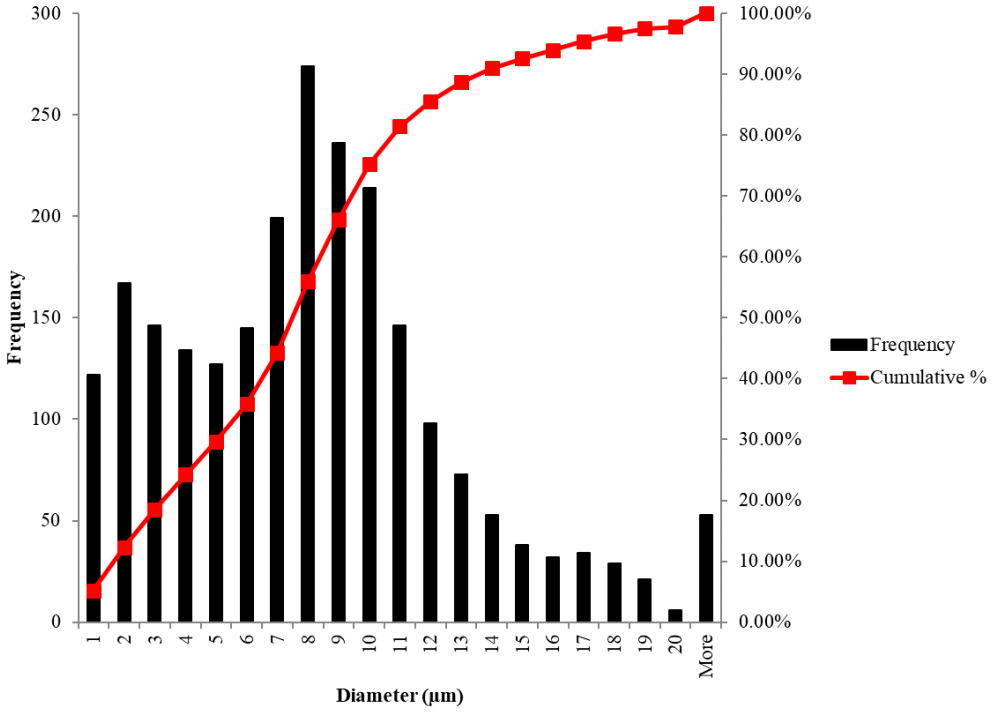

A13 Frequency distribution of $SH_{0.50}DBiB_{0.50}$-*p*($OEGMA_{50}$-*co*-$EGDMA_{0.8}$) stabilised squalene macroemulsion.

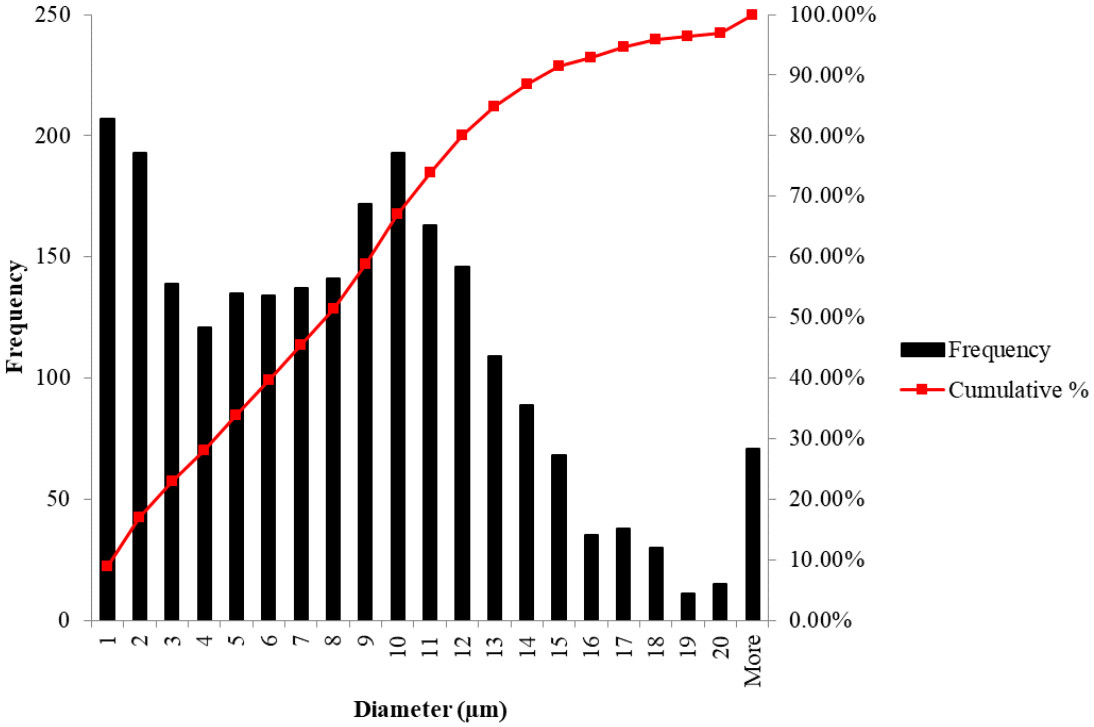

A14 Frequency distribution of $SH_{0.10}DBiB_{0.90}$-*p*($OEGMA_{50}$-*co*-$EGDMA_{0.8}$) stabilised squalene macroemulsion.

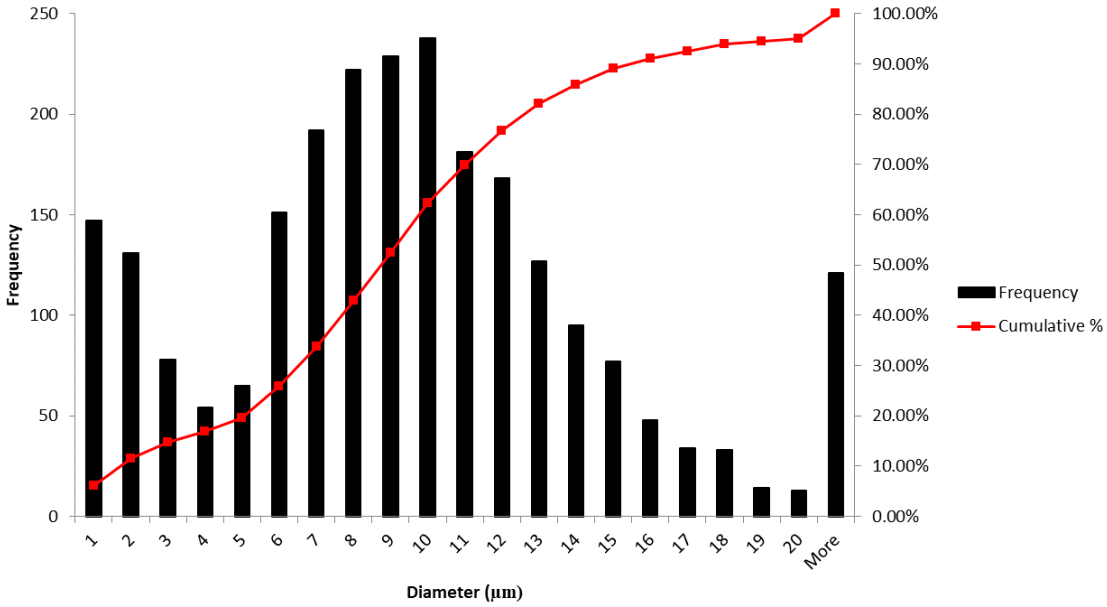

A15 Frequency distribution of $SH_{0.75}DBiB_{0.25}$-*p*($OEGMA_{50}$-*co*-$EGDMA_{0.8}$) stabilised squalene macroemulsion.

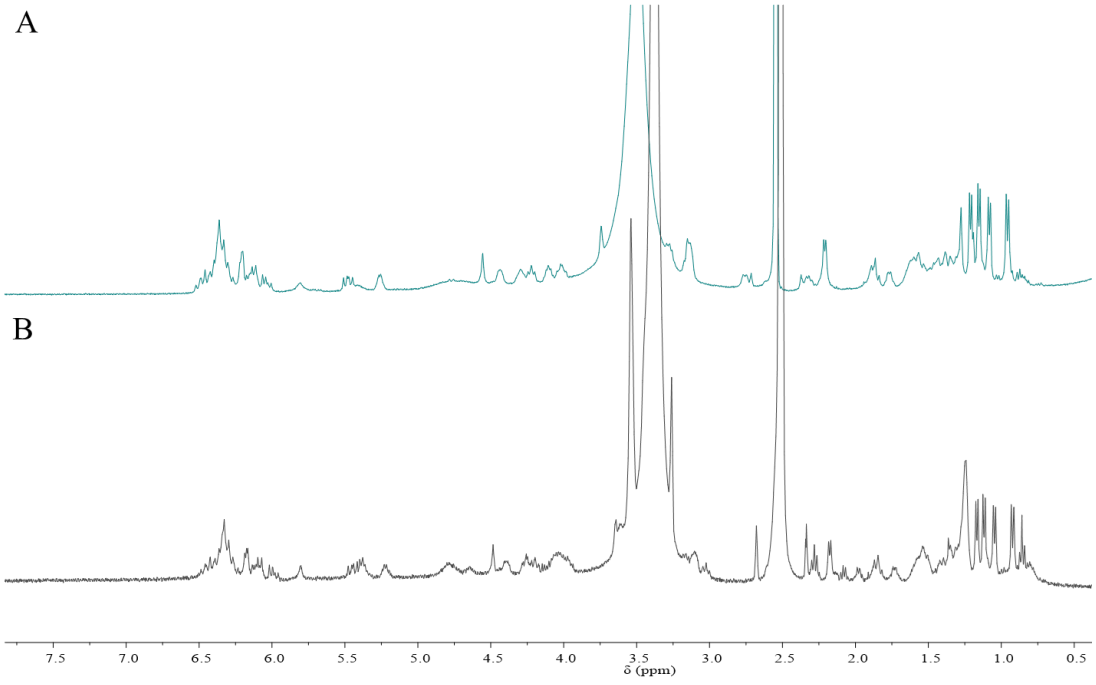

A16 ^{1}H NMR (DMSO, 400 MHz) of A) Pure Amp B and B) Amp B pellet after centrifugation of sedimented free drug.

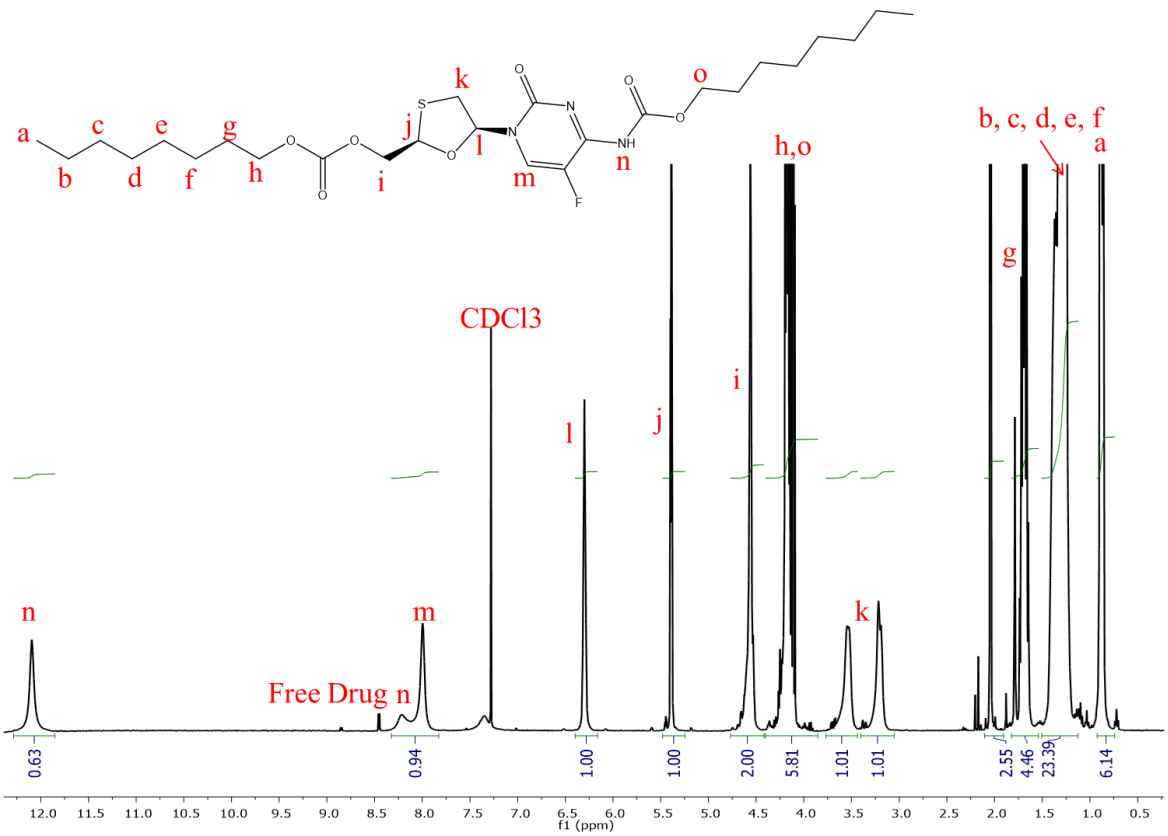

A17 ^{1}H NMR (DMSO, 400 MHz) of FTC-prodrug.

Table A1 DLS analysis of tailored nanoemulsion droplets by varying the ratio of volatile:non-volatile oil, with $SH_{0.75}DBiB_{0.25}$-*p*($OEGMA_{50}$-*co*-$EGDMA_{0.8}$) as polymeric surfactant.

Polymer	EtOAc:cast or oil	D_z (nm)	D_n (nm)	PdI
$SH_{0.75}DBiB_{0.25}$-*p*($OEGMA_{50}$-*co*-$EGDMA_{0.8}$)	50:50	1370	1220	0.11
	60:40	960	870	0.14
	70:30	706	670	0.02
	80:20	620	580	0.18
	90:10	530	480	0.12
	99:1	280	270	0.13

REFERENCES

1 C. Atuma, V. Strugala, A Allen and L. Holm, *Am. J. Physiol. Gastrointest. Liver Physiol.*, 2001, **280**, G922-9.

2 B. M. Boddupalli, Z. N. Mohammed, R. A. Nath and D. Banji, *J. Adv. Pharm. Technol. Res.*, 2010, **1**, 381–387.

3 J. H. Rothchild, Allergies & Your Gut, http://allergiesandyourgut.com/tag/intestinal-epithelium/, (accessed 26 September 2018).

4 M. E. V. Johansson, H. Sjövall and G. C. Hansson, *Nat. Rev. Gastroenterol. Hepatol.*, 2013, **10**, 352–361.

5 M. E. V. Johansson, J. M. H. Larsson and G. C. Hansson, *Proc. Natl. Acad. Sci.*, 2011, **108**, 4659–4665.

6 V. V. Khutoryanskiy, *Adv. Drug Deliv. Rev.*, 2018, **124**, 140–149.

7 S. K. Lai, Y. Y. Wang and J. Hanes, *Adv. Drug Deliv. Rev.*, 2009, **61**, 158–171.

8 L. M. Ensign, R. Cone and J. Hanes, *Adv. Drug Deliv. Rev.*, 2012, **64**, 557–570.

9 P. E. King-Smith, B. A. Fink, R. M. Hill, K. W. Koelling and J. M. Tiffany, *Curr. Eye Res.*, 2004, **29**, 357–368.

10 F. J. Holly and M. A. Lemp, *Surv. Ophthalmol.*, 1977, **22**, 69–87.

11 J. I. Prydal, P. Arral, H. Woon, F. W. Campbell and J. I. Prydal, *Invest. Ophthalmol. Vis. Sci.*, 1992, **33**, 2006–2011.

12 F. J. O. Varum, F. Veiga, J. S. Sousa and A. W. Basit, *J. Pharm. Pharmacol.*, 2012, **64**, 218–227.

13 C. Atuma, V. Strugala, a Allen and L. Holm, *Am. J. Physiol. Gastrointest. Liver Physiol.*, 2001, **280**, G922-9.

14 J. Perez-vilar and R. L. Hill, *Biochemistry*, 1999, **274**, 31751–31754.

15 Y. S. Kim and S. B. Ho, *Curr. Gastroenterol. Rep.*, 2010, **12**, 319–330.

16 S. Bafna, S. Kaur and S. K. Batra, *Oncogene*, 2010, **29**, 2893–2904.

17 T. Pelaseyed, J. H. Bergstrom, J. K. Gustafsson, A. Ermund, G. M. H. Birchenough, A. Schutte, S. van der Post, F. Svensson, A. M. Rodriguez-Pineiro, E. E. L. Nystrom, C. Wising, M. E. V Johansson and G. C. Hansson, *Immunol. Rev.*, 2014, **260**, 8–20.

18 S. B. Ho, K. Takamura, R. Anway, L. L. Shekels, N. W. Toribara and H. Ota, *Dig. Dis. Sci.*, 2004, **49**, 1598–1606.

19 N. G. Karlsson, A. Herrmann, H. Karlsson, M. E. V Johansson, I. Carlstedt and G. C. Hansson, *J. Biol. Chem.*, 1997, **272**, 27025–27034.

20 J. M. Holmen Larsson, K. A. Thomsson, A. M. Rodriguez-Pineiro, H.

Karlsson and G. C. Hansson, *AJP Gastrointest. Liver Physiol.*, 2013, **305**, G357–G363.

21 B. J. Van Klinken, K. M. Tytgat, H. A. Buller, A. W. Einerhand and J. Dekker, *Biochem Soc Trans*, 1995, **23**, 814–818.

22 P. J. Puiman, M. Jensen, B. Stoll, I. B. Renes, A. C. J. M. de Bruijn, K. Dorst, H. Schierbeek, M. Schmidt, G. Boehm, D. G. Burrin, P. T. Sangild and J. B. van Goudoever, *J. Nutr.*, 2011, **141**, 1306–1311.

23 M. Boegh and H. M. Nielsen, *Basic Clin. Pharmacol. Toxicol.*, 2015, **116**, 179–186.

24 T. Inatomi, A. S. Tisdale, Q. Zhan, S. Spurr-Michaud and I. K. Gipson, *Biochem. Biophys. Res. Commun.*, 1997, **236**, 789–797.

25 M. Garcia-Diaz, D. Birch, F. Wan and H. M. Nielsen, *Advanced Drug Deliv. Rev.*, 2017, **124**, 107–124.

26 A. Allen, R. Pain and T. Robinson, *Nature*, 1976, **264**, 319–324.

27 P. Argueso and I. K. Gipson, *Exp. Eye Res.*, 2001, **73**, 281–289.

28 J. R. Gum, J. W. Hicks, N. W. Toribara, E. M. Rothe, R. E. Lagace and Y. S. Kim, *J. Biol. Chem.*, 1992, **267**, 21375–21383.

29 A. Allen, *Trends Biochem. Sci.*, 1983, **8**, 169–173.

30 S. J. Gendler and A. P. Spicer, *Annu. Rev. Physiol.*, 1995, **57**, 607–634.

31 B. S. Turner, K. R. Bhaskar, M. Hadzopoulou-Cladaras and J. T. Lamont, *Biochim. Biophys. Acta - Gene Struct. Expr.*, 1999, **1447**, 77–92.

32 M. P. Suárez, , DOI:10.1674/0003-0031-169.1.179.

33 S. L. Bell, G. Xu and J. F. Forstner, *Biochem. J.*, 2001, **357**, 203 LP-209.

34 R. Bansil and B. S. Turner, *Curr. Opin. Colloid Interface Sci.*, 2006, **11**, 164–170.

35 M. T. Cook and V. V. Khutoryanskiy, *Int. J. Pharm.*, 2015, **495**, 991–998.

36 S. K. Lai, D. E. OHanlon, S. Harrold, S. T. Man, Y.-Y. Wang, R. Cone and J. Hanes, *Proc. Natl. Acad. Sci.*, 2007, **104**, 1482–1487.

37 O. Lieleg, I. Vladescu and K. Ribbeck, *Biophys. J.*, 2010, **98**, 1782–1789.

38 S. S. Olmsted, J. L. Padgett, I. Yudin, K. J. Whaley, T. R. Moench and R. A. Cone, *Biophys. J.*, 2001, **81**, 1930–7.

39 M. Abdulkarim, N. Agulló, B. Cattoz, P. Griffiths, A. Bernkop-Schnürch, S. Gómez Borros and M. Gumbleton, *Eur. J. Pharm. Biopharm.*, 2015, **97**, 230–238.

40 B. H. Bakja, N. M. Rigby, K. L. Cross, A. Macierzanka and A. R. Mackie, *Colloids Surfaces B Biointerfaces*, 2015, **135**, 73–80.

41 A. N. Round, N. M. Rigby, A. Garcia De La Torre, A. MacIerzanka, E. N. C. Mills and A. R. MacKie, *Biomacromolecules*, 2012, **13**, 3253–3261.

42 S. K. Linden, P. Sutton, N. G. Karlsson, V. Korolik and M. A. McGuckin, *Mucosal Immunol.*, 2008, **1**, 183–197.

43 G. Mustata and S. M. Dinh, *Crit. Rev. Ther. Drug Carrier Syst.*, 2006, **23**, 111–135.

44 H. H. Sigurdsson, J. Kirch and C. M. Lehr, *Int. J. Pharm.*, 2013, **453**, 56–64.

45 A. MacAdam, *Adv. Drug Deliv. Rev.*, 1993, **11**, 201–220.

46 H. M. Yildiz, C. A. McKelvey, P. J. Marsac and R. L. Carrier, *J. Drug Target.*, 2015, **23**, 768–774.

47 A. Macierzanka, N. M. Rigby, A. P. Corfield, N. Wellner, F. Böttger, E. N. C. Mills and A. R. Mackie, *Soft Matter*, 2011, **7**, 8077.

48 K. Maisel, M. Reddy, Q. Xu, S. Chatoopadhyay, R. Cone, L. M. Ensign and J. Hanes, *Nanomedicine*, 2016, **11**, 1337–1343.

49 J. das Neves, M. Amiji and B. Sarmento, *Wiley Interdiscip. Rev. Nanomedicine Nanobiotechnology*, 2011, 3, 389–399.

50 K. Vermani and S. Garg, *Pharm. Sci. Technol. Today*, 2000, **3**, 359–364.

51 Adhesion, https://en.oxforddictionaries.com/definition/adhesion, (accessed 26 September 2018).

52 M. A. Longer and J. R. Robinson, *Pharm. Int.*, 1986, **7**, 114–117.

53 Y. Gurukul and K. Road, *Int. J. Pharma Bio Sci.*, 2010, **1**, 1–32.

54 S. N. K and A. Bhattacharya, *Int. J. Pharm. Clin. Res.*, 2009, **1**, 10–14.

55 J. D. Smart, *Adv. Drug Deliv. Rev.*, 2005, **57**, 1556–1568.

56 B. V. Derjaguin, Y. P. Toporov, V. M. Muller and I. N. Aleinikova, *J. Colloid Interface Sci.*, 1977, **58**, 528–533.

57 R. P. Campion, *J. Adhes.*, 1975, **7**, 1–23.

58 D. Kaelble and J. Moacanin, *Polymer (Guildf).*, 1977, **18**, 475–482.

59 J. R. R. J W Lee, J H Park, *J. Pharm. Sci.*, 2000, **89**, 850–866.

60 J. L. Chen and G. N. Cyr, *Adhes. Biol. Syst. Academic Press*, 1970, 163–181.

61 J. D. Smart, I. W. Kellaway and H. E. C. Worthington, *J. Pharm. Pharmacol.*, 1984, **36**, 295–299.

62 O. Ben-Zion and A. Nussinovitch, *Food Hydrocoll.*, 1997, **11**, 429–442.

63 A. Bernkop-Schnürch, V. Schwarz and S. Steininger, *Pharm. Res.*, 1999, 16, 876–881.

64 V. M. Leitner, G. F. Walker and A. Bernkop-Schnürch, *Eur. J. Pharm. Biopharm.*, 2003, **56**, 207–214.

65 M. K. Marschütz and A. Bernkop-Schnürch, *Eur. J. Pharm. Sci.*, 2002, **15**, 387–394.

66 C. E. Kast and A. Bernkop-Schnürch, *Biomaterials*, 2001, 22, 2345–2352.

67 A. Bernkop-Schnürch and A. Greimel, *Am. J. Drug Deliv.*, 2005, **3**, 141–154.

68 A. Bernkop-Schnürch, U. M. Brandt and A. . Clausen, *Sci. pharma*, 1999, **67**, 196–208.

69 A. Bernkop-Schnürch, A. E. Clausen and M. Hnatyszyn, *Int. J. Pharm.*, 2001, **226**, 185–194.

70 G. H. Snyder, M. K. Reddy, M. J. Cennerazzo and D. Field, *Biochim. Biophys. Acta (BBA)/Protein Struct. Mol.*, 1983, **749**, 219–226.

71 J. O. Morales and J. T. McConville, *Drug Dev. Ind. Pharm.*, 2014, **40**, 579–590.

72 J. Bibette, F. L. Calderon and P. Poulin, *Reports Prog. Phys.*, 1999, **62**, 969–1033.

73 S. Slomkowski, J. V. Alemán, R. G. Gilbert, M. Hess, K. Horie, R. G. Jones, P. Kubisa, I. Meisel, W. Mormann, S. Penczek and R. F. T. Stepto, *Pure Appl. Chem.*, 2011, **83**, 2229–2259.

74 T. G. Mason, J. N. Wilking, K. Meleson, C. B. Chang and S. M. Graves, *J. Phys. Condens. Matter*, 2006, **18**, R635–R666.

75 M. K. Sharma and D. O. Shah, *Macro- and Microemulsions*, 1985, **272**, 1–18.

76 D. J. McClements, *Soft Matter*, 2012, **8**, 1719–1729.

77 K. Bouchemal, S. Braincon, E. Perrier and H. Hessi, *Pharm. Nanotechnol.*, 2004, **280**, 241–251.

78 C. Solans, P. Izquierdo, J. Nolla, N. Azemar and M. J. Garcia-Celma, *Curr. Opin. Colloid Interface Sci.*, 2005, **10**, 102–110.

79 C. Solans, D. Morales and M. Homs, *Curr. Opin. Colloid Interface Sci.*, 2016, **22**, 88–93.

80 S. A. Vitale and J. L. Katz, *Langmuir*, 2003, **19**, 4105–4110.

81 T. F. Tadros, *Emulsion formation and stability*, 2013.

82 P. Fernandez, V. André, J. Rieger and A. Kühnle, *Colloids Surfaces A Physicochem. Eng. Asp.*, 2004, **251**, 53–58.

83 T. F. Tadros, *Emulsion Science and Technology*, Wiley-VCH Verlag GmBH, 2009.

84 M. M. Robins, *Curr. Opin. Colloid Interface Sci.*, 2000, 5, 265–272.

85 R. P. Borwankar, L. A. Lobo and D. T. Wasan, *Colloids and Surfaces*, 1992, 69, 135–146.

86 B. P. Binks, W. G. Cho, P. D. I. Fletcher and D. N. Petsev, *Langmuir*, 2000, **16**, 1025–1034.

87 P. W. Voorhes, *J. Stat. Phys.*, 1985, **38**, 231–252.

88 G. de G. Francoise Brochard-Wyart and D. Quere, *Capillary and Wetting Phenomena - Drops, Bubbles, Pearls, Waves*, Springer, New York, 1st edn., 2002.

89 J. Marqusee and J. Ross, *J. Chem. Phys.*, 1984, **80**, 536–543.

90 R. M. Boom, *Food Materials Science: Princples and Practice*, Springer-Verlag, New York, 1st edn., 2007.

91 M. J. Rosen and J. T. Kunjappu, *Surfactants and Interfacial Phenomena*, 2012.

92 R. Murakami, H. Moriyama, T. Noguchi, M. Yamamoto and B. P. Binks, *Langmuir*, 2014, **30**, 496–500.

93 K. L. Thompson, N. Cinotti, E. R. Jones, C. J. Mable, P. W. Fowler and S. P. Armes, *Langmuir*, 2017, **33**, 12616–12623.

94 C. J. Mable, K. L. Thompson, M. J. Derry, O. O. Mykhaylyk, B. P. Binks and S. P. Armes, *Macromolecules*, 2016, **49**, 7897–7907.

95 R. T. Woodward, R. a Slater, S. Higgins, S. P. Rannard, A. I. Cooper, B. J. L. Royles, P. H. Findlay and J. V. M. Weaver, *Chem. Commun. (Camb).*, 2009, **0**, 3554–3556.

96 W. C. Griffin, *J. Cosmet. Chem.*, 1949, **1**, 311–328.

97 R. Sharma, in *Surfactant Adsorption and Surface Solubilization*, American Chemical Society, 1996, vol. 615, p. 1.

98 P. Alexandridis, *Macromolecules*, 1998, **31**, 6935–6942.

99 S. U. Pickering, *J. Chem. Soc. Trans.*, 1907, **91**, 2001–2021.

100 J. Frelichowska, M. A. Bolzinger and Y. Chevalier, *Colloids Surfaces A Physicochem. Eng. Asp.*, 2009, **343**, 70–74.

101 Q. Monégier du Sorbier, A. Aimable and C. Pagnoux, *J. Colloid Interface Sci.*, 2015, **448**, 306–314.

102 P. Finkle, H. D. Draper and J. H. Hildebrand, *J. Am. Chem. Soc.*, 1923, **45**, 2780–2788.

103 B. P. Binks and S. O. Lumsdon, *Langmuir*, 2000, **16**, 8622–8631.

104 G. Xie, P. Krys, R. D. Tilton and K. Matyjaszewski, *Macromolecules*, 2017, **50**, 2942–2950.

105 J. V. M. Weaver, R. T. Williams, B. J. L. Royles, P. H. Findlay, A. I. Cooper and S. P. Rannard, *Soft Matter*, 2008, **4**, 985–992.

106 J. V. M. Weaver, S. P. Rannard and A. I. Cooper, *Angew. Chemie*, 2009, **121**, 2165–2168.

107 J. J. Hobson, S. Edwards, R. A. Slater, P. Martin, A. Owen and S. P. Rannard, *RSC Adv.*, 2018, **8**, 12984–12991.

108 F. Y. Hern, A. Hill, A. Owen and S. P. Rannard, *Polym. Chem.*, 2018, **9**,

1767–1771.

109 F. L. Hatton, L. M. Tatham, L. R. Tidbury, P. Chambon, T. He, A. Owen and S. P. Rannard, *Chem. Sci.*, 2015, **6**, 326–334.

110 K. Matyjaszewski, *Macromolecules*, 2012, **45**, 4015–4039.

111 K. Matyjaszewski and J. Xia, *Chem. Rev.*, 2001, **101**, 2921–2990.

112 K. A. Davis, H. Paik and K. Matyjaszewski, *Macromolecules*, 1999, **32**, 1767–1776.

113 J.-L. Wang, T. Grimaud and K. Matyjaszewski, *Macromolecules*, 1997, **30**, 6507–6512.

114 Y. Li and S. P. Armes, *Macromolecules*, 2005, **38**, 8155–8162.

115 I. Bannister, N. C. Billingham, S. P. Armes, S. P. Rannard and P. Findlay, *Macromolecules*, 2006, **39**, 7483–7492.

116 T. He, D. J. Adams, M. F. Butler, T. Y. Chert, A. I. Cooper and S. P. Rannard, *Angew. Chemie - Int. Ed.*, 2007, **46**, 9243–9247.

117 X.-S. Wang, S. F. Lascelles, R. a. Jackson and S. P. Armes, *Chem. Commun.*, 1999, 1817–1818.

118 K. Matyjaszewski, J.-L. Wang, T. Grimaud and D. A. Shipp, *Macromolecules*, 1998, **31**, 1527–1534.

119 J. Queffelec, S. G. Gaynor and K. Matyjaszewski, *Macromolecules*, 2000, **33**, 8629–8639.

120 Horiba Scientific, *A guidebook to particle size analysis*, 2017.

121 A. Scarpa and A. Guerci, *J. Ethnopharmacol.*, 1982, **5**, 117–137.

122 N. Aboelsoud, *J. Med. Plants Res.*, 2010, **4**, 82–86.

123 J. Jena and A. K. Gupta, *Int. J. Pharm. Pharm. Sci.*, 2012, **4**, 25–29.

124 F. L. Hatton, P. Chambon, T. O. McDonald, A. Owen and S. P. Rannard, *Chem. Sci.*, 2014, **5**, 1844.

125 F. Y. Hern, A. Hill, A. Owen and S. P. Rannard, *Polym. Chem.*, 2018, **9**, 1767–1771.

126 P. J. Roth, T. P. Davis and A. B. Lowe, *Macromolecules*, 2012, **45**, 3221–3230.

127 Z. Hu, T. Cai and C. Chi, *Soft Matter*, 2010, **6**, 2115–2123.

128 T. Young, *Philos. Trans. R. Soc. London*, 1805, **95**, 65–87.

129 Y. Yuan and T. R. Lee, in *Surface Science Techniques*, eds. G. Bracco and B. Holst, Springer-Verlag, Berlin, 51st edn., 2013, vol. 51, pp. 3–32.

130 R. J. Good, *J. Adhes. Sci. Technol.*, 1992, **6**, 1269–1302.

131 Z.-Q. Zhu, Y. Wang, Q. Liu and J.-C. Xie, *Microgravity Sci. Technol.*, 2012, **24**, 181–188.

132 H. W. Fox and W. A. Zisman, *J. Colloid Sci.*, 1950, **5**, 514–531.

133 J. Zhang, J. Li and Y. Han, *Macromol. Rapid Commun.*, 2004, **25**, 1105–1108.

134 R. J. Williams, J. N. Phillips and K. J. Mysels, *Trans. Faraday Soc.*, 1955, **51**, 728–737.

135 P. M. Holland and D. N. Rubingh, ed. M. J. Comstock, American Chemical Society, Washington, 1st edn., 1992, vol. 501, pp. 2–30.

136 H. Akbaş, T. Sidim and M. Işcan, *Turkish J. Chem.*, 2003, **27**, 357–363.

137 Y. Yang, Z. Fang, X. Chen, W. Zhang, Y. Xie, Y. Chen, Z. Liu and W. Yuan, *Front. Pharmacol.*, 2017, **8**, 1–20.

138 S. E. R. Auty, O. Andrén, M. Malkoch and S. P. Rannard, *Chem. Commun.*, 2014, **50**, 6574.

139 D. J. Hall, O. V Khutoryanskaya and V. V Khutoryanskiy, *Soft Matter*, 2011, **7**, 9620–9623.

140 E. E. Hassen and J. M. Gallo, *Jounal Pharm. Resarch*, 1990, **7**, 491–495.

141 H. E. Friedl, S. Dünnhaupt, C. Waldner and A. Bernkop-Schnürch, *Biomaterials*, 2013, **34**, 7811–7818.

142 G. S. Irmukhametova, G. A. Mun and V. V Khutoryanskiy, *Langmuir*, 2011, **27**, 9551–9556.

143 C. A. Withers, M. T. Cook, L. Methven, M. A. Gosney and V. V Khutoryanskiy, *Food Funct.*, 2013, **4**, 1668–1674.

144 S. Flynn, S. D. Dale, A. B. Dwyer, P. Chambon and S. P. Rannard, *J. Polym. Sci. Part A Polym. Chem.*, 2017, **55**, 3963–3967.

145 M. Boegh, Baldursdottir, S. G, A. Mullertz and H. M. Nielsen, *Eur. J. Pharm. Biopharm.*, 2014, **87**, 227–235.

146 G. Lafitte, O. Söderman, K. Thuresson and J. Davies, *Biopolym. Orig. Res. Biomol.*, 2007, **86**, 165–175.

147 S. K. Lai, D. E. O'Hanlon, S. Harrold, S. T. Man, Y.-Y. Wang, R. Cone and J. Hanes, *Proc. Natl. Acad. Sci.*, 2007, **104**, 1482 LP-1487.

148 J. S. Suk, S. K. Lai, N. J. Boylan, M. R. Dawson, M. P. Boyle and J. Hanes, *Nanomedicine (Lond).*, 2011, **6**, 365–375.

149 J. Suh, M. Dawson and J. Hanes, *Adv. Drug Deliv. Rev.*, 2005, **57**, 63–78.

150 R. A. Cone, *Adv. Drug Deliv. Rev.*, 2009, **61**, 75–85.

151 A. W. Larhed, P. Artursson, J. Gråsjö and E. Björk, *J. Pharm. Sci.*, 1997, **86**, 660–665.

152 A. W. Larhed, P. Artursson and E. Björk, *Pharm Res*, 1998, **15**, 66–71.

153 A. Macierzanka, A. R. Mackie, B. H. Bajka, N. M. Rigby, F. Nau and D. Dupont, *PLoS One*, 2014, **9**, 1–11.

154 R. Williams, R. Lace, S. Kennedy, K. Doherty and H. Levis, *Adv. Healthc. Mater.*, 2018, **7**, 1–13.

155 A. Swidsinski, V. Loening-Baucke, F. Theissig, H. Engelhardt, S. Bengmark, S. Koch, H. Lochs and Y. Dorffel, *Gut*, 2007, **56**, 343–350.

156 H. Eyring, *J. Chem. Phys.*, 1935, **3**, 107–115.

157 F. Lallemand, P. Daull and J.-S. Garrigue, in *Mucosal Delivery of Biopharmaceuticals*, eds. J. das Neves and B. Sarmento, Springer, Boston, 1st edn., 2014, pp. 517–535.

158 P. Ames and A. Galor, *Clin. Investig. (Lond).*, 2015, **5**, 267–285.

159 T. J. Millar and B. S. Schuett, *Exp. Eye Res.*, 2015, **137**, 125–138.

160 F. Paulsen, G. Langer, W. Hoffmann and M. Berry, *Cell Tissue Res.*, 2004, **316**, 167–177.

161 B. A. Nichols, M. L. Chiappino and C. R. Dawson, *Investig. Ophthalmol. Vis. Sci.*, 1985, **26**, 464–473.

162 S. Mishima, *Arch. Ophthalmol.*, 1965, **73**, 233–241.

163 E. W. Gower, L. J. Keay, R. A. Oechsler, A. Iovieno, E. C. Alfonso, D. B. Jones, K. Colby, S. S. Tuli, S. R. Patel and S. M. Lee, *Ophthalmology*, 2010, **117**, 2263–2267.

164 R. L. Sun, D. B. Jones and K. R. Wilhelmus, *Am. J. Ophthalmol.*, 2007, **143**, 1043–1045.

165 K. Morand, A. C. Bartoletti, A. Bochot, G. Barratt, M. L. Brandely and F. Chast, *Int. J. Pharm.*, 2007, **344**, 150–153.

166 K. C. Gray, D. S. Palacios, I. Dailey, M. M. Endo, B. E. Uno, B. C. Wilcock and M. D. Burke, *Proc. Natl. Acad. Sci.*, 2012, **109**, 2234–2239.

167 N. R. H. Stone, T. Bicanic, R. Salim and W. Hope, *Drugs*, 2016, **76**, 485–500.

168 F. Lallemand, O. Felt-Baeyens, K. Besseghir, F. Behar-Cohen and R. Gurny, *Eur. J. Pharm. Biopharm.*, 2003, **56**, 307–318.

169 F. Lallemand, M. Schmitt, J. L. Bourges, R. Gurny, S. Benita and J. S. Garrigue, *Eur. J. Pharm. Biopharm.*, 2017, **117**, 14–28.

170 H. Liang, C. Baudouin, P. Daull, J.-S. Garrigue and F. Brignole-Baudouin, *Mol. Vis.*, 2012, **18**, 2195–2204.

171 P. A. Hunter, K. R. Wilhelmus, N. S. Rice and B. R. Jones, *Clin. Exp. Immunol.*, 1981, **45**, 173–177.

172 A. K. Leck, P. A. Thomas, M. Hagan, J. Kaliamurthy, E. Ackuaku, M. John, M. J. Newman, F. S. Codjoe, J. A. Opintan, C. M. Kalavathy, V. Essuman, C. A. N. Jesudasan and G. J. Johnson, *Br. J. Ophthalmol.*, 2002, **86**, 1211–1215.

173 M.-A. Javadi and S. Feizi, *J. Ophthalmic Vis. Res.*, 2011, **6**, 192–198.

174 S. C. Pflugfelder, *Am J Opthalmol*, 2004, **137**, 337–342.

175 R. A. Laibovitz, S. Solch, K. Andriano, M. O'connell and M. H. Silverman, *Cornea*, 1993, **12**, 315–323.

176 D. Stevenson, J. Tauber and B. L. Reis, *Ophthalmology*, 2000, **107**, 967–974.

177 J. Scruggs, T. Wallace and C. Hanna, *Ann. Ophthalmol.*, 1978, **10**, 267–271.

178 M. R. Prausnitz and J. S. Noonan, *J. Pharm. Sci.*, 1998, **87**, 1479–1488.

179 M. Peduzzi, A. Debbia and A. Monzani, in *Ophthalmic Drug Delivery*, eds. M. F. Saettone, M. Bucci and P. Speiser, Springer, New York, 1st edn., 1987, pp. 1–5.

180 G.M. Cooper, *The Cell: A Molecular Approach*, Sinauer Associates Incorporated, Sunderland, 2nd edn., 2000.

181 S.-Y. Chiang, J. Welch, F. J. Rauscher III and T. A. Beerman, *Biochemistry*, 1994, **33**, 7033–7040.

182 R. Buntrock, in *Journal of the American Chemical Society*, eds. M. J. O'Neil, P. E. Heckelmen, C. B. Koch and K. J. Roman, American Chemical Society, Whitehouse Station, 14th edn., 2007, vol. 129, pp. 2197–2564.

183 Q. Zia, O. Mohammad, M. A. Rauf, W. Khan and S. Zubair, *Sci. Rep.*, 2017, **7**, 1–19.

184 D. Borchman, M. C. Yappert, S. E. Milliner, R. J. Smith and R. Bhola, *Lipids*, 2013, **48**, 1269–1277.

185 D. Borchman, G. Georgiev, M. Yappert and N. Yokoi, *Invest. Ophthalmol. Vis. Sci.*, 2013, **54**, 927.

186 G. Ismailos, C. Reppas, J. B. Dressman and P. Macheras, *J. Pharm. Pharmacol.*, 1991, 43, 287–289.

187 C. Maïssa, M. Guillon, P. Simmons and J. Vehige, *Contact Lens Anterior Eye*, 2010, **33**, 76–82.

188 M. M. Hom and P. A. Simmons, *Rev Optom.*, 2003, **140**, 124–126.

189 E. Goto, J. Shimazaki, Y. . Monden, Y. Takano, Y. Yagi, S. Shimmura and K. Tsubota, *Ophthalmology*, 2002, **109**, 2030–2035.

190 J. J. Hobson, A. Owen and S. P. Rannard, *The potential value of nanomedicine and novel oral dosage forms in the treatment of HIV*, 2018.